SP-434

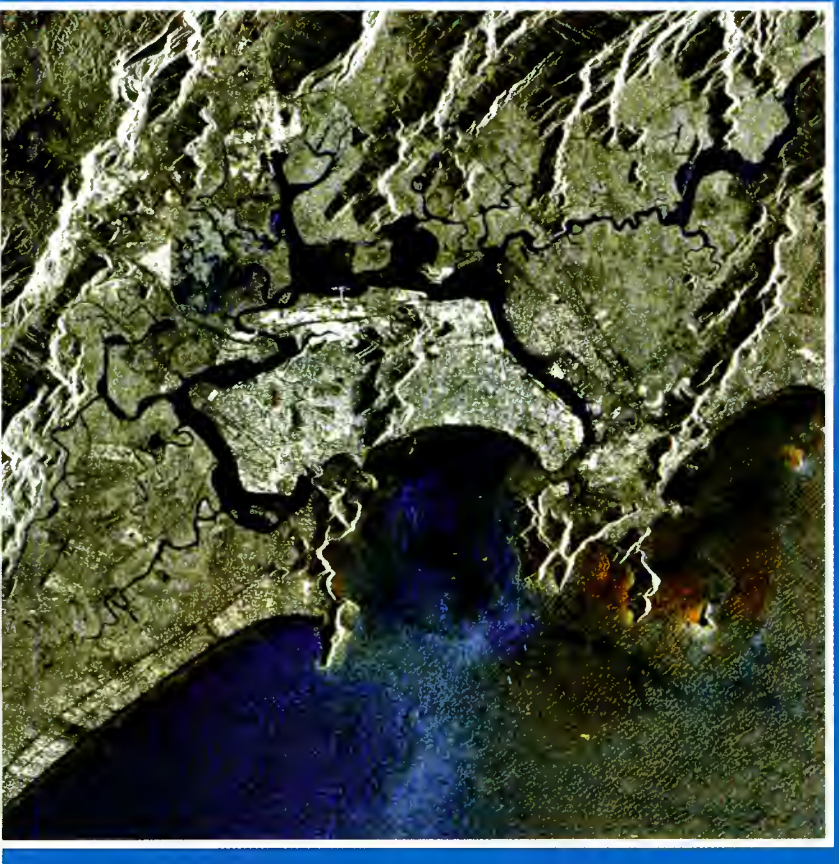

SECOND LATINO-AMERICAN SEMINAR ON RADAR REMOTE SENSING

# Image Processing Techniques

Santos, Sao Paulo, Brazil
11-12 September 1998

European Space Agency
Agence spatiale européenne

**esa SP-434**
ISBN 92-9092-736-4
October 1998

*SEGUNDA JORNADA LATINO-AMERICANA*
*DE SENSORIAMENTO REMOTO POR RADAR*

**Técnicas de Processamento de Imagens**

SECOND LATINO-AMERICAN SEMINAR ON
RADAR REMOTE SENSING

# Image Processing Techniques

Santos, Sao Paulo, Brazil
11-12 September 1998

*Co-Sponsors:*

Instituto Nacional de Pesquisas Espacias (*INPE*)
Comisión Nacional de Actividades Espaciales (*CONAE*)
European Space Agency (*ESA*)
Departamento de Informática da Universidade de Pernambuco (*DI-UFPE*)

Cover image : *Multitemporal RGB colour composite image of the Santos region, Brazil, generated from two SAR scenes of ERS-2 satellite, acquired respectively on 8 May (red) and 4 April 1996 (blue) at Cuiabá station, Brazil.*

---

**IMAGE PROCESSING TECHNIQUES** *(ESA SP-434)*

*Proceedings of the Second Latino-American Seminar on Radar Remote Sensing*
Santos, SP Brazil, 11-12 September 1998

| | |
|---|---|
| *Proceedings published by:* | ESA Publications Division<br>ESTEC, Noordwijk, The Netherlands |
| *Compiled by :* | Tan-Duc Guyenne |
| *Price :* | 70 Dfl. |
| *Copyright :* | © 1998 European Space Agency |
| *ISBN 92-9092-736-4* | Printed in The Netherlands |

# Contents

## Radar 1

*Coordinators:* Jorge Lira, *UNAM* &
Corina da Costa Freitas, *INPE*



## Radar 2

*Coordinators:* Laura Frulla, *CONICET* &
Sidnei J.S. Sant'Anna, *INPE*

## Radar 3

*Coordinators:* Alejandro C. Frery, *UFPE &*
Thuy Le Toan, *CESBIO*



## Radar 4

*Coordinators:* David Fernandes, *ITA &*
Maurizio Fea, *ESA/ESRIN*

# Radar 1

*Coordinators:* Jorge Lira, *UNAM* &
Corina da Costa Freitas, *INPE*

# THE USE OF MODELS FOR UNDERSTANDING SAR IMAGES

C J Oliver
DERA, St Andrews Road, Malvern, Worcs., WR14 3PS, UK.
Tel: (44) 1684 895165; Fax: (44) 1684 894481; E-mail: chris@sar.dera.gov.uk

## ABSTRACT

This paper comprises a review of methods for extracting information from SAR images. We begin by considering the process of image understanding in the context of a SAR exploitation application. We show that information is extracted in terms of combination of data and world models. These are then exploited using optimised estimators based on the distribution of the image intensity. We demonstrate the importance of providing a rigorous theoretical framework for this process.

## INTRODUCTION

Human perception is based on a sophisticated set of internal rules, developed during the early years of our lives, and is extremely effective at understanding images. For computer-based image understanding it is necessary to define an appropriate set of rules to achieve the same goal. Unfortunately we are unable to specify the rules by which our visual understanding is achieved and it is necessary to define suitable rules from scratch. These will depend on a variety of models to describe the properties of the data and the scene itself. Initially, the process starts with a particular data set (or image). This may take a variety of forms from a single intensity image, to interferometric, polarimetric or multi-temporal data. The choice of the form of input data must be determined by the final application. Sensor properties such as polarisation, wavelength, resolution and incidence angle all effect the nature of the image data through the physics of the scattering and imaging process. Clearly it is unprofitable to attempt to extract information for the desired application if the physical process of imaging does not preserve this information. Thus an understanding of the physics of the scattering mechanism is crucial to the selection of the original image data.

Assuming that appropriate data is available, the image understanding process then follows the flow diagram shown in figure 1. A particular feature of the data is selected for study. As shown by the diagram this is controlled by a 'data model'. This encapsulates properties of the form of the data itself, given some underlying scattering cross-section. It may have a physical origin, as in speckle, or depend on phenomenological properties of the scene, such as clutter texture. In each case the precise form of the model will determine the optimum feature of the data to select in order to extract the desired information. This provides one input for determining the form of the image interpretation technique. The other input to the technique is determined by a 'world model', which encapsulates typical properties of the scene, for example that neighbouring pixels tend to have similar intensity. When these two models are exploited correctly, the information they provide should be optimised for the application, the form of the data and the scene properties. Once this information is derived it can be provided to the application. If the information is inadequate at this stage, it might imply that the original physical or phenomenological description requires modification. In fact there are many other feedback paths, not illustrated, in the process of optimising the image interpretation technique.

In this paper we discuss the roles of these different models in a variety of image-understanding functions; each of which addresses different applications. The material is largely extracted from a recent book on the topic [1]. The reader is referred to this for more detail, including the theoretical derivations of the different algorithms and a bibliography of original work in this area. Many of the algorithms described here have been implemented in the CAESAR software package [2].

## DATA MODELS

The justification for two of the most important data models are visible in the different regions of clutter identified in figure 2. This figure shows a small region of high-resolution clutter. We observe man-made structural features, such as a road, field boundaries, the edges of wooded areas etc., which correspond to the type of information represented on a map.



**Image Processing Techniques** *Proceedings of the 2nd Latino-American Seminar on Radar Remote Sensing held at Santos, Sao Paulo, Brazil, 11-12 September 1998* (ESA SP-434, October 1998).

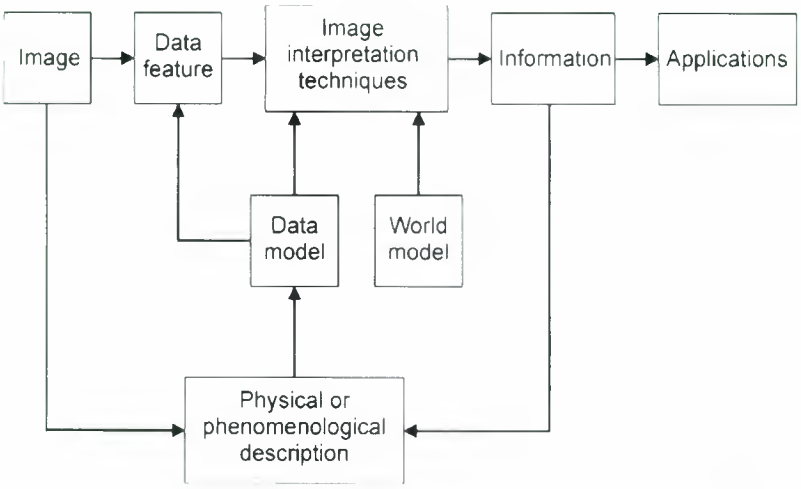


Figure 1: Flow chart showing the interrelation of measurements, data models and information.

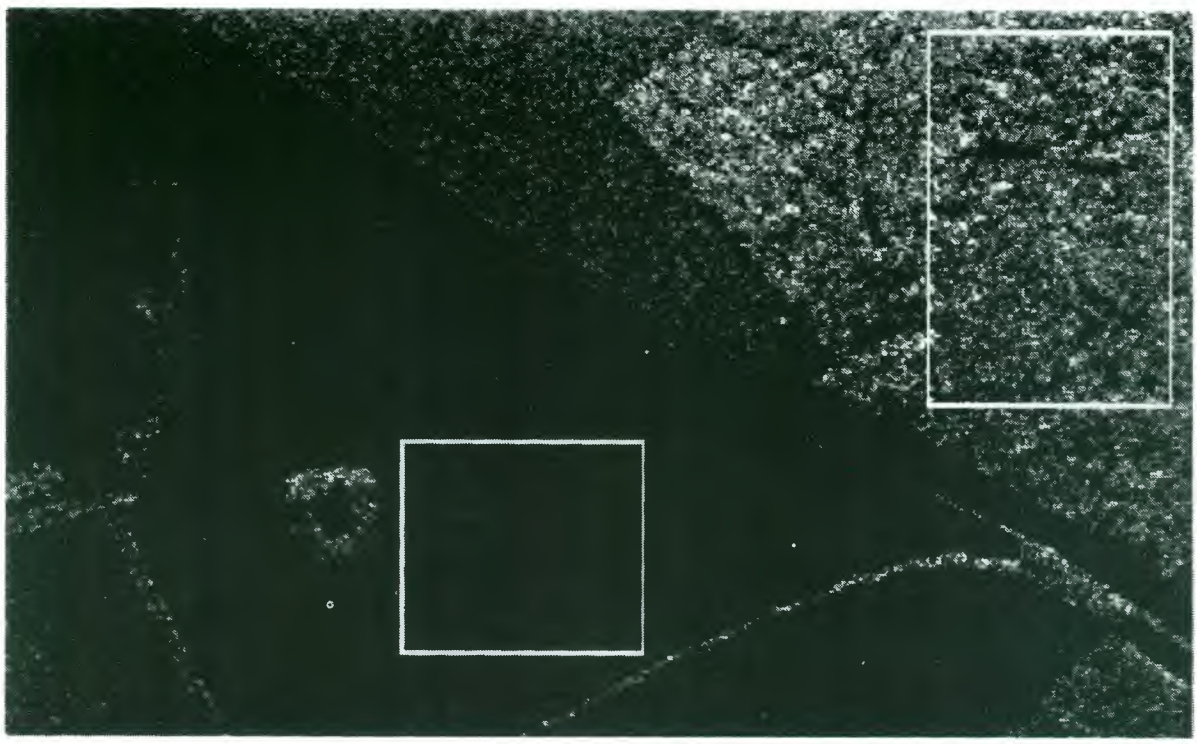

Figure 2: High-resolution image of region of English countryside showing different types of natural clutter.

The region of field identified shows little sign of underlying cross-section fluctuation. Coherent interference between the many random scatterers within a resolution cell gives rise to a complex Gaussian received field, a negative exponential intensity distribution and a Rayleigh-distributed amplitude. This characterises the physically-based 'speckle model' which underlies nearly all SAR data. The area of woodland identified in figure 2, on the other hand, shows evidence of additional fluctuations arising from bright returns from tree crowns with associated shadowing behind the trees. This leads to a 'product model' representation for SAR images in which an underlying radar cross section (RCS) is combined with the speckle model during imaging [3]. These variations in RCS are encapsulated in an 'RCS model'. For many natural clutter scenes, a gamma-distributed noise process provides a suitable form for the RCS model. When this gamma-distributed RCS is combined with speckle during imaging the resultant intensity or amplitude would be K-distributed [3-5].

## IMAGE UNDERSTANDING USING THE SPECKLE MODEL

We now develop a series of image-understanding techniques which combine different data models with world models which describe those aspects of the scene which relate to the required application. Initially we restrict our attention to the exploitation of image intensity. The discussion will be illustrated by considering the test image illustrated in figure 3. Structural features are clearly evident, as is the presence of speckle. Note in particular the discrete scatterers in the field at the bottom left of the image.

Let us first address the problem of removing the noise-like effects of speckle so evident in regions of uniform RCS. In order to achieve this we introduce a 'correlated neighbourhood' world model, which asserts that neighbouring pixels are similar. This can be exploited in a variety of algorithms leading to the results shown in figures 4(a)-(d). Figure 4(a) shows the consequence of applying a local average to the data. This corresponds to assuming that the RCS over the averaging window is constant. Clearly this achieves good despeckling in uniform regions at the expense of averaging out structure. Figures 4(b) and (c) make use of the statistical properties within the window to improve the estimate of the centre pixel. Minimum mean-square error filtering, shown in figure 4(b) [6,7], minimises the error for a measured variance whereas in figure 4(c) the intensity within the window is assumed to be gamma-distributed and the corresponding Maximum a Posteriori (MAP) reconstruction provided [8,9]. Both give good speckle smoothing in uniform regions and retain structural detail. However, both show increased noise in the reconstruction surrounding image structure. The gamma MAP reconstruction has been widely and successfully used for speckle reduction in applications where this uncertainty near edges is not a problem. A different approach to despeckling is illustrated in figure 4(d). A simulated annealing algorithm identifies which 3-pixel configuration within a 3×3 window is most probable [10]. The reconstructed pixel value is then the gamma MAP estimator for that configuration. Since speckle reduction over such a small window is very weak, the process is iterated many times until the reconstruction converges on the global optimum. Visually, the quality of figure 4(d) is much better than the other results, giving good speckle reduction in uniform regions without the noisy reconstruction around structure.

Figure 3: Sample of high-resolution X-band imagery use to test algorithms.

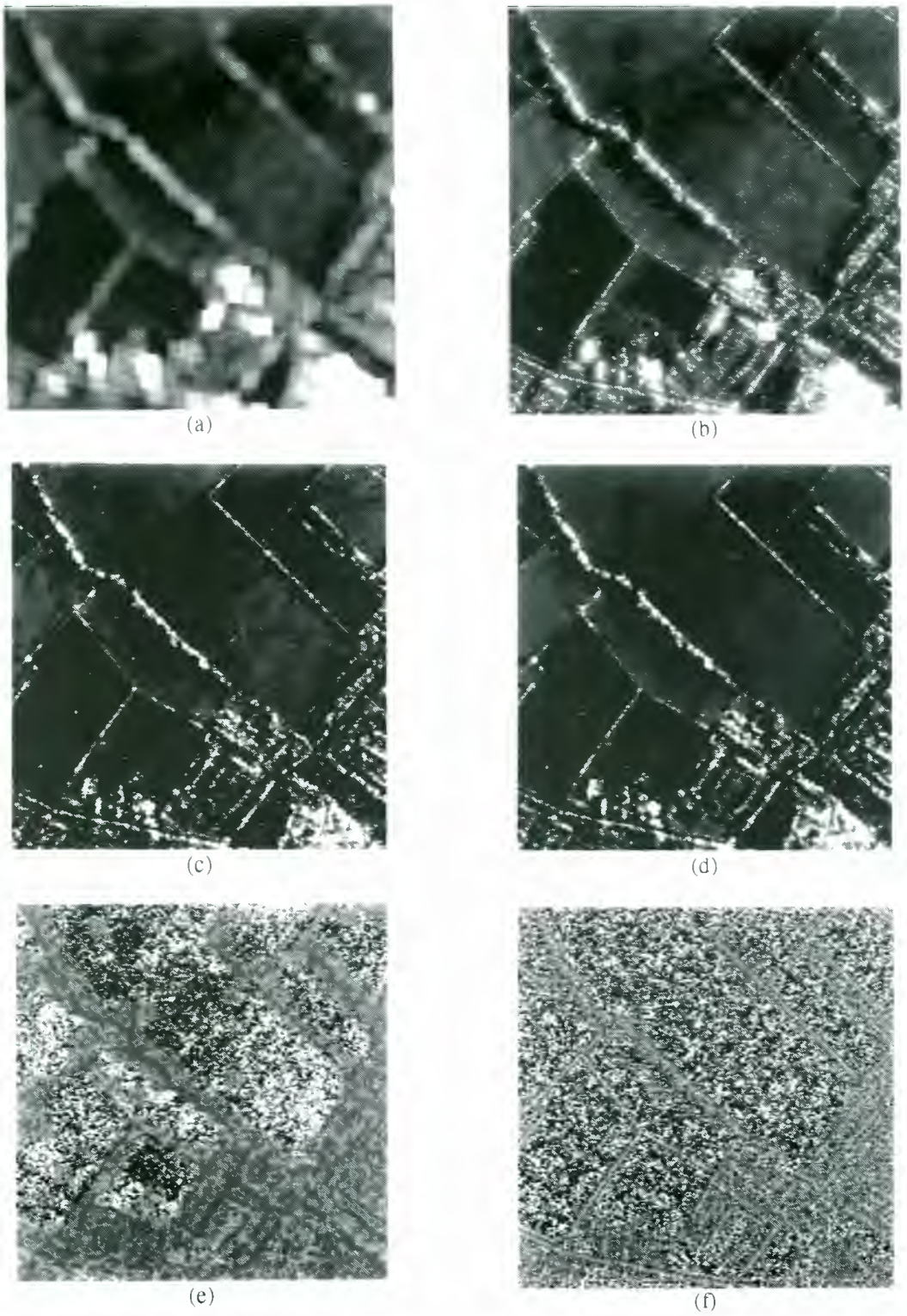


Figure 4: Despeckled reconstructions of the test image in figure 2: (a) local averaging; (b) minimum mean-square error; (c) gamma MAP; (d) simulated annealing. Ratio test applied to (e) gamma MAP and (f) simulated annealing.

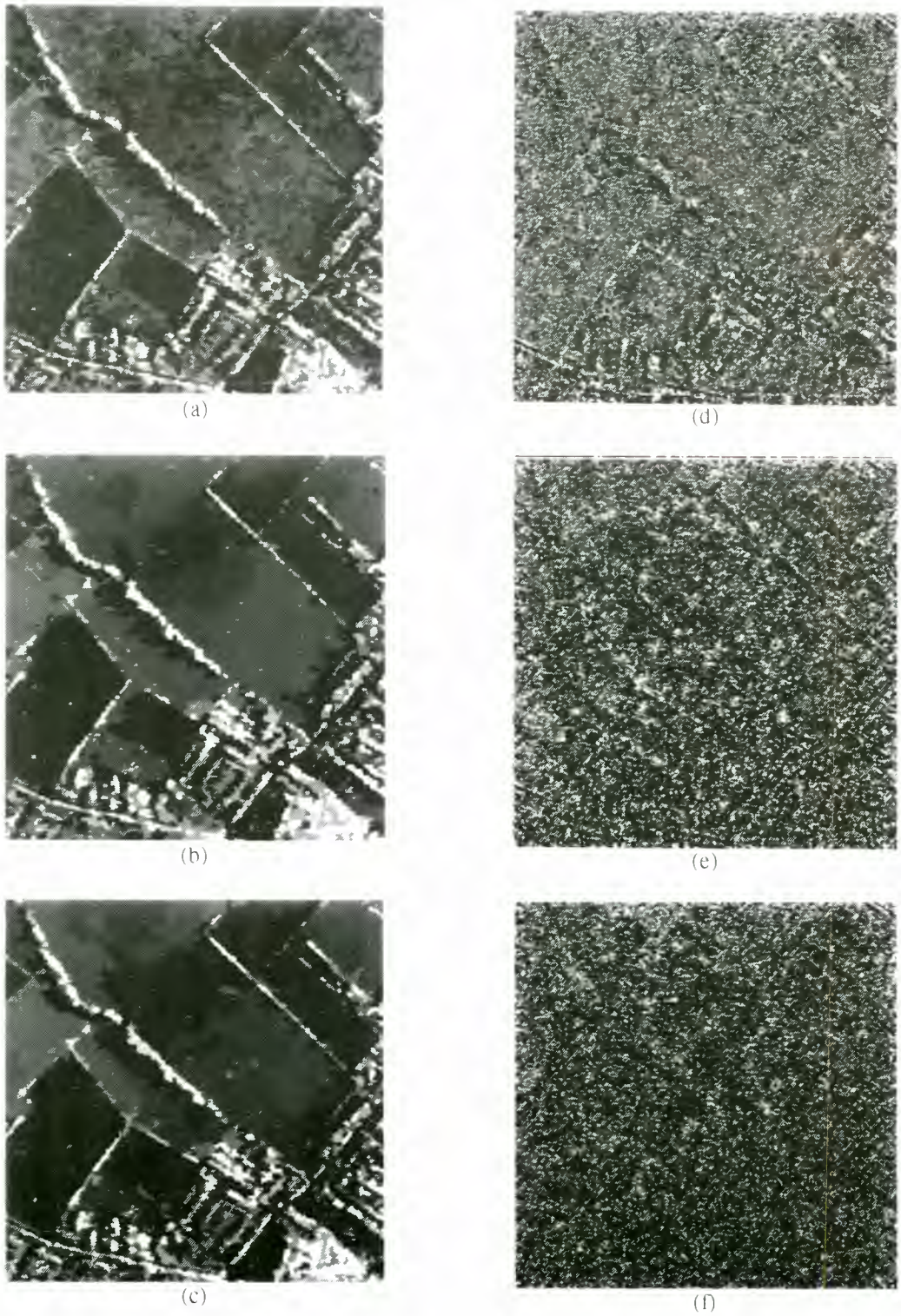


Figure 5: Segmented reconstructions of figure 2: (a) RWSEG, (b) MUM, (c) anneal. Ratio tests of quality of reconstruction: (d) RWSEG, (e) MUM and (f) anneal.

A demonstration of the quality of these reconstructions can be obtained by considering the ratio of the original image to its reconstruction [11]. If the reconstruction reproduced the underlying RCS precisely, the speckle model would assert that this ratio should correspond to pure speckle. Any evidence of structure, or a failure to retain the correct statistics, would indicate a failure of the technique to apply the speckle model correctly. We illustrate this ratio for the gamma-MAP and simulated annealing methods in figures 4(e) and (f) respectively. Both show considerable residual structure indicating that the reconstruction techniques are not recovering the true RCS.

The 'cartoon model' provides an alternative world model which asserts that images are made up of regions of uniform RCS. The role of the reconstruction is to identify the edges of these regions and their strength. Note that this imposes a stronger constraint than the correlated neighbourhood model. The result of applying an edge-detection and region-growing algorithm (RWSEG) is illustrated in Figure 5(a) [12]. This provides an adaptive test for the presence of edges within windows of increasing size. Strong edges can be detected with small windows so that high resolution is preserved. As the window size increases more sensitive edge detection is possible but the resolution is degraded. The results are structurally reasonable. Indeed, if we perform the quality test using the ratio of the original image to its reconstruction, it is clear that the result in figure 5(b) conforms much more closely to the speckle model than the previous despeckling techniques. However, there is still much evidence of distortion around scene structure. An alternative algorithm, Merge Using Moments (MUM) [13], yields the results shown in figure 5(c). This approach tests whether regions of pixels should be merged with their neighbours on the basis of the statistics. It is capable of operating on single pixel regions with single-look SAR images. Figure 5(d) shows a considerable improvement in reconstruction quality compared with 5(b). The final example, illustrated in figure 5(e), is a consequence of applying a simulated annealing algorithm to determine which configuration of a specified number of regions provides the optimum reconstruction, given the speckle and cartoon models. An additional constraint on the curvature of region edges is also introduced [14]. Figure 5(f) reveals that this reconstruction is closest to corresponding to the models. This achieved, however, at the expense of increased processing time.

## IMAGE UNDERSTANDING USING THE TEXTURE MODEL

Earlier we demonstrated that the RCS of natural clutter is often consistent with a gamma-distributed noise process. This will only be observed, of course, if the resolution of the sensor is adequate to preserve this image texture, which limits the range of sensor systems to which such an approach is feasible. In figure 6 we show a typical SAREX image of part of the Tapajos rain forest, obtained with the 6-look CCRS C-band SAR with a resolution of about 6m and an incidence angle of 65°. The Santarem-Cuiaba highway runs from top right to bottom left. The land on the left of this highway is predominantly primary forest while that to the right is a mixture of primary forest, regenerating regions and clearings. The human observer is able to classify at least into forest/not forest categories on the basis of the texture in the image. Clearings have very little texture, corresponding merely to 6-look speckle, whereas primary forest has fluctuations corresponding to an order parameter value of about 1.

In order to provide an automatic technique to exploit the texture it is essential to determine the form of the distribution, derive the corresponding optimum texture measure and then exploit rigorous methods which preserve the information while determining the global optimum. For multi-look SAR the clutter would be expected to be approximately gamma-distributed since the speckle fluctuations are largely averaged out. The Maximum Likelihood texture measure is then the normalised log of the intensity defined by $U \equiv \overline{\ln I} - \ln \bar{I}$, where the bars denote local averages over a window [14]. The corresponding value for figure 6, derived over a 16×16 window is shown in figure 7(a). Regions of uniform texture in the clearings have smaller values of the texture measure than primary forest regions. However, there is still considerable variation caused by the speckle. This can be reduced following the same techniques that were developed for intensity images. In fact $U$ can be approximated by a gamma distribution of order 0.5. Figure 7(b) then shows the result of segmenting this texture estimator.

Once the statistical uncertainty in the definition of the texture measure is reduced, it is possible to assign a threshold to the data, corresponding to an order parameter of about 3.0, to classify the image into forest and not forest regions. The boundary between these regions is overlaid on the original image in figure 8. Clearly there is reasonable consistency between this classification and that provided by a human interpreter. The effectiveness of the method can only be quantified, however, by comparison with the classifications yielded by other sensors and ground truth measurements.

Figure 6: C-band SAREX image of region of Tapajos rain forest.

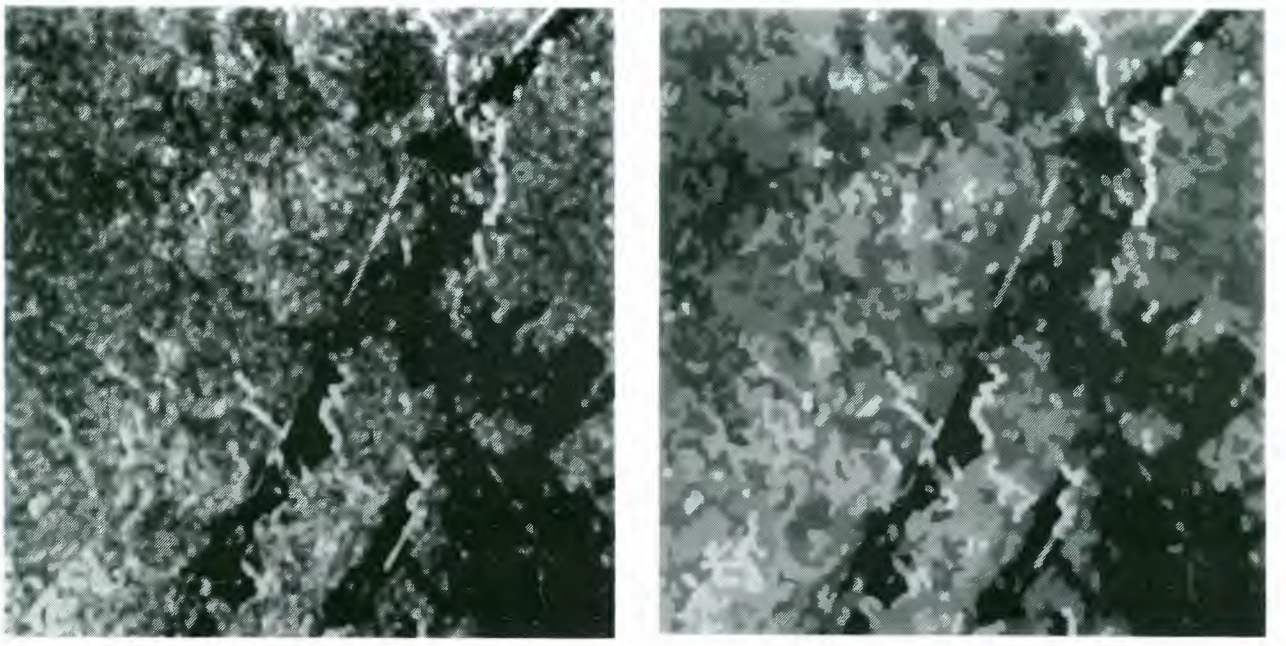

(a) (b)

Figure 7: (a) Normalised log texture and (b) annealed texture for figure 6.

## CONCLUSIONS

This presentation has been concerned with the introduction of image interpretation tools based on the rigorous exploitation of a variety of data and world models. The results show promise for both intensity and texture segmentation and texture classification. Note that the discussion has been centred on high-resolution systems. The texture measure in particular cannot be applied in the same way to low resolution data. It is essential in any study of the use of image-interpretation techniques to keep the final application firmly in mind. It might well be that totally different methods, using different sensors and depending on different image properties, could be preferable for a particular application. The user must identify the correct tool for his application.

## REFERENCES


[1] Oliver C J and Quegan S, 'Understanding Synthetic Aperture Radar Images', 1998, Artech House: Boston.

[2] CAESAR SAR exploitation software provided by N A Software, Liverpool, UK.

[3] Ward K D, 'Compound representation of high resolution sea clutter', *Electron. Lett.*, Vol. 17, 1981, pp. 561-565.

[4] Jakeman E and Pusey P N, 'A model for non-Rayleigh sea echo', *IEEE Trans. Antennas Propagation*, Vol. 24, 1976, pp. 806-814.

[5] Oliver C J, 'Correlated K-distributed clutter models', *Opt. Acta*, Vol. 32, 1985, pp.1515-1547.

[6] Lee J S, 'Digital image enhancement and noise filtering by use of local statistics', *IEEE Trans. Pattern Anal. Mach. Intell.*, 1982, pp. 157-166.

[7] Kuan D T, Sawchuk A A, Strand T C and Chaval P C, 'Adaptive restoration of images with speckle', *IEEE Trans. Acoust. Speech Process.*, Vol. 35, 1987, pp. 373-383.

[8] Oliver C J, 'Information from SAR images', *J. Phys. D: Appl. Phys.*, Vol. 24, 1991, pp. 1493-1514.

[9] Lopes A, Nezry E, Touzi R and Laur H, 'Structure detection and adaptive speckle filtering in SAR images', *Int. J. Remote Sens.*, Vol. 14, 1993, pp. 1735-1758.

[10] White R G, 'A simulated annealing algorithm for radar cross-section estimation and segmentation', *SPIE Int. Conf. on Applications of Artificial Neural Networks V*, Orlando, Florida, *SPIE Proc.*, Vol. 2243, 1994, pp. 231-241.

[11] White R G, 'Change detection in SAR imagery', *Int. J. Remote Sens.*, Vol. 12, 1991, pp. 339-360.

[12] Cook R, McConnell I and Oliver C J, 'MUM (Merge Using Moments) segmentation for SAR images', *Europto Conf. on SAR Data Processing for Remote Sensing*, Rome, *SPIE Proc.*, Vol. 2316, 1994, pp. 92-103.

[13] Cook R, McConnell I, Stewart D and Oliver C J, 'Segmentation and simulated annealing', *Europto Conf. on SAR Image Analysis, Simulation and Modelling II*, Taormina, Italy, *SPIE Proc.*, Vol. 2958, 1996, pp. 30-37.

[14] Oliver C J. 'Optimum texture measures for SAR clutter', *J. Phys. D: Appl. Phys.*, Vol. 26, 1993, pp. 1824-1835.

[15] Oliver C J. 'Rain forest classification based on SAR texture', 1998, submitted to *IEEE Trans. Geosci. Remote Sens.*

Figure 8: Overlay of forest/non forest region boundaries on original image from figure 6.

# Analysing multitemporal SAR images

SHAUN QUEGAN[1]
THUY LE TOAN[2]
[1]Sheffield Centre for Earth Observation Science
University of Sheffield, Sheffield S3 7RH, UK
S.Quegan@sheffield.ac.uk
[2]Centre d'Etudes Spatiales de la Biosphère
18 avenue Belin, 31055 Toulouse, CEDEX France
thuy.letoan@cnes.cesbio.fr

**Abstract.** Applications of multitemporal SAR data in many cases require accurate estimates of the backscattering coefficient at each time. Here we describe how multitemporal and spatial filtering can be combined in a processing chain to greatly improve the radiometric accuracy of the data and how the general methods can be simplified in the case of ERS data. The results will be illustrated using ERS-2 images in the context of exploiting change detection for forest applications.

**Keywords:** Change detection, image filtering.

## 1 Introduction

A major advantage of satellite SAR is its ability to acquire precisely calibrated images which are unaffected by cloud. This means that time series of accurate measurements are available for environmental monitoring and applications. Although interferometric coherence and phase difference can be measured under certain time interval and baseline conditions, changes in the backscattering coefficient may be more useful for operational applications, since these are routinely available under almost all conditions for a satellite SAR. For mapping purposes, this requires making use of the differing temporal signatures of different land cover types. Important examples are found in forestry and agriculture. Forestry exploits the low temporal change of forests compared to other cover types (Grover *et al.*, 1998; Le Toan *et al.*, 1995). By contrast, rice mapping relies on the high temporal change associated with wetland rice (Le Toan et al., 1997). In more general agriculture, temporal signatures have been used to separate different crop types (for several examples, see Wooding *et al.*, 1994).

However, exploiting such time series requires a processing chain which can first produce registered, calibrated images, then reduce the radiometric uncertainty in the measurements by temporal and spatial filtering and finally use the time sequence of backscattering coefficients to make decisions, for example about the type of land cover. Our main concern in this paper is the filtering step in the processing chain, whose purpose is to provide a best estimate of $\sigma^0$ at each pixel and at each time, given a multitemporal sequence of registered images. Multitemporal filtering is an example of a more general class of problems where several images of the same scene are available (for example, at different frequencies and polarisations) and we wish to combine them in some optimal way to recover the information they contain at each pixel. In Section 2, after displaying the general solution to this problem, we will describe how it becomes modified in the case of ERS 35 day repeat PRI images from vegetated regions, to provide a particularly simple and effective algorithm.

The apparent simplicity of the algorithm is, however, complicated by the fact that it relies on local properties of the individual images in the multitemporal sequence. These must be estimated from the data, which introduces a spatial dimension into the algorithm and requires adaptive methods if spatial resolution is not to be severely degraded. These methods, and their effects on the statistics of the filtered image, are described in Section 3.

Filtering may be used to improve the visual appearance of an image, but it is often also used as a precursor to a decision step such as classification. In this case, the radiometric properties of the classes we wish to separate provide constraints on the accuracy with which $\sigma^0$ must be estimated. In forest classification, the improvement in the estimates of $\sigma^0$ provided by multitemporal filtering is often insufficient to meet the required accuracy. Accuracy is here thought of in terms of classification error, which in simple thresholding schemes is dependent on the overlap in the probability density functions (PDFs) of the different

classes being considered. This overlap depends on the differences between the backscattering coefficients of the cover types we wish to discriminate and the width of the PDFs. A convenient measure of the width is given by the equivalent number of looks (ENL), which is defined by

$$\text{ENL} = \frac{\text{mean}^2}{\text{variance}} \qquad (1)$$

In this expression, the statistical quantities are appropriate to an ideal, uniform (untextured) target in which the only sources of fluctuation come from speckle, after whatever filtering operations have been applied to produce the final data. Increasing the ENL is equivalent to decreasing the width of the PDF. We assume that the ENL of the original data is known (for ERS PRI data, ENL = 3).

The ENL of the PRI data is inadequate for most classification purposes but can be greatly improved by multitemporal filtering, up to a limit imposed by the number of independent images available. Spatial filtering may then be necessary if successful classification relies on further increases in the ENL. There are many algorithms available to perform this task, but in Section 4 we will explain how the properties of ERS data from the 35 day repeat cycle suggest that a simple approach is most suitable when our interest is in vegetated targets. Section 5 provides a brief summary and our conclusions.

## 2 Multitemporal filtering

The problem of combining several images from the same scene in order to provide optimal reduction of speckle has been addressed by a number of authors (Oliver and Quegan, 1998; Bruniquel and Lopes, 1997; Novak *et al.*, 1993). If only intensity data are available, as in our case, the general linear solution for producing a single image with minimal normalised variance is given in Oliver and Quegan (1998) as a weighted sum

$$J(x,y) = \sum_{i=1}^{M} A_i(x,y)\, I_i(x,y), \qquad (2a)$$

where $I_i$ , $i = 1,..., M$, is the intensity value at position $(x, y)$ in channel $i$ out of $M$ (registered) channels. The weighting coefficients are defined by the relation

$$\mathbf{A} \propto C_I^{-1}\sigma \qquad (2b)$$

where $A^t = (A_1, \ldots, A_M)$, $\sigma^t = (\sigma_1,\ldots,\sigma_M) = (\langle I_1\rangle,\ldots,\langle I_M\rangle)$ and $C_I$ is the covariance matrix of the intensity data

$$C_I(i,j) = \langle I_i I_j\rangle - \langle I_i\rangle\langle I_j\rangle \qquad (3)$$

In these expressions and subsequently we omit the positional coordinates $(x, y)$.

In this solution a single image is produced in which the speckle has been minimised, but in fact the image it produces is essentially featureless, unless there are strong variations in the local correlation structure. A more useful approach is to form $M$ images of the form

$$J_k = \sum_{i=1}^{M} A_{ki} I_i \quad k = 1,\ldots, M \qquad (4a)$$

under the condition that $J_k$ is unbiased, so that $\langle J_k\rangle = \langle I_k\rangle$, and $J_k$ has minimum variance. This problem has the solution

$$A_k^t = \sigma_k \frac{C_I^{-1}\sigma}{\sigma . C_I^{-1}\sigma} \qquad (4b)$$

where $A_k$ is the $k$th row of the coefficient matrix $A$. Notice that this simply normalises the core speckle-reduced image (equation (2)) and multiplies it by the local mean value of intensity in each of the $M$ images. Hence it retains the optimising property of (2) while inputting structure into the $M$ speckle-reduced images. The explicit scheme for calculating the $A_k$ given by (4) also has an implicit form given in Bruniquel and Lopes (1997).

This treatment is designed for the general case where the set of images may be correlated, but becomes much simpler when correlation can be neglected. In this case, $C_I$ reduces to a diagonal matrix in which

$$C_I(i,j) = \sigma_i^2 \delta_{ij} \qquad (5)$$

where $\delta_{ij}$ is the Kronecker delta, and the speckle reduction scheme becomes

$$J_i = \frac{\sigma_i}{M}\sum_{j=1}^{M}\frac{I_j}{\sigma_j} \qquad i = 1, \ldots, M. \qquad (6)$$

Here the core speckle reducing filter (equivalent to (2)) is given by the summation; the scaling appropriate to each temporal image is provided by the $\sigma_i$ outside the summation. In principle, the operation described by (6) should provide filtered images with ENL = $M$ x $L$. Measured values are reported in Section 3.2.

### 2.1 Comparison with ERS data

The expression given in (6) appears to be the most appropriate for ERS data from the 35 day repeat cycle over vegetated areas, since the residual correlation over this period is likely to be negligible. This is because, at C band, the primary scatterers are leaves, twigs and small branches. Over a month, this population of

scatterers is unlikely to remain stable enough to maintain coherence. As a test of this, we show in Figure 1 the histogram of correlation coefficients for registered ERS images of West Harling (an area of forest and farmland) on 5/5/92 and 22/9/92, using a window size of 5 x 5 pixels in calculating the correlation. Although the histogram is centred on 0, large values of the correlation coefficient occur. These values can be attributed to two factors. The first arises from sampling statistics. Calculations of the correlation coefficient between completely uncorrelated pairs of simulated images gave rise to fairly wide histograms, suggesting that much of the correlation indicated in Figure 1 is simply a sampling effect. The second is that in the ERS image there are objects, such as buildings, which would be expected to give high correlation. These make up a fairly small proportion of the scene, but contribute significantly to the tails of the histogram.

If we accept the arguments above, then it is not only inefficient to use the general expression (4) to filter the data, but this is in fact the wrong method to use, since it involves estimating a covariance matrix of intensity, with spurious non-zero values in the off-diagonal components associated with sampling. These non-zero values pass into the solution scheme and introduce error. For this reason, the simplified scheme given by (6) is more correct. It is also very easy to implement, involving no matrix operations, just weighting by the estimated mean local backscattering coefficients in the $M$ images.

If we were using data from the Tandem missions, the full scheme described by (4) would be more appropriate, but the sampling problems described above would still occur. The only way around them appears to be to use sampling windows sufficiently large to reduce the tails of the sampling distribution.

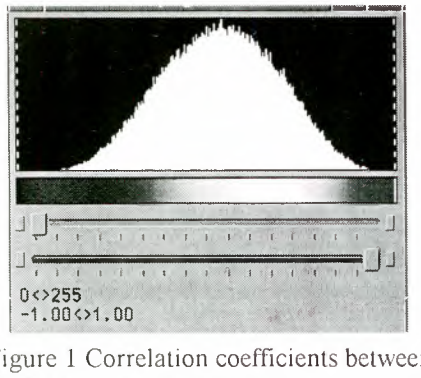


Figure 1 Correlation coefficients between ERS-1 images of West Harling on 5/5/92 and 22/9/92, estimated over a 5x5 window.

## 3 Spatial adaptivity

One of the potential advantages in using multitemporal filtering is that it appears to provide speckle reduction while preserving spatial resolution. However, it is important to observe that equation (6) requires local estimates of $\sigma^o$ in each image. This involves using a window surrounding the pixel at the $(x, y)$ position of interest, so that the multitemporal filtering includes spatial averaging. In order to prevent an associated loss of resolution, it is necessary to use an estimation scheme which is spatially adaptive. This is based on the approach in Lopes *et al.* (1993).

The filter adapts to local structure by first using the local coefficient of variation (CV) to test whether the region within the processing window is uniform and responding with various geometric detectors if this is found not to be the case. Within the window, the CV is estimated by $\hat{\sigma} / \hat{\mu}$, where the unbiased estimates of the the mean, $\hat{\mu}$, and standard deviation, $\hat{\sigma}$, of the intensity are given by

$$\hat{\mu} = \frac{1}{N} \sum_{i=i}^{N} I_i \qquad (7)$$

and

$$\hat{\sigma} = \sqrt{\frac{\sum_{i=1}^{N} (I_i - \hat{\mu})^2}{N-1}} \qquad (8)$$

Here $I_{1....N}$ are the intensity values of the $N$ pixels within the window. The theoretical distribution of the estimate $\hat{\sigma} / \hat{\mu}$ is unknown but found be to distributed around $1/\sqrt{L}$, where $L$ is the number of looks in the image. By adding a small value, $\delta$, determined by a chosen confidence interval, to $1/\sqrt{L}$, the central pixel in the window is considered to belong to a homogeneous class if $\hat{\sigma} / \hat{\mu} \leq 1/\sqrt{L} + \delta$ (note that this is one-sided), otherwise to a heterogeneous class. A filter which is trying to estimate the local value of $\sigma^0$ can be made adaptive by the following algorithm (Lopes *et al*, 1993):

(1) If $\hat{\sigma} / \hat{\mu} \leq 1/\sqrt{L} + \delta$, area is homogeneous, average over the whole window.

(2) If $\hat{\sigma} / \hat{\mu} > 1/\sqrt{L} + \delta$, area is heterogeneous:

(2.1) Then apply structure (line and edge) detection.

(2.2) If no structure detected, apply point detection.

(2.3) If neither structure nor point is found, the area is textured.

Appropriate detectors are needed to perform the structure and point detections in steps (2.1) and (2.2). These are all developed from the ratio PDF for SAR images (Touzi *et al*, 1988).

### 3.1 The ratio PDF

Assume we have two uniform regions, containing $N_1$ and $N_2$ pixels respectively, whose true intensity ratio is $R = \sigma_1 / \sigma_2$, where $\sigma_1$ and $\sigma_2$ are the mean intensities of the two regions. If $A_1, A_2, \ldots A_{N_1}$ and $B_1, B_2, \ldots, B_{N_2}$ are the two sets of pixel intensity values then the maximum likelihood estimate, $\hat{r}$, of $R$ is given by the ratio of the average intensities:

$$\hat{r} = \frac{\overline{A}}{\overline{B}}. \qquad (9)$$

Ratio detection should be independent of whether we choose $\frac{\overline{A}}{\overline{B}}$ or $\frac{\overline{B}}{\overline{A}}$ as the test ratio, so following Touzi *et al* (1988), we define a normalized ratio measure

$$\hat{r}_N = \min\left(\frac{\overline{A}}{\overline{B}}, \frac{\overline{B}}{\overline{A}}\right) \qquad (10)$$

which can never exceed the value 1. The conditional PDF of $\hat{r}$, given $R$, is (Lopes *et al*, 1993)

$$p(\hat{r}_N | R) = \frac{1}{B(N_1 L, N_2 L)\cdot \hat{r}_N}(Z + H) \qquad (11)$$

with

$$Z = \frac{\left(\frac{N_2}{N_1}\right)^{N_2 L}\left(\hat{r}_N \frac{1}{R}\right)^{N_1 L}}{\left[\hat{r}_N\left(\frac{1}{R}\right) + \left(\frac{N_2}{N_1}\right)\right]^{(N_1 L + N_2 L)}}$$

$$H = \frac{\left(\frac{N_1}{N_2}\right)^{N_1 L}\left(\hat{r}_N R\right)^{N_2 L}}{\left[\hat{r}_N (R) + \left(\frac{N_1}{N_2}\right)\right]^{(N_1 L + N_2 L)}}$$

where $L$ is the number of looks, and $B$ is the Beta function:

$$B(z, w) = \frac{\Gamma(z)\Gamma(w)}{\Gamma(z + w)}$$

Defining the contrast ratio of two homogeneous areas by $C = \max[R, 1/R]$, we note that $p(\hat{r}_N | R) = p(\hat{r}_N | 1/R) = p(\hat{r}_N | C)$.

The ratio PDF in (11) can be easily developed into PDFs of edge, line and point ratios by selecting the appropriate geometry in the processing window and modifying the values of $N_1$ and $N_2$ accordingly. The false alarm probability (the probability that $r_N$ is less than some threshold when the two regions in fact have the same backscattering coefficient) can then be calculated for each of these PDFs, and is given by $\int_0^{r_T} p(r_N | 1) dr_N$, where $r_T$ is the detection threshold, since the PDF for a uniform region simply sets $C = 1$.

The edge and line detectors are made independent of orientation by testing for edges and lines in several different directions. For a square window, horizontal, vertical and two diagonal orientations are used. The minimum values of the edge ratio, $r_E$, and the line ratio, $r_L$, calculated over all tested directions are used, as they provide the strongest evidence for an edge or line. These ratios are compared with the chosen thresholds for edge and line detections, $r_{Emax}$ and $r_{Lmax}$. If $r_E \leq r_{Emax}$, an edge is detected, and if $r_L \leq r_{Lmax}$, a line is detected. The thresholds are all uniquely associated with the required false alarm using (10).

The intensity point ratio detector, $r_p$, uses the ratio of the average intensity in a point target region (a cross shape representing the point spread function of the imaging system) and the averaged intensity from the rest of the window. We then test whether the observed ratio of the average intensity of the point region and the pixels in the rest of the region is likely to have arisen purely from speckle, again using a threshold based on a fixed false alarm probability.

If, as a result of these tests, any feature or point is found, the filter estimates the mean intensity by averaging pixels only in the detected edge, line or point regions to which the central pixel belongs. This helps to preserve resolution and prevent blurring of features. Full details can be found in Lopes *et al.* (1993).

### 3.2 Examples of multitemporal adaptive filtering

In Figure 2 we illustrate the multitemporal filtering concepts introduced in Sections 2 and 3.1. Figure 2(a) shows a single ERS image from a sequence of 11 images available for the West Harling, UK, testsite in 1997. Figure 2(b) is the 'featureless' result of the optimal speckle reducing operation resulting from equation (2), after combining all the images, but without correcting for the local intensity. The presence of features in the image indicates failures in the spatial adaptivity when the filter window used for estimating the local intensity straddles an edge. Figure 2(c) shows the filtered image corresponding to Figure 2(a) after correction for the local intensity. Although a significant improvement on Figure 2(a), this image is still not very useful for feature detection. A marked further improvement in interpretability is provided when we

combine images as multitemporal overlays, as in Figure 2(d), where the temporally filtered images for 23/5/97, 5/9/97 and 14/3/97 are overlaid as red, green and blue respectively. Here we have used the spatially adaptive estimates of local mean intensity.

An important issue for their subsequent use is the ENL of the filtered images. In principle, if the $M$ $L$-look images are uncorrelated, the operation described by (6) should provide filtered images with ENL = $M$ x $L$. Hence, the eleven 3-look ERS-2 images used to form Figure 2(b, c) should give rise to 33-look data after filtering. Measured values are of the order 22. This deviation from the ideal value can be explained by the errors in estimating the local intensity in (6): if this estimate is not accurate, the filter is no longer optimal and the ENL will decrease. Larger errors are likely when spatial adaptivity causes averaging over fewer pixels. Hence, the ENL is likely to vary spatially within the filtered image.

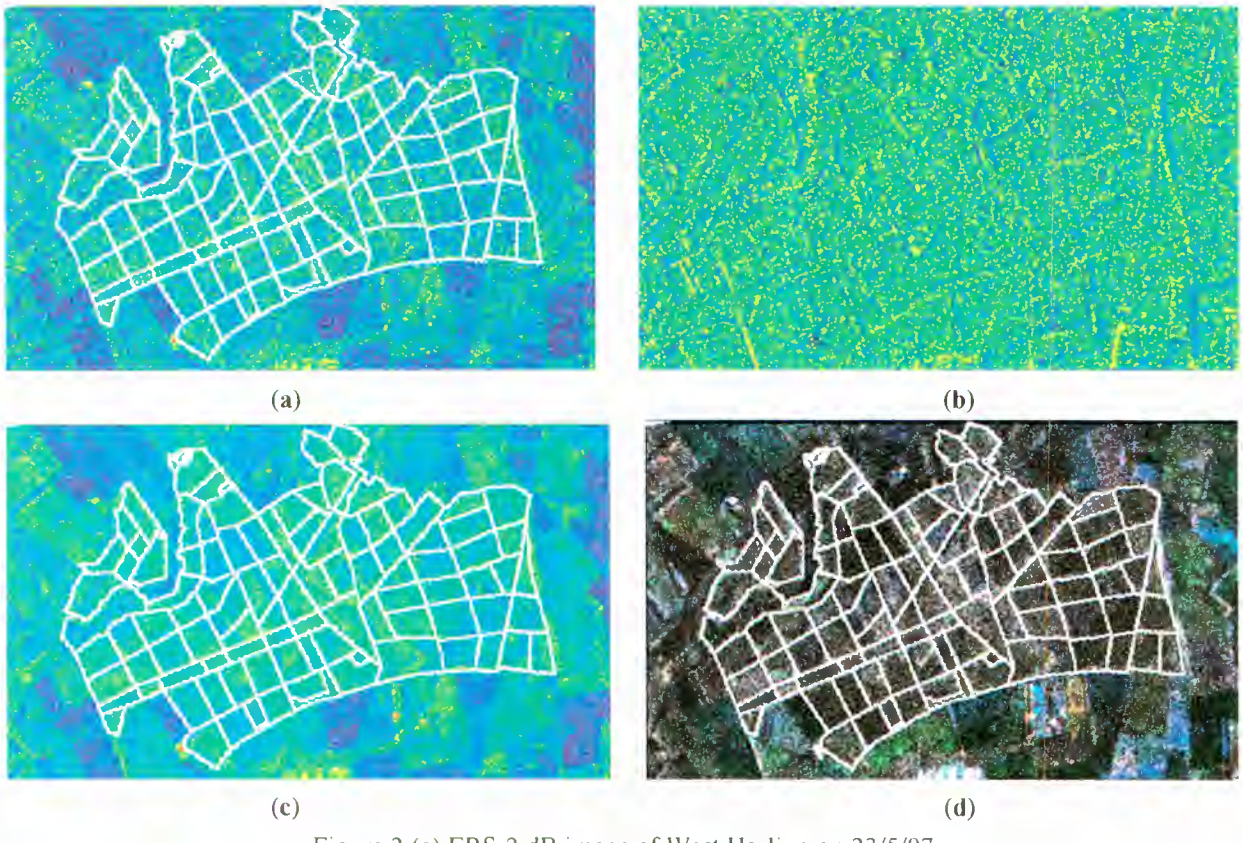

(a) (b)

(c) (d)

Figure 2 (a) ERS-2 dB image of West Harling on 23/5/97
(b) Featureless core (dB) image using 1997 ERS-2 data of West Harling
(c) Temporal filtered image corresponding to 2(a)
(d) Overlay of temporal filtered images
(23/5/97 in red, 5/9/97 in green and 14/3/97 in blue)

## 4. Spatial filtering

For many purposes, the level of speckle filtering achievable by temporal filtering alone will be insufficient for the success of subsequent operations, such as classification. For example, probability of error is strongly dependent on ENL and acceptable false alarm rates often require large ENL (Oliver and Quegan, 1998; Rignot and van Zyl, 1997). In order to increase the ENL, spatial filtering is required after the temporal filtering. In the same way that consideration of the properties of the ERS 35 day repeat data led us to a particularly simple form of the multitemporal filter, we now use further arguments about these properties to derive the appropriate form of the spatial filter.

The essence of the spatial filtering approach lies in the formulation of the reconstruction problem; this is discussed at length in Oliver and Quegan (1998). For our purposes, we consider two approaches: local averaging (box filter) and local maximum a posteriori filtering with a gamma distributed prior (GMAP; Lopes *et al.*, 1993).

Local filtering makes assumptions about the statistical distribution of the backscattering coefficients of the population contained within the processing window. For averaging it is assumed uniform, while for GMAP it is assumed to be gamma distributed, so that the data are textured. In combination with speckle, these two models lead to the observed data being either gamma or K distributed, respectively. In addition, the GMAP filter makes use of the order parameter (ENL) of the speckle distribution and in its simple form assumes that this is the same everywhere. Both filters assume that the pixels within the filter window are uncorrelated.

Most of the assumptions of GMAP are violated at the spatial resolution and incidence angle of ERS PRI data. In most cases, there is little or no evidence for measurable texture in forest or agricultural areas, particularly at the scale of typical processing windows. (An important exception can occur in regions of medium scale topographic variation. Recent work has shown that for such regions in tropical forest, marked texture in the deforested areas provides good discrimination from the untouched forest. However, this is not the general situation.) Since GMAP is specifically designed for gamma distributed texture, this suggests it is not the appropriate filter to use. In addition, after temporal filtering, the data are spatially correlated (both because of point spread function effects in the original data and as a consequence of overlaps in the windows used to estimate local parameters at different pixels). This adversely affects GMAP's estimate of the order of the underlying gamma distribution. Finally, sampling errors cause the equivalent number of looks to vary within the temporally filtered image, as discussed in Section 3.2.

Both the latter effects also have an impact on the box filter. It is readily shown that for independent pixels drawn from the same gamma distribution, the box filter provides the maximum likelihood estimate of $\sigma^0$. However, this is no longer true in the presence of either spatial correlation or variation in the ENL. The box filter nonetheless still provides a very simple unbiased estimate of $\sigma^0$ under the assumption that its underlying distribution is uniform, rather than textured. There seems no reason from observations on the ERS PRI data to assume anything else in either forest regions or agricultural fields.

The discussion of spatial adaptivity in Section 3 was concerned with providing estimates of an image parameter using spatial averages in the presence of image structure. Although discussed in the context of temporal filtering, this is obviously equally applicable to spatial filtering and uses exactly the same methods. The only difference in the case of these two filters is in their response to the presence of texture; for GMAP the output will then be given by the filter developed by Lopes *et al.* (1993) while the box filter will treat this as a statistical fluctuation and average across the whole window.

Figure 3(a) shows the effects of spatial filtering of the image shown as Figure 2(c) using the box filter, while Figure 3(b) and (c) show the overlay of the three spatially filtered images making up Figure 2(d), using the box and GMAP filters respectively.

(a)

(b)

(c)

Figure 3. (a) The image in Figure 2(c) spatially filtered by a 3x3 box filter
(b) Overlay of the images in Figure 2(d) spatially filtered by a 3x3 box filter
(c) As in (b), but using GMAP

It can be seen that the GMAP filter leads to images which appear sharper, probably because this filter does less averaging near edges. In effect, while box filtering can respond to edges only through the adaptivity of its processing window, GMAP gets a second chance through the statistical model it uses for the data. (This is a by-product, not a design feature of the filter, which as we have noted uses what is probably an inappropriate model for the ERS data.) The crisper aspect of the GMAP filtered data is related to the fact that it has done insufficient smoothing to produce good classification results in many circumstances, so that a further filtering step is required (Le Toan *et al.*, 1995, 1997).

As with temporal filtering, the appropriate window size needs to be selected for use in either of these filters, but the problem is different. For the temporal filtering, the windows need to be big enough to allow accurate estimates of the local value of $\sigma^0$ in each image in the temporal sequence. In this case, the temporal filter will be close to its optimal performance and will yield an ENL near to its ideal value of $ML$ (see Section 3). No further improvement in the ENL is possible using temporal filtering. For the spatial filter, bigger windows lead to continued improvements in ENL until the window size exceeds the scale length of the homogeneous land unit in the image (and assuming that the spatial adaptivity performs adequately). Hence the choice of window size is determined by the nature of the subsequent classification step and the ENL necessary to provide successful separation of the different classes.

Figure 4. Forest/non-forest map of the Kuayagang area in Sumatra, derived from two ERS-1 images acquired on 1/12/93 and 5/8/94.

Note that the GMAP filter has been successfully used in several studies involving post filtering classification of ERS data (Le Toan *et al.*, 1995, 1997). An example is shown in Figure 4, which is a forest/non-forest map of the Kuayagang area in Sumatra, derived from two ERS-1 images acquired on 1/12/93 and 5/8/94. Green is assigned to pixels with temporal change less than 1 dB, corresponding to forest, whereas the grey colour shows non-forest areas with higher temporal change between the wet and dry seasons. The different grey tones represent the backscatter intensity of the dry season data, used as an indicator of oil palm plantations (bright grey), rubber plantations (medium grey) and bare or agricultural fields (dark grey). Here the discrimination based on change was aided by the large backscatter variation and the large dimension of the non-forest areas in the two images.

In this example, GMAP has been followed by a second spatial filtering step to remove excess variability in its output. Similar smoothing has been necessary in other applications of GMAP, either involving simple box averaging after filtering or post-classification cleaning. This suggests that the filtering step has not met its aim of providing a sufficiently accurate estimate of $\sigma^0$. Indeed, the assumption of an underlying gamma distribution for the backscattering coefficient will lead to unacceptably high numbers of large pixel values in the output if it is incorrect. Attempts to use GMAP for tropical forest classification without subsequent operations on the filtered data did not prove successful, as the direct output from the filter was too noisy (Grover *et al.*, 1998).

## 5 Conclusions

Multitemporal SAR data can be exploited to take advantage of information carried by changes in backscattering coefficient, which are relevant in many applications. Having multitemporal data available also allows us to improve the radiometric quality of the images by means of multitemporal filtering techniques. In the general case, the optimal speckle-reducing filter makes use of the correlation between images from different dates. However, for ERS data in the 35 day repeat cycle, the correlation between different dates over vegetated targets is normally very low. This leads to a particularly simple and easily implemented form of the temporal filter. Although in principle this preserves resolution, it requires local estimates of the backscattering coefficient, which both reduces the degree of filtering and leads to unwanted spatial blurring. In order to combat the latter, the estimates need to be made within locally adaptive windows. In many cases, the degree of smoothing afforded by temporal filtering alone is insufficient to support successful post-filtering operations such as classification, and spatial filtering is also necessary. The appropriate type of filtering depends on the correct model for the data of interest. The resolution and

incidence angle of ERS mean that texture is only weakly present, if at all, at the scale of typical processing windows. This allows a rather simple approach to spatial filtering to be used, which again is much aided by being made adaptive.

**Acknowledgement**

We would like to thank Jiong Jiong Yu of SCEOS and Florence Ribbes of CESBIO for much help, expecially preparation of figures. We also thank the European Space Agency for the supply of ERS data.

**References**

Bruniquel, J. and Lopes, A., 1997, "Multi-variate optimal speckle reduction in SAR imagery", *Int. J. Remote Sensing* **18**, 603-627.

Grover, K.D., Quegan, S and Yanasse, C.C.F., 1998, "Quantitative estimation of tropical forest cover by SAR", *I.E.E.E. Trans. on Geoscience and Remote Sensing* (in press).

Le Toan, T., Hahn, T., Floury, N. Ribbes, F., Bruniquel, J. Lopes, A. and Wasrin, U.R., 1995, "Assessment of multitemporal ERS-1 data for deforestation monitoring in South Sumatra", TREES ERS-1 Study Final Workshop, JRC Ispra, February 1995.

Le Toan, T., Ribbes, F., Wange, L.F., Floury, N., Ding, K.H., Kong, J.A., Fujita, M. and Kurosu, T., 1997, "Rice crop mapping and monitoring using ERS-1 data based on experiment and modelling results", *I.E.E.E. Trans. on Geoscience and Remote Sensing*, **35**, 41-56.

Lopes, A., Nezry, E., Touzi, R., and Laur, H., 1993, "Structure detection and statistical adaptive speckle filtering in SAR images", *Int. J. Remote Sensing*, **14**, No.9, 1735-1758.

Novak, L.M., Burl, M.C. and Irving W.W., 1993, "Optimal polarimetric processing for enhanced target detection", *I E.E.E. Trans. Aerospace Elect. Systems*, **29**, 293-305.

Oliver, C.J. and Quegan, S., 1998, "Understanding synthetic aperture radar images", Artech House.

Rignot, J.M. and van Zyl, J.J. 1993, "Change detection techniques for ERS-1 SAR data", *I.E.E.E. Trans. on Geoscience and Remote Sensing*, **31**, No. 4, 896-906.

Touzi, R., Lopes, A., and Bousquet, P., 1988, "A statistical and geometrical edge detector for SAR images", *I.E.E.E. Trans. on Geoscience and Remote Sensing*, **26**, 764-773.

Wooding et al., 1995, "Satellite radar in agriculture: Experience with ERS-1", ESA SP-1185.

# Radar 2

*Coordinators:* Laura Frulla, *CONICET* &
Sidnei J.S. Sant'Anna, *INPE*

# APPROXIMATION OF THE $\mathcal{K}_A$ DISTRIBUTION BY THE $\mathcal{G}_A^0$ DISTRIBUTION

Marta Mejail[1], Alejandro C. Frery[2], Julio Jacobo-Berlles[1], Fernando Kornblit[1]

[1]Universidad de Buenos Aires-Departamento de Computación
Pabellón I, Ciudad Universitaria, 1428 Buenos Aires, Argentina
Tel: 54(1)7889101/07, Fax: 54(1)7830729
{marta, jacobo, fk5o}@dc.uba.ar

[2]UFPE-DI
CP 7851
50732-970 Recife, PE, Brazil
Tel: 55-81-2718430, Fax: 55-81-2718438
frery@di.ufpe.br

## ABSTRACT

In the field of processing and analysis of Synthetic Aperture Radar (SAR) images, the returned signal can be modelled as the product of the inherent *speckle* noise and the terrain backscatter. For amplitude SAR images, the data can be fitted with several distributions depending, among other considerations, on the degree of homogeneity of the areas under study. In zones where the backscatter can be considered homogeneous (crops, pastures, etc.) the $\Gamma^{1/2}$ distribution is a good model for the returned signal. The $\mathcal{K}_A$ distribution gives a good fit for homogeneous areas as well as for heterogeneous areas (forest on flat terrain) but there are numerical problems caused by the presence of Bessel functions. When the area under study is extremely heterogeneous (cities, forest on undulated terrain) the $\Gamma^{1/2}$ distribution and the $\mathcal{K}_A$ distribution fail to fit these data. In this case, the $\mathcal{G}_A^0$ distribution behaves very well. Taking also into account that this last distribution fits equally well homogeneous and heterogeneous areas, and that its use is more computational and theoretically tractable, it is desirable to substitute the $\mathcal{G}_A^0$ distribution for the $\mathcal{K}_A$ distribution. In this work the feasibility of this substitution is studied. To this end, a correspondence between the parameters of both distributions is proposed in order to approximate, in some sense, the $\mathcal{K}_A$ distribution by the $\mathcal{G}_A^0$ distribution. The minimisation of a distance between both densities will be considered, and the goodness of fit of between $\mathcal{K}_A$ distributed data by the $\mathcal{G}_A^0$ distribution model will be measured, using the $\chi^2$ adherence test in a Monte Carlo experience.

**Keywords:** statistical models, $\mathcal{G}_A^0$ distribution, $\mathcal{K}_A$ distribution, SAR.

## INTRODUCTION

In the field of Synthetic Aperture Radar (SAR) image processing, the multiplicative model is widely used. Within it, the return is modelled as the product of the *speckle* noise and the terrain backscatter. SAR amplitude data can be fitted by several distributions depending, among other factors, on the degree of homogeneity of the areas under study. In this work, unless otherwise stated, linear detection (amplitude) data will be used.

For zones where the backscatter can be considered homogeneous, like crops and pastures, the $\Gamma^{1/2}$ distribution is a good model for the returned data. The $\mathcal{K}_A$ distribution models data coming from homogeneous zones (with certain restrictions due to numerical problems arising from the use of Bessel functions) as well as data coming from heterogeneous zones, like forest on flat relief. The $\Gamma^{1/2}$ however, does not fit heterogeneous data appropriately.

When the area under study is extremely heterogeneous , as it is the case for urban areas or forest over undulated relief, the $\Gamma^{1/2}$ distribution as well as the $\mathcal{K}_A$ distribution do not model the data adequately. In this case the $\mathcal{G}_A^0$ distribution behaves remarkably well. Taking into account that this distribution models very well data from heterogeneous and homogeneous areas too, and that its use is more computationally and theoretically tractable, it is advisable to substitute the $\mathcal{G}_A^0$ distribution for the $\mathcal{K}_A$ distribution.

In this work, the feasibility of this substitution is studied. To this end, a correspondence between the parameters of both distributions will be considered in order to approximate, in some sense, the $\mathcal{G}_A^0$ distribution to the $\mathcal{K}_A$ distribution. This study is made up of two parts:

- Minimisation in $L_2$ of the distance between the respective densities, in order to obtain a correspondence between distributions.
- The goodness of fit of the $\mathcal{G}_A^0$ distribution to $\mathcal{K}_A$ distributed data will be measured using the $\chi^2$ test in a Monte Carlo experiment.

## MAIN PROPERTIES OF THE $\mathcal{K}_A$ AND THE $\mathcal{G}_A^0$ DISTRIBUTIONS

The $\mathcal{G}_A^0(\alpha_G, \gamma, n)$ and the $\mathcal{K}_A(\alpha_K, \lambda, n)$ distributions we will use are characterised by the following densities

$$f_G(z) = \frac{2n^n \Gamma(n-\alpha_G) z^{2n-1}}{\gamma^\alpha \Gamma(n)\Gamma(-\alpha_G)(\gamma + nz^2)^{n-\alpha_G}} \qquad (1)$$

where $-\alpha_G, \gamma, n, z > 0$, and

$$f_K(z) = \frac{4(\sqrt{\lambda n})^{\alpha_K+n}}{\Gamma(n)\Gamma(\alpha_K)} z^{n-\alpha_K+1} K_{n-\alpha_K}\left(2z\sqrt{\lambda n}\right) \qquad (2)$$

where $\alpha_K, \lambda, n, z > 0$ and $K_\nu$ is the modified Bessel function of the third kind and order parameter $\nu$.

There are not many computational implementations of this Bessel function (see Gordon et al.(1995)), for a recent algorithm). On the other hand, the only special function in the $\mathcal{G}_A^0$ distribution is the $\Gamma$ function, for which there are many reliable implementations.

This is the first computational argument in favour of the $\mathcal{G}_A^0$ distribution and against the $\mathcal{K}_A$ distribution. The second computational argument is aimed in the same direction and requires the definition of the cumulative distribution functions for both distributions.

Let the random variables $V$ and $W$ be $\mathcal{G}_A^0(\alpha_G, \gamma, n)$ and $\mathcal{K}_A(\alpha_K, \lambda, n)$ respectively. The cumulative distribution function of the first one is given by

$$\Pr(V \le v) = \frac{n^{n-1}}{\gamma^n} \frac{\Gamma(n-\alpha_G)}{\Gamma(n)\Gamma(-\alpha_G)} v^{2n} \cdot \cdot H\left(n, n-\alpha_G, n+1; -\frac{n}{\gamma} v^2\right) \qquad (3)$$

where $H$ is the hypergeometric function. This function is easy to evaluate using the Snedecor's $\mathcal{F}$ distribution, as can be seen in the appendix of this work.

In order to write the cumulative distribution function of the second random variable it is necessary to impose restrictions on the variation domain of its parameters. Originally, the parametric space of the $\mathcal{K}_A(\alpha_K, \lambda, n)$ distribution is $\mathbb{R}_+^3$ but, to be able to write its cumulative distribution function in a recursive form, it is necessary to restrict the variation of $\alpha_G$ or the variation of $n$ to the integers. For the second case ($n$ integer), this function is given by

$$\Pr(W \le w) = 1 + \frac{2^{2-\alpha-n}}{\Gamma(\alpha_K)\Gamma(n)} g(\nu, k, z) \qquad (4)$$

where $z = 2w\sqrt{\alpha n}$, $k = 2n-1, \nu = \alpha - n$ and the function $g(\nu,k,z)$ is given by the following recursive formula

$$\begin{cases} -z^{\nu+1} K_{\nu+1}(z), & \text{for } k = 1 \\ (k-1)(2\nu + k - 1) g(\nu, k-2, z) - \\ \quad - z^{\nu+k} K_{\nu+1}(z) (k-1) z^{\nu+k-1} K_\nu(z), & \text{for } k \ge 2 \end{cases}$$

More details of this recursive solution for the accumulated distribution function of $\mathcal{K}_A$ distributed variables can be found in Yanasse et al.(1995).

From the considerations above on the accumulated distribution functions for $\mathcal{G}_A^0$ and $\mathcal{K}_A$ distributions we can deduce the following advantages of the first one over the second one: it is easier to implement, it uses reliable and immediately obtainable implementations, and it does not impose restrictions on the original parameter space.

The importance of the availability of reliable implementations of the accumulated distribution function arises from the need of carrying out goodness of fit tests and from the use of these functions in estimators based on order statistics.

To the stated advantages in the areas of modelling and computational tractability, additional advantages in the fields of inference which favour even more the use of the $\mathcal{G}_A^0$ distribution instead of the $\mathcal{K}_A$ distribution, can be added.

For the estimation of the homogeneity parameter of both distributions using the maximum likelihood method, the estimator of $\alpha_K$ is difficult to calculate due to the presence of the derivative of the Bessel function of the third kind with respect to the order parameter. The maximum likelihood estimator of $\alpha_G$ entails the use of the digamma function, which has been widely studied and implemented. These estimators are the solutions of the following equations:

Let us consider the sample $z_1, \ldots, z_k$ of independent observations. The maximum likelihood estimator of the $\alpha_K$, knowing $n$ and $\lambda$ is

$$k\Psi(\hat{\alpha}_K) - \sum_{i=0}^{k} \frac{\partial}{\partial \hat{\alpha}_K} \log K_{\hat{\alpha}_K - n}\left(2z_i\sqrt{\lambda n}\right) = \frac{k}{2}\log\lambda + \sum_{i=0}^{k} \log z_i$$

analogously, for the maximum likelihood estimator of $\alpha_G$ knowing $n$ and $\gamma$ is:

$$\Psi(n - \hat{\alpha}_G) - \Psi(-\hat{\alpha}_G) = -\log\gamma + \frac{1}{k}\sum_{i=0}^{k} \log(\gamma + nz_i^2)$$

where $\Psi$ is the digamma function and $k$ is the sample size.

## MINIMISATION OF THE DISTANCE BETWEEN THE $\mathcal{G}_A^0$ AND THE $\mathcal{K}_A$ DISTRIBUTIONS

In this section, a method by which a $\mathcal{G}_A^0$ distribution approximates a $\mathcal{K}_A$ distribution, under the constraint that both must have a mean value equal to one, is described.

In other words, given the sets of $\mathcal{G}_A^0$ and $\mathcal{K}_A$ distributions with mean value equal to one, a correspondence of elements of the first one to elements of the second one , trough a numerical minimisation of an also numerical integration, will be sought. This correspondence will then be established by parameter pairs (see Figure 1).

In this figure, the set $\mathcal{K}_A(n)$ ($\mathcal{G}_A^0(n)$ respectively) is formed by all the $\mathcal{K}_A$ ($\mathcal{G}_A^0$, resp.) distributions with $n$ looks and mean value equal to one. These distributions have only one free parameter: the homogeneity parameter $\alpha_K$ ($\alpha_G$ resp.), because the scale parameter $\lambda$ ($\gamma$ resp.) must be chosen as a function of the number of looks and the homogeneity parameter, in order to guarantee the constraint of unitary mean.

The objective of this work is to approximate the $\mathcal{K}_A$ distribution by the $\mathcal{G}_A^0$ distribution. To do this, it is necessary to previously define the approximation criterion. Let us consider then, the set of all the distributions that admit a density and call it $\mathcal{D}$. To establish the notion of proximity between distributions in $\mathcal{D}$ we will use a distance we will denote $d:\mathcal{D}\times\mathcal{D}\rightarrow[0,\infty)$, through the relation

$$d(\mathcal{D}_1,\mathcal{D}_2)=\int_{-\infty}^{\infty}\left|f_1(z)-f_2(z)\right|^2 dz$$

Where $f_1$ and $f_2$ are the densities that characterise the $\mathcal{D}_1$ and the $\mathcal{D}_2$ distributions respectively. This metric has been already used in a similar context in Joughin et al. (1993).

Due to reasons that will be explained later, only those distributions $\mathcal{K}_A(\alpha_K,\lambda,n)$ and $\mathcal{G}_A^0(\alpha_G,\gamma,n)$ with mean equal to one will be studied. In this way, when the number of looks $n$ and the homogeneity parameter $\alpha_K$ are known, the scale parameter $\lambda$ is given by:

$$\lambda=\frac{1}{n_0}\left(\frac{\Gamma(\alpha_K+1/2)\Gamma(n+1/2)}{\Gamma(\alpha_K)\Gamma(n)}\right)^2 \qquad (5)$$

Analogously, the $\mathcal{G}_A^0$ distributions (with the same number of looks $n$) will be indexed only by their respective homogeneity parameter $\alpha_G$ because its scale parameter is given by:

$$\gamma=n\left(\frac{\Gamma(-\alpha_G)\Gamma(n)}{\Gamma(-\alpha_G-1/2)\Gamma(n+1/2)}\right)^2 \qquad (6)$$

We want to find the value of $\alpha_G$ that minimises the distance

$$d=\int_0^{\infty}\frac{4}{\Gamma(n)}\left|2(\lambda n)^{(\alpha_K+n)/2}z^{\alpha_K+n-1}K_{\alpha_K-n}\left(2z\sqrt{\lambda n}\right)-\right.$$

$$\left.-\frac{n^n\gamma^{-\alpha_G}\Gamma(n-\alpha_G)z^{2n-1}}{\Gamma(-\alpha_G)\left(\gamma+nz^2\right)^{n-\alpha_G}}\right|^2 dz \qquad (7)$$

where the values $\lambda=\lambda(\alpha_K,n)$ and $\gamma=\gamma(\alpha_G,n)$ are the ones that make the mean value equal to one. Then, the value of $\alpha_G<0$ that minimises numerically that integral will be sought.

Although $\alpha_K$ varies over all the positive real numbers, for the purposes of this study the search will be done within the interval [4,12]. Very small values of $\alpha_K$ ($0<\alpha_K<4$ for instance) correspond to data from extremely heterogeneous areas, which are not well modelled by the $\mathcal{K}_A$ but by the $\mathcal{G}_A^0$ distribution., as can be seen in Frery et al.(1997); then, for these data, it is not necessary to have an approximation. For values of $\alpha_K$ larger than 15, the observed data can be modelled by the $\Gamma^{1/2}$ distribution, (see Frery et al.(1997), Yanasse et al. (1995) and Yanasse et al.(1993)), which is also a particular case of the $\mathcal{G}_A^0$ distribution. So, the only region in which it is necessary to approximate the $\mathcal{K}_A$ distribution by the $\mathcal{G}_A^0$ distribution is the one that corresponds to values of $\alpha_K$ within the interval [4,12].

For these values of $\alpha_K$, the corresponding values of $\alpha_G$ obtained as a result of the minimisation of the integral in formula (7), are shown in the following tables.

| $n=1$ | | | |
|---|---|---|---|
| $\alpha_K$ | $\alpha_G$ | $\lambda$ | $\gamma$ |
| 4. | -4.3 | 2.95 | 4.15 |
| 5. | -5.3 | 3.73 | 5.42 |
| 6. | -6.3 | 4.52 | 6.09 |
| 7. | -7.3 | 5.30 | 7.96 |
| 8. | -8.3 | 6.09 | 9.23 |
| 9. | -9.3 | 6.87 | 10.50 |
| 10. | -10.3 | 7.66 | 11.78 |

| $n=2$ | | | |
|---|---|---|---|
| $\alpha_K$ | $\alpha_G$ | $\lambda$ | $\gamma$ |
| 4. | -4.4 | 3.32 | 3.68 |
| 5. | -5.4 | 4.20 | 4.81 |
| 6. | -6.4 | 5.08 | 5.94 |
| 7. | -7.4 | 5.96 | 7.07 |
| 8. | -8.3 | 6.85 | 8.21 |
| 9. | -9.3 | 7.73 | 9.34 |
| 10. | -10.3 | 8.61 | 10.47 |

| $n=4$ | | | |
|---|---|---|---|
| $\alpha_K$ | $\alpha_G$ | $\lambda$ | $\gamma$ |
| 4. | -2.9 | 3.53 | 3.45 |
| 5. | -5.5 | 4.46 | 4.53 |
| 6. | -6.4 | 5.40 | 5.59 |
| 7. | -7.4 | 6.34 | 6.65 |
| 8. | -8.4 | 7.28 | 7.72 |
| 9. | -9.4 | 8.22 | 8.78 |
| 10. | -10.4 | 9.16 | 9.84 |

Figure 2 shows the densities of some of the $\mathcal{K}_A$ and $\mathcal{G}_A^0$ distributions for a fixed value of $\alpha_K$ and its corresponding value of $\alpha_G$. In it, it can be noticed that for $\alpha_K = 4$ and $\alpha_G = -4.3$, with $n = 1$, the difference between both distributions is very small.

Figure 3 shows the values of the integral (7) for $\alpha_K = 4$ and for $\alpha_K = 8$ as a function of $-\alpha_G \in [4,10]$, the minimum is reached for $\alpha_G = -4.3$ and $\alpha_G = -8.3$.

## GOODNESS OF FIT OF $\mathcal{K}_A$ DISTRIBUTED DATA USING THE $\mathcal{G}_A^0$ DISTRIBUTION

To measure the goodness of the fit of $\mathcal{K}_A$ distributed data using the $\mathcal{G}_A^0$ distribution, we will use the $\chi^2$ adherence test in a Monte Carlo experiment.

### $\chi^2$ TEST

To test if the simulated $\mathcal{K}_A(\alpha_K, \lambda, n)$ distributed data can be fitted by the $\mathcal{G}_A^0(\alpha_G, \gamma, n)$ distribution, the Pearson's $\chi^2$ statistic will be used:

$$\chi^2 = \sum_{i=0}^{k} \frac{(h_i - mp_i)^2}{mp_i} \qquad (8)$$

where $m$ is total number of $K_A$ distributed data, $h_i$ is the number of data in each interval, $k$ is the number of intervals, $p_i = F(z_i) - F(z_{i-1})$, where $F$ is the cumulative distribution function and the interval $i$ is given by $[z_{i-1}, z_i]$.

Let $\mathbf{z}_A$ be a sample of size $m$ of $\mathcal{K}_A(\alpha_K, \lambda(\alpha_K, n), n)$ distributed data, with $\lambda(\alpha_K, n)$ as defined in (5). From this sample $\alpha_G$, the homogeneity parameter of the $\mathcal{G}_A^0(\alpha_G, \gamma(\alpha_G, n), n)$, is estimated using the maximum likelihood estimator considering $\gamma(\alpha_G, n)$ as defined in (6).

If the random variable $Z$ is $\mathcal{G}_A^0(\alpha_G, \gamma, n)$ distributed, then its cumulative distribution function is given by:

$$F_{Z_A}(z) = \frac{n^{n-1}\Gamma(n-\alpha)z^{2n}}{\gamma^n \Gamma(n)\Gamma(-\alpha)} H(n, n-\alpha; n+1; -nz^2/\gamma) \qquad (9)$$

where $H$ is the hypergeometric function and can be evaluated using

$$F_{Z_A}(z) = \Upsilon_{2n,-2\alpha}\left(\frac{-\alpha}{\gamma} z^2\right) \qquad (10)$$

where $\Upsilon$ is the cumulative distribution function of a Snedecor distributed random variable.

### MONTE CARLO EXPERIMENT

A Monte Carlo experience was carried out generating $\mathcal{K}_A(\alpha_K, \lambda, n)$ distributed data which were fitted with a $\mathcal{G}_A^0$ distribution. The values of the parameters $\alpha_K$ and $\alpha_G$ were estimated by the maximum likelihood method and by the ½ order moment estimator method (see Mejail et al. (1998)). The goodness of fit was evaluated using the p-value of the $\chi^2$ test.

For a number $R$ of replications, the following steps were performed:

- For each $\alpha_K \in [4,12]$ $\mathcal{K}_A$ distributed samples were generated.
- For each of these $\mathcal{K}_A$ distributed samples the roughness parameter $\alpha_G$ and the parameter $\gamma$ of the $\mathcal{G}_A^0$ distribution were estimated.
- The goodness of fit was evaluated using the $p$-value of the $\chi^2$ test.

The $\mathcal{K}_A$ distributed samples were generated for values of $\alpha_K \in [4,12]$ with number of replications $R = 100$, 1000 and 10000, sample sizes $T = 1000$ and 10000 and significance level 0.01.

As a particular case, the figures for $\alpha_K = 4$ are shown in the following table, where for each value of number of replications $R$ and each sample size $T$, the mean value of the estimated $\alpha_G$, the mean square error $mse$ and the rejection percentage $r_{0.01}$ are presented.

| $\alpha_K = 4$, $n = 1$ | | | | % |
|---|---|---|---|---|
| $R$ | $T$ | $\alpha_G$ | $mse$ | $r_{0.01}$ |
| 100 | 10000 | -4.50 | 0.13 | 11.0 |
| 1000 | 1000 | -4.78 | 1.80 | 1.5 |
| 1000 | 10000 | -4.53 | 0.14 | 10.0 |
| 10000 | 1000 | -4.79 | 2.08 | 1.3 |
| 10000 | 10000 | -4.52 | 0.13 | 12.0 |

This shows that there is no reason to suppose that the $\mathcal{K}_A$ and $\mathcal{G}_A^0$ distributions are different at the proposed significance level.

The next table shows the values corresponding to the mean value of the estimated $\alpha_G$ with $\alpha_K \in [5,10]$ and $n = 1$.

| $R = 1000$, $T = 10000$, $n = 1$ | | | |
|---|---|---|---|
| $\alpha_K$ | $\alpha_G$ | $mse$ | $r_{0.01}$ |
| 5. | -5.53 | 0.25 | 3.4 |
| 6. | -6.55 | 0.50 | 2.2 |
| 7. | -7.61 | 0.95 | 1.0 |
| 8. | -8.73 | 1.93 | 1.1 |
| 9. | -9.69 | 2.448 | 1.3 |
| 10. | -10.83 | 4.61 | 0.7 |
| 11. | -11.98 | 6.80 | 0.7 |

In figures 4 and 5, the histograms of the estimated $\alpha_G$ for a sample size $T = 10000$ and number of replications $R = 10000$, generated with $\alpha_K = 4$ and $\alpha_K = 8$ respectively. Notice that, in each case, the corresponding $\alpha_G$ that minimise integral (7) are –4.3 and –8.3 respectively.

Gordon, S.D. and Ritcey, J.A. Calculating the K distribution by saddlepoint integration. In: *IEE Proceedings in Radar, Sonar and Navigation*. Vol:142, N:4, pp:162-165, 1995

Joughin, I.R, Percival, D.B and Winebrenner, D.P. Maximum likelihood estimation of $\mathcal{K}$ distribution parameters for SAR data. In: *IEEE Transactions on Geoscience and Remote Sensing*. Vol:31, N: 5, ,pp: 989-999, september, 1993

Mejail, M, .Jacobo-Berlles, J.C, Frery, A.C and Bustos, O.H. Parametric roughness estimation in amplitude SAR images under the multiplicative model. To appear, 1998.

Yanasse, C.C.F, Frery, A.C and Sant'Anna, S.J.S. Stochastic distributions and the multiplicative model: relations, properties, estimators and applications to SAR image analysis. In: *Technical Report 5630-NTC/318, INPE*, São José dos Campos, SP, Brazil, 1995.

Yanasse, C.C.F, Frery, A.C, Sant'Anna, S.J.S, Hernandez, P.F. and Dutra. , L.V.Statistical analysis of SAREX data over Tapajós – Brazil. In: *SAREX-92: South American Radar Experiment*, M.Wooding and E.Attema, editors. pp:25-40, ESA, Paris, 1993.

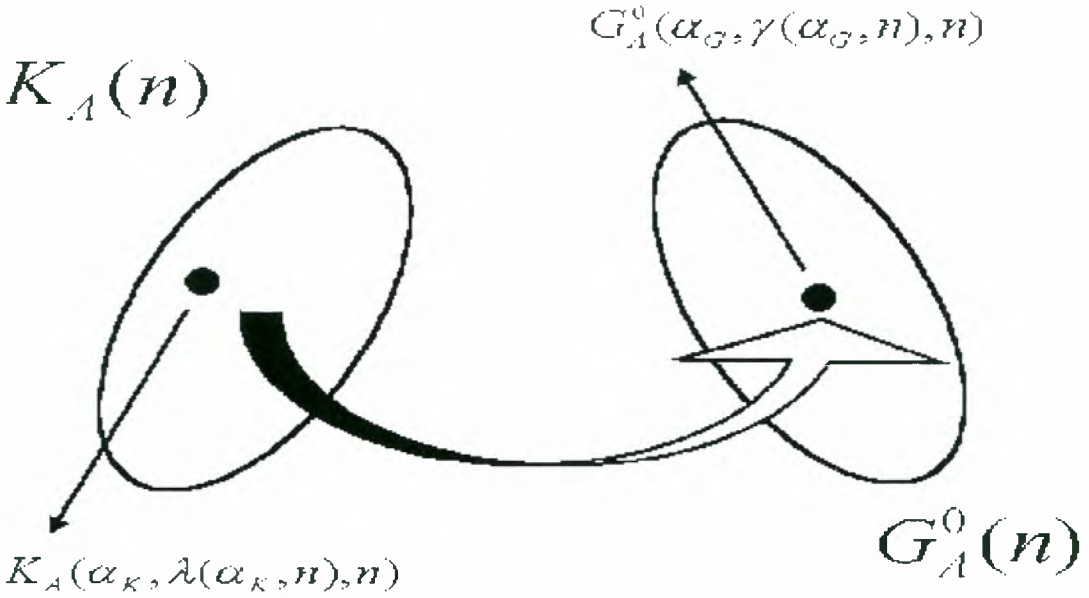


Figure 1: Correspondence between the $\mathcal{K}_A$ and the $\mathcal{G}_A^0$ distributions.

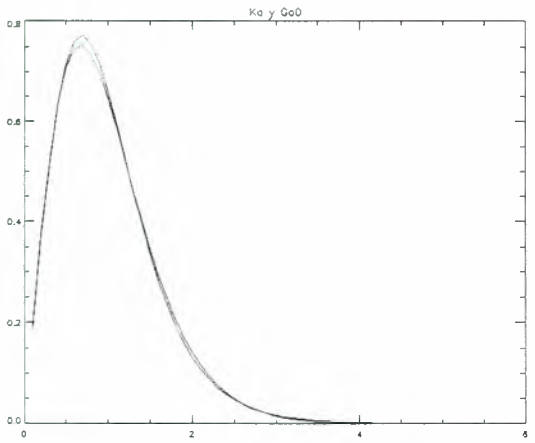


Figure 2: Densities of $\mathcal{K}_A$ and $\mathcal{G}_A^0$ distributions for $\alpha_K = 4$ and $\alpha_G = -4.3$ , with $n = 1$ .

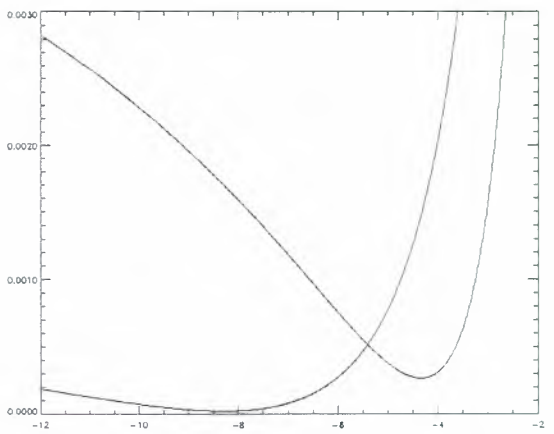

Figure 3: Distance between both distributions as a function of $\alpha_G$ for $\alpha_K = 4$ and for $\alpha_K = 8$ .

# GENETIC-ANNEALING PARAMETER ESTIMATION FOR INTENSITY SAR DATA

Paulo Ricardo dos Santos Mendonça[1], Alejandro C. Frery[2]

[1]Fallside Lab
Cambridge University Engineering Department
Trumpington Street, Cambridge
CB2 1PZ United Kingdom
prdsm2@eng.cam.ac.uk

[2]UFPE-DI
CP 7851
50732-970 Recife, PE, Brazil
Tel: 55-81-2718430, Fax: 55-81-2718438
frery@di.ufpe.br

## ABSTRACT

Finding the maximum likelihood estimators for some distributional parameters of intensity data in Synthetic Aperture Radar (SAR) images is a very difficult optimisation problem due to, among other reason, the presence of several local maxima in the objective function, the analytical intractability of the expressions involved and numerical instabilities. A possible approach to this problem is the use of stochastic optimisation techniques, such as simulated annealing and genetic algorithms, that do not get trapped into local maxima hills and, thus, make it possible to deal with very general distributions. This work shows the results of such approach in real situations, with images obtained from urban areas.

**Keywords:** Remote Sensing, SAR images, multiplicative model, parameter estimation, stochastic optimisation.

## INTRODUCTION

Statistical tools have long been used to tackle some problems related to images. The stochastic nature of these objects, and the excellent results frequently obtained with this statistical approach, stimulated the development of a vast bulk of methods and techniques.

Most of these tools are based either on quite mild hypothesis (for instance, histogram equalisation that assumes no distribution at all) or on the Gaussian distribution (Wiener filter, usual maximum likelihood classification etc.).

Statistical modelling and parameter estimation are very important issues in the problem of processing and analysis of SAR images. These parameters can be associated to types of targets and, therefore, they can be used as important features for image classification.

The Gaussian distribution is so frequently used because, among other reasons, there are many techniques associated to this hypothesis. This distribution has been used for two centuries, and its properties are well known and many computational methods are available to deal with it. Synthetic Aperture Radar (SAR) images can be successfully modelled by a class of distributions that do not belong to the Gaussian distribution.

When SAR images are used, instead of optical data, the exception becomes the rule: the Gaussian hypothesis is seldom confirmed. This is mainly due to the coherent nature of the illumination, and the consequences of this departure range from poor results, when classical tools are applied, to the need of studying and proposing new methods for SAR image processing and analysis. Therefore, parameter estimation is a problem to be carefully addressed.

Among the several estimators available, the maximum likelihood ones are those with the "best" theoretical characteristics, like asymptotic convergence to normality, asymptotic consistency and efficiency, etc. Therefore, it would be desirable to estimate the parameters of distributions of SAR images data with those estimators. Nevertheless, the complexity of the models for such images usually yields to intractable problems, both from an analytical or numerical view point (Frery et al, 1997). To deal with that situation, the use of a stochastic optimisation technique, that combines genetic algorithms and simulated annealing into a single evolutionary strategy, is proposed in this work.

In next sections the general problem of maximum likelihood estimation is posed; data models for distributions of SAR images are recalled, and the problem of maximum likelihood estimation for the particular distributions that model SAR images data is also discussed. Then, an overview of stochastic optimisation is given, with a short description of simulated annealing, genetic algorithms and the hybrid

genetic annealing algorithm. The results of the last section are then applied to the design of an algorithm aiming at solving the aforementioned estimation problem. Experimental results are finally shown, along with the conclusions.

## MAXIMUM LIKELIHOOD ESTIMATION PROBLEM

Given the data set $\mathbf{x} = \{x_i\}_{i=1}^{N}$ of $N$ independent samples of a random variable and the probability distribution $F_{\mathbf{p}}$ with density $f_{\mathbf{p}}$ under the vector of real parameters $\mathbf{p} = (p_1, \ldots, p_m)$, the *maximum likelihood estimator* for the vector of parameters $\mathbf{p}$ under the data set $\mathbf{x}$ and the distribution $F_{\mathbf{p}}$ is (if it exists) the vector $\hat{\mathbf{p}}$ such that $V(\hat{\mathbf{p}}) = \prod_{i=1}^{N} f_{\mathbf{p}}(x_i)$ is maximum. Since the logarithmic function is a strictly increasing function, the maximisation of this function is equivalent to the problem of finding $\max_{\mathbf{p}} \sum_{i=1}^{N} f_{\mathbf{p}}(x_i)$.

For some particular distributions, e. g. Gaussian, the maximum likelihood estimation problem has simple analytical and well known solutions. But if the modelling distribution is more complex, analytical solutions may not be feasible. When faced to this situation, the analyst has to choose between using other estimation technique (the substitution method, for instance) and looking for optimisation tools. This is the case for the models presented in this work, and the use of a numerical method to find the estimator vector $\hat{\mathbf{p}}$ is presented.

## MODELS AND INFERENCE FOR SAR IMAGES

Data from SAR images can be modelled as the product of two independent random components: one due to the terrain backscatter and one due to the speckle noise. The usual model for $n$ looks intensity speckle is a Gamma distribution, denoted as $Y_l \sim \Gamma(n, n)$, with density given by

$$f_{Y_l}(y) = \frac{n^n}{\Gamma(n)} y^{n-1} \exp(-ny), \quad y, n > 0$$

The number of looks, namely $n$, can be assumed known beforehand. A possible model for the distribution of the intensity backscatter return is the inverse generalised Gaussian, denoted as $X_l \sim N(\alpha, \gamma, \lambda)$ with density

$$f_{X_l}(x) = \frac{(\lambda/\gamma)^{\alpha/2}}{2K_\alpha(2\sqrt{\lambda\gamma})} x^\alpha \exp\left(-\frac{\gamma}{x} - \lambda x\right), \quad x > 0$$

where $K_\alpha$ is the modified Bessel Function of the third kind, and parameters space

$$\begin{cases} \gamma > 0, & \lambda \geq 0, \quad \text{if } \alpha < 0, \\ \gamma > 0, & \lambda > 0, \quad \text{if } \alpha = 0, \\ \gamma \geq 0, & \lambda > 0, \quad \text{if } \alpha > 0. \end{cases}$$

The intensity return corresponds to the product of the aforementioned backscatter and speckle $Z_l = X_l \cdot Y_l$ results in a distribution denoted as $G_l(\alpha, \gamma, \lambda, n)$ with density

$$f_{Z_l}(z) = \frac{n^n (\lambda/\gamma)^{\alpha/2}}{\Gamma(n) K_\alpha(2\sqrt{\lambda\gamma})} z^{n-1} \left(\frac{\gamma + nz}{\lambda}\right)^{\frac{\alpha-n}{2}} K_\alpha\left(2\sqrt{\lambda(\gamma+nz)}\right), \quad z > 0$$

The above distribution has several limit cases of interest, depending on the parameters, which are presented and discussed in Frery et al. (1997). The particular case that will be here discussed in that corresponding to the situation $-\alpha, \gamma > 0$, $\lambda = 0$, that yields to a distribution known as $G_l^0(\alpha, \gamma, n)$, whose density is given by

$$f_{Z_l}(z) = \frac{n^n \Gamma(n-\alpha) z^{n-1}}{\gamma^\alpha \Gamma(n)\Gamma(-\alpha)(\gamma + nz)^{n-\alpha}}$$

Solving the maximum likelihood problem for the data set $(z_1, \ldots, z_N)$ and the distribution characterised by the density given above consists of maximising the following equation with respect to both variables $\alpha$ and $\lambda$:

$$\ell(\alpha, \lambda) = N \log \frac{n^n \Gamma(n-\alpha)}{\gamma^\alpha \Gamma(n)\Gamma(-\alpha)} + (n-1) \sum_{1 \leq i \leq N} \log z_i + (\alpha - n) \sum_{1 \leq i \leq N} (\gamma + n z_i)$$

This maximisation is the problem addressed in the next sections.

## STOCHASTIC OPTIMISATION

Optimisation is the search for parameters or solutions for a given problem that minimise or maximise a certain function or functional, conditioned or not to a set of restrictions.

There is a restricted class of optimisation problems with a simple analytical solution, that can be found by usual methods of calculus (Apostol, 1967a; Apostol, 1967b). Nevertheless such approach is not feasible in most of the optimisation problems of real interest due to, among other reasons, the computational complexity aspects as well as the lacking of closed analytical expressions for the involved functions.

On the other hand, Nature is every time dealing (quite successfully) with optimisation problems of extreme complexity. Two examples are the evolution of species and the annealing of molten metals. In the former example living beings, mankind for instance, are exposed to natural competition and to the influence of the environment. Those best adapted survive to keep on fighting, wile the weaker are eliminated of the evolutive competition.

The annealing of molten metals is strongly connected to an amazing optimisation problem, stated as the Second

Law of Thermodynamics: *closed systems evolve so that its entropy raises* (Hill, 1960). Each atom of a system behaves in order that this condition is satisfied. In a molten metal, numbers of the order of $10^{23}$ atoms, in random motion, build into a single crystal, among the almost uncountable possible arrangements, in obedience to the Second Law.

Besides being natural phenomena, the two above examples have in common the presence of random elements. The crossover and mutation of species are affected by so many different and fuzzy parameters that a single deterministic analysis of this problems becomes impossible and useless. In the state transition of metals, the success of Statistical Thermodynamics over the Laplacian deterministic approach clearly shows that such problem cannot be properly coped without the aid of an stochastic approach. Thus, in the solution of these two formidable optimisation problems, Nature deals with or uses randomness. That is the basis for the study of stochastic optimisation. Without loss of generality, will we consider in the next sections only minimisation problems.

## SIMULATED ANNEALING ALGORITHMS

The fundamental ideas of simulated annealing algorithms were first introduced by Metropolis et al (1953), as a method to determine physical and chemical properties of a set of atoms in transition to thermal equilibrium. In this seminal work this technique did not used any cooling schedule, a central issue in annealing algorithms, since this cooling idea had no connection with the problem under analysis. The use of the Metropolis method in the search for the solution for more generic optimisation problems is due to Kirkpatrick et al (1983), where the concept of cooling schedule was also introduced. Geman and Geman (1984) were the first to state an lower bound to the temperature decay rate that guarantees the convergence of the algorithm to a global minimum or maximum point. A basic simulated annealing algorithm is described in the next scheme.

1 Generate initial state $\mathbf{x}_t$
2 Generate noise with temperature $T$: $\mathbf{r}_t$
3 Generate candidate to new state $\mathbf{c} = \mathbf{x}_t + \mathbf{t}_t$
4 Test the acceptance of candidate:
  4.1 If candidate is accepted then $\mathbf{x}_{t+1} = \mathbf{c}$
  4.2 Else $\mathbf{x}_{t+1} = \mathbf{x}_t$
5 Decrease $T$
6 Goto step 2

## THE METROPOLIS ALGORITHM

Let $S$ be a closed system, and $X$ be the set of possible states in $S$. Consider also $\mathbf{x}_t, \mathbf{x}_{t+1} \in X$, with associated internal energies, or cost functions, $E(\mathbf{x}_t)$ and $E(\mathbf{x}_{t+1})$. Finally, define $\Delta E(\mathbf{x}_t) = E(\mathbf{x}_t) - E(\mathbf{x}_{t+1})$.

The Transition Acceptance Probability (TAP) between the states $\mathbf{x}_t$ and $\mathbf{x}_{t+1}$ is defined as

$$\Pr(\mathbf{x}_t, \mathbf{x}_{t+1}) = \begin{cases} \exp(-\Delta E(\mathbf{x}_t)/(kT(t))) & \text{if } \Delta E(\mathbf{x}_t) < 0 \\ 1 & \text{else} \end{cases}$$

where $T(t)$ is the current temperature of the process and $k$ is a positive constant. This probability benefits transitions from states with larger costs to states with smaller associated costs. Next result shows another (less intuitive) advantage of using this TAP.

**Theorem 1:** if all states in a system with transitions ruled by the TAP can visited at any temperature $T > 0$, the set of states distribution converges to a Boltzmann-Gibbs distribution, i.e.,

$$\lim_{t\to\infty} \Pr(\mathbf{x}_t = \mathbf{x}) = \frac{\exp(-E(\mathbf{x})/(kT))}{\sum_{\hat{\mathbf{x}}} \exp(-E(\hat{\mathbf{x}})/(kT))}$$

## THE STATE VISITING PROCESS

Nothing was said about the rules of visiting of states so far. This issue and the concept of cooling schedule are the fundamental differences between the Metropolis Algorithm and simulated annealing. In the former, a state $\mathbf{x}_{t+1}$ is randomly selected "around" the previous state $\mathbf{x}_t$ with uniform distribution among its neighbours. In a simulated annealing algorithm the selection of a new state is done by a temperature dependent distribution. The time variation of the temperature is the called "cooling schedule". Expressing the temperature as a monotonic decreasing function of time, i.e. the probability density of the distribution probability that selects states in an annealing algorithm denoted $g_t(\cdot)$, must satisfy the relation $g_t(\cdot) \to \delta(\cdot)$ as $t \to \infty$.

A formal approach to realisations of $g_t$ can be found in Mendonça (1997). For the purposes of this work, it is enough to consider that $g_t$ depends only on the distance $\Delta\mathbf{x}_t = \|\mathbf{x}_{t+1} - \mathbf{x}_t\|$ between the current and visited states, i.e., $g_t(\mathbf{x}_{t+1}, \mathbf{x}_t) = g_t(\Delta\mathbf{x}_t)$, and on the result stated in the following Theorem.

**Theorem 2:** A sufficient and necessary condition for the convergence of an annealing algorithm is that $\sum_{t=t_0}^{\infty} g_t(\Delta\mathbf{x}_t) = \infty$.

This theorem is a landmark in the theory of simulated annealing, since if establishes an analytical tool in the design of algorithms with assured convergence.

## THE N-FAST SIMULATED ANNEALING ALGORITHM

The algorithm introduced in Geman and Geman (1984) could not be directly used due to its slow convergence

speed. This problem was overcame in Szu and Hartley (1987), with the development of the *Fast Simulated Annealing Algorithm* (FSA), and further improvement was obtained in Mendonça (1997) and Mendonça and Caloba (1997), with the *n-Fast Simulated Annealing Algorithm* (*n*-FSA), whose main results are highlighted in the following. Consider

```
1   P ← generate initial population
2   while the stopping criteria is not satisfied
    2.1 (a'', a''') ← crossover(a, a'', P)
    2.2 P ← substitution_criterion_1(a'', a''', P)
    2.3 b' ← mutation(b)
    2.4 P ← substitution_criterion_2(b', P)
3   endwhile
```

- A random variable, corresponding to the state visiting distribution probability $nR = (1+R)^n - 1$, where $R$ is the norm of a $D$-dimensional Cauchy distributed random vector in polar co-ordinates;
- The cooling schedule for convergence $T_{n,R}(t) = T(0)/(1+t)^n$

**Theorem 3:** Let $\alpha$ be the desired probability of a transition between states at a distance $L$ apart at $t = 0$. Then the initial temperature for the cooling schedule must be $T(0) = L/((1+\tan(p_D^{-1}(1-\alpha)))^n - 1)$, where $p_D = \int_0^{\varphi} D\Gamma((1+D)/2)/(\sqrt{\pi}(1+D)/2)\operatorname{sen}^{D-1} d\theta$, in order to guarantee convergence.

## THE BASIC GENETIC ALGORITHM

The basic structure of a genetic algorithms is presented in the next scheme. The first step of the algorithm is the generation of a population of feasible solutions to the optimisation problem. This population must have great diversity and must be as uniformly distributed over the space of search as possible. Then, while the stopping criteria is not satisfied, i.e., while a "good" solution is not found among the individuals of the population, the crossover and mutation operators are executed.

The crossover corresponds to a binary operation between two selected individuals, yielding to an offspring or pair of offspring. This operator is usually designed so that the offspring has as many common good characteristics to its parents as possible. This results in an heuristic local search procedure, since the solution found by crossover may not be too apart from its parents.

Then the offspring (or offspring) is added to the original population and from this new set of individuals, one (or two) are removed, keeping the size of the initial population. The substitution criteria must be coherent with the evolution of the population.

The mutation is an unary operation that corresponds to the adding of a random perturbation in a selected individual, producing a mutant. Again, the mutant individual is added to the population, and a consistent substitution criteria is used to keep its size. The substitution criteria for mutation does not have to be the same as the one for the crossover. This loop goes on until the stopping criteria is fulfilled.

There are some doubts related to the validity of the genetic operator of mutation. Some serious researchers believe that the use of this operator may degenerate the algorithm to a random exhaustive (Tanomaru, 1995). Let us now consider this question from a different point of view.

## GENETIC OR ANNEALING?

Several works in simulated annealing stress the advantages of this algorithm over genetic algorithms, and vice-versa. It is evident that certain algorithms are better suited to particular problems than others, and this contributes to this discussions (Wolpert and Macready, 1995).

Some claimed advantages of genetic algorithms over simulated annealing are their flexibility and ease of parallel implementations. Annealing, on the other hand, has stronger analytical fundaments, resulting in a better understanding and control of the algorithm; it also has a convergence proof. In general, genetic algorithms have a greater adaptability to combinatorial problems, while continuous or piecewise continuous cost functions are better handled by annealing algorithms.

## METROPOLIS IN GENETIC ALGORITHMS

Due to the difficulty in modelling the evolution of species, there are few analytical tools involved in the study and development of genetic algorithms. In opposition, the simulated annealing algorithms are based in Statistical Thermodynamics and, therefore, supported by strong mathematical arguments.

If the state transition probability, i.e. the probability of substitution of an old individual by a new one, is given by the TAP, and if the visited state, or individual generation, is such that all states can always be visited, the state distribution will converge to a Boltzmann-Gibbs distribution (Theorem 1).

The point now is how to ensure that all states can always be visited. The crossover genetic operator is designed in such way that the common characteristics of its parents are preserved and, thus, it is not suitable to yield to populational diversity. However, the mutation operator can be easily projected to guarantee the variety in the generation of individuals. So applying TAP as a substitution criteria *between the original and the mutant individuals* for the mutation operator results in a Boltzmann-Gibbs distribution for the population, and in the convergence of the Genetic-Metropolis Algorithm.

## ANNEALING IN GENETIC ALGORITHMS

Now it is possible to introduce a cooling schedule into the Genetic-Metropolis Algorithm, resulting in a full Genetic-Annealing Algorithm. To obtain that it is enough to generate the mutant by the addition of a perturbation under a probability distribution with the distribution presented in Section 0, and an appropriate cooling schedule. Details can be found in Mendonça (1997) and Mendonça and in Mendonça and Caloba (1997).

## PARAMETER ESTIMATION FOR THE $G_I^0$ DISTRIBUTION

The flexibility and power of the Genetic Annealing Algorithm motivated its use in the problem of parameters estimation of the $G_I^0$ distribution. Forthcoming sections will present particular aspects of the implementation of the algorithms, and the simulation results for real data.

## IMPLEMENTATION OF THE ALGORITHM

The Genetic Annealing Algorithm starts with the generation of a population of individuals. In Frery et al (1997) parameter estimation is performed by the moments method. In this manner, the population of estimators *around* this previous estimator can be generated, obtaining with a good chance that the solution found for the maximisation of the aforementioned likelihood equation has a greater likelihood than that of the estimator found by the moments method.

In all the tested situations, a initial population of 100 individuals (or estimators) was large enough to find a good solution with less than 1000 generations, and all images were sub sampled to a matrix of size $20\times20$. For technical details about the images, shown in the next Figure, the reader is referred to Frery et al (1997).

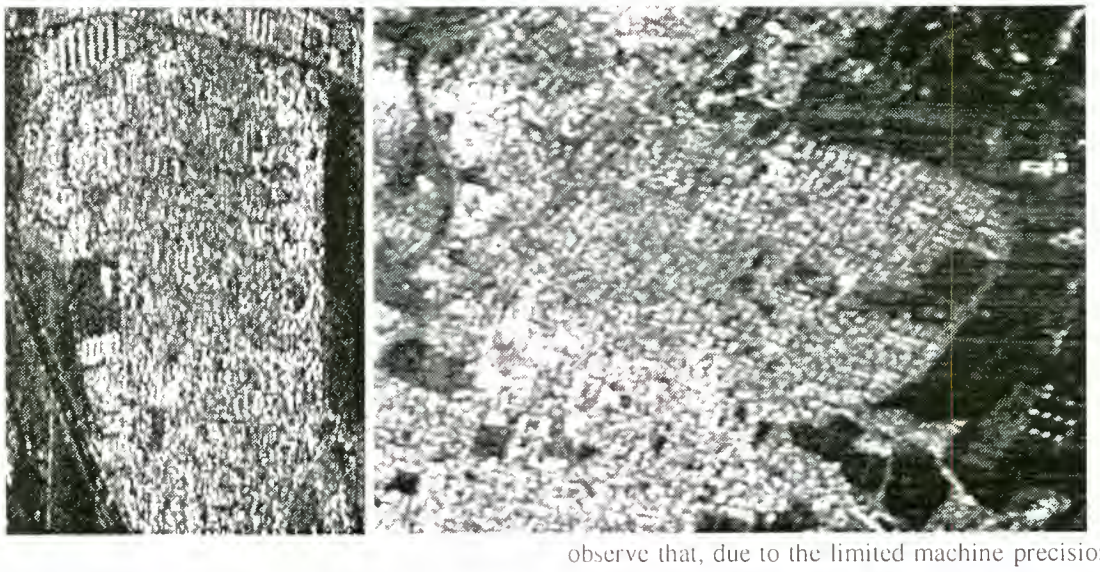

## REPRESENTATION OF THE POPULATION

The actual representation of parameters was (Mendonça, 1997), due to its simplicity and to the continuous nature of the problem. The population was the generated as a $100\times4$ matrix, following the scheme bellow:

| | $\hat{\alpha}$ | $\hat{\gamma}$ | Prob. Selection | Likelihood |
|---|---|---|---|---|
| Entry for ind. 00 | • | • | • | • |
| Entry for ind. 01 | • | • | • | • |
| ... | ... | ... | ... | ... |
| Entry for ind. 98 | • | • | • | • |
| Entry for ind. 99 | • | • | • | • |

The likelihood column corresponds to the value of the log-likelihood function evaluated at the parameters in the corresponding line. The matrix is then sorted from the best to the worst individual. It is important to observe that, due to the limited machine precision, the final values of this column may equal infinity, and the correspondent degenerated individuals must be discarded from the population. This results in an effective population of size $N$, with a few less individuals than previously designed. Nevertheless, the number of degenerated individuals must be small, since the estimator found by the moments method is an excellent starting point.

The column **Probability of Selection** is filled with a positive parameter proportional to the difference between the correspondent value in the likelihood column plus a threshold, chosen here as 1, and the likelihood of the worst (or last, since they are already sorted) individual. The column is then normalised so that it sums to 1. This procedure, shown in detail in the following equation, generates a number that will be used as a probability of selection for individuals in the

crossover and mutation operators, selecting with greater probability those individuals with a better adaptation. Denoting the likelihood as $\ell$ and a certain threshold as $d$ :

$$\text{Prob. Selection}(i) = \frac{\ell(i) - \ell(N-1) + d}{\sum_{j=1}^{N-1} \ell(j) - N(\ell(N-1) - d)}$$

## CROSSOVER OPERATOR

The first step in the application of the crossover operator is the selection of a pair of individuals, henceforth named $r_1$ and $r_2$ (for *relatives*). The column with the assigned probabilities is used in this task. First, a random number $x$ in the interval [0,1] is generated. Given the set of probabilities $\{p_j\}_{j=0}^{N-1}$, the index $i$ of the selected individual is $i = \sum_{j=0}^{N-1} u(x - p_j)$, where $u$ is the unitary step function. This procedure is repeated until a pair of different individuals is selected.

The crossover itself is done by convex combination of the parents, and the offspring is generated as shown

$$(\hat{\alpha}_{\text{offspring}}, \hat{\gamma}_{\text{offspring}}) = \frac{p_1(\hat{\alpha}_{r_1}, \hat{\gamma}_{r_1}) + p_2(\hat{\alpha}_{r_2}, \hat{\gamma}_{r_2})}{p_1 + p_2}$$

where $\hat{\alpha}_{r_i}, \hat{\gamma}_{r_i}$ and $p_i$ are the parameters $\alpha, \gamma$ and the probability of selection of the relative $i$.

The log-likelihood of the offspring is evaluated, and compared to the log-likelihood of its relatives. If it is greater than any one of them, the offspring replaces the relative with smaller adaptation. Then, the probabilities of selection are re-evaluated, and the mutation operator is again applied.

## MUTATION OPERATOR

Analogously to the crossover operator, the probabilities of selection are used to choose an individual $m$ that will mutate. The mutation itself is processed in a quite similar way as in the crossover, from an individual $i$ and a perturbation $j$ : $(\hat{\alpha}_m, \hat{\gamma}_m) = (\hat{\alpha}_i, \hat{\gamma}_i) + (\hat{\alpha}_j, \hat{\gamma}_j)$.

The log-likelihood of the mutant is evaluated, and a selection between the original individual and the mutant is done, under the rule given in Theorem 1.

An important detail is that this operation is **not** used when the selected candidate to mutation is the best individual. Such procedure is necessary since, on the contrary to a simple annealing algorithm, there are no guarantees that the same individual will be obtained in the next generation, so it must ensured that the best individual is not lost by mutation.

## EXPERIMENTAL RESULTS

This section presents comparisons between the genetic annealing algorithm and the moments method (MO for short), presented in Frery et al (1997). All images were sub-sampled to $20 \times 20$, which is an immediate advantage of the proposed method over the moments, since the last need samples of sizes as large as 100000.

The next Table summarises the results of the first and second experiments. Next figure shows the fit of the estimated densities over the image histogram.It is evident that in both cases the log-likelihood obtained by the optimisation procedure is higher than that attained by the moments method. This yields to a better representation of the data, a quite desirable feature for processing and analysis algorithms.

It is important to note that the log-likelihood in the tables is evaluated for the whole images data set, although the ML estimator is evaluated only for a small sub-sampled set of the image data, while the moments method uses all the available data.

## CONCLUSIONS

This work presented a novel approach to the problem of maximum likelihood estimation for some SAR image data distributions, based on a fusion of genetic algorithms and simulated annealing. The results obtained are superior, in the log-likelihood sense, to those obtained by the moments method. The method itself is more general and robust, and allows the use of smaller samples than the moments technique.

The next step of this work will be the use of this method in the estimation of parameter of the $G_I$ distribution. Parallel implementations will also be considered.

## ACKNOWLEDGMENTS

This work was partially supported by grants from CNPq (Proc. 523469/96-9) and FACEPE (APQ 0707-1.03/97).

## REFERENCES

Apostol, T.M. *Calculus*, vol. 1. John Wiley & Sons, Singapore, 2. Ed., 1967.

Apostol, T.M. *Calculus*, vol. 2. John Wiley & Sons, Singapore, 2. Ed., 1967.

Frery, A.C.; Müller, H.J.; Yanasse, C.C.F; Sant'Anna, S.J.S. A model for extremely heterogeneous clutter. *IEEE Trans. Geosc. Rem. Sens.*, 35(3):1–12, 1997a.

Geman, S; Geman, D. Stochastic relaxation, Gibbs distributions and the Bayesian restoration of images. *IEEE Trans. Patt. An. Mach. Int.*, 6:721–741, 1984.

Hill, T.L. *Introduction to statistical thermodynamics*. Addison-Wesley, MA, 1960.

Kirkpatrick, S.; Gelatt Jr., C.D.; Vecchi, M.P. Optimization by simulated annealing. *Science*, 220:671–680, 1983.

Mendonça, P.R.S. *Novos algoritmos de simulated annealing*. MSc Thesis, COPPE/PEE, Universidade Federal de Rio de Janeiro, 1997.

Mendonça, P.R.S.; Caloba, L.P. New simulated annealing algorithms. In: *Proceedings 1997 IEEE International Symposium on Circuits and Systems*, June 1997, to appear.

Metropolis, N.; Rosenbluth, A.W.; Rosenbluth, M.N. Equation of state calculation by fast computing machines. *Jr. Chem. Phys.*, 6:1087–1092, 1953.

Szu, L; Hartley, H. Fast simulated annealing. *Phys. Lett. A*, 122(3,4):157–162, 1987.

Tanomaru, J. Motivação, fundamentos e aplicações de algoritmos genéticos. In: *II Congresso Brasileiro de Redes Neurais*, Curitiba, 1995.

Wolpert, D.H.; Macready. W.G. *No free lunch theorems for search*. Technical report, Santa Fe Institute, 1995.

| | $\hat{\alpha}$ | | $\hat{\gamma}$ | | Log-likelihood | |
|---|---|---|---|---|---|---|
| MO | −2.018 | −1.807 | 401329 | 124839000 | −1234378.2 | −2.146947.6 |
| ML | −1.770 | −2.416 | 317960 | 202774000 | −1234334.1 | −2145896.4 |

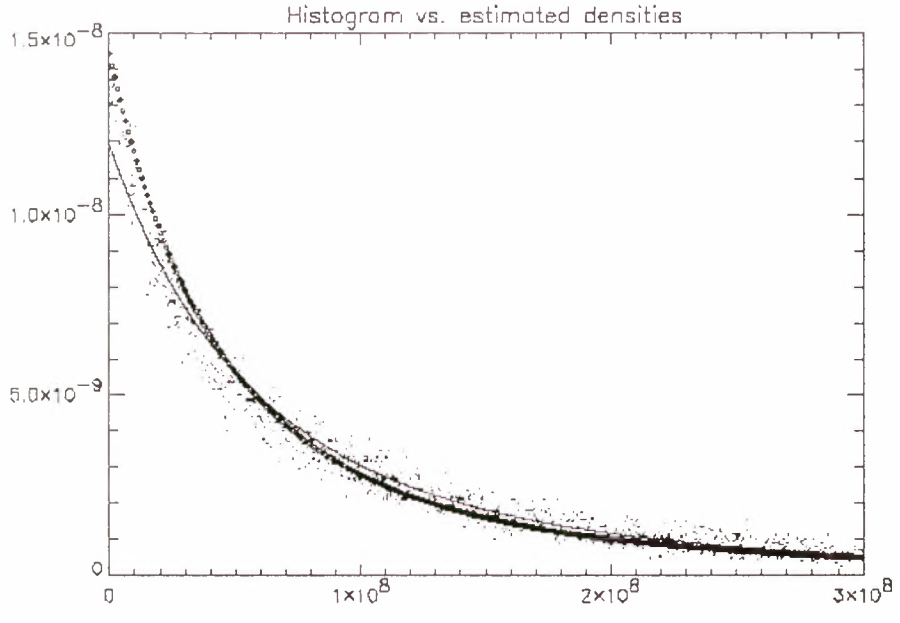


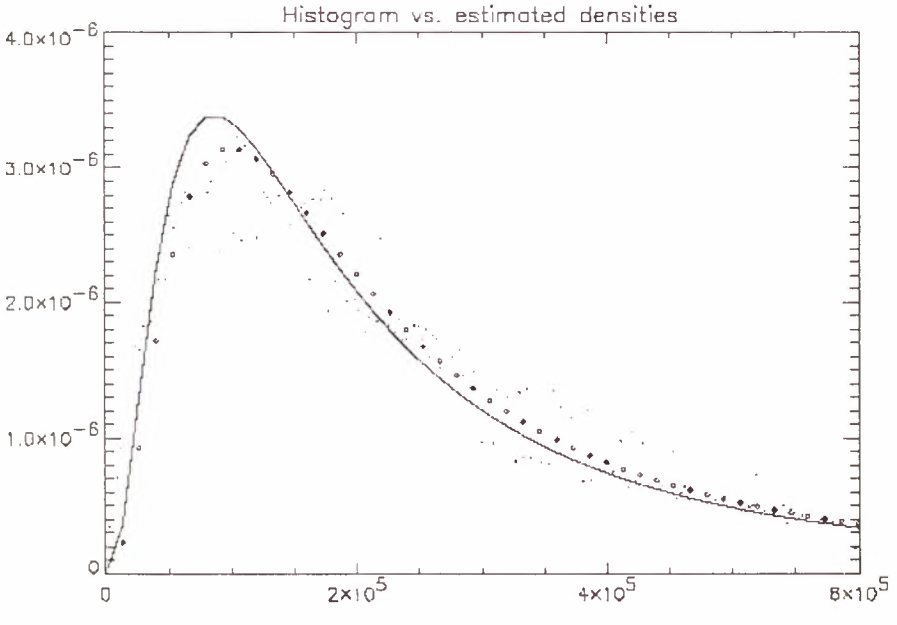

# BIAS CORRECTION FOR COVARIANCE PARAMETERS ESTIMATES IN POLARIMETRIC SAR DATA MODELS

Luciano B. da Silva[1], Klaus L. P. Vasconcellos[1], Alejandro C. Frery[2]

[1]UFPE-DE
Cidade Universitária, 50740-540 Recife, PE, Brazil
{lbs,klaus}@de.ufpe.br

[2]UFPE-DI
CP 7851
50732-970 Recife, PE, Brazil
Tel: 55-81-2718430, Fax: 55-81-2718438
frery@di.ufpe.br

## ABSTRACT

This paper obtains an expression for the second-order bias of the maximum likelihood estimates of the parameters in the covariance matrix of the polarimetric SAR observation vectors, which are assumed to follow a complex normal distribution. The second-order biases are very simple functions of the parameters, and, consequently, the second-order bias corrected estimates are very easy to compute. In particular, we discuss the performance of the corrected estimate of the absolute value of the complex correlation coefficient, which is a crucial parameter in the practical study of polarimetric SAR data

**Keywords:** Bias correction, complex correlation coefficient, complex normal distribution, maximum likelihood, polarimetric SAR

## INTRODUCTION

The synthetic aperture radar – SAR- is an important conquest of the modern remote sensing technology. Through this kind of radar, important characteristics of the target returns can be studied, such as phase difference information, intensity ratio of different polarisations, etc. Applications include geology, oceanography, environmental sciences, planing for the use of the land, among others.

Data captured by this sort of radar are very rich in information and increasingly sophisticated techniques have been employed to extract this information.

As many other sciences working in the field of remote sensing, statistics has been an increasingly powerful tool in the hands of specialists in the area. This area of knowledge has served to model the information acquiring process and, in particular, to help the interpretation and classification of data through specific techniques.

In this work, we depart from a commonly accepted hypothesis about the statistical properties of targets: the normality hypothesis for homogeneous areas. From this hypothesis, we consider the maximum likelihood estimation of a very important parameter, the complex correlation coefficient between two elements of the polarisation vector. Then, we calculate a bias-corrected estimator of the absolute value of this complex correlation coefficient.

The rest of this paper is structured as follows: Section 2 sets up a complex normal model for the polarimetric data we are working with, in Section 3 we obtain the second-order bias of the MLE (maximum likelihood estimate) of the covariance parameters in this model, and, finally, in Section 4, the main conclusions are summarised.

## A MODEL FOR POLARIMETRIC DATA

A polarimetric radar is a type of radar which works in all possible polarisations. In other words, it emits and receives signals in parallel polarisation $(HH, VV)$ or crossed polarisation $(HV, VH)$ and data captured by its sensors form the complete polarimetric matrix, defined as follows:

$$\begin{pmatrix} S_{HH} & S_{HV} \\ S_{VH} & S_{VV} \end{pmatrix} \qquad (1)$$

where $S_{kj}$ is the signal that is emitted in polarisation $k$ and received in polarisation $j$, where $k, j \in \{H, V\}$. Each element of this matrix is modelled as a complex random variable, i.e., $S_{kj} = X_{kj} + iY_{kj}$, where $i = \sqrt{-1}$. In general it is assumed that $\mathrm{Cov}(S_{kk}, S_{kj}) = 0$, and this hypothesis has been used for the calibration of radar sensors.

This work is restricted to monostatic SAR, where the signal is emitted and received with the same antenna

configuration. In this case, the matrix presented in eq. (1) is somewhat redundant. Since for this kind of sensors it holds that $S_{HV} = S_{VH}$, it is possible to use a more compact scattering matrix of the form

$$\begin{pmatrix} S_1 \\ S_2 \\ S_3 \end{pmatrix} \qquad (2)$$

where, for the sake of simplicity, the following notation is used $S_{HH} = S_1$, $S_{VV} = S_2$ and $S_{HV} = S_3$.

Following Lee at al., 1994 let us admit that the polarimetric vector presented in eq. (2) can be modelled as a complex normal random vector. A complex random vector $U$ is said to be complex normal if its real and imaginary parts, denoted by $X$ and $Y$ respectively, have bivariate normal joint distribution. In other words, $(X,Y) \sim N_2(\mu \quad ,C)$ where $\mu$ and $C$ are, respectively, the vector of means and the covariance matrix. Therefore, the density of $U$ is given by (Wooding, 1956).

$$f_U(u) = \frac{1}{\pi^p \mid C \mid} \exp\left(-u^* C^{-1} u\right) \qquad (3)$$

where $u^*$ is the transpose complex conjugate of $u$.

In this work a special case of the complex normal distribution is studied, one that is relevant for polarimetric SAR data modelling. This model, which consists of a restriction in the structure of the covariance matrix (Goodman, 1963; Lee et al., 1994) is defined by the conditions below. Let $S_k = X_k + iY_k$ be any complex component of the vector given in eq. (2), then

i) $\mathrm{E}(X_k) = \mathrm{E}(Y_k) = 0, \forall k$ ;

ii) $\mathrm{E}(X_k^2) = \mathrm{E}(Y_k^2), \forall k$ ;

iii) $\mathrm{E}(X_k Y_k) = 0, \forall k \neq j$

iv) $\mathrm{E}(X_k X_j) = \mathrm{E}(Y_k Y_j), \forall k, j$ ;

v) $\mathrm{E}(X_k Y_j) = -\mathrm{E}(Y_k X_j), \forall k, j$ .

Under the aforementioned restrictions, it is said that the complex random vector defined in (2) obeys a circular complex normal distribution.

For purposes of inference, we remind that data will be always available in one of the following formats: intensity pair, intensity-phase pair, phase difference or intensity ratio. In any of these formats, we can only recover information on two of the three components of the random vector defined in (2). For this reason, we can assume that our observations are two-dimensional complex random vectors, constituting a subset of (2). Our main goal is to obtain, from these two dimensional observations, the MLE of the relevant parameters in the above model, together with their second-order bias correction, as explained in the next section.

## SECOND ORDER BIAS CORRECTION

It is well known that MLEs are, in general, biased estimators of the true parameter values. This bias can be ignored in many practical situations, since it is typically of order $O(n^{-1})$, while the asymptotic standard deviation of the estimator has order $O(n^{-1/2})$, where $n$ is the sample size. However, for small values of $n$, or, more generally, when there is little information, bias can constitute a problem and correction efforts are worthy.

Let $\hat{\theta}$ be the MLE of the parameter $\theta$. It can be proved that, under very mild conditions, it holds that

$$\mathrm{E}(\hat{\theta}) = \theta + B(\theta) + O(n^{-2})$$

where $B(\theta)$ is of order $O(n^{-1})$ and it is called "the second order bias" of $\hat{\theta}$. It can be shown that the bias of $\tilde{\theta} = \hat{\theta} - B(\hat{\theta})$ has order $O(n^{-2})$. Therefore, the estimator $\tilde{\theta}$ constitutes a bias correction of $\hat{\theta}$.

We want to derive the second-order bias of the MLEs of the parameters in the covariance structure of the vector presented in (2), where these MLEs have to be obtained from observing a two dimensional sub-vector of (2). In particular, we are interested in obtaining a corrected estimate for the absolute value $\mid \rho_c \mid$ of the complex correlation coefficient. This quantity measures the degree of linear relationship between two complex random variables, i.e., if $A$ and $B$ are two complex random variables with zero mean, then $\mid \rho_c \mid = 1$ if and only if there is a complex constant $z$ such that $B = zA$.

Following Lee et al. (1994), this complex correlation coefficient $\mid \rho_c \mid$ between any pair of elements $S_k$ and $S_j$ of the polarimetric vector is defined as

$$\rho_c = \frac{E S_k S_j^*}{\sqrt{E \mid S_k \mid^2 \; E \mid S_j \mid^2}} = \mid \rho_c \mid e^{i\theta} \qquad (4)$$

Since $\mid \rho_c \mid$ is directly involved in the densities of the models used for multilook amplitude and intensity SAR data, this is the quantity to be addressed here.

Let $S$ be a two-dimensional sub-vector of $U$, say $S^T = (S_k, S_j)$ where $S_p = X_p + iY_p$, for $p = k, j$ and $j,k = 1,2,3$. In this case the complex covariance matrix associated to $S$ is defined as

$$\mathrm{E}(SS^*) = \begin{pmatrix} \mathrm{E}S_k S_k^* & \mathrm{E}S_k S_j^* \\ \mathrm{E}S_j S_k^* & \mathrm{E}S_j S_j^* \end{pmatrix} \qquad (5)$$

Since any complex number can be represented as a two-dimensional vector, we can consider a four-dimensional real covariance matrix corresponding to (5).

Let $\sigma_p^2 = \mathrm{E}S_p S_p^* = \mathrm{E} \mid S_p \mid^2$. Applying restriction (ii) of Section 2, we obtain

$$\sigma_p^2 = \mathrm{E}X_p^2 + \mathrm{E}Y_p^2 = 2\mathrm{E}X_p^2 \Rightarrow \mathrm{E}X_p^2 = \frac{\sigma_p^2}{2} \qquad (7)$$

The off-diagonal terms in (5) can be written as

$$ES_k S_j^* = E(X_k + iY_k)(X_j - iY_j) =$$
$$E(X_k X_j + Y_k Y_j) + iE(Y_k X_j - X_k Y_j)(8)$$

and, from restrictions (iv) and (v) in the last section, we get

$$ES_k S_j^* = 2EX_k X_j - i2EX_k X_j(9)$$

Also, it can be readily seen from equation (4) that

$$ES_k S_j^2 = |\rho_c|(\cos(\theta) + i\,\mathrm{sen}(\theta))\sigma_k\sigma_j(9)$$

and, equating real and imaginary parts in (8) and (9), we get

$$EX_k X_j = \frac{|\rho_c|\cos(\theta)\sigma_k\sigma_j}{2}$$

and

$$EX_k Y_j = \frac{-|\rho_c|\,\mathrm{sen}(\theta)\sigma_k\sigma_j}{2} \qquad (10)$$

Let's consider the four-dimensional real random vector $Z$, containing the real and imaginary parts of the components of $S$. Hence, we have

$$Z = \begin{pmatrix} X_k \\ Y_k \\ X_j \\ Y_j \end{pmatrix}$$

and the covariance matrix of $Z$ is given by

$$\Sigma = EZZ^T = \begin{pmatrix} EX_k^2 & EX_kY_k & EX_kX_j & EX_kY_j \\ EY_kX_k & EY_k^2 & EY_kX_j & EY_kY_j \\ EX_jX_k & EX_jY_k & EX_j^2 & EX_jY_j \\ EY_jX_k & EY_jY_k & EY_jX_j & EY_j^2 \end{pmatrix} \qquad (11)$$

Applying restrictions (i) to (v) of Section 2 and the results in (6) and (10), we arrive at

$$\Sigma = \frac{1}{2}\begin{pmatrix} \sigma_k^2 & 0 & |\rho_c|\cos(\theta)\sigma_k\sigma_j & -|\rho_c|\,\mathrm{sen}(\theta)\sigma_k\sigma_j \\ 0 & \sigma_k^2 & |\rho_c|\,\mathrm{sen}(\theta)\sigma_k\sigma_j & |\rho_c|\cos(\theta)\sigma_k\sigma_j \\ |\rho_c|\cos(\theta)\sigma_k\sigma_j & |\rho_c|\,\mathrm{sen}(\theta)\sigma_k\sigma_j & \sigma_j^2 & 0 \\ -|\rho_c|\,\mathrm{sen}(\theta)\sigma_k\sigma_j & |\rho_c|\cos(\theta)\sigma_k\sigma_j & 0 & \sigma_j^2 \end{pmatrix} (12)$$

The quantities in (12) are unknown and will, in practice, be estimated. Let $\sigma^T = (\sigma_k, \sigma_j, |\rho_c|, \theta)$ be the vector of the parameters in (12). Then, the total log-likelihood for this vector of unknown parameters, given the $n$ observable data $Z_1, \ldots, Z_n$ is

$$l(\sigma) = -\frac{1}{2}\left\{4n\log(2\pi) + n\log|\Sigma| + \sum_i z_i^T\Sigma^{-1}z_i\right\}$$

and the maximum likelihood estimates are obtained by solving a system of four equations:

$$\sum_i z_i^T\Sigma^{-1}\Sigma_k\Sigma^{-1}z_i = n\,tr(\Sigma^{-1}\Sigma_k); \quad k = 1,\ldots,4(13)$$

where $\Sigma_k$ is a matrix representing the derivative of the covariance matrix with respect to the $k$th element of $\sigma$ and $tr$ stands for the trace of the matrix. The equations in (13) are, in general, non-linear, but can be solved by Fisher's scoring method or any iterative re-weighted least squares.

We proceed to the calculation of the second-order bias of the parameters. From Cordeiro and Vasconcellos (1997), the vector $B(\sigma)$ containing the respective second-order biases of the components of the parameter vectors can be calculated as

$$B(\sigma) = (V^T\underset{\sim}{\Sigma}^{-1}V)^{-1}V^T\underset{\sim}{\Sigma}^{-1}\xi(13)$$

where

$$\xi = -\frac{1}{n}Wvec[(V^T\underset{\sim}{\Sigma}^{-1}V)^{-1}]$$
$$W = (vec(\Sigma_{11}), vec(\Sigma_{12}), \ldots, vec(\Sigma_{43}), vec(\Sigma_{44}))$$
$$V = (vec(\Sigma_1), \ldots, vec(\Sigma_4))$$
$$\underset{\sim}{\Sigma} = \Sigma \otimes \Sigma$$

with $\Sigma_{kj}$ being the second derivative of the covariance matrix with respect to the $k$-th and $j$-th components of the vector $\sigma$, for $k, j = 1,\ldots,4$, $\otimes$ is the Kronecker product and *vec* is the vec operator, which transforms a matrix into a vector by stacking the columns of the matrix one underneath the other.

After some manipulations, we obtain

$$B^T(\sigma) = \left(-\frac{\sigma_k}{8n}, -\frac{\sigma_j}{8n}, \frac{(1-|\rho_c|^2)^2}{4n|\rho_c|}, 0\right)(14)$$

where each element of the vector $B$ is the second-order bias of the corresponding element of the vector $\sigma$.

We define the corrected estimate of the absolute value of the complex correlation coefficient as:

$$|\tilde{\rho}_c| = |\hat{\rho}_c| - B(|\hat{\rho}_c|) \Rightarrow$$
$$|\tilde{\rho}_c| = |\hat{\rho}_c| - |\hat{\rho}_c|\left(\frac{(1-|\hat{\rho}_c|^2)^2}{4n|\hat{\rho}_c|^2}\right) \Rightarrow$$
$$|\tilde{\rho}_c| = |\hat{\rho}_c|\left(1 - \left(\frac{(1-|\hat{\rho}_c|^2)^2}{4n|\hat{\rho}_c|^2}\right)\right) \qquad (16)$$

On the graphs below, we present the value of the corrected MLE against the uncorrected one, for the sample sizes $n$ = 40, 60, 100, 500. It can be observed that:

- $|\hat{\rho}_c| \approx |\tilde{\rho}_c|$ when $n$ is large (as expected)
- the bias of the estimator is always positive
- the second-order bias correction leads to a reasonable estimator only if the maximum likelihood estimator is greater than $\sqrt{n+1} - \sqrt{n}$ (after this value, the corrected estimator becomes negative).

Also, we observe that the second-order bias correction can be an important tool to calibrate the image system, when we have little information in our sample or when the sample size is small.

By the results obtained through simulation, three situations have been noticed:

1. when $|\rho_c| \leq 0.3$ the uncorrected ML estimator is the best choice;
2. when $|\rho_c| > 0.8$ the corrected and uncorrected estimators are alike;
3. in the remaining situations the corrected ML estimator is the best choice.

## CONCLUSIONS

We have calculated the second-order bias of the MLE of the complex correlation coefficient, assuming data has a complex normal distribution. From this second-order bias, we obtained a new estimator, corrected up to the second order. This correction is important, since, for small sample sizes, the bias correction can bring our estimates towards the true parameter value. However, the corrected estimator has some deficiencies. The bias of the estimator was proven to be positive and, therefore, the uncorrected estimator always overestimates the true value of the module of the complex correlation coefficient. This evidence points towards the hypothesis that those small values reported in the literature may be due to mere bias, instead of being a symptom of system malfunctioning. Corrected hypothesis tests are being developed to help lighten this issue.

## ACKNOWLEDGEMENTS

This work was partially developed with resources from CNPq (351612/97-1 and 300458/93-2) and FACEPE (APQ-0707-1.03/97).

## REFERENCES

Cordeiro, G.M. and Vasconcellos, K.L.P., (1997), Bias correction for a class of multivariate nonlinear regression models, *Statistics and Probab. Lett.*, 35:155–164.

Goodman, N.R., (1963), Statistical analysis based on a certain multivariate complex gaussian distribution (na introduction), *Ann. Of Mathemat. Statist*, 34:152–177.

Lee, J.S., Hoppel, K.W., Mango, S.A. e Miller, A.R., (1994), Intensity and phase statistics of multilook polarimetric and interferometric SAR imagery, *IEEE Trans. Geoci. Remote Sensing*, 32:1017–1028.

TCI Software Research (New Mexico, USA) Scientific Workplace V. 2.50, 1996, Software set.

Wooding, R.A., (1956), The multivariate distribution of complex normal variables, *Biometrica*, 43:212–215.

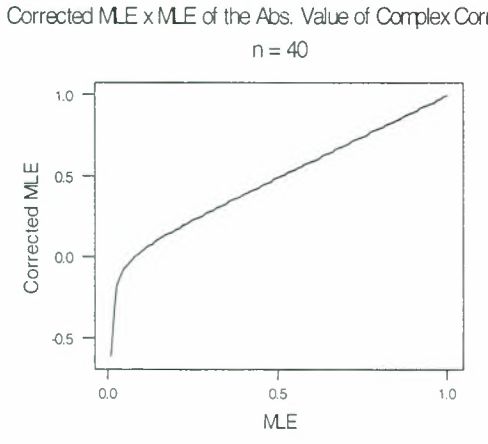


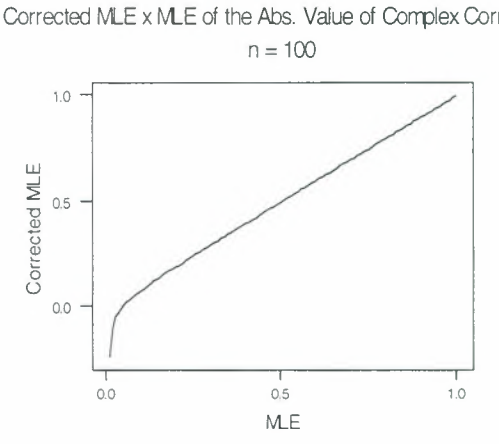


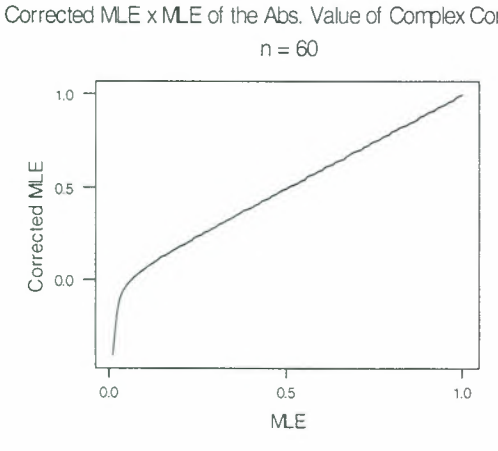


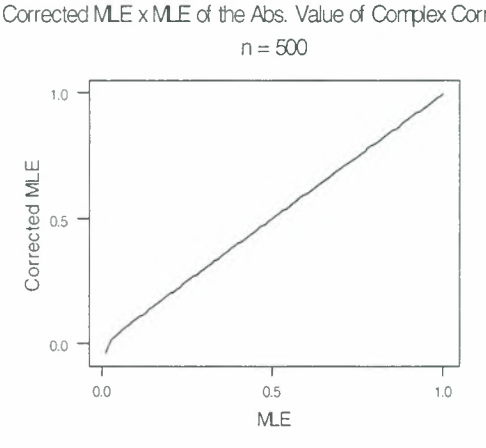

# ROBUST RA ESTIMATORS IN AR-2D MODELS FOR IMAGES

**Silvia Maria Ojeda**

Facultad de Matemática Astronomía y Física. U.N.C.
Haya de la Torre y Medina Allende
Ciudad Universitaria-C.P. 5000 Córdoba. República Argentina.
Ph.N. 54+51+334055 – Fax 54+51+334054
E-mail: ojeda@mate.uncor.edu

**Abstract**

Usually it is adopted for processing and analysis of images SAR, the multiplicative model $Z_{(m,n)} = X_{(m,n)}Y_{(m,n)}$, where $Z$ are the observations, $X$ is the backscatter process and $Y$ the noise speckle. In Frost et al [2] (mentioned by Sant'Anna [7]) a model AR-2D is suggested for the process $X$. Because the noise speckle is not cleaned totally, the robust methods are the most appropriate alternative to estimate this model's parameters. The purpose of this paper is to present a proposal of robust estimation in the AR-2D contaminated model: The RA estimators. They conform the bidimensional version of the estimators based on the residual covariances for the ARMA unidimensional models, introduced by Bustos and Yohai [1].

**Keywords**: Robustness

## 1. Models for Images and Robustness

Among the models of mayor importance in the treatment and processing of images are very important the ARMA-2D models and particularly the AR-2D ones; in these models, it is very common to assume that the intensity matrix of the image has got a multivariate gaussiana distribution; however it is well known that in many applications the gaussiana supposition is not the appropriate one. As a result it comes out a difficult hypothesis to hold. A very much realistic supposition consists of considering the presence of a contaminated gaussiano noise.

Unfortunately the least square estimators and maximum likelihood estimators are very sensitive when the gaussian supposition is not fulfilled. So the development of robust techniques and the proposal a new robust estimators are very important for the estimation of the parameters in models for images. Kashyap and Eom [5] present the M robust estimator in a model AR-2D, which is contaminated by two different processor of outliers. These estimators are very highly superior to the classic estimators.The proposal of RA estimators make up a robust estimation alternative in the AR-2D contaminated model. The basic idea to build the RA estimators consists of showing the usual least square estimators so that they involve the so-called residual covariances and finally the least square estimators are strengthened by making this covariances robust.

## 2. AR-2D Model

Before referring to this model it will be necessary to present some concepts:

First we will call $Z$ the set of integer numbers and we will call $C$ the set of complex numbers. So $Z^2$ tells us the set of all the pairs $(m,n)$ the integers numbers, and $C^2$ will show the set of all pairs $(z,w)$ of complex numbers. Let $S$ is a configuration of pixels so that $X(s)$ with $s \in S$ represent a random variable such as color, intensity of energy, light or grey level, etc. in the pixel or $s$ place. Considering that $S = Z^2$, the result is that $(X(s): s \in S)$ is a random process. Thus, when this process is performed, an image is obtained. If the random variables $X(s)$ are independent, and $E(X(s)) = E(X(\tilde{s})$ for all $s, \tilde{s} \in S$, we obtain the so-called white noise. Let $X = (X(s): s \in S)$ a week stationary random process (i.e. $E(|X(s)|^2)$ is a finite number for all $s \in S$, $E(X(s)) = E(X(\tilde{s})$ for all $s, \tilde{s} \in S$, and the autocovariance function of $X$ process depends only on the difference of its arguments), $E(X(s)) = 0 \forall s \in S$ and let

$\varepsilon = (\varepsilon(s): s \in S)$ a white noise process (Whittle, [8]). So we say that $X = (X(s): s \in S)$ is a process AR$(P, \varepsilon)$ if:

$$X(m,n) - \sum_{(k,l)\in T} a(k,l)X(m-k,n-l) = \varepsilon(m,n)$$

Where $T$ is a finite subset of $S$ and

$$P(z,w) = 1 - \sum_{(k,l)\in T} a(k,l)z^k w^l$$

is a polinomic function with real coefficients, which is not annulled in the set $\{(z,w) \in C^2 : |z| = |w| = 1\}$, and $T$ is contained in positive quadrant of the plan. (Guyon, [3]).

The modelling of images using AR-2D models very often used. They not only have a good performance for modelling images but besides they have a structure much more simple than other models for images. That's why the efficient methods of estimation of its parameters are so important to develop.

### 3. The Least Square Estimators In The AR-2D Model

Let $X$ an AR ( $P, \varepsilon$ ) model with zero mean observed a window strongly causal $W$, where:

$$P(z,w) = 1 - \sum_{(k,l)\in T} a(k,l)z^k w^l$$

and $T = \{(k,l) \in S: 0 \le k,l \le L\}$ being $L$ a natural number. Then:

$$a = \begin{bmatrix} 1 & a(0,1) & a(0,2) & .... & a(0,L) \\ a(1,0) & a(1.1) & : & : & a(1,L) \\ a(2,0) & a(2,1) & : & : & \\ : & : & : & : & \\ a(L,0) & a(L,1) & .... & .... & a(L,L) \end{bmatrix}$$

is the matrix of parameters to be estimated in the referred model AR$(P, \varepsilon)$.

Let $B^{(k,l)}$ the operator which lets $X(m,n)$ "goes back" $k$ units in the first coordinate and $l$ units in the second one; i.e.:

$$B^{(k,l)}(X(m,n)) = X(m-k,n-l)$$

$\forall (k,l) \in S, \forall (m,n) \in S$. The least square estimator $\hat{a}$ of $a$, minimizes the expression:

$$\sum_{(k,l)\in W \approx T} r^2_{(k,l)}(a) \qquad (3.1)$$

where $W \approx T$ is a subset of window $W$. Precisely:

$$W \approx T = \{(k,l) \in W: B^{(k,l)}(X(m,n)) \in W\}$$

and $r_{(k,l)}(a)$ is the residual in the pixel or place $s = (k,l)$. It is defined by (3.2):

$$r_s(a) = \begin{cases} -\sum_{(k,l)\in T} a(k,l)B^{(k,l)}X(s) & (s) \in (W \approx T) \\ 0 & c.c. \end{cases}$$

The estimator $\hat{a}$ observes a good behaviour supposing that for all $s \in S$, $\varepsilon(s)$ has a normal distribution; but it is not robust in the sense that it is badly affected by the presence of observations that move slightly away from the normal hypothesis.

In the next section a robust estimator will be proposed to estimate the parameters in the AR-2D model contaminated by innovation outliers. This distortion appears when the process $\varepsilon$ has a normal distribution contaminated given by:

$$F = (1-\delta)N(0,\sigma^2) + \delta G$$

where $0 < \delta < 0.5$, $N(0,\sigma^2)$ represents the normal distribution with mean zero and variance $\sigma^2$ and $G$ is an unknown arbitrary distribution with dispersion $\tau^2 \ge \sigma^2$. Finally, the process $\varepsilon$ has distribution $N(0,\sigma^2)$ with probability $(1-\delta)$ and has distribution $G$ with probability $\delta$. The random variables $\varepsilon(k,l)$ are considered outliers when they respond to $G$ distribution.

## 4. RA Robust Estimators in the AR-2D Models contaminated by Innovation Outliers

Let $X$ the AR ( $P,\varepsilon$ ) model of the previous section distorted by the presence of innovation outliers and observed in the window strongly causal $W$. Let the least square estimator $\hat{a}$ of $a$, which is obtained by minimizing in equation 3.1. Differentiating this expression we obtained the following equations:

$$\sum_{(k,l)\in W\approx T} r_{(k,l)}(\hat{a})\left(\partial r_{(k,l)}(\hat{a}) \Big/ \partial \hat{a}_{(i,j)}\right) = 0 \qquad (4.1)$$

$\forall(i,j) \in T$. An auxiliary calculus let us demonstrate that:

$$\left(\partial r_{(k,l)}(\hat{a}) \Big/ \partial \hat{a}_{(i,j)}\right) = -P^{-1}(B) r_{(k-i,l-j)}(\hat{a}) \qquad (4.2)$$

$\forall(i,j) \in T$, $\forall(k,l) \in W \approx T$; where:

$$P^{-1}(z,w) = \sum_{(s,t)\in S} p(s,t) z^s w^t$$

and so:

$$P^{-1}(B) = \sum_{(s,t)\in S} p(s,t) B^{(s,t)} \qquad (4.3)$$

Then, we can write:

$$\sum_{(k,l)\in W\approx T} r_{(k,l)}(\hat{a})\left(\sum_{(s,t)\in S} p(s,t) r_{(k-i-s,l-j-t)}(\hat{a})\right) = 0 \qquad (4.4)$$

$\forall(i,j) \in T$.

Due to equation 3.1, the residual in $(k-i-s,l-j-t)$ is null except over a finite subset $D$ of $S$ (the exact expression of $D$ depends on $L,(i,j)$ and the size of the window $W$). Thus, we rewrite equation 4.4 as :

$$\sum_{(k,l)\in W\approx T} r_{(k,l)}(\hat{a})\left(\sum_{(s,t)\in D} p(s,t) r_{(k-i-s,l-j-t)}(\hat{a})\right) = 0 \qquad (4.5)$$

$\forall(i,j) \in T$.

Interchanging the order of summations, we obtain equaation (4.6):

$$\sum_{(s,t)\in D} p(s,t)\left(\sum_{(k,l)\in W\approx T} r_{(k-i-s,l-j-t)}(\hat{a}) r_{(k,l)}(\hat{a})\right) = 0$$

$\forall(i,j) \in T$. For each $(u,v) \in S$, we define:

$$(W \approx T)_{(u,v)} = \{(m-u,n-v):(m,n) \in (W \approx T)\}$$

So, equation 4.6 is equivalent as equation (4.7):

$$\sum_{(s,t)\in D} p(s,t)\left(\sum_{(k,l)\in (W\approx T)_{(s,t)}} r_{(k+i+s,l+j+t)}(\hat{a}) r_{(k,l)}(\hat{a})\right) = 0$$

$\forall(i,j) \in T$. Now, for each $(u,v) \in S$ we define a residual covariance in $(u,v)$ to:

$$\gamma_{(u,v)}(\hat{a}) = \sum_{(k,l)\in (W\approx T)_{(u,v)}} r_{(k+u,l+v)}(\hat{a}) r_{(k,l)}(\hat{a}) \qquad (4.8)$$

So, according to equations 4.8 and 4.7 becomes to:

$$\sum p(s,t)\gamma_{(s+i,t+j)}(\hat{a}) = 0 \quad \forall(i,j) \in T \qquad (4.9)$$

As we have said at the end of section 2, the least square estimators of $a$ will be strengthened by making robust the residual covariances. For doing this we will replace equation 4.8 by equation (4.10):

$$\varphi_{(u,v)}(\hat{a}) = \sum_{(k,l)\in (W\approx T)_{(u,v)}} \eta\left(\frac{r_{(k,l)}(\hat{a})}{\hat{\sigma}}, \frac{r_{(k-u,l-v)}(\hat{a})}{\hat{\sigma}}\right)$$

$\forall(u,v) \in S$, where $\eta$ is a continual, bounded and odd function in each variable and $\hat{\sigma}$ is a robust estimator of the scale factor of $\varepsilon$ process. Thus, we define the RA robust estimator of $a$, by means of the following equations:

$$\sum_{(s,t)\in D} p(s,t)\varphi_{(s+i,t+j)}(\hat{a}) = 0 \qquad (4.11)$$

$\forall(i,j) \in T$.

where $\hat{\sigma}$ is simultaneously calculated by means of the expression:

$$\hat{\sigma} = \frac{Med\left(\left|r_{(k,l)}(\hat{a})\right| : (k,l) \in W \approx T\right)}{0.6745}$$

where 0,6745= $Med(|X|)$ and $X$ has distribution $N(0,1)$.

## 5. Further Investigations

The AR (1) is unidimentional model is generalized by AR-2D Models which has a good performance to model images; besides its structure is very simple. Kashyap and Eom [4] introduce the M robust estimators for this contaminated model, and Nasburg and Kashyap [6] prove the consistency and asymptotic normality of these estimators. So it is interesting to study the properties of R.A. estimators such as consistency and asymptotic normality in AR-2D model.

On the other hand, the RA estimators in the ARMA unidimentional models contain the class of M estimators, we have already introduced for the AR-2D models, whether contain or not to the class of M estimators.

## 6. References

[1] Bustos, O. H. and Yohai, V. J., *Robust Estimates for ARMA Models*. Journal of the American Association. Vol. 81 N° 393. Theory and Methods, March 1986.

[2] Frost, V. S., Stiles, J. A., Shanmugan, K. S. and Holtzman, J. C., *A Model for Radar Images and its Applications to Adaptive Digital Filtering of Multiplicative Noise*. IEEE Transactions on Pattern Analysis and Machine Intelegence, Vol. 4 (2), pp 157-166, 1982.

[3] Guyon, X., *Parameter Estimation for a Stationary Process on a d-Dimensional Lattice*. Biometrika, 69, 1, pp. 95-105, 1982.

[4] Kashyap, R. L, Characterization and Estimation of Two Dimensional ARMA Models. IEEE Transactions on Information Theory, Vol IT-30, N° 5, September 1984.

[5] Kashyap, R. L. and Eom, K. B., Robust Image Modeling Techniques with an Image Restoration Application. IEEE Transactions on Acoustics, Speech and Signal Processing, Vol. 36, N° 8, August 1988.

[6] Nasburg, R. E. and Kashyap, R. L. *Robust Parameter Estimation in Dynamic Systems*. Proc. Inf. Science and Systems, Baltimore, 1975.

[7] Sant'Anna, S. J. S. *Avaliação do Desempenho de Filtros Redutores de Speckle, em Imagens de Radar de Abertura Sintética de Maestrado em Sensoriamento Remoto/Procesamiento de Imagens*. INPE-6125 – TDI/586, São José dos Campos, Brasil, 1995.

[8] Whittle, P., *On Stationary Processes in the Plane*, Biometrika, Vol. 41. 1954.

# Digital Image Restoration Using Autoregressive Time Series Type Models *

Héctor Allende O.
Departamento de Informática. Universidad Técnica Federico Santa María
Escuela de Ingeniería Industrial, Universidad "Adolfo Ibáñez"
Casilla 110-V, Valparaíso. Chile. Phone: (56) 32 - 645242 Fax: (56) 32 797513
E-mail: hallende@inf.utfsm.cl
Jorge Galbiati R.
Instituto de Estadística. Universidad Católica de Valparaíso.
Casilla 4059, Valparaíso. Chile. Phone: (56) 32 - 274051 Fax: (56) 32 274040
E-mail: jgalbiat@ucv.cl
Ronny Vallejos A.
Departamento de Estadística. Universidad de Valparaíso.
Casilla 5030, Valparaíso. Chile Phone: (56) 32 - 281946 Fax: (56) 32 344 928
E-mail: rvallejo@uv.cl

**Abstract**

We consider a non-symmetric half plane autoregressive image, where the image intensity of a point is a linear combination of the intensitites of the eight nearest points located on one quadrant of the coordinate plane, plus a normal white noise innovations process.

Two types of contaminations are considered. Innovation outliers, where a fraction of innovations are corrupted with a heavy tailed outlier generation process, and additive outliers, where a fraction of observations are corrupted.

We develop a $GM$-estimator for the robust estimation of parameters of a contamined autoregressive image model, based on time series $GM$-estimators introduced by Denby & Martin (1979) applied to the restoration of radar generated images.

Ordinary least-squares estimators are asymptotically efficient with a non-contamined gaussian process, like the one considered here. $M$-estimators behave better when innovation outliers are present, but are very sensitive to additive outliers. A simulation study is carried out, which shows that the $GM$-estimator introduced here has a better performance with an additive outlier contamined image model than $M$-estimators and ordinary least squares estimators.

**Keywords:** $GM$-estimators, Image Restoration Robust Estimation, Two-Dimensional Autoregressive Models.

*This work was supported by FONDECYT grant N° 1960521

## 1. Introduction

Restoration of an image in the presence of noise is one of the fundamental problems in image processing. Parametric representations of two-dimensional

processes suitable for this problem, have been well studied. However, in these models, the image intensity array is assumed to be a two-dimensional Gaussian Process. There are many image restoration methods based on the Gaussian assumption. For instance, Chellepa and Kashyap (1982) used spatial interaction models to represent image intensity arrays and restored images obtained with minimum mean square error criterion. However, when the image is contamined with outliers, the estimated parameters obtained from the Gaussian model do not appear to be appropiate. A more realistic assumption for the image model is a contaminated Gaussian noise.

The importance of the $\epsilon$-contaminated models has been legitimated by numerous publications about applied works in the area of image processing and image analysis. See for instance Kashyap and Eom (1988).

We develop a restoration method based on a robust image model in this work. In the proposed method, the image intensity array is represented by a causal autoregressive model. A robust parameter estimation algorithm and a data cleaning procedure is applied to restore contaminated images. The restoration algorithm based on the robust modelling is tested with several simulated images.

Our contributions are threefold. We first develop an algorithm for the robust estimation of parameters of an image model in which the innovations process is a mixture of a Gaussian and an outlier process. It is a $GM$-estimator. We prove the convergence and confirm the convergence via simulation. Next we consider the robust estimation of the parameters of a model where the image obeying the model is not available, the corrupting innovations process being a mixture of a Gaussian process and an outlier process.

We develop an algorithm to recover the parameters of the model from a noisy image. The procedure involves alternate parameter estimation and data cleaning.

We provide intuitive reasons for the convergence of the procedure and confirm our intution by several simulations. Finally, we use the above results to restore an image corrupted by different types of outliers.

## 2. The additive outlier in nonsymmetric half-plane autoregressive models

Consider a nonsymmetric half-plane autoregressive two dimensional model with additive outliers. Assume that the image intensity of an image follows the nonsymmetric half-plane model. Let $(i, j)$ be an index for the coordinate location, and $y(i, j)$ be the intensity at the coordinate $(i, j)$.

Let us define a nonsymmetric half-plane (NSHP) model as follows:

$$\begin{aligned} \Omega_- : \; = \; & \{(i,j) : (i = 0 \text{ and } j < 0) \text{ or} \\ & (i < 0 \text{ and } j \text{ is arbitrary}\} \end{aligned} \tag{2.1}$$

Let $u$ and $v$ be indexes for two-dimensional coordinate locations. One important property of $\Omega_-$ is that if $u \in \Omega_-$ and $v \in \Omega_-$ then $(u + v) \in \Omega_-$.

And NSHP autoregressive model can be written as

$$y(u) = \sum_{v \in N_1} \underline{\alpha}_v y(u + v) + \mu + a(u) \tag{2.2}$$

where $a(u)$ are independent identically distributed random variables with a symmetric distribution $G$ with mean zero and scale $\sigma_a$. The density of $G$ will be denoted by $g$. The $a's$ are called innovations. The neighborhood set $N_1$ is a subset of the nonsymmetric half-plane $\Omega_-$. The NSHP autoregressive model (2.2) can be written in the linear model form

$$y(u) = \underline{\alpha}^T z(u) + a(u) \tag{2.3}$$

where $\underline{\alpha}^T$ is a parameter vector and $z(u)$ is a vector which consists of intensities of pixels in the neighborhood set $N_1$ and unity. The last element of the vector $z(u)$ is required to represent a constant gray level in the image.

If

$$\begin{aligned} N_1 \; = \; & \{(0,-1),(-1,0),(-1,-1),(0,-2), \\ & (-1,-2),(-2,0),(-2,-1),(-2,-2)\} \end{aligned}$$

the NSHP autoregressive model (2.2) can be rewritten as follows:

$$Y(i, j) = \underline{\alpha}^T Z(i, j) + a(i, j) \tag{2.4}$$

where

$$[Z(i,j)]^T = [(Y(i,j-1), Y(i-1,j), Y(i-1,j-1), Y(i,j-2), Y(i-1,j-2), Y(i-2,j), Y(i-2,j-1), Y(i-2,j-2), 1)]$$

The model given in (2.4) is called an eight neighbor causal autoregressive model, and this model is used in our simulation study.

Suppose now that the NSHP autoregressive process cannot be perfectly observed because a small fraction $\epsilon$ (in practice we usually have $\epsilon \leq 0.1$) of observations are distributed by an outlier-generating process $\{\nu(i,j)V(i,j)\}$, where $\{\nu(i,j)\}$ is one or zero, with $P(\nu(i,j)=1)=\epsilon$, $P(\nu(i,j)=0)=1-\epsilon$, and the variables $V(i,j)$ have arbitrary distribution function $H$. Thus the observational model is

$$X(i,j) = Y(i,j) + \nu(i,j)V(i,j) \qquad \begin{matrix} i = 1,\cdots,n \\ j = 1,\cdots,m \end{matrix} \tag{2.5}$$

Therefore with probability $(1-\epsilon)$ the NSHP autoregressive process $Y(i,j)$ itself is observed, and with probability $\epsilon$ the observations $X(i,j)$ are corrupted by an error with distribution $H$.

It is well known that the $LS$ estimates are asymptotically normal and asymptotically efficient when $G$ is Gaussian and $V(i,j)=0$. However, when the innovations density is non-Gaussian (Innovative Outliers), the above estimates are no longer efficient and heavy-tailed innovation distributions can result in large losses of efficiency.

The latter fact suggests that a good alternative to the $LS$ estimate can be the $M$-estimate as proposed by Huber (1981) for the NSHP autoregressive case (Kashyap and Eom, 1988). However, the $LS$ estimate and even the $M$-estimate are extremaly sensitive to the presence of additive outliers (AOs). This fact is reported by Bustos and Yohai (1986) for one dimensional autoregressive processes. In this work we present the results of a Monte Carlos simulation which shows that for a two dimensional eight neighbor causal autoregressive model the $LS$ and $M$-estimates are more sensitive to AO-s than in the case of causal autoregressive with innovative outliers.

## 3. Generalized $M$-estimates

Consider the parameter estimate in the NSHP autoregressive process. In the least squares estimation, we need to minimize the function

$$\sum_{i,j} \left[X(i,j) - \underline{\alpha}^T Z(i,j)\right]^2 \tag{3.1}$$

with respect to $\underline{\alpha}$, where $Z(u)$ is a vector which consists of the observations $X(i,j)$ in the neighbor set $N_1$.

The idea of a least squares estimation is to minimize the residuals. However, if one observation is an outlier, then the corresponding residual is very large, and the least squares estimator is not robust.

Similarly, the class of $M$-estimators proposed by Kashyap and Eom (1988) for causal autoregressive processes, defined by minimizing the function of a finite sample of observations

$$Q(\underline{\alpha},\sigma) = \frac{1}{mn}\sum_{i,j}\left[\rho\left(\frac{X(i,j)-\underline{\alpha}^T Z(i,j)}{\sigma}\right) + \frac{1}{2}\right]\sigma. \tag{3.2}$$

is robust for innovative outliers, when the function $\rho$ has bounded influence. But the situation is totally different when the contamination model is given by (2.5), that is, when the autoregressive model is disturbed by additive outliers. This suggests introducing a more general class of robust estimators, known as $GM$-estimators, which are an extension of the $M$-estimators, obtained by assigning a weight function to the observations of the model. The residuals $X(i,j) - \underline{\alpha}^T Z(i,j)$ in a NSHP autoregressive model contamined with additive outliers may be very large. The way the $GM$-estimators reduces this effect is by introducing smaller weights to larger residuals. A $GM$-estimator for the parameters $\underline{\alpha}^T$ and $\sigma$ of model (2.5) is the solution to the problem of minimizing the non-quadratic function defined by

$$Q(\underline{\alpha},\sigma) = \sum_{i,j}\frac{l_{ij}t_{ij}}{mn}\left[\rho\left(\frac{X(i,j)-\underline{\alpha}^T Z(i,j)}{l_{ij}\sigma}\right) + \beta\right]\sigma. \tag{3.3}$$

where $\rho$ is a differentiable function, convex, symmetric with respect to the origin, with bounded derivative, and such that $\rho(0) = 0$. The $l_{ij}$ and $t_{ij}$ are the weights corresponding to the respective $Z(i,j)$. In order to obtain consistency of the scale estimate at the normal model, we consider $\beta = E_\phi[X]$ (see Huber 1981).

The $GM$-estimator is obtained by solving the equations

$$\sum_{i,j} t_{ij}\psi\left[\frac{X(i,j)-\underline{\alpha}^T Z(i,j)}{l_{ij}\sigma}\right] Z^T(i,j) = \underline{0} \quad (3.4)$$

$$\sum_{i,j} l_{ij}t_{ij}\left[\chi\left(\frac{X(i,j)-\underline{\alpha}^T Z(i,j)}{l_{ij}\sigma}\right) - \beta\right] = 0 \quad (3.5)$$

where $\psi(x) = \dfrac{\partial\rho(x)}{\partial x}$, $\chi(x) = x\psi(x) - \rho(x)$ and $\psi$ is a bounded and continuous function. There are several proposals for the choice of $\psi$ due to the fact that the robustness of the procedure and the rate of convergence of the procedure depend on these functions: the Huber hard-limiter type, given by $\psi_H(x) = \text{sgn}(x)\cdot\min\{|x|, c\}$ and Tuckey's redescending bisquare function given by

$$\psi_B(x) = \begin{cases} x[1-[x/a]^2]^2 & , \quad |x| \le a \\ 0 & , \quad , |x| > a \end{cases}$$

Typical values for the adjusting constant $c$ in $\psi_H$ range from 1.5 and 2.0 and for $a$ in $\psi_B$ range from 4.5 and 6.

The principal types of $GM$-estimators are:

i) Mallows type, where $l_{ij} = 1$ and $t_{ij} = \dfrac{\psi(b_{ij}/c_r)}{b_{ij}/c_r}$ with $b_{ij} = p^{-1}Z^T(i,j)\hat{C}^{-1}Z(i,j)$, where $\hat{C}^{-1}$ a robust estimate of $C^{-1}$ and $C$ is the a priori unknown covariance matrix for the NSHP autoregressive process, which may be expressed as $C(\underline{\alpha})$. The construction of $\hat{C}^{-1}$ is described by Martin (1980).

ii) Schweppe type, $l_{ij} = t_{ij} = \dfrac{\psi(b_{ij}/c_r)}{b_{ij}/c_r}$.

## 4. Implementation of $GM$-estimates

Assuming that an estimate of $C^{-1}$ required to construct the weights $t_{ij}$, is available, then good approximate solutions of equations (3.4) and (3.5) can be conveniently obtained by using an iterately-weighted-least-squares (IWLS) technique similar to that described by Martin (1980).

It may be shown that the estimating equations (3.4) and (3.5) have a unique solution when $\psi$ is strictly monotone.

The $GM$-estimation of the NSHP autoregressive model under regularity conditions preserve the properties of consistency and asymptotic normality of the unidimensional autoregressive models. But they also have their computation difficulties, because they involve the minimization of a non quadratic function of multiple parameters. To obtain the $GM$-estimator of $\underline{\alpha}$ and $\sigma$ we use the algorithm known as IWLS, whose convergence is established in Huber (1981).

### IWLS algorithm

Let $X(i,j)$ be the observations of the contamined causal autoregressive model defined in (2.5) and let $\underline{\alpha}^{(0)}$ and $\sigma^{(0)}$ be the initial values, $\epsilon$ a tolerance value and weights $l_{ij}, t_{ij}$, $i = 1,\cdots,n$, $j = 1,\cdots,m$, starting values.

1. Set $k = 0$.

2. At the $k$-th iteration of $\underline{\alpha}^{(k)}$ obtain the residual

$$r^{(k)}(i,j) = X(i,j) - \underline{\alpha}^{(k)}Z(i,j), i = 1,\cdots,n, \quad j = 1,\cdots,m$$

3. Compute the new value of $\sigma$ using $\hat{\sigma} = 1.483Med\{|r^{(0)}_{(i,j)} - Med|r^{(0)}_{(i,j)}||\}$.

4. Compute the weights $W_{ij}$, from $r(i,j), l_{ij}$ and $t_{ij}$ for the Mallows or the Schweppe type $GM$-

estimators.

$$W_{ij}^{(k)} = \begin{cases} t_{ij} \cdot \psi \left( \frac{r_{(i,j)}^{(k)}}{l_{ij}\hat{\sigma}} \right) / \left( \frac{r_{(i,j)}^{(k)}}{\hat{\sigma}} \right) & \\ \quad \text{if } r_{(i,j)}^{(k)} \neq 0,\ l_{ij} \neq 0 & \\ t_{ij}/l_{ij} \quad \text{if } r_{(i,j)}^{(k)} = 0,\ l_{ij} \neq 0 & \\ 1 \quad \text{if } r_{(i,j)}^{(k)} = l_{ij} = t_{ij} = 0 & \\ 1 \quad \text{if } r_{(i,j)}^{(k)} \neq 0,\ l_{ij} = t_{ij} = 0, & \\ \quad \psi_1(t) = t & \\ 0 \quad \text{if } r_{(i,j)}^{(k)} \neq 0,\ l_{ij} = t_{ij} = 0, & \\ \quad \psi_1 \text{ is bounded} & \end{cases}$$

where $i = \overline{1,n}$, $j = \overline{1,m}$. Define $W^{(k)}$ as a diagonal matrix with $W_{ij}^{(k)}$ as its $[(n-1)(j+1)+i-1]$-th diagonal element.

5. Solve $\sum_{ij} \left[ r^{(k)}(i,j) - Z^T(i,j)\underline{\tau}^{(k)} \right]^2 W_{ij}^{(k)} = \min$ for $\underline{\tau}^{(k)}$, the solution given by

$$\hat{\underline{\tau}}^{(k)} = \left[ Z^T W^{(k)} Z \right]^{-1} Z^T W^{(k)} \cdot X - \underline{\alpha}^{(k)}$$

where the rows of $Z^T$ are the $Z(i,j)$ defined in (2.4), and $X$ is the vector of observations.

6. Compute the new value of $\underline{\alpha}$, $\underline{\alpha}^{(k+1)} = \underline{\alpha}^{(k)} + \lambda\hat{\underline{\tau}}^{(k)}$ with $0 < \lambda < 2$, an arbitrary relaxation constant.

7. Repeat 2 to 6 until the stopping rule:

$$\|\underline{\alpha}^{(k)} - \underline{\alpha}^{(k+1)}\| = |\lambda\underline{\tau}^{(k)}| < \epsilon\hat{\sigma} \quad \text{is reached.}$$

## 5. Applications to Image Restoration

Restoration of an Image in the presence of noise is one of the fundamental problems in image processing. The image degradation process can be modeled by the observational model (2.5). We assume that the observation $X(i,j)$ is corrupted by a contamined process which contains a small fraction of additive outliers.

There are many image restoration methods based on the Gaussian noise assumption. Chellapa and Kashyap (1982) used a spatial interaction model to represent an image intensity array and restored images with minimum mean square criterion. Geman and Geman (1984) used the equivalence of Markov random field and Gibbs distribution and restored images by a stochastic relaxation method with maximum a posteriori criterion. Wu (1985) used a multimensional Kalman filtering approach and nonsymmetric half plane autoregressive model.

Unfortunately, most image restoration methods based on the Gaussian assumption are not effective to impulse noise.

Image restoration is an estimation of original intensity $Y(i,j)$ from the observation $X(i,j)$. For a small size image, the original image intensity can be modeled by a causal autoregressive model. If the original image intensity follows a causal autoregressive model, then the original image intensity can be easily restored by data cleaning with robust parameter estimation. The data cleaning procedures removes outliers at each iteration without degrading the original signal.

The restoration method based on the robust image model has an advantage over conventional methods such as median filter or $\underline{\alpha}$-trimmed mean filter. The robust image model based method does not produce blurred images after restoration. Conventional methods, such as median filter or $\underline{\alpha}$-trimmed mean filter, replace every pixel by its location estimates. Because these methods are based on the constant intensity assumption, the details of the original image are significantly blurred.

This procedure is described in the following algorithm.

### Restoration Algorithm Based on a Robust Model

1. Initially, set $Y^{(0)}(i,j) = X(i,j)$. Compute the initial estimate $\underline{\alpha}^{(0)}, \sigma^{(0)}$ from the contaminated observation $X(i,j)$ by the least squares algorithm.

2. Consider the $k$-th iteration, where $Y^{(k)}$ and $\underline{\alpha}^{(k)}$ are available. Obtain the updated estimate

$Y^{(k+1)}(\cdot)$ from $Y^{(k)}(\cdot)$ by the following recursive equation

$$r^{(k)}(i,j) = Y^{(k)}(i,j) - \underline{\alpha}^{(k)^T} Z^{(k)}(i,j)$$
$$\hat{r}^{(k)}(i,j) = \psi\left[\frac{r^{(k)}(i,j)}{\sigma^{(k)}}\right]\hat{\sigma}$$

where $\psi$ is one of the bounded and continuous functions as discussed in the $GM$-estimation.

3. Restore the image $Y^{(k+1)}(i,j)$ using

$$Y^{(k+1)}(i,j) = \underline{\alpha}^{(k)} Z^{(k)}(i,j) + \hat{r}^{(k)}(i,j)$$

4. Obtain estimators $\underline{\alpha}^{(k+1)}$ from the cleaned data $Y^{(k+1)}$ by minimizing the function

$$Q(\underline{\alpha},\sigma) = \\ = \sum_{i,j} \frac{l_{ij}t_{ij}}{mn}\left[\rho\left[\frac{Y^{(k+1)}(i,j)-\underline{\alpha}^T Z^{(k+1)}(i,j)}{l_{ij}\sigma}\right] + \beta\right]\sigma$$

This can be computed by the IWLS Algorithm.

5. Repeat Steps 2-4 until the diference of estimates between iteration becomes small.

## 6. Simulation Study

A simulation study was conducted to observe the behaviour of the $GM$-estimator and compare it with the $LS$ and $M$ estimators.

In each case one hundred $50 \times 50$ images were generated using (2.4), with additive contamination generated by (2.5), with $H$ a large variance ($\sigma_H^2$) normal distribution. The parameter values were

$$\underline{\alpha}^T = (-0.12; 0.37; -0.16; 0.25; 0.13; 0.24; 0.40; -0.16)$$

and $\sigma_a = 0.01$.

The following cases were simulated:

No contamination
5 % contamination , $\sigma_H = 0.1$ and 0.5
10% contamination, $\sigma_H = 0.1$ and 0.5
15% contamination, $\sigma_H = 0.1$ and 0.5

Each case was run three times, estimated using $LS$, $M$ and $GM$, respectively.

The mean square error of the estimated $\alpha$ parameters is used as a measure of performance of the estimators.

The results are shown in Table 1.

**Table 1.** Comparison of $GM$-estimador, $M$-estimator and least squares estimator for $NSHP$ autoregressive model with additive contaminarion. Number of runs in each case is 100. Image size is $50 \times 50$.

| % of outliers | Outlier Standard Deviation | Estimator | | |
|---|---|---|---|---|
| | | $LS$ | $M$ | $GM$ |
| | | Mean Square Error | | |
| 0 | 0 | 0.0177 | 0.0184 | 0.0197 |
| 5 | 0.1 | 0.1019 | 0.0474 | 0.0447 |
| 10 | 0.1 | 0.1389 | 0.0760 | 0.0714 |
| 15 | 0.1 | 0.1572 | 0.0985 | 0.0942 |
| 5 | 0.5 | 0.2155 | 0.1051 | 0.0925 |
| 10 | 0.5 | 0.2274 | 0.1357 | 0.1218 |
| 15 | 0.5 | 0.2336 | 0.1555 | 0.1411 |

After observing the results of the simulation study, we conclude that robust estimators have a better performance than the $LS$-estimator. The $GM$ estimator is better than the $M$ estimator in all cases, except when there is no contamination. The improvement is higher with larger outlier standard deviation.

# References

[1] H. Allende and S. Heiler, "Recursive Generalized $M$-estimates for Autorregresive Moving-Average Models". Journal of Time Series Analysis, Vol. 13, N° 1. 1992.

[2] Boente, G., Fraiman, R. and Yohai, V. J. "Qualitative Robustness for General Stochastics Process", Technical Report N° 26. Department of Statistics. University of Washington. Seattle. WA. (1982).

[3] H.O. Bustos "General $R$-Estimates for contaminated ph-order autorregresive processes: consistency and asymptotic normality", Z. Wahrscheinlich. Verw. Geb. 49, 491-504. 1982.

[4] H. O. Bustos and V. J. Yohai, "Robust estimates for ARMA models". J. Anv. Statist. Assoc. 81(393), 155-68. 1986.

[5] J. Denby and R.D. Martin "Robust estimation of the firstorder autorregressive Parameter". J. Am. Statist. Assoc. 74(365), 1979.

[6] R. Dutter, "Robuste Regression". Bericht N$^o$ 135, Math. Statist. Eidgenoessische Techn. Hochschule. Zürich 1980.

[7] R. Dutter and P.J. Huber, "Numerical Methods for the Nonlinear Robust Regression Problem", J. Statist. Comput. Simul. Vol. 13,2, 79-114. 1981.

[8] F.R. Hampel, "A General Qualitative Definition of Robustness", Ann. Math. Statist. 43, 1971.

[9] F.R. Hampel, "Robust Estimation: a Condensed Partial Survey". Z. Wahrscheinlich. Verw Geb. 27. 1973.

[10] F.R. Hampel, *"Robust Statistics"*, New York: Wiley. 1986

[11] P. J. Huber, *"Robust Statistics"*. New York: Wiley, 1981.

[12] R. L. Kashyap, IEEE Trans. on Pattern Analysis and Machine Intelligence, Vol PAMI-4. 1982.

[13] R. L. Kashyap and K. B. Eom, "Robust Image Techniques with an Image Restoration Application" IEEE Trans. on Acoustics, Speech, and Signal Processing, Vol. 36, N$^o$ 8, pp. 1313-1325, Aug. 1988.

[14] B. Kleiner, R.D. Martin and D.J. Thomson, "Robust Estimation of Power Spectra" J. Roy. Soc., Series B, Vol. 41, N$^o$ 3, pp. 313-351, 1979.

[15] Technical Report C.L. Mallows "On some topics in robustness". Technical Memorandum, Bell Laboratories, Murray Hill. NJ. 1975.

[16] R.D. Martin and J.E. Zeh, "Generalized $M$-Estimates for Autorregresions, Incluiding Small-Sample Efficency Robustness". Techn. Rep. N$^o$ 214, Department of Electrical Engineering, University of Washington, Seattle. 1978.

[17] R.D. Martin, *"Robust estimation for Autorregressive Models"*, In: Brillinger D.R. and G.,C. Tiao (Eds.): Directions in Time Series. Inst. Math. Statist. Publications, Haywood, C.A., 1980.

[18] R.D. Martin and V. J. Yohai, *"Robustness in time series and estimatin ARMA models"*. Handbook of Statistics Vol. 5 (eds. E. J. Hanann, P.R. Krishnaiah and M.M. Rao), 1985.

[19] P. J. Rousseuw "Least median of Squares regression". J.Am. Assoc. 79, 1984.

[20] J.E. Zeh, *"Efficiency Robustness of Generalized M-Estimates for Autorregression and their use in determining outliers Type"*. Ph.D. Thesis. University of Washington. Seattle. 1979.

[21] R. Chellepa and R.L. Kashyap: "Digital Image Restoration Using Spatial Interaction Models". IEEE Trans. on Acoustics, Speech and Signal Processing, Vol 30 N$^o$ 3, pp 461-472, June 1982.

[22] S. Geman and D. Geman: "Stochastic relaxation, Gibbs distributions, and Bayesian restoration of images". IEEE Trans. Pattern Anal. Machine Intell. Vol 6 pp 721-741 Nov. 1984.

[23] Z. Wu: "Multidimensional state-space model Kalman filtering with application to image restoration". IEEE Trans. Acoust. Speech. Signal Processing Vol 33 pp 1253-1263 Oct. 1985.

# ESTIMATION OF SPECTRUM FROM SPECKLED SAR IMAGES

Oscar Humberto Bustos
Ana Georgina Flesia
Facultad de Matemática, Astronomía y Física
Universidad Nacional de Córdoba
Ph.N. 54+51+334051 - FAX 54+51+334054
e-mail *bustos* and *flesia@mate.uncor.edu*

**Abstract**

The multiplicative model can be used to describe SAR image formation. In this context, the effect and nature of coherent speckling on the spectrum of SAR images is investigated. A method for estimate the spectrum of the backscatter image, based on estimates of the spectrum of the speckled image and noise is developed.

## 1 Introduction

Images and signals produced by coherent systems are subject to the phenomena of speckle. This kind of noise appears due to interference phenomena between the incident and reflected signals. The result makes visual and automatic interpretation a difficult task, thought it may carry some important information.

Usually, images suffering from speckle noise should not be treated with the usual additive-noise derived tools (Wiener filter, for instance), since speckle corrupts the signal in the multiplicative manner and in the amplitude and intensity formats it is non-gaussian [5][8].

Other schemes have been proposed to deal with it, such multi look processing (incoherent average), or various types of linear and adaptive filters. These efforts have generally been directed toward improvement of the signal in the image domain.

However, application exist in which the spectrum of the output is of primary interest [1], but even in linear or adaptive filtering aimed at image improvement, it would be useful to have a good estimate of the underlying image spectrum rather than work from a priori assumption such as is often done.

This paper extends one-dimensional results on the problem of estimating the spectrum for speckled data [4]. We first discuss the effects of speckle in SAR images and the mathematical framework used to explain the statistical behavior of this kind of data. Then we prove that, as long as the output $Z$ is stationary, the power spectral density of $Z$ will be a convolution of the power spectral densities of the backscatter $X$ and the speckle $Y$ in the intensity format. In view of that, we consider three special cases. These cases are uniform target, white uncorrelated speckle and nearest neighbor correlation.

The last section presents an estimate of the underlying spectrum based on classical estimates of the return and noise spectrum. We shall study the performance of that estimate based on the performance of the other estimates involved in making it.

## 2 Notational conventions and general definitions

The set of real numbers is denoted by $\mathbf{R}$, the set of natural numbers by $\mathbf{N}$ and the set of integers numbers by $\mathbf{Z}$. The generic points of the two-dimensional set of integers $\mathbf{Z}^2$ are denoted by $(s_1, s_2)$, where $s_1$ always represents the horizontal coordinate, and $s_2$ the vertical coordinate.

Random processes will be denoted by $X = \{X_{(s_1,s_2)} : (s_1, s_2) \in \mathbf{Z}^2\}$. A common underlying probability space will be assumed throughout this work $(\Omega, \mathcal{A}, P)$, where $\Omega$ denotes the sample set, $\mathcal{A}$ its $\sigma$-algebra, and $P$ a probability. Therefore, real or complex-valued random processes are collections of measurable functions of the form $X_{(s_1,s_2)} : \Omega \to \mathbf{R}$ or $X_{(s_1,s_2)} : \Omega \to \mathbf{C}$ indexed in $\mathbf{Z}^2$.

Let's $k \in \mathbf{Z}$ and $N \in \mathbf{N}$, we denote by $\omega_{k,N}$ the $N^{th}$ unit's root

$$\omega_{k,N} = \exp(\tfrac{2\pi k}{N} i).$$

They have the following properties:

a) $\omega_{0,N} + \ldots + \omega_{N-1,N} = 0$, since $\omega_{k,N}$ with $0 \leq k \leq$

$N-1$ are the roots of the equation $z^N - 1 = 0$.
$\omega_{k+rN,N} = \omega_{k,N}$ for all $r \in \mathbf{Z}$ and $0 \leq k \leq N-1$.
$\omega^*_{k,N} = \omega_{-k,N} = \omega_{N-k,N}$ for all $0 \leq k \leq N-1$.
$\omega_{p0,N} + \ldots + \omega_{p(N-1),N} = \begin{cases} N & \text{if } p = 0 \\ 0 & \text{if } p \neq 0 \end{cases}$ for all $0 \leq p \leq N-1$, with $p \in \mathbf{N}$.
Finally: $set2 = \{(k_1, k_2) \ / \ 0 \leq k_1, k_2 \leq N_1\}$ or $\{(l_1, l_2) \ / \ 0 \leq l_1, l_2 \leq N_2\}$,
$set2\infty = \{(k_1, k_2) \ / \ -\infty < k_1, k_2 < +\infty\}$ and
$set = \{(k_1, k_2, l_1, l_2) \ / 0 \leq k_1, k_2 \leq N_1, 0 \leq l_1, l_2 \leq N_2\}$.

# 3 The multiplicative model and the speckle noise

The multiplicative model has been widely used in the modeling, processing, and analysis of synthetic aperture radar images. This model states that, under certain conditions [5][8], the return results from the product between the speckle noise and the terrain backscatter.
Based upon this model, we assume that the observed value in each pixel within this kind of images is the outcome of the product of two independent two-dimensional random processes: one $X$ modeling the terrain backscatter, and other $Y$ modeling the speckle noise. The former is many times considered real and positive, while the latter could be complex (if the considered image is in the complex format) or positive and real (intensity and amplitude formats).
Therefore, the observed value is the outcome of the random process defined by the product

$$Z_{(s_1,s_2)} = X_{(s_1,s_2)} Y_{(s_1,s_2)} \qquad \forall\, (s_1, s_2) \in \mathbf{Z}^2,$$

where $(s_1, s_2)$ denotes the spatial position of the pixel. We will say that the process $Z_I$ is the intensity return process if $Z_I = |Z|^2$, and $Z_A$ is the amplitude return process if $Z_A = |Z|$.
The complex format has been used as a flexible tool for the statistical modeling of SAR data. However, in several cases, complex data are not available or exists computational limitations imposed by the imaging system that not allow us to work with them. In order to that, intensity format and amplitude format are frequently considered in the literature.
In many cases, it is easier to derive the statistical properties of the intensity data rather than amplitude data. For instance, the intensity speckle noise modeled as the sum of independent and exponentially distributed random variables has well know distribution, the Gamma distribution, but this is not the case for amplitude speckle noise, since the convolution of Rayleigh distributions has not closed form.[9]

In this work, we want to estimate the spectrum of the backscatter based on the spectrum of the return, in the intensity format.
Following the description that Frery, Müller, Yanasse and Sant'Anna [3] realize about the appropriate distributions for this model, complex speckle is assumed to have a bivariate normal distribution, with independent identically distributed components having zero mean and variance $1/2$. These marginal distributions are denoted here as $N(0, 1/2)$, therefore

$$Y_{C(s_1,s_2)} = (Re(Y_{(s_1,s_2)}), Im(Y_{(s_1,s_2)})) \sim N^2(0, \mathbf{1/2})$$

denotes the distribution of a pair.
$n$-look intensity speckle results from taking the average over $n$ independent samples of $Y_{I(s_1,s_2)} = |Y_{C(s_1,s_2)}|^2$ leading, thus, to a Gamma distribution denoted here as $Y_{I(s_1,s_2)} \sim \Gamma(n, n)$ and characterized by the density

$$f_{Y_I}(y) = \frac{n^n}{\Gamma(n)} y^{n-1} e^{-ny} \qquad y > 0,\ n > 0.$$

Several distributions could be used for the backscatter, aiming at the modeling of different types of classes and their characteristic degrees of homogeneity. For instance, for some sensor parameters (wavelength, angle of incidence, polarization, etc.), pasture is more homogeneous than forest, which, in turn, is more homogeneous than urban areas.
The basic hypothesis that governs the modeling of homogeneous regions is that the backscatter is constant, thought its value is unknown. When the region is non homogeneous, the backscatter can be modeled for a more convenient distribution.
The distribution of the intensity return arises from the product $Z_I = X_I . Y_I$. For instance, in the homogeneous case, we consider $X_I$ a constant $\beta^2$ and the multilook intensity speckle $X_I \sim \Gamma(n, n)$, then the return $Z_I$ can be modeled by a Gamma distribution, denoted by $Z_{I,(s_1,s_2)} \sim \Gamma(n, n/\beta^2)$.

# 4 Periodic processes and discrete Fourier series

We wish to derive some properties of the spectrum of a random process present in an image that has been speckled by the multiplicative manner described above. Since the data are usually only available in discrete regions, we can restrict our attention to periodic random processes, which we define below.
A complex two-dimensional random process $X$ is said to be periodic with period of $N_1 \times N_2$ when $X_{(s_1,s_2)} = X_{(s_1+N_1,s_2)} = X_{(s_1,s_2+N_2)}$ for all $(s_1, s_2) \in \mathbf{Z}^2$. Since $X_{(s_1,s_2)} r_1^{-s_1} r_2^{-s_2}$ for all $(s_1, s_2) \in \mathbf{Z}^2$ is not absolutely

summable for any $r_1$, $r_2$, neither the Fourier transform or the $Z$-transform uniformly converges for periodic processes.
The discrete Fourier series (**DFS**) is a frequency domain representation of a periodic process. The sequence of **DFS** coefficients of $X$, whose are denoted by $X_{(s_1,s_2)}$, are determined for the equation

$$\tilde{X}_{(s_1,s_2)} = \frac{1}{N_1 N_2} \sum_{s\epsilon l2} X_{(k_1,k_2)} \omega^*_{s_1 k_1, N_1} \omega^*_{s_2 k_2, N_2} \quad (1)$$

$\forall 0 \leq s_1 \leq N_1 - 1,\ 0 \leq s_2 \leq N_2 - 1$.
Usually, for convenience and by convention, $X$ is defined to be periodic with a period of $N_1 \times N_2$, that is,

$$X_{(s_1,s_2)} = \sum_{s\epsilon l2\infty} X_{(s_1 - k_1 N_1, s_2 - k_2 N_2)},$$

but, for our purposes, it is clearly enough to deal with equation (1).
Then, the power spectral density, (**psd**), of the signal $X$ is the periodic sequence with a period of $N_1 \times N_2$, defined by

$$S_X(s_1,s_2) = E(X^*_{(s_1,s_2)} X_{(s_1,s_2)}), \quad (2)$$

$\forall 0 \leq s_1 \leq N_1 - 1,\ 0 \leq s_2 \leq N_2 - 1$, where $E(.)$ represents the mathematical expectance.
If we suppose that $X$ is stationary in the wide sense we have

$$E(X^*_{(s_1,s_2)} X_{(t_1,t_2)}) = R_X(s_1 - t_1, s_2 - t_2), \quad (3)$$

$\forall (s_1,s_2), (t_1,t_2) \in \mathbf{Z}^2$.where $R_X$ is the autocorrelation function of $X$.
Expanding the product $X^*_{(s_1,s_2)} X_{(t_1,t_2)}$, and using the stationarity, we obtain

$$E(X^*_{(s_1,s_2)} X_{(t_1,t_2)}) = \frac{1}{N_1^2 N_2^2} \sum_{s\epsilon l} R_X(k_1 - l_1, k_2 - l_2) \times \omega_{k_1 s_1 - l_1 t_1, N_1} \omega_{k_2 s_2 - l_2 t_2, N_2}.$$

For a **real** stationary periodic random process, making appropriate changes of variable and noting that the periodicity implies that all arithmetic is modulo $N_1$ or $N_2$, we can transform the equation (3) yielding

$$E(X^*_{(s_1,s_2)} X_{(t_1,t_2)}) = 0 \qquad \text{if } (s_1,s_2) \neq (t_1,t_2),$$

and

$$E(X^*_{(s_1,s_2)} X_{(s_1,s_2)}) = \frac{1}{N_1 N_2} \sum_{s\epsilon l2} R_X(k_1,k_2) \times \omega_{k_1 s_1, N_1} \omega_{k_2 s_2, N_2}.$$

Then, equation (2) becomes

$$S_X(s_1,s_2) = \frac{1}{N_1 N_2} \sum_{s\epsilon l2} R_X(k_1,k_2) \omega_{k_1 s_1, N_1} \omega_{k_2 s_2, N_2}.$$

# 5 Effect of speckling

Consider the intensity return process $Z_I$ given by

$$Z_{I(s_1,s_2)} = X_{I(s_1,s_2)} Y_{I(s_1,s_2)},$$

where $X_I$ and $Y_I$ are real periodic independent stationary random processes, with the same period $N_1 \times N_2$. Let's $X_I$, $Y_I$ and $Z_I$ the respective **DFS** of the processes $X_I$, $Y_I$, and $Z_I$.
Given the relation under the random processes $X_I$, $Y_I$ and $Z_I$, it is not difficult to prove that

$$S_{Z_I}(s_1,s_2) = \sum_{s\epsilon l} E(X^*_{I(k_1,k_2)} X_{I(l_1,l_2)}) \times E(Y^*_{I(s_1-k_1,s_2-k_2)} Y_{I(s_1-l_1,s_2-l_2)}) = \sum_{s\epsilon l2} E(X^*_{I(k_1,k_2)} X_{I(k_1,k_2)}) \times E(Y^*_{I(s_1-k_1,s_2-k_2)} Y_{I(s_1-k_1,s_2-k_2)}).$$

Thus

$$S_{Z_I}(s_1,s_2) = \sum_{s\epsilon l2} S_{X_I}(k_1,k_2) S_{Y_I}(s_1-k_1, s_2-k_2) \quad (4)$$

and, as long as $X_I$ and $Y_I$ are stationary, the power spectral density of $Z_I$ will be the convolution of the power spectral density of $X_I$ and $Y_I$.
Let us assume that $a_Y : \mathbf{Z}^2 \to \mathbf{C}$ is the normalized autocorrelation function of the noise process $Y_I$. Then

$$a_Y(s_1,s_2) = \frac{R_{Y_I}(s_1,s_2) - E(Y_{I(0,0)})^2}{[R_{Y_I}(0,0) - E(Y_{I(0,0)})]^2} = \frac{R_{Y_I}(s_1,s_2) - E(Y_I)^2}{Var(Y_{I(0,0)})}.$$

Notice that, if $Y_I \sim \Gamma(n,n)$, it holds that $E(Y_{I(s_1,s_2)}) = 1$ and $Var(Y_{I(s_1,s_2)}) = \frac{1}{n}$, therefore $R_{Y_I}(s_1,s_2) = \frac{1}{n}(a_Y(s_1,s_2) + 1)$ and

$$S_{Y_I}(s_1,s_2) = \frac{1}{n} a_Y(s_1,s_2) + \delta(s_1,s_2). \quad (5)$$

where $\delta$ is the periodic function defined by

$$\delta(s_1,s_2) = \begin{cases} 0 & \text{if } (s_1,s_2) \neq (0,0) \\ 1 & \text{if } (s_1,s_2) = (0,0) \end{cases}$$

and $0 \leq s_1 \leq N_1,\ 0 \leq s_2 \leq N_2$.
Using the relation (5) and the definition of **DFS**, equation (4) becomes

$$S_{Z_I}(s_1,s_2) = S_{X_I}(s_1,s_2) + \frac{1}{n} \sum_{s\epsilon l2} S_{X_I}(k_1,k_2) a_Y(s_1 - k_1, s_2 - k_2). \quad (6)$$

We will consider three special cases.

### 5.1 Case 1: Uniform target

If the target is uniform, the power spectrum of the intensity backscatter can be modeled by

$$S_{X_I}(s_1, s_2) = \beta^2 \delta(s_1, s_2),$$

where $\beta^2$ is a constant.
Then, the spectrum of the speckled image is given by

$$S_{Z_I}(s_1, s_2) = \beta^2(\delta(s_1, s_2) + \frac{1}{n} a_{Y_I}(s_1, s_2)).$$

Since that equation can be solve to give $a_{Y_I}$ in terms of $S_{Z_I}$, it is possible to determine the speckle process autocorrelation function when the target is assumed to be uniform with known $\beta$.
The significance of this lies in the fact that the speckle correlation is often produced by the imaging system being used, and thus, this property of the system can be studied by deliberate viewing a uniform target.
A similar one-dimension technique has been used in the analysis of SEASAT-A image spectra [2].

### 5.2 Case 2: White uncorrelated speckle

In this case, we have $a_Y(s_1, s_2) = \delta(s_1, s_2)$, and $\hat{Y}(s_1, s_2) = \frac{1}{N_1 N_2}$. Therefore,

$$S_{Z_I}(s_1, s_2) = S_{X_I}(s_1, s_2) + \frac{1}{nN_1N_2} \sum_{set2} S_{X_I}(k_1, k_2).$$

We let $\overline{S_{X_I}} = \frac{1}{N_1 N_2} \sum_{set2} S_{X_I}(k_1, k_2)$ the average spectral power, then

$$S_{Z_I}(s_1, s_2) = S_{X_I}(s_1, s_2) + \frac{1}{n}\overline{S_{X_I}}. \qquad (7)$$

Therefore, the power spectral density **(psd)** of the speckled signal is proportional to that of the unspeckled signal, but has added to it a bias proportional to the average **psd**. Hence, a **psd** that is sharply peaked will stand out more strongly against the bias than will one that is broader.

### 5.3 Case 3: Nearest Neighbor correlation

We assume that nearest neighbor points are correlated to some extent. That is, we let

$$a_Y(s_1, s_2) = \delta(s_1, s_2) + \epsilon(\delta(s_1 - 1, s_2) + \delta(s_1 + 1, s_2) + \delta(s_1, s_2 - 1) + \delta(s_1, s_2 + 1))$$

In order to this, we can prove that the **DFS** of the normalized autocorrelation function is given by

$$\hat{a}_Y(s_1, s_2) = \frac{1}{N_1 N_2}(1 + 2\epsilon\cos(\frac{2\pi s_1}{N_1}) + 2\epsilon\cos(\frac{2\pi s_2}{N_2})).$$

Putting this equation into equation (6) we obtain

$$S_{Z_I}(s_1, s_2) = S_{X_I}(s_1, s_2) + \frac{1}{n}\overline{S_{X_I}}$$
$$+ \frac{2\epsilon}{nN_1N_2} \sum_{set2} S_{X_I}(k_1, k_2)$$
$$\times[\cos(\frac{2\pi(s_1 - k_1)}{N_1}) + \cos(\frac{2\pi(s_2 - k_2)}{N_2})].$$

It is important to note that, while uncorrelated speckle merely added a bias to the spectrum, correlated speckle add power that is not uniform in wavenumber, thus changing the shape of the spectrum.
The question of how the underlying spectrum is best to be estimated is taken up in the next section.

## 6 Estimation of spectrum

To estimate the spectrum $S_{X_I}$ from the speckled spectrum $S_{Z_I}$, it is necessary to invert (6).
Then, defining

$$\mathbb{S}_{X_I}(k_1, k_2) = \frac{1}{N_1 N_2} \sum_{set2} S_{X_I}(l_1, l_2)\omega_{l_1 k_1, N_1}\omega_{l_2 k_2, N_2} \qquad (8)$$

and using the definition of Fourier transform, equation (6) becomes

$$S_{Z_I}(s_1, s_2) = S_{X_I}(s_1, s_2) +$$
$$\frac{1}{n}\sum_{set2} \mathbb{S}_{X_I}(k_1, k_2) a_Y(k_1, k_2)\omega^*_{s_1 k_1, N_1}\omega^*_{s_2 k_2, N_2}.$$

Let is now

$$\mathbb{S}_{Z_I}(k_1, k_2) = \frac{1}{N_1 N_2} \sum_{set2} S_{Z_I}(l_1, l_2)\omega_{l_1 k_1, N_1}\omega_{l_2 k_2, N_2}.$$

Then, multiplying both side of the above equation by $\exp(\frac{2\pi l_1 k_1}{N_1} i)\exp(\frac{2\pi l_2 k_2}{N_2} i)$ and summing the result over all $(k_1, k_2)$ in the period, we obtain

$$\mathbb{S}_{X_I}(k_1, k_2) = \frac{1}{n(n + a_Y(k_1, k_2))}\mathbb{S}_{Z_I}(k_1, k_2).$$

Putting the last equation into equation (8) and solving for $S_{X_I}$, we obtain the desired spectral estimate

$$S_{X_I}(s_1, s_2) = \frac{1}{n^2}[S_{Z_I}(s_1, s_2) -$$
$$\sum_{set2} \frac{a_Y(k_1, k_2)}{n + a_Y(k_1, k_2)}\mathbb{S}_{Z_I}(k_1, k_2)\omega_{s_1 k_1, N_1}\omega_{s_2 k_2, N_2}].$$

This equation is our general result. We consider two special cases.

### 6.1 Case 1: White uncorrelated speckle

In this case, a straightforward procedure, using the fact that $a_Y(s_1, s_2) = \delta(s_1, s_2)$, allow us that
$S_{X_I}(s_1, s_2) = \frac{1}{n^2}[S_{Z_I}(s_1, s_2) - \frac{1}{1+n}\overline{S_{Z_I}}]$
where $\overline{S_{Z_I}} = \frac{1}{N_1 N_2} \sum_{set2} S_{Z_I}(k_1, k_2)$.
Thus estimation of the spectrum on the case of uncorrelated speckle is accomplished by substraction of an appropriate bias.

### 6.2 Case 2: Nearest Neighbor correlation

Also in this case, a straightforward procedure, allow us that

$$S_{X_I}(s_1, s_2) = \frac{1}{n^2}[S_{Z_I}(s_1, s_2) - \frac{1}{n-1}\overline{S_{Z_I}} - \frac{2\epsilon}{n+\epsilon}\frac{1}{N_1 N_2}\sum_{set2} S_{Z_I}(k_1, k_2) \times (\cos(\frac{2\pi}{N_1}(s_1 - k_1)) + (\cos(\frac{2\pi}{N_2}(s_2 - k_2))).$$

Therefore, a priori knowledge of the speckle autocorrelation function, such as is available through the study of uniform targets, allows the underlying image spectrum to be estimated. The correction is, however, more complicated than merely the subtraction of a bias.

## 7 Conclusions

The technique presented in this paper provides an exact representation of the power spectral density of the backscatter process. However, this representation depends strongly on the **psd** of the speckled process, which is unknown. Thus, the estimation of the underlying spectrum is accomplished by the election of an appropriate estimate for the spectrum of the speckled signal, in the most of the cases.

We can choose conventional estimates, based on the Fourier transform, like the periodogram, or the class of smoothed periodograms, but for small $N_1$, $N_2$ the resolution of them can be rather poor. It exists other spectral estimation methods based on maximum likelihood or maximum entropy which give higher resolution than the conventional estimates. However, since the various methods were developed on the basis of different assumptions, and since only limited comparisons of the method's performance are available, choosing the best method for a given application problem is a difficult task.


[1] R.C. Beal (1980) Spaceborne imaging radar: monitoring ocean waves. *Science*, June 1980, Vol 1, pp 148-156.

[2] R.C. Beal,A. D. Goldfinger, A. G. Tilly, W.J. Geckle. (1981) System calibration strategies for spaceborne synthetic aperture radar for oceanography. *Report CP 084*, Dec.1981. Johns Hopkins University Applied Physics Laboratory.

[3] A. C. Frery, H. J. Müller, C. C. F. Yanasse, S. J. S. Sant'Anna (1997) A model for extremely heterogeneous clutter. *IEEE Transactions on Geoscience and Remote Sensing*, Vol. 35, no. 3, pp. 1-12.

[4] A.D. Goldfinger (1982) Estimation of spectra from speckled images. *IEEE transactions on aerospace and electronic systems*, Vol AES-18(5), pp 675-681.

[5] J.W.Goodman (1976) Some fundamental properties of speckle. *Journal of the optical society of America*, Nov. 1976, Vol 66, pp 1145-1150.

[6] A.K.Jain (1989) Fundamentals of digital image processing. Prentice Hall International .

[7] J.S. Lim (1990) Two dimensional signal and image processing. Prentice Hall International .

[8] M.Tur, K.C.Chin, and J.W.Goodman (1982) When is speckle noise multiplicative?. *Appl. Opt.* Vol 21, pp 1157-1159.

[9] C.C.F. Yanasse, A.C. Frery, S.J.S. Sant'Anna(1995) Stochastic distribution and multiplicative model: Relations, properties and applications to SAR Image Analysis. *Technical Report INPE-5630-NTC/318*, INPE, São Jose dos Campos, Brazil. .

# AN ADAPTIVE CLUSTERING MAP ALGORITHM TO FILTER SPECKLE IN MULTILOOK SAR IMAGES

Fátima N. S. Medeiros[1,3]
Nelson D. A. Mascarenhas[2]
Luciano da F. Costa[1]

[1] Cybernetic Vision Group IFSC -University of São Paulo
Caixa Postal, 369, SP,13560-970,Brasil
Phone: +55 (16) 273 98 58
Fax: +55 (16) 271 36 16
e-mails: {luciano,fsombra}@ultra3000.ifsc.sc.usp.br

[2] UFSCar - DC
Via Washington Luiz Km 235, Caixa Postal 676
13565-905 - São Carlos, SP, Brasil
nelson@dc.ufscar.br

[3]UFCe- DEE
Campus do PICI Bloco 705
60455-760 - Fortaleza,CE, Brasil
fsombra@dee.ufc.br

## Abstract

SAR images are generally affected by a multiplicative noise, called speckle, which degrades the quality of these images. Using this model we present an algorithm based on the Maximum a Posteriori (MAP) criterion to reduce speckle noise of multilook amplitude data. The speckle in these images is approximately described by the Square Root of Gamma distribution, which is used to develop MAP filters using different a priori distributions. We also suggest the combined use of MAP and the k-means clustering algorithm as a formal way to choose the best window size to update noisy pixels. We conclude this work by calculating the coefficient of variation, defined as the ratio of the standard deviation to mean, of MAP filtered images and of the original image to measure the reduction of the speckle in homogeneous areas.

**Keywords:** Multilook image, MAP estimator, k-means classifier, speckle noise, filtering.

## 1. Introduction

Speckle noise is one of the main characteristics present in images obtained by coherent imagery systems such as synthetic aperture radar (SAR), lasers, and ultrasound images. This kind of signal-dependent noise limits the visual interpretation of these images because it obscures the scene content. It is recommended to overcome this difficulty prior to classification procedures, for example. In such cases, filtering algorithms used as "a prior" step would improve the classification performance. In the literature, classical filters, like Lee (Lee, 1980), Kuan, (Kuan et al. 1985), Sigma (Lee, 1983), Frost (Frost et al., 1982), Median (Castleman, 1996) amongst others aim to reduce the noise speckle. The ideal filter must smooth the noise without eliminating radiometric and textural information that are fundamental for detail preservation (Lopes et al., 1988).

It has been experimentally verified in several works that for SAR images over homogeneous areas, the standard deviation of the signal is proportional to its mean Lee (1981). This fact suggests the use of the multiplicative model for the speckle and it was used by Kuan et al. (1987) to propose an adaptive non-linear pointwise filter that satisfies the MAP criterion for single look, quadratic detection and Gaussian "a priori" density.

The variance ratio of the original and noisy image is used as a measure of local properties by the adaptive filters to control filter window size (Li, 1988). By combining the MAP filter and the k-means clustering algorithm over Changle Li's variance ratio (Li, 1988) it is possible to classify the noisy image in regions of homogenous statistics. In order to adapt the MAP filtering to the local statistics, the thresholds on the variance ratio are chosen equispaced over the interval [0,1] to determine the window sizes for parameter estimation.

In practical applications the noise is often reduced by multilook processing, which can be done by averaging independent samples of several images. With an increasing number of averaged samples, the Rayleigh distribution of a signal approximates a Gaussian distribution (Hagg et al., 1996). Although improving the signal to noise ratio by $\sqrt{N}$, where N is the number of looks used to generate the image, this technique also diminishes the spatial resolution.

In this work the speckle distribution over multilook amplitude data is modelled by a Square Root of Gamma and we use it in the proposed MAP filter. The statistical parameters in the filtering algorithm are calculated by

using a fixed window size (5x5) around each pixel or choosing a window size according to the degree of roughness of the non-noisy signal around the pixel. The clustering of the coefficients of variation determines the suitable filtering window size in a more formal way that was proposed by Li(1988). It will be shown in this article that this fact leads to a better filtering result.

In section II we present the multiplicative model for the speckle and derived from this model in section III the MAP estimator is formulated using the "a priori" Gaussian, Gamma, Chi-square, Exponential and Rayleigh densities. There is a brief discussion about the implementation results in section IV. Section V summarizes the conclusions and section VI outlines possibilities for future work.

## 2. Multiplicative Model and Speckle Statistics

The model used to describe the speckle is given in terms of a multiplicative noise given by equation (1), where $z_A$ describes the amplitude SAR noisy image, $x$ is the original signal and $n_A$ is the noise with unitary mean and standard deviation $\sigma_n$. The multiplicative model is a good model over homogeneous areas because the standard deviation is proportional to the mean. The speckle noise and the original image are assumed to be independent.

$$z_A = x.n_A \tag{1}$$

Equation 2 represents the β index which is the ratio of the standard deviation to the mean used to measure the strength of the speckle in this kind of image and N is the number of looks.

$$\frac{\sigma}{\mu} = \frac{0.5227}{\sqrt{N}} \tag{2}$$

The speckle for 1 look amplitude SAR image obeys a Rayleigh distibution as in equation 3. An N look intensity speckle image is obtained by averaging N intensity single look images and is modelled as a Gamma distribution (equation 3.a). The multilook amplitude speckle can be obtained by averaging the N amplitude single look images or by averaging the N intensity images and then taking the square root (Frery et al., 1997). The latter follows a Square Root of Gamma distribution (Lee et al.,1994) as describes the equation 3.b. The former is described by the convolution of N Rayleigh distributions and for N=2 there is a closed form for it and as there is no closed form for the distribution for N≥3 it is costumary to make an approximation (Yanasse et al., 1995) and describe it by the Square Root of Gamma distribution.

$$f(g) = \frac{g}{\sigma^2} e^{-\frac{g^2}{2\sigma^2}} \tag{3}$$

where g is the random variable with parameter σ.

$$f(g) = \frac{\sigma}{\Gamma(\lambda)} (\sigma g)^{\lambda-1} e^{-\sigma g}, g > 0 \tag{3.a}$$

where Γ(λ) is a value of the gamma function and g is the random variable with parameters σ and λ. For λ=1 the Gamma distribution is identical to the Exponential distribution. For λ=$n$/2 ($n$>0) and σ=1/2 the Gamma distribution is equivalent to a Chi-square distribution.

$$f(g) = \frac{2N^N}{\sigma^{2N}\Gamma(N)} (g)^{2N-1} e^{-\frac{Ng^2}{\sigma^2}}, g, N > 0 \tag{3.b}$$

## 3. MAP Estimator

The MAP estimator of $x$ is obtained by maximizing the "a posteriori" probability density function $f(x|z)$, which can be related to the "a priori" distribution $f(x)$ through equation (4). To simplify the notation, the indexes (A) in the following equations are dropped out. The conditional distribution $f(z|x)$ which describes the model follows a Square Root of Gamma distribution is given by the equation (5).

$$f(x|z) = \frac{f(z|x)f(x)}{f(z)} \tag{4}$$

$$\frac{\partial \ln f(z|x)}{\partial x} + \frac{\partial \ln f(x)}{\partial x}\Big|_{x=\hat{x}_{MAP}} = 0 \tag{4.b}$$

$$f(z|x) = \frac{2N^N}{\sigma^{2N}\Gamma(N)} (x)^{2N-1} e^{-\frac{Nx^2}{\sigma^2}} \tag{5}$$

where N is the number of looks. This follows from the multiplicative model (equation 1) since given the signal $x$, the conditional probability density of $z$ is a Square Root of Gamma density with mean value $x$ (the mean value of $n$ is one).

$$\frac{\partial \ln}{\partial x}[f(z|x)] = -\frac{2N}{x} + \frac{2z^2\Gamma^2(N+1/2)}{\Gamma^2(N)x^3} \tag{6}$$

We formulated several MAP filters using different "a priori" densities. These MAP equations are presented in the following.

**3.1** Given the Gaussian "a priori" density

$$f(x) = \frac{1}{\sigma_x\sqrt{2\pi}} e^{-\frac{1}{2}\left(\frac{x-\mu_x}{\sigma_x}\right)^2} \tag{7}$$

The Gaussian MAP filter is given by the solution of the equation (8). This equation was obtained using the "a priori" knowledge from (7) combined with (6) in equation (5).

$$x^4\Gamma^2(N)-x^3\Gamma^2(N)\mu_x+x^2\Gamma^2(N)2N\sigma_x^2-$$
$$\sigma_x^2 2z^2\Gamma^2(N+1/2)=0 \quad (8)$$

The estimators for $\mu_x$ and $\sigma_x^2$ are obtained by the following expressions:

$$\hat{\mu}_x=\hat{\mu}_z=m=\frac{1}{w}\sum_{i=1}^{w}z_i$$
$$\hat{\sigma}_x^2=\frac{\sigma_z^2-\hat{\mu}_z^2.\sigma_n^2}{1+\sigma_n^2} \quad (9)$$
$$R=\frac{\hat{\sigma}_x^2}{\sigma_z^2}$$

where $w$ is the number of pixels in the window around the filtered pixel and $\sigma_n^2$ is the noise variance, which is a constant determined by the number of looks and the type of detection. The Changle Li's parameter ($R$) is the local ratio of original and noisy image variance. The set of expressions in equation (9) arose from the multiplicative model with unitary mean for the speckle noise.

Before filtering the noisy image, we calculate the local $R$ (Li's ratio) parameter for all pixels using 3x3 windows. The one dimensional k-means algorithm over Li's ratio classifies pixels with similar statistics. Pixels assigned to the same cluster are filtered with the same window size for parameter estimation (3x3 or 5x5). The real and positive roots of the MAP equations whose values are between the mean and the observed pixel are taken as the filtered pixel values.

**3. 2** Given the Gamma "a priori" density

$$f(x)=\frac{\sigma_x}{\Gamma(\lambda)}(\sigma_x x)^{\lambda-1}e^{-\sigma_x x} \quad (10)$$

The MAP estimator is given by the solution of the equation

$$x^3\Gamma^2(N)\sigma_x+x^2\Gamma^2(N)(2N-\lambda+1)-$$
$$2z^2\Gamma^2(N+1/2)=0 \quad (11)$$

$$\hat{\lambda}=\frac{\hat{\mu}_x^2}{\hat{s}_x^2} \qquad \hat{\sigma}_x=\frac{\hat{\mu}_x}{\hat{s}_x^2} \quad (12)$$

where the parameters $\sigma_x$ and $\lambda$ are estimated by the sample mean and the sample variance through the method of moments, using the multiplicative model. The estimated parameter $\hat{s}_x^2$ is the variance of the original signal calculated from the noisy signal through equation 9.

**3.3** Given the Chi-square "a priori" density

$$f(x)=\frac{1}{2^{n/2}\Gamma(n/2)}x^{n/2-1}e^{-x/2} \quad (13)$$

where $n$ denotes a Chi-square distribution with $n$ degrees of freedom.

The MAP equation is given by

$$x^3\Gamma^2(N)+x^2\Gamma^2(N)[2+4N-n]-$$
$$4z^2\Gamma^2(N+1/2)=0$$
$$\hat{n}=\hat{\mu}_x=\hat{\mu}_z=\frac{1}{w}\sum_{k=1}^{w}z_k \quad (14)$$

**3.4** Given the Exponential "a priori" density

$$f(x)=\sigma_x e^{-\sigma_x x} \quad (15)$$

The noisy pixel is updated with the solution of the MAP equation

$$x^3\Gamma^2(N)\sigma_x+x^2\Gamma^2(N)2N-2z^2\Gamma^2(N+1/2)=0$$
$$\hat{\sigma}_x=\frac{1}{\hat{\mu}_x} \quad (16)$$

**3.5** Given the Rayleigh "a priori" density

$$f(x)=\frac{x}{\sigma_x^2}e^{\frac{-x^2}{2\sigma_x^2}} \quad (17)$$

The MAP estimator is given by the solution of the equation

$$x^4\Gamma^2(N)+x^2\Gamma^2(N)\sigma_x^2(2N-1)-$$
$$2z^2\sigma_x^2\Gamma^2(N+1/2)=0$$
$$\hat{\sigma}_x=\hat{\mu}_x\sqrt{\frac{2}{\pi}} \quad (18)$$

## 4. Experimental Results

The original image in **Figure 1.a** is a piece of a 481x481 pixels image of the National Forest of Tapajós, Pará, Brazil, taken on June, 26, 1993 by the JERS-1 satellite. It is a three looks, amplitude detected image.

The presented filters were applied and their performance was evaluated in terms of the the speckle reduction index, $\beta$, which is the ratio between the standard deviation and the mean over homogeneous areas. In **Table 1**, the estimated $\beta$ indexes in a 41x41 pixels piece of the original image with initial coordinates (51,376) over a forest region are shown.

The last row are the theoretical and practical values of $\beta$ indexes over this region.The closeness of the theoretical and practical $\beta$ coefficients implies that this forest area can be considered homogeneous. In the first column are the estimated $\beta$ indexes in the MAP filtered area without k-means and in the second column are the $\beta$ indexes in the MAP filtered area with the k-means algorithm.

| MAP FILTER | $\beta=\sigma_z/\mu_z$ (without k-means) | $\beta=\sigma_z/\mu_z$ (with k-means) |
|---|---|---|
| GAUSSIAN | 0.113 | 0.017 |
| GAMMA | 0.137 | 0.019 |
| CHI-SQUARE | 0.126 | 0.071 |
| EXPONENTIAL | 0.200 | 0.182 |
| RAYLEIGH | 0.192 | 0.162 |
| HOMOGENEOUS REGION (41X41 PIXELS) | 3 LOOKS THEORETICAL 0.2941 | PRACTICAL 0.3029 |

**Table 1-Estimated β indexes**

## 5. Conclusions

The nonlinear, adaptive algorithms based on the MAP criterion proposed in this paper, besides decreasing substantially the standard deviation to the mean ratio improved the discrimination of the predominant classes (regeneration and forest) as shown by the histograms. The smoothing of the speckle in the Gaussian, Gamma, Chi-square, Exponential and Rayleigh MAP filtered images has been evaluated by the $\beta$ index in **Table 1** and from the histograms. The indexes were calculated over an homogeneous area of forest (41x41 pixels). Some speckle reduction can be discerned in **Figures 2.a**, **3.a**, **4.a** and **5.a** which presented the best $\beta$ indexes and in **Figures 3.b** and **5.b** the discrimination of classes has been improved by the use of the k-means algorithm. In the Chi-square MAP filtered image histogram, **Figure 9.b**, the classes are better discriminated than for the other distributions. The $\beta$ indexes for the Exponential and Rayleigh MAP filters were the lowest, and even when using k-means the classes discrimination is not as evident as in **Figures 6.b** and **11.b**. Based on these results, the improvement obtained through the use of the k-means algorithm become clear. A further result is the use of a formal criterion based on the one-dimensional k-means clustering algorithm over Li's ratio (Li, 1988) to choose the thresholds that determine the window size for parameter estimation.

## 6. Further Developments

Future developments will use region growing techniques to determine windows with adaptive size and shape (not necessarily square) to estimate the local parameters of the MAP filters.

## Acknowledgements

Mrs. Fátima N. S. Medeiros was partially supported by a PICD-CAPES scholarship.
The authors wish to thank Sidnei J. S. Sant'Anna, Pedro R. Vieira, Antônio M. V. Monteiro Alejandro C. Frery and Corina C. F. Yanasse for their assistance with test data set.

## References

Lee, J.S. Digital Image Enhancement and Filtering by Use of Local Statistics, *IEEE Trans. on Pattern Analysis and Machine Intelligence*, Vol. 2, No.2, pp. 165-168, 1980.

Lee, J.S. Speckle Analysis and Smoothing of Synthetic Aperture Radar Images, *Computer Graphics and Image Processing*, vol. 17, pp. 24-32, 1981.

Lee, J.S. Digital Smoothing and the Sigma Filter, *Computer Vision, Graphics and Image Processing*, vol. 17, pp. 255-269, 1983.

Lee, J.S.; Jurkevich, I.; Dewaele, P.; Wambacq, P.; Oosterlinck, A. Speckle Filtering of Synthetic Aperture Radar Images: A Review, *Remote Sensing Reviews*, vol. 8, pp. 313-340 , 1994.

Yanasse, C.C.F.; Frery, A.C.; Sant'Anna, S.J.S. Stochastic Distributions and the Multiplicative Model: Relations, Properties, Estimators and Applications to SAR Images Analysis, Technical Report 5630-NTC/318, INPE, São José dos Campos, SP, Brazil,1995.

Li, C. Two Adaptive Filters for Speckle Reduction in SAR Images by Using the Variance Ratio, *International Journal of Remote Sensing,* vol. 9, No. 4, pp. 641-653, 1988.

Lopes, A.; Touzi, R. Adaptive Speckle Filtering for SAR Images, *International Geoscience and Remote Sensing Symposium (IGARSS'88),* pp. 1263-1266, 1988.

Kuan, D.T.; Sawchuck, A.A.; Strand, T.C.; Chavel, P. Adaptive Noise Smoothing Filter for Images with Signal–Dependent Noise, *IEEE Trans. on Pattern Analysis and Machine Intelligence*, Vol. 7, No.2, pp. 165-177, 1985.

Kuan, D.T.; Sawchuck, A.A.; Strand, T.C.; Chavel, P. Adaptive Restoration of Images with Speckle, *IEEE Trans. on Acoustics Speech and Signal Processing*, vol. 35, No.3, pp. 373-383, 1987.

Frost, V.; Stiles, J.A.; Shanmugan, K.S.; Holtzman, J.C. A Model for Radar Images and its Application to Adaptive Digital Filtering of Multiplicative Noise, *IEEE Trans. on Pattern Analysis and Machine Intelligence*, Vol. 4, No.2, pp. 157-166, 1982.

Frery, A.C.; Müller, H.J.; Yanasse, C.C.F.; Sant'Anna, S.J. A Model for Extremely Heterogeneous Clutter, *IEEE Trans. on Geoscience and Remote Sensing*, Vol.35, No.3, May 1997.

Hagg, W.; Sties, M. The EPOS Speckle Filter: A Comparison with Some Well-Known Speckle Reduction Techniques, *Proc. XVIII ISPRS Congress*, Comission II, Austria, July, 1996, pp.135-140.

Castleman, K.R. *Digital Image Processing*, Prentice-Hall, 1996.

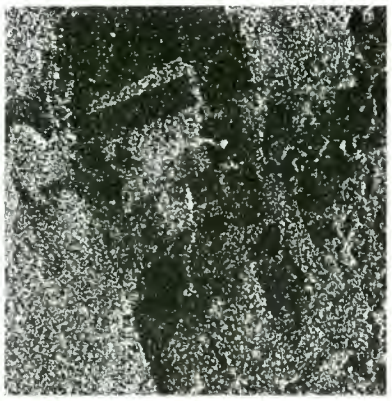

(1.a) ORIGINAL JERS-1 IMAGE

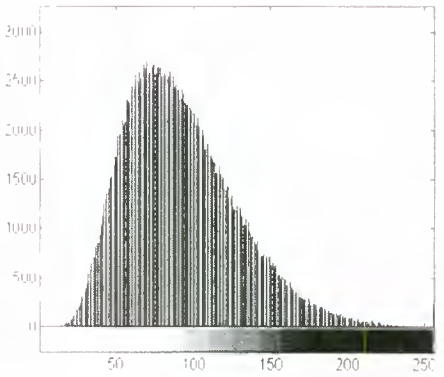


(1.b) ORIGINAL HISTOGRAM

(2.a) GAUSSIAN MAP FILTERED
(without k-means)

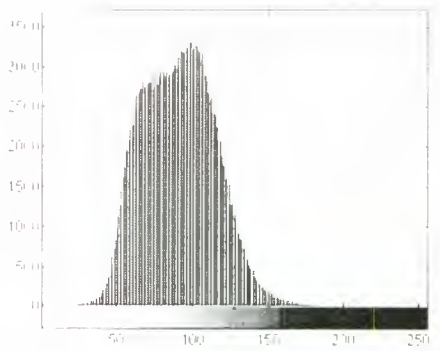

(2.b) GAUSSIAN MAP FILTERED HISTOGRAM
(without k-means)

(3.a) GAUSSIAN MAP FILTERED IMAGE
(with k-means)

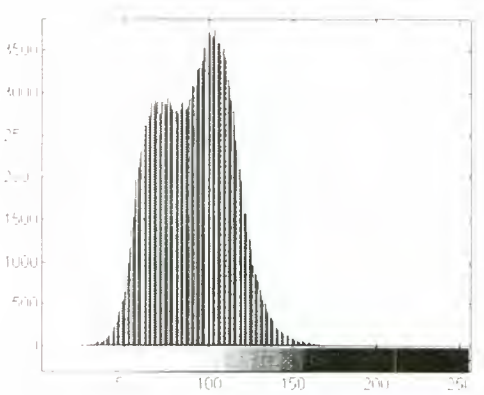


(3.b) GAUSSIAN MAP FILTERED IMAGE HISTOGRAM
(with k-means)

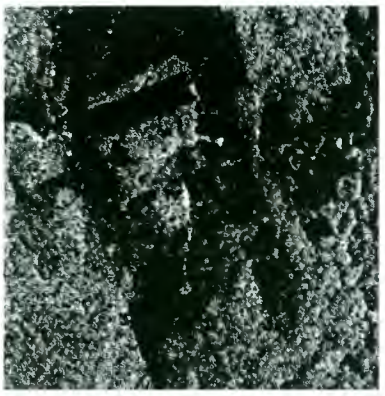

(4.a) GAMMA MAP FILTERED IMAGE
(without k-means)

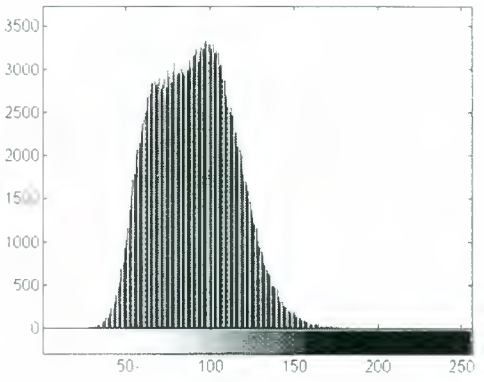


(4.b) GAMMA MAP FILTERED IMAGE HISTOGRAM
(without k-means)

(5.a) GAMMA MAP FILTERED IMAGE
(with k-means)

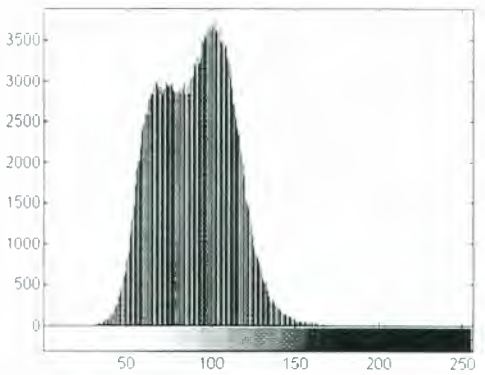


(5.b) GAMMA MAP FILTERED IMAGE HISTOGRAM
(with k-means)

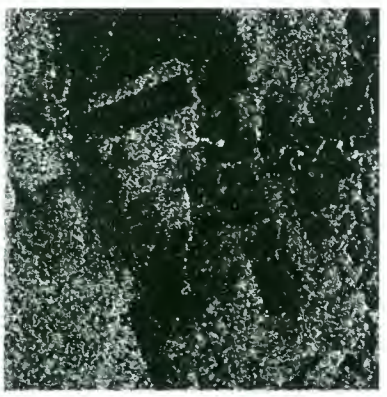

(6.a) EXPONENTIAL MAP FILTERED IMAGE
(without k-means)

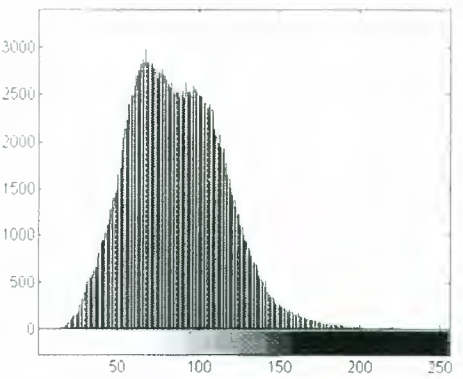


(6.b) EXPONENTIAL MAP FILTERED IMAGE HISTOGRAM
(without k-means)

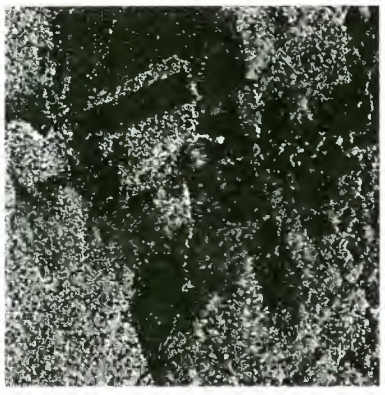

(7.a) EXPONENTIAL MAP FILTERED IMAGE
(with k-means)

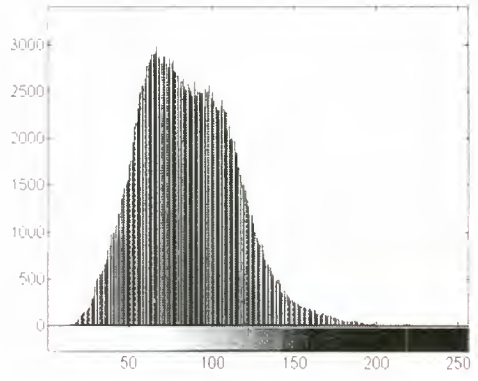


(7.b) EXPONENTIAL MAP FILTERED IMAGE HISTOGRAM
(with k-means)

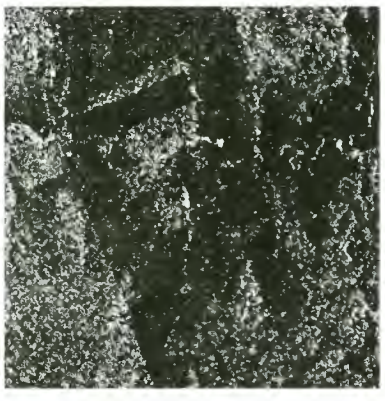

(8.a) CHI-SQUARE MAP FILTERED IMAGE
(without k-means)

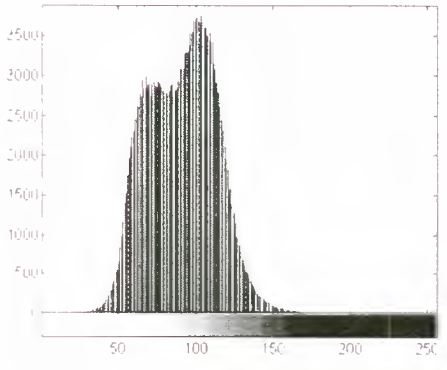


(8.b) CHI-SQUARE MAP FILTERED IMAGE HISTOGRAM
(without k-means)

(9.a) CHI-SQUARE MAP FILTERED IMAGE
(with k-means)

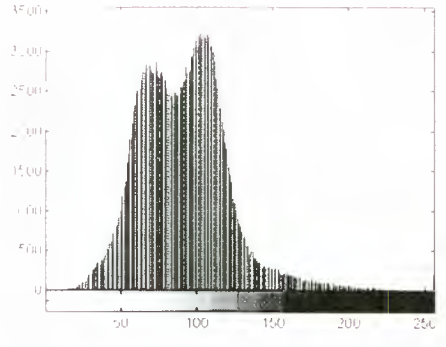


(9.b) CHI-SQUARE MAP FILTERED IMAGE HISTOGRAM
(with k-means)

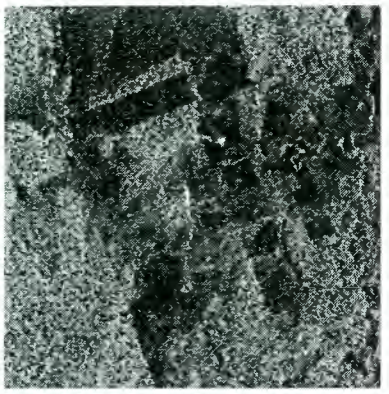

(10.a) RAYLEIGH MAP FILTERED IMAGE
(without k-means)

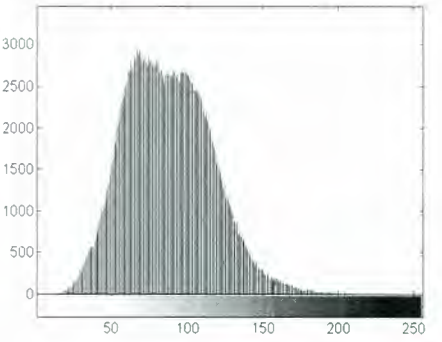


(10.b) RAYLEIGH MAP FILTERED IMAGE HISTOGRAM
(without k-means)

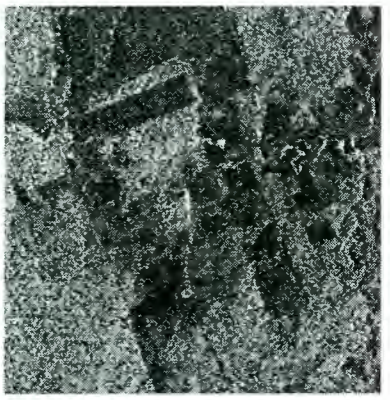

(11.a) RAYLEIGH MAP FILTERED IMAGE
(with k-means)

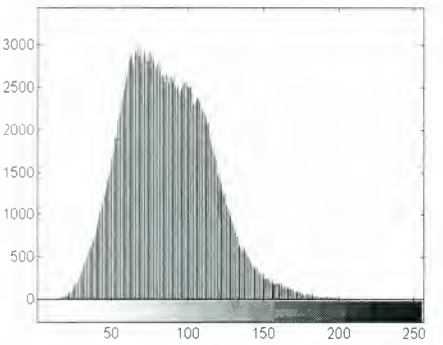


(11.b) RAYLEIGH MAP FILTERED IMAGE HISTOGRAM
(with k-means)

# PARTICLE FILTERING OF RADAR SIGNALS FOR NON-COOPERATING TARGET IMAGING

Marco Antonio Chamon[1]
Gérard Salut[2]

[1] INPE-Instituto Nacional de Pesquisas Espaciais
Caixa Postal 515, 12201-970 São José dos Campos, SP, Brasil
Phone: (+55) 12-345-6229
Fax: (+55) 12-345-6225
e-mail: chamon@dea.inpe.br

[2] LAAS- Laboratoire d'Analyse et d'Architecture des Systèmes
7, avenue du Colonel Roche, 31077 Toulouse Cedex 4, France
Phone: (+33) 5.61.33.62.93
Fax: (+33) 5.61.55.35.77
e-mail: salut@laas.laas.fr

**Abstract.** This paper describes the application of the optimal nonlinear/non-Gaussian filtering theory to the radar signal processing problem. This approach, made feasible by a new technique named *Particle Filtering*, may cope with nonlinear models as well as non-Gaussian dynamic and observation noises. The *Particle Filter* constructs the conditional probability of the state variables, with respect to the measurements, through a random exploration of the state space by particles, which obey the conditional probability generator. The application of this new filter to the inverse synthetic aperture radar (ISAR) technique allows the joint estimation of the path and the image of a maneuvering target in weak signal to noise ratio situations.

**Keywords:** Inverse Synthetic Aperture Radar, ISAR, Radar Imaging, Nonlinear Filtering, Particle Filtering.

## 1. Introduction

Nowadays, the synthetic aperture radar is the main technique adopted to image moving targets, like airplanes, with a ground radar. This technique, that exploits the relative motion between target and radar, is based on the coherent sum of a sequence of backscattered radar pulses, each pulse corresponding to a different angular position (attitude) of the target.

Usually, the image reconstruction of a fixed target by a moving radar is named synthetic aperture radar (SAR) while the symmetric case, i.e., imaging a moving target with a fixed radar, is called *inverse* SAR (ISAR). In both situations, the knowledge of the relative radar-target motion is essential to the imaging algorithm. In SAR problems, one normally knows the (nominal) trajectory of the on board radar and can use external information (such as an inertial navigation system) or some autofocusing technique to motion compensate the image data (Buckreuss, 1991; Moreira, 1989). Imaging a moving, non-cooperating target, where the path is *a priori* unknown or poorly determined, is a bit more involved. Specific trajectory estimation algorithms need to be developed to track maneuvering targets and compensate the radar signals. Once the trajectory is estimated, one can phase compensate the returned pulses and coherently sum them to exploit the imaging capability of synthetic aperture techniques.

Most of the actual ISAR algorithms utilizes this approach, i.e., some kind of data preprocessing is done to ensure separability between tracking and imaging problems. The main difficulty with this approach is the need of a stable strong scatterer on the target that can be tracked as a reference point. In a complex target, such a reference point can disappear during the observation time or jump abruptly from one strong point to another.

The new method proposed in this paper, based on nonlinear filtering theory, allows simultaneous radar tracking and imaging of a complex non-cooperating target. This technique can integrate the extended nature of the target in the tracking algorithm and needs no isolated strong scatterer as a reference.

The organization of the paper is as follow. In section 2, we develop the models for target movement, target electromagnetic response and radar measurements which are needed to state the radar signal processing as a filtering problem. Particle Filtering is introduced in section 3. Tracking and imaging are then considered in Section 4 using the models and the algorithm described in sections 2 and 3. In section 5 we present some simulation results and the conclusion is drawn in section 6.

## 2. Modeling

### 2.1- The Spatial Target Model

Most imaging algorithms use (sometimes implicitly) the so-called "weak scatterer" approximation to represent

the target to be imaged (Chassay, 1983; Borden, 1994). In this approximation, the target is equivalent to a set of point-like scatterers and the backscattered electrical field $\mathbf{E}_{scat}$ is the superposition of each individual scatterer response to the incident electrical field. Interaction among scatterers, multipath, shadow effects and diffraction are disregarded. Moreover, the backscatter coefficients $\sigma_i$ are assumed to be isotropic (invariant for small changes of target attitude during the considered portion of flight). That is the simplest geometrical optics model for the backscattering phenomenon.

With these assumptions, the target can be modeled by a grid of N elementary scatterers with backscatter coefficients $\sigma_i$:

$$T(\bar{x}) = \sum_{i=1}^{N} \sigma_i \delta(\bar{x} - \bar{x}_i) \qquad (2.1)$$

where $\delta(\cdot)$ is the Dirac measure, $\sigma_i$ is a complex constant and $\mathbf{x}_i$ is the position of the scatterer. Complex coefficients $\sigma_i$ indicate local amplitude and phase of the backscatter field.

More sophisticated models can be envisaged to take into account scattering perturbation effects, that are frequency- (f) and target attitude- ($\theta$) dependent. In this paper we shall consider a narrow band signal, and dependency with respect to $\theta$ along the portion of target movement may appear as a random drift with suitable characteristics. Despite these simplifications, the model accounts for important phenomena found in radar signal processing, such as glint, and constitutes a basic approximation for the radar imaging problem.

### 2.2- Coherent Radar Signal

Consider that the transmitted signal is given by

$$s(t) = h(t)\Re e\{\exp(j\omega_0 t + \varphi_0)\} \qquad (2.2)$$

where $f_0 = \omega_0/2\pi$ is the carrier frequency, h(t) is the signal envelope and $\varphi_0$ is the phase of the transmitted signal. If the target is modeled by the equation 2.1, the amplitude of the scattered field can be written as

$$Y(t) = \sum_i \frac{K}{R_i^2} G(\theta_i) h(t - \tau_i) \sigma_i \exp[j\omega_0 (t - \tau_i) + j\varphi_0] \qquad (2.3)$$

with $\tau_i = 2R_i/c$ the signal delay for the scatterer located at a distance $R_i$ to the radar, $G(\theta_i)$ the antenna gain in the direction $\theta_i$ and $1/R_i^2$ the free space attenuation of the signal amplitude. After carrier suppression by complex demodulation one gets:

$$Y(t) = \sum_i \frac{K_i}{R_i^2} h(t - \frac{2R_i}{c}) \sigma(R_i, \theta_i) \exp\left[-j\frac{4\pi}{\lambda} R_i\right] \qquad (2.4)$$

with $K_i = KG(\theta_i)\exp(j\varphi_0)$.

For a rigid target, we can consider an arbitrary reference point $(R_0, \theta)$ and describe the scatterers distribution in a target coordinate system (**figure 2.1**). Therefore, a target point i= (x,y) can be represented by

$$R_i = R(x,y) = R_0 + x \cdot \sin\theta + y \cdot \cos\theta$$

under the assumption that target span is much smaller than $R_0$. That is the plane wave far-field approximation. For sake of simplicity we don't indicate the time dependency of $R_0$ and $\theta$.

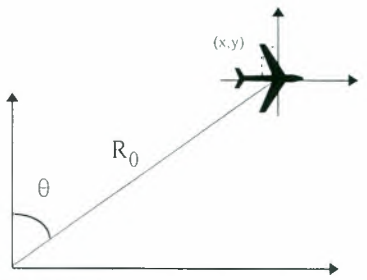


Fig. 2.1- Relation between radar and target coordinate systems.

Now, equation 2.4 can be rewritten as

$$Y(t) = \sum \frac{K_i}{R_i^2} h(t - \frac{2[R_0 + x.\sin\theta + y.\cos\theta]}{c}) \sigma(x,y) \exp(-j\frac{4\pi}{\lambda}[R_0 + x.\sin\theta + y.\cos\theta]) \qquad (2.5)$$

Moreover, a noise $v(t)$ adds to this returned signal. With the usual assumptions on the matched input filter and optimal sampling, this noise can be modeled as a complex white Gaussian process with zero mean and variance $E(vv^*) = R$, where $v^*$ indicates the transpose complex conjugate of $v$.

Note that distance variations among different scatterers i= (x,y) are mainly important at signal phase level, with little impact on signal amplitude. We can therefore simplify the equation above by neglecting amplitude fluctuation due to the term $K_i/R_i^2$ and approximate it by $K_0/R_0^2$, where $K_0 = G(\theta_0).\exp(j\varphi_0)$. At this stage $K_0$ appears as a single phase/amplitude reference, which may be discarded by immersion into $\sigma(x,y)$ when necessary.

Equation 2.5 allows us to retrieve several classical radar imaging formulations, as tomographic reconstruction and Fourier transform techniques (Mensa, 1991). All these techniques suppose an *a priori* knowledge of target path, i.e., of $R_0$ and $\theta$ as a function of time. For non-cooperating targets, trajectory must be accurately estimated (with relative variations not exceeding a fraction of wavelength) before image formation. Next section presents some popular methods

for separate target motion estimation, before we introduce the joint tracking/imaging procedure.

### 2.3- Motion Compensation

Synthetic aperture formation depends on a coherent sum of successive pulses backscattered by an uniform rotating target, placed at a constant distance of radar. Therefore, some kind of motion compensation is necessary if the target trajectory departs from this simple scheme. Motion compensation is normally divided into two steps: range bin alignment and phase compensation.

Range bin misalignment is due to radial motion of the target. Scatterers travel several range bins during the observation time, so that signals in a specific bin correspond to different scatterers. A correction step is needed to keep the scatterers in their initial range bins. To cope with the range misalignment problem, most algorithms use the correlation between adjacent returned pulses, as is done by the Spatial Domain Realignment and Frequency Domain Realignment algorithms proposed in (Chen and Andrews, 1980) or by the synthetic reference envelope algorithm proposed in (Delisle and Wu, 1994).

Concerning transversal motion, the target induces two kinds of phase variation: motion of the target center along radar line-of-sight, and rotation relative to the target center as viewed from the radar. Only the target rotation creates cross-range resolution (differential Doppler) and a phase compensation algorithm is required to eliminate the translational motion effect.

Most compensation techniques propose to track a strong, steady scatterer on the target that can be used as a reference point for the target path. This reference point may correspond to an isolated scatterer, like a wing tip, that represents a peak in the signal return. One can also track the range bin where the normalized variance of the returned signal amplitude is minimal. This range bin is supposed to contain a strong scatterer, called dominant scatterer (Steinberg, 1988), that gives a reference for the phase compensation.

#### 2.3.1- Motion Model

None of the above techniques can be applied at low signal-to-noise ratio (track before detect), or with no dominant scatterer. We propose here a global nonlinear filtering approach to process the radar signals for simultaneous detection, tracking and imaging of complex targets.

To apply stochastic filtering techniques we need to model the motion as a dynamic random process and its measurements by the radar. This approach, which is embedded in usual radar tracking in a linear filtering stage, is considerably more sophisticated in nonlinear tracking, such as proposed in this paper.

Linear algorithms are used for smoothing models of target motion, with Gaussian assumptions for the driving process. The Singer model (Singer, 70) is the simplest of them for the tracking of maneuvering targets. It is a modified triple integrator system where the motion are considered independent in each Cartesian axis and driven by a correlated Gaussian acceleration. We use here (**figure 2.2**) a more realistic version of this model, where acceleration and speed are physically limited and maneuvers decisions are represented by a random point process.

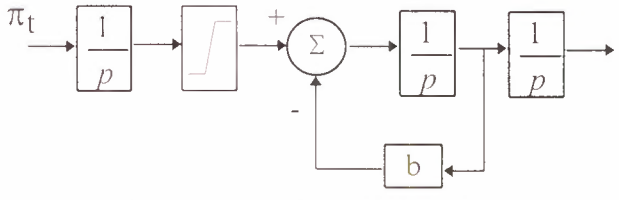


Fig. 2.2 - Modified Singer model.

The system is driven by the doubly stochastic process $\pi_t$ that adds random jumps to the acceleration to represent realistic maneuver controls. These maneuvers follow a Poisson process with mean time $T_m$ between jumps. Their amplitude is normally distributed with variance $\sigma_0^2$. Actual control is limited by saturation to take into account physical constraints on target thrust and maneuvering capabilities.

## 3. The Particle Filter

Nonlinear filtering is the natural frame to state global estimation problems where a dynamic stochastic process (here the target motion) is partially observed (by a nonlinear measuring device - the radar) and corrupted by an additive stochastic process (the noise). The difficulty with nonlinear filtering formulation comes from the infinite dimensional character of the solution, which can not be derived in closed form. Approximate solutions based on local linearisation of system and measuring equations and/or moment truncation of density probability can not maintain guaranteed performance or even stability of the filter.

The particle filtering technique (Rigal, 1993; Noyer, 1996) may cope with nonlinear models as well as non-Gaussian dynamic and observation noises. It recursively constructs the conditional probability measure $dP(x_t \mid y_0^t)$ of the state variables $x_t$, with respect to all available measurements $y_0^t$, through a random exploration of the state space by entities called particles. Particles obey the conditional probability generator which involves a Bayes correction term based on measurements. Its main advantage relies on probabilistic properties of the procedure, which lead to global convergence.

Particle filtering works in a evolution/correction basis dictated by the system equations. Each particle

simulates an admissible trajectory (candidate) of the state variables followed by a correction step due to measurements. As the number of particles increases, the particle filter converges to the optimal state estimator. Uniform convergence has been shown for one of the versions of the algorithm in (Del Moral and Salut, 1995).

### 3.1- Particle Filter Algorithm

Let the following equations represent a discrete dynamic system X with Y as a measurement:

$$\begin{cases} X_{k+1} = f(X_k, k, \pi_{k+1}), \ X_0 \text{ initial condition} \\ Y_k = h(X_k, k) + \nu_k \end{cases} \quad (3.1)$$

where $\pi_k$ and $\nu_k$ are independent white noises with known probability distributions.

Particle filtering approximates the probability $dP(x_0)$ at initial time by a set of *N* Dirac distributions and applies the dynamic of the system to this set. In other words, one "randomly selects N particles" from the probability distribution $dP(x_0)$ to represent it as:

$$dP(x_0) \approx \frac{1}{N} \sum_{i=1}^{N} \delta(x_0 - x_0^i) \quad (3.2)$$

where $\delta$ is the Dirac delta.

Next, each particle i follows the system dynamic $f(x_0^i, 0, \pi_0^i)$ with noise samples $\pi_0^i$ generated from its a priori probability. Time evolution of Dirac point measures is given by sequential application of this procedure. **Figure 3.1** shows the evolution of a set of particles. Dot lines represent the trajectory of each particle.

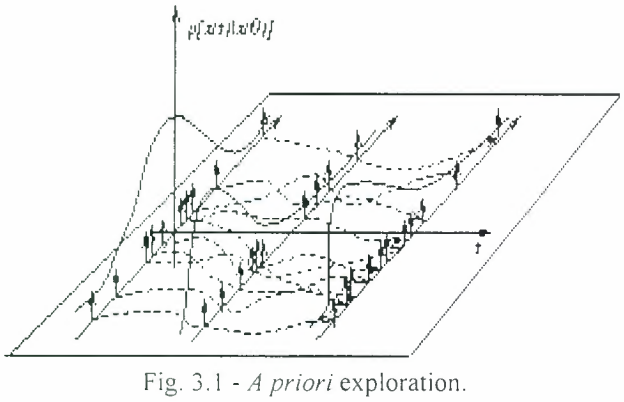

Fig. 3.1 - *A priori* exploration.

Next step is to introduce information carried by the measure $y_0^k$. This is done by the term $p(y|x_t)$ in the Bayes's theorem. Information given by measure $y_k$ "weights" the trajectory of each particle i. The particle estimation (with *N* particles) of any measurable function $\varphi(\cdot)$ of the state $X_k$ is given by:

$$\hat{\varphi}^N(X_k) = \sum_{i=1}^{N} p_k^i \varphi(x_k^i),$$

$$\text{with } p_k^i = \frac{Z_k^i}{\sum_{j=1}^{N} Z_k^j} \text{ and } Z_k^i = \prod_{\tau=1}^{k} p(y_\tau | x_\tau^i) \quad (3.3)$$

Therefore the "weight" $p_k^i$ corrects the representation given in **figure 3.1**, where all particles had the same weight 1/N. The particle estimation of the conditional probability is showed in the **figure 3.2**. Here, dot lines give the trajectories and the arrows' amplitude represents the weight of each particle.

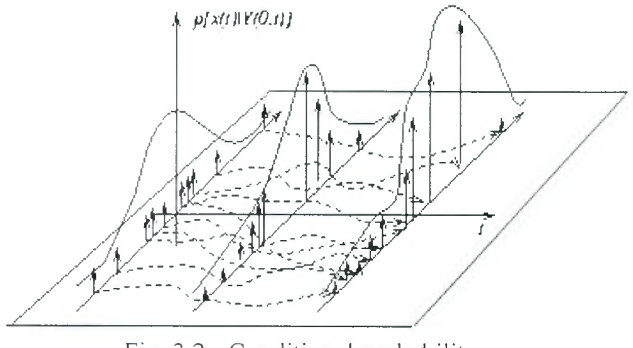

Fig. 3.2 - Conditional probability.

### 3.2- Regularisation Techniques

If the state space is unbounded (as is the case for target positions), particle trajectories diverge. Furthermore, in the absence of regularisation, particle weights degenerate and the law of large numbers is no more applicable. This second phenomenon is due to the finite number of particles *N* used in the algorithm. To cope with this, some kind of regularisation must be applied. A possible technique, in the first case, is the forgetting of old data, frequently used to adapt filter parameters to unknown system's evolution or poor modeling.

We use here a resampling technique that solves both difficulties at the same time. The algorithm is restarted at an instant t using the estimated conditional probability as an initial distribution. All particles are redistributed among the states $x_t^i$ according to the weight attributed to them. All particles take the same weight 1/N after the redistribution.

Therefore, most probable states, corresponding to "heavy" particles, give rise to several new particles while least probable ones are "killed". Redistribution locates particles where they are needed, in a probabilistic way.

### 4. Tracking / Imaging Particle Algorithm

As indicated in section 2.3, synthetic aperture imaging can be applied if the target trajectory is a priori known. In this case one can compensate the translation motion and just keep the rotational motion about a reference

point, that induces differential Doppler, to obtain cross-range resolution.

Classical imaging techniques usually estimate target trajectory *before* imaging. As target motion/image estimation from radar measurements is a nonlinear operation, such a separation approach is not optimal, as can be noticed in practice when glint is present in radar data.

Particle filtering can be applied to jointly estimate motion and image, using optimally the available information. Glint and other interference effects are eliminated or greatly reduced by modeling and processing a multi-scatterer target that take into account the extended nature of the target.

### 4.1- Image Formation

As one can see in equation (2.5), measurements Y(t) are linearly related to backscatter coefficients σ(x,y), for a given target trajectory. Sampling of Y(t) results into a data vector where each sample corresponds to a range bin, with radial resolution c/2B (c - light speed; B - receiver bandwidth).

Time discretisation gives a nonlinear system of equations

$$Y(t) = H_t(x,y)D_t(e^{-j\phi})\sigma \qquad (4.1)$$

where each line of matrix H corresponds to the amplitude of the scatterers in a range bin and D is a diagonal matrix with phase terms $\exp[-j\Phi(x,y)]$, $\Phi(x,y)= (4\pi/\lambda)R(x,y)$.

As previously mentioned, this structure of radar signal allows to compute σ(x,y) as a linear estimation conditionally to the trajectory $R_t$. Consequently, each particle i in the algorithm is associated to:

- an estimated trajectory, according to the motion model of the target;
- a grid of points (x,y), moving with the particle and representing the target's reflectivity model;
- a linear estimator of the target image $\sigma_t(x,y)$ for the grid points;
- a probabilistic "weight", given by the Bayes correction.

#### 4.1.1- Conditional Linear Filter

Consider a grid of points (x,y) whose center follows a given trajectory $R_t$. Along this trajectory, the radar imaging reconstruction can be viewed as the solution of the following filtering problem (Chamon, 1996):

$$\begin{cases} \sigma_{t+1} = \sigma_t & \sigma_0 \approx N(0, P_0) \\ Y_t = H_t(x,y)D_t(e^{-j\phi})\sigma_t(x,y) + v_t \end{cases} \qquad (4.2)$$

The image $\hat{\sigma}(x,y)$ is given by the following regularized pseudo-inverse:

$$\begin{cases} \hat{\sigma}_{t+1} = P_{t+1}\left(\sum_{\tau=0}^{t+1} D_\tau^* H_\tau^* R^{-1} Y_\tau\right) \\ P_{t+1}^{-1} = P_0^{-1} + \sum_{\tau=0}^{t+1} D_\tau^* H_\tau^* R^{-1} H_\tau D_\tau \end{cases} \qquad (4.3)$$

where A* is the transpose conjugate of A and R= E(vv*) is the noise covariance matrix. For a uniform array of N antennas this solution generalizes in a straightforward way to

$$\hat{\sigma}_t = \left(\sum_\tau D_0^* H_0^* H_0 D_0 + \frac{rP_0^{-1}}{N}\right)^{-1} \sum_\tau D_0^* H_0^* \frac{\sum_{n=0}^{N-1} Y_n e^{-jn\phi}}{N} \qquad (4.4)$$

Here time dependence τ is not indicated, $H_0D_0$ represents the first antenna in the array and R= rI is the noise covariance, with I the identity matrix. The term $\phi_n$, that represents the phase delay to the n-th antenna, can be written in terms of the phase of first antenna as $\phi_n = \phi_0 - (2\pi d/\lambda).n.\sin\theta$, where *d* is the inter-element spacing in the array and θ is the direction of signal arrival.

This result shows that σ estimation is obtained by coherent summation of data both in space (sum over N antennas) and in time (time variation of H, D and ϕ). Phase equalization of data over the array (the term $Y_n e^{-jn\phi}$) just points the antenna diagram to the target.

### 4.2- Motion Estimation

Motion estimation is accomplished by the particle filter that uses the image reconstructed by the conditional filter to calculate the likelihood (or equivalently the "weight") of each particle trajectory in state space. We can note that target image and trajectory are jointly estimated by the filter: a "good" image indicates a "good" trajectory and conversely, a "good" trajectory yields an accurate image. The particle algorithm is schematically described in **figure 4.1**.

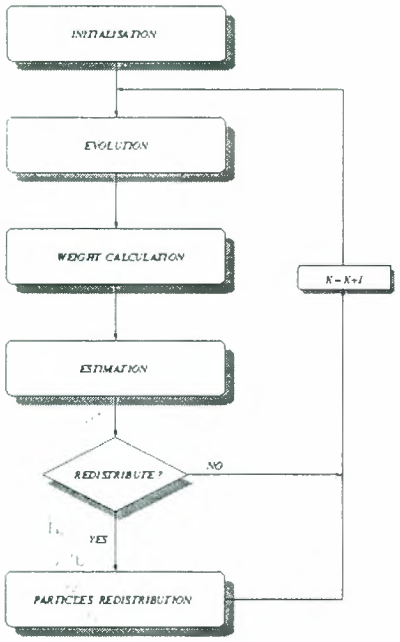


Fig. 4.1 - The particle algorithm.

## 5. Simulation Results

We presents in this section simulation results for the extended target indicated in **figure 5.1**. It represents the signal reflected by 10000 elementary scatterers with unity amplitude and random distributed phases.

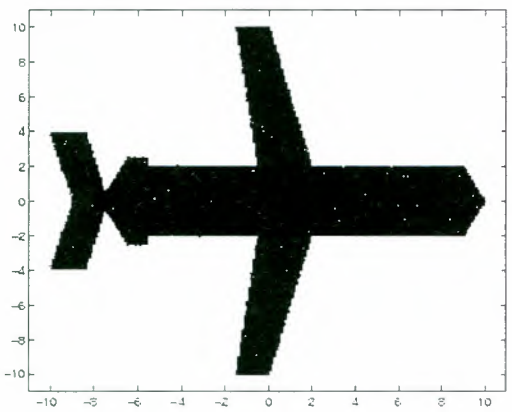

Figure 5.1- Target model used in simulations

The following parameters was used in the simulation:

a) Radar characteristics

| | |
|---|---|
| Frequency | 10 GHz |
| Pulse Duration | 6.7 ns (1 m resolution) |
| Pulse Repetition Interval | 0.2 ms |
| Antenna Array | Two omni antennas with spacing d= 50 λ/2 (20 mrad beamwidth) |
| Signal to Noise Ratio | 0 dB |
| Integration Time | 3 s |

b) Trajectory characteristics

| Parameter | Nominal Value | Initial Uncertainty |
|---|---|---|
| angular position | 0 rad | +/- 1 mrad |
| distance | 10000 m | +/- 5 m |
| velocity (angular direction) | 250 m/s | +/- 20 m/s |
| velocity (radial direction) | -20 m/s | +/- 5m/s |

### 5.1- Radar Imaging with Known Trajectory

For a perfectly known trajectory, we show in the **figure 5.2** the result of the radar signal processed by the conditional filter. In the **figure 5.2a** we see the output amplitude for each point of the grid (x,y) that represents the target (note that the number of points in the grid is much smaller than that of the simulated target). **Figure 5.2b** shows the same data interpolated for a finer grid.

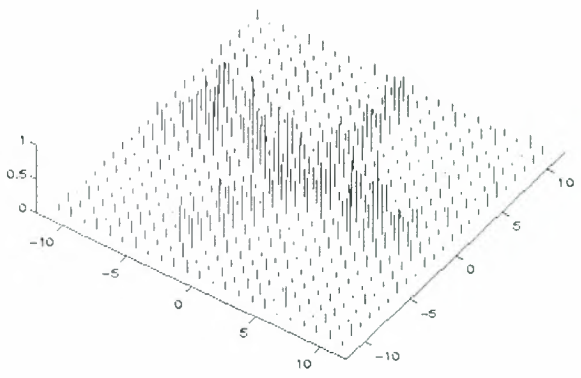

(a)

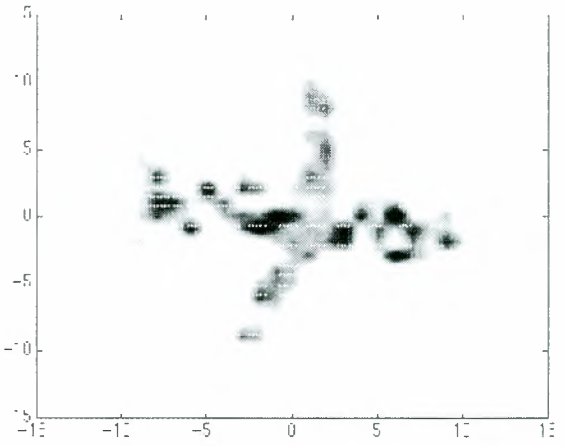

(b)

Figure 5.2- Image results with a known trajectory.
a) Filter output. b) Interpolated image.

### 5.2- Radar Imaging of a Non-Cooperating Target

When the trajectory and the target backscatter coefficients $\sigma_i$ are jointly estimated by the particle filter, we get the image indicated in **figure 5.3** below. The result, if compared with the images in **figure 5.2**, is necessarily less precise but we note that the regions of strong reflectivity are suitably estimated and the target's general shape is reconstructed.

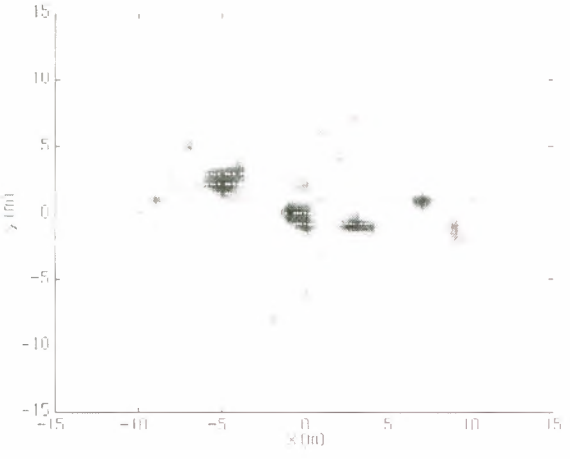


Figure 5.3- Image result with an estimated trajectory.

### 6. Conclusion

We have developed a new approach to filter radar signals and jointly estimate the path and the image of a maneuvering target. The proposed filter allows the processing of nonlinear/non-Gaussian models for target dynamics and represents an asymptotic approximation of the optimal solution for the general nonlinear filtering problem. Images obtained with this technique faithfully reconstruct the path and the general shape of the target. It's worthwhile to note that the same algorithm can be applied for trajectory estimation only of a complex target, filtering out glint and other scintillation phenomena. In this case, a coarse grid, representing just some strong scatterers, can be used in the target model, as detailed image is no longer required.

Because particle filtering makes use of a random exploration of the state space, computational cost is a main concern. In fact, each particle needs to calculate the pseudo-inverse of a huge matrix (associated to the grid that represents the target) to evaluate the "weight" of its trajectory. As particles evolve in a independent way, communicating only for redistribution and likelihood normalization, a parallel version of the algorithm is a current subject of interest to speed up the image estimation. Moreover, we may consider adaptive features, where the grid is refined as the trajectory is more precisely estimated.

### References


Borden, B. Problems in Airborne Radar Target Recognition. *Inverse Problems*, 10:1009-1022, 1994.

Buckreuss, S. Motion Errors in an Airborne Synthetic Aperture Radar System. *ETT Journal*, 2(6):655-664, 1991.

Chamon, M.A. *Filtrage particulaire et ouverture synthétique inverse sur cibles radar non-coopératives*. Thèse de doctorat, Ecole Nationale Supérieure de l'Aéronautique et de l'Espace, Toulouse, 1996.

Chassay, G. Justification du modèle des points brillants. Intégration dans le modèle des intéractions entre les différentes parties d'une cible. In: IX Colloque sur le Traitement du Signal et ses Applications, Nice, mai 1983.

Chen, C.C. & Andrews, H.C. Target-motion-induced Radar Imaging. *IEEE Transactions on Aerospace and Electronic Systems*, AES-16(1):2-14, jan. 1980.

Delisle, G.Y. & Wu, H. Moving Target Imaging and Trajectory Computation Using ISAR. *IEEE Transactions on Aerospace and Electronic Systems*, AES-30(3):887-899, jul. 1994.

Del Moral, P & Salut, G. Filtrage non-linéaire : résolution particulaire à la Monte Carlo. *C.R. Acad. Sci.*, 320(I):1147-1152, Paris, 1995.

Mensa, D.L. *High Resolution Radar Cross-Section Imaging*. Artech House, London, 1991.

Moreira, J.R. A New Method of Aircraft Motion Error Extraction from Radar Raw Data for Real Time SAR Motion Compensation. In: IGARSS Symposium, Vancouver, 1989.

Noyer, J.C. *Traitement non-linéaire du signal radar par filtrage particulaire*. Thèse de doctorat, Université Paul Sabatier, Toulouse, 1996.

Rigal, G. *Filtrage non-linéaire, résolution particulaire et applications au traitement du signal*. Thèse de doctorat, Université Paul Sabatier, Toulouse, 1993.

Singer, R.A. Estimating Optimal Tracking Filter Performance for Manned Maneuvering Targets. *IEEE Transactions on Aerospace and Electronic Systems*, AES-6(4):473-483, jul. 1970.

Steinberg, B.D. Microwave Imaging of Aircraft. *Proceedings of IEEE*, 76(12):1578-1592, dec. 1988.

# Target Recognition using Constructive Neural Networks

E. C. Vargas, H. C. Sousa, A. C. P. L. F. Carvalho

Computational Intelligence Laboratory
University of São Paulo
Caixa Postal 668, So Carlos, SP, Brazil

## ABSTRACT

This paper presents the use of Constructive Neural Networks for Patterns Recognition. The work presented here is part of the SAPRI project (System for Acquisition, Processing and Images Recognition) which is being developed for the Brazilian Navy. The objective of this paper is to investigate the behavior of Constructive Neural Networks in image recognition tasks, specially with images from the SAPRI project. Constructive Neural Networks differ from standard networks due to their ability to change their own number of elements, adding or removing units and connections. Four constructive algorithms are presented in this paper: Cascade Correlation, Tower, Pyramid and Upstart.

Keywords: Pattern Recognition, Neural Networks.

## 1 Introduction

This work is part of the development of a System for Acquisition, Processing and Recognition of Images (SAPRI, 1997). This system will be directed to radar images handling, providing the specification of an environment to help the safety of navigation and control of air and sea traffic. The main goal of the SAPRI project is to develop a image processing system which, based in advanced computational methods, is able to support the handling process and the radar images interpretation. The SAPRI project consists of 4 modules which include the steps of acquisition, image processing, pattern recognition and interpretation.

Although conventional Neural Networks have achieved adequate performance in pattern recognition tasks, this performance is directly influenced to the choice of the network topology. There are four approaches (Parekh et al., 1997) to define a Neural Network topology. The Empiric approach consists in testing and comparing several topologies until an acceptable performance is reached. The Genetic approach generates several variations of networks and combine the features of those with the best performance, thus generating new networks with improved performances. The third approach, known as Pruning, optimizes a trained network by removing neurons and connections which are irrelevant or redundant. Finally, the fourth approach is the Constructive. In this case, the network starts its training with a minimal topology and, according to the problem necessity, new neurons and connection are inserted, improving the network performance.

The work presented in this paper aims to support the pattern recognition module investigating the behavior of Constructive Neural Networks. These networks had adapted the perceptron networks to allow the incorporation of new elements during the training phase. Thus, a network with a minimal topology is trained and it grows according to the application's necessity.

Section 2 introduces the concept of target recognition, and Section 3 presents the description of four training algorithms for Constructive Neural Networks. Practical experiments were done using the data set provided by the SAPRI project. These experiments are presented in Section 4. Finally in Section 5, the conclusions are presented.

## 2 Target Recognition as Patterns

Automatic target recognition (ATR) refers to the task of identifying and classifying targets. The execution of this task depends on four distinct steps. The first step is the choice of the method used to capture the image, or the most appropriate sensor to be used in the problem at issue. The quality of the information

generated by the sensor and its fidelity to the image, are of great importance to assure the adequate performance of the next steps. The image capture must be standardized, thus no relevant characteristic of the problem goes unnoticed.

The second step is the pre-processing and segmentation of the received information. The pre-processing is necessary to dampen the noise and to eliminate incorrect information in the image. The goal of segmentation is to separate targets that may be connected to each other in their capture.

Next step is the Features Extraction and Selection, where the targets' relevant information is detected. At the end of these steps, a more compact data set is obtained. These steps are necessary to avoid waste of processing by analyzing unnecessary information.

Finally, the Classification associates each pattern generated by the previous steps to a class. This phase is the most important to the system, since an error can become a major problem in real applications.

In the SAPRI project, vessels' images were captured from a radar, and organized in four classes. Figure 1 presents an example of each class.

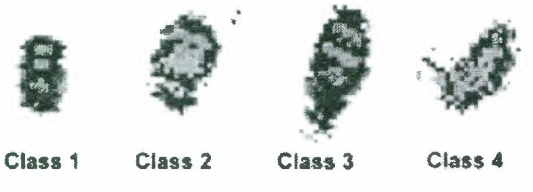


Figure 1: Vessels images after the pre-processing.

# 3 Constructive Neural Networks (CNN)

Artificial Neural Networks (ANNs) have achieved a good performance when applied to patterns classification. However, the topology of a conventional ANN, like Multilayer Perceptron (Freeman & Skapura, 1993), must be chosen before the beginning of its training. There are no rules to determine the network topology, hence, its choice depends basically on empiric knowledge. Therefore, several topologies must be trained and compared before the choice of a ultimate topology. This disadvantage of conventional ANN models becomes more apparent if, after the choice of the best topology, the patterns set is changed, making a new choice of the topology necessary to retrain the network.

Constructive Neural Networks provide an attractive approach for the gradual construction of Neural Networks. The network starts with a minimal topology consisting of input and output layers only. Each of these layers has the exact number of neurons necessary to map the issued problem. During the training phase, the network changes its topology by inserting or removing elements, thus avoiding the necessity of choosing the topology empirically.

The increase of elements in the networks is controlled by the training algorithm used. Four constructive algorithms were analysed in this work. They are detailed in Sections 3.1, 3.2, 3.3 and 3.4.

## 3.1 Cascade Correlation

The Cascade Correlation algorithm (Fahlman & Lebiere, 1991) uses a supervised learning technique to train ANNs. This algorithm starts with a minimal network (input and output layers only) and, during its training, inserts new units, one at a time, creating a multilayer structure.

The new neuron is connected to the input, output, and all hidden layer in the network. When the hidden unit is inserted, the weights related to its inputs (connections) are frozen. This neuron starts to permanently act on the network operations, being used to detect new features in the patterns set.

The unit to be inserted in the network can be selected in a candidates set organized in a layer. This candidates layer is connected to the input layer and all hidden layers in the network, but it is not connected to the output layer, since the candidates must not directly influence the network result. The selection criteria for a candidate is the correlation between this candidate's activation with the network output error. The higher the correlation, the larger the influence this candidate will have in the network performance. Hence, the weights of the connections between the candidates and the input and hidden layers must be changed in such a way to maximize the candidates correlation. The candidate with the highest correlation value will be included in the network as a new hidden layer, being connected to all layers in the networks, as shown in Figure 2.

Among the advantages of the Cascade Correlation networks, one can mention its training speed, which can be flexible depending on the number of new hidden units inserted. The training of these networks can be more clearly observed in the Figures 3, 4, and 5, where a network grows from a minimal topology to a cascade shaped topology.

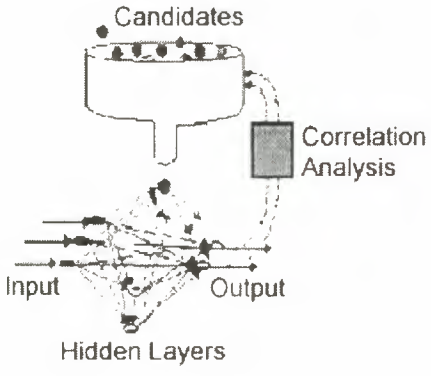


Figure 2: Selection of a new unit among a set of candidates.

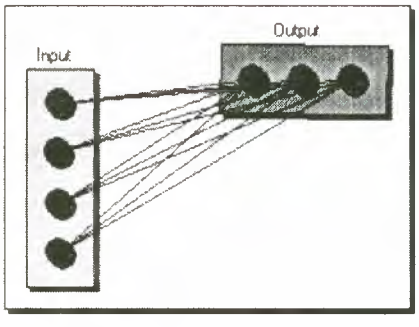


Figure 3: Selection of a new unit among a set of candidates.

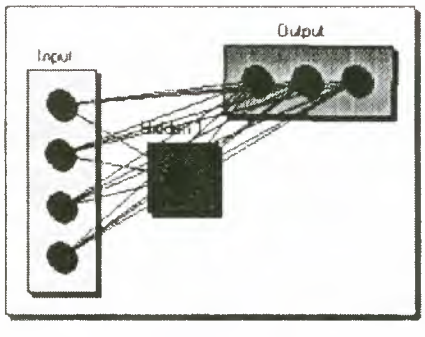


Figure 4: Selection of a new unit among a set of candidates.

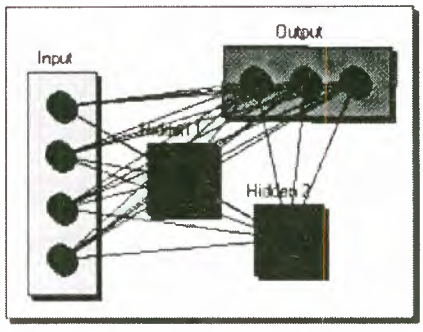


Figure 5: Selection of a new unit among a set of candidates.

### 3.2 Tower

The Tower algorithm (Parekh et al., 1997) builds a tower of perceptron units, also known as Threshold Logic Units (TLUs). Different from the Cascade Correlation algorithm, which inserts one unit at a time, this algorithm inserts a layer with a fixed number of neurons.

The new inserted layer has the same number of neurons as the output layer, and it is connected to the input layer and to the output layer. The output layer becomes a hidden layer, and the inserted layer becomes the new output layer. This procedure is repeated until the classification accuracy is reached or the maximum number of layer is reached. The Figures 6, 7, and 8 illustrate the insertion process.

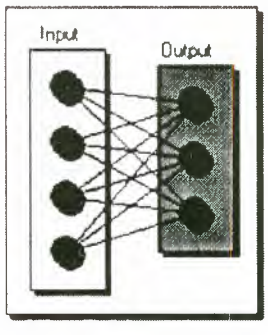


Figure 6: Initial state of the Tower network.

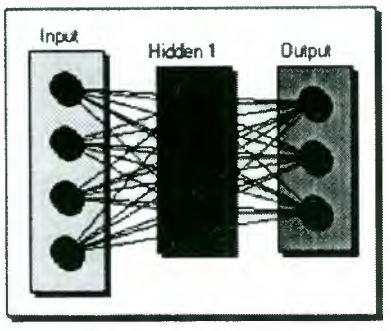


Figure 7: Insertion of a new layer, the output layer becomes a hidden layer.

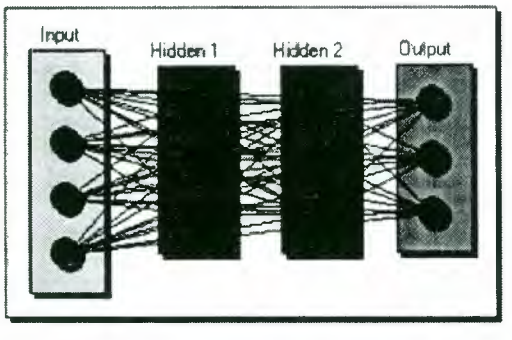


Figure 8: Insertion of a second layer, once again, the output layer becomes a hidden layer.

### 3.3 Pyramid

The Pyramid algorithm (Parekh et al., 1997) is an extension of the Tower algorithm. This algorithm differs from the Tower only in the way the connections between the new layer and the network are made. The inserted layer is connected to the input and output layers as in the Tower algorithm, but it is also connected to every hidden layer within the network, making the network units totally interconnected to each other. Figure 9 presents a trained network with two hidden layers. Notice that the layer Hidden 1 is connected to the new output layer, different from the Tower algorithm.

### 3.4 Upstart

The Upstart algorithm (Frean, 1990) inserts neurons in pairs (units X and Y), building a sturcture with the shape of a binary tree starting from a neuron from the output layer. Each pair of neurons is inserted to correct the error of the unit which it is connected to. Once trained, the new neurons allow the insertion of new pairs of neurons, until the network presents an acceptable error. Figures 10 and 11 ilustrate this algorithm.

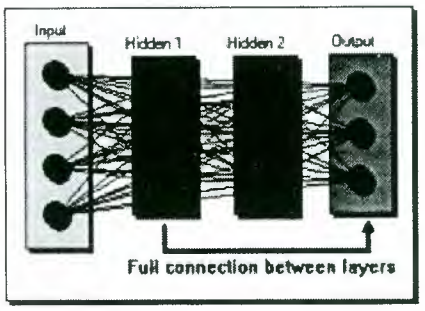


Figure 9: Pyramid network. The arrow idicates the connection between the layer Hidden 1 and the output layer.

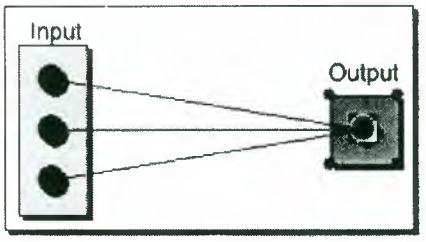


Figure 10: Initial state of the Upstart network with a single output neuron.

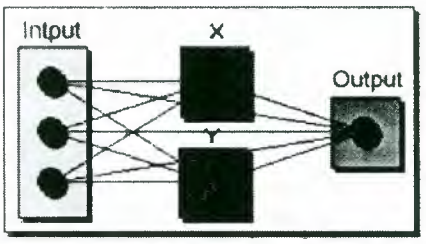


Figure 11: Upstart network after the insertion of the X and Y units.

At the end of its training, the resultant network might be too deep, i.e., with a large number of hidden units. Another disadvantage of this algortithm is its limitation a single category classification problem.

In order to overcome these disadvantages, another approach was analysed. The new approach (Parekh et al., 1997) creates an equivalent structure, though all the new neurons are grouped in a single hidden layer. The process of adding new units in this layer can be detailed like:

1. after the minimal network is trained, the output neuron which has the highest error rate is

selected;

2. depending on whether kind of error is more frequent, wrongly on (output=1 and desired output=0) or wrongly off (output=0 and desired output=1), a unit X or Y is created to correct some of the errors in the selected output neuron;
3. the new unit is connected to the input layer and its weights are trained separately according to the kind of error this unit will correct;
4. the new unit is added to the hidden layer and connected to the output layer, so the training may proceed.

This approach also allows to use the algorithm in multicategory networks. Figure 12 shows a network with three previously inserted neurons in the hidden layer, and Figure 13 ilustrates the insertion of a new unit, represented by the selected neuron.

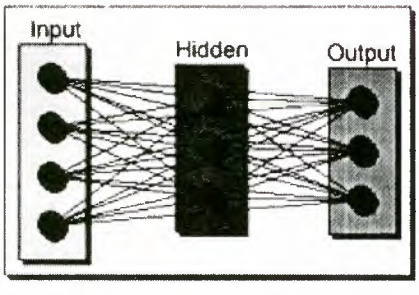


Figure 12: Upstart network with three previously inserted neurons.

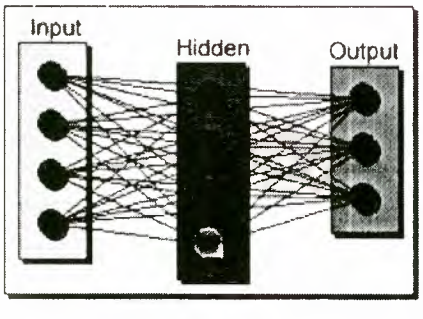


Figure 13: Insertion of a new neuron in the Upstart network.

## 4 Experiments

Experiments using the constructive algorithms Cascade Correlation and Tower were conducted. The obtained results were compared with the results obtained from a MLP network trained with the Backpropagation algorithm. The data set used were vessel images provided by the Institute of Research of the Brazilian Navy (IPqM).

The ship images patterns, provided by the SAPRI project are vectors of 1024 elements with hexadecimals values. These values represent the color intensity level of a pixel in a captured image from the radar.

This data was normalized, i.e., organized in matrixes of order 32, and the values converted in real numbers in the interval [0, 1] according to the SNNS format (Zell et al., 1995).

The set contains 800 patterns, with 200 representing each one of the four classes. The classes are related to a specific vessel, and the separation of ships in classes was carried out during the image capture.

During the experiment, the 800 patterns were randomly distributed in three sets, each set divided in training, validation, and test subsets, with proportions of 50%, 25%, and 25%, respectively, following the rules described in Proben1 (Prechelt, 1994). The benchmark rules described in Proben1 specify some standards in an attempt to reduce errors in the experiment authenticity.

The topology of the MLP network trained with the Backpropagation algorithm was fixed in 1024-8-4 (number of neurons in the input layer, hidden layer and output layer, respectively), obtained by empirical experimentation. Tables 1, 2 and 3 illustrates the means of the proportion of patterns correctly recognized (%) followed by its respective standard deviation.

| | Training |
|---|---|
| Back Propagation | 99.70 ± 0.326 |
| Cascade Correlation | 99.60 ± 0.326 |
| Tower | 100.00 ± 0.000 |

Table 1: Training results of networks using image patterns from the Brazilian Navy.

| | Validation |
|---|---|
| Back Propagation | 98.30 ± 1.151 |
| Cascade Correlation | 96.40 ± 1.140 |
| Tower | 95.70 ± 2.683 |

Table 2: Validation results of networks using image patterns from the Brazilian Navy.

These results indicate that all algorithms presented satisfactory results. All networks achieved good recog-

| | Test |
|---|---|
| Back Propagation | 98.40 ± 1.557 |
| Cascade Correlation | 97.40 ± 1.387 |
| Tower | 96.90 ± 1.084 |

Table 3: Test results of networks using image patterns from the Brazilian Navy.

nition rates and showed a good generalization. The MLP network trained with the Backpropagation algorithm presented the best result in the validation and test sets. However, the topology used was chosen after several comparisons with other topologies. The main advantage in using constructive algorithms is the saving of time and effort in finding a topology that is adequately efficient in the problem resolution and, at the same time more compact.

The remain algorithms presented in this paper are currently in development and experimentation, thus no conclusive results are available. Among the algorithms implemented or in development are: Back Propagarion, Cascade Correlation, Upstart, Tower and Pyramid. It is intended to implement other constructive algorithms, such as RBF-DDA and Tiling (Parekh et al., 1997) for future use in the SAPRI project.

## 5 Conclusion

This work presented some models of Constructive Neural Networks (CNNs) that were used in target recognition tasks. CNNs improve their performance by inserting new neurons, layers or connections. The insertion of new units is in charge of the constructive algorithm used. Among the presented algorithms, the Cascade Correlation and Upstart inserts one neuron at a time, whereas the Tower and Pyramid algorithms insert one layer with a fixed number of neurons at a time. In this way, the constructive algorithms attempt to define the best topology to reduce their error rates and improve their performance.

Comparing the use of constructive algorithms to conventional Neural Networks with fixed topology, a better functioning of the constructive algorithms can be observed. Contrary to the empirical approach, the CNN adjust themselves according to the problem at hand. This avoids the waste of effort and time in finding the best topology for each problem.

In order to execute the experiments described in Section 4, a Constructive Neural Network Simulator - Kipu, (Cuadros et al., 1998) was used. This simulator is being developed in the Institute of Mathematics and Computer Science (ICMC) of the University of So Paulo (USP) with the support of CAPES and CNPq. The figures of Neural Networks shown in this paper were also captured from this simulator.

### Acknowledgements

The authors would like to acknowledge the CAPES, CNPq and FAPESP for the support provided, and to Kate Sessions for the contributions to this text.

## References

Cuadros, E., Álvarez, M., & Carvalho, A. C. P. L. F. (1998). Multi-threads object oriented simulator for ontogenic neural networks. *Proceedings of the International Conference on Computational Intelligence and Multimedia Applications. World Scientific*, pages 276–281.

Fahlman, S. E. & Lebiere, C. (1991). The cascade-correlation learning architecture. *Technical Report. School of Computer Science. Carnegie Mellon university.*

Frean, M. (1990). The upstart algorithm: a method for constructing and training feed-forward neural networks. *Technical Report. Department of Physics and Centre for Cognitive Science. Edinburgh University.*

Freeman, J. & Skapura, D., editors (1993). *Neural Networks, Principles, Algorithms, and Applications.* Addison Wesley.

Parekh, R., Yang, J., & Honavar, V. (1997). Constructive neural network learning algorithms for multi-category real-valued pattern classification. *Technical Report. Department of Computer Science. Iowa State University.*

Prechelt, L. (1994). Proben1 - a set of neural network benchmark problems and benchmarking rules. *Technical Report. Fakult Karlsruhe*, (21/94).

SAPRI (1997). Image Acquisition, Processing, and Recognition System(SAPRI). URL:http://www.di.ufpe.br/ sapri.

Zell, A., Mamier, G., & Vogt, M. (1995). Snns stuttgart neural network simulator user manual version 4.1. URL:http://www.informatik.uni-stuttgart.de/ipvr/bv/projekte/snns/snns.html.

# Radar 3

*Coordinators:* Alejandro C. Frery, *UFPE* &
Thuy Le Toan, *CESBIO*

# SIMULTANEOUS GENERATION AND REGISTRATION OF SAR IMAGES

**David Fernandes**

Instituto Tecnológico de Aeronáutica (ITA)
Centro Técnico Aeroespacial (CTA)
Praça Mal. Eduardo Gomes, 50
12228-900 São José dos Campos, SP - Brasil
Tel. +55.12.347.5879, FAX: +55.12.347.5878
david@ele.ita.cta.br

**Abstract**: Registration of SAR images is required for interferometric processing and multitemporal analysis. A procedure which allows simultaneous generation and registration of SAR images from spaceborne sensors is presented. The procedure is based on the properties of the chirp scaling algorithm and is used in a interferometric processor to generate the interferogram, the fringes and the coherence map.

Keywords: synthetic aperture radar, SAR image, registration of SAR images, SAR interferometry.

## 1 Introduction

To calculate the interferogram, the fringes and the coherence map of SAR images, the original Single-Look-Complex (SLC) SAR images must be registered. The miss registration decreases the correlation of the images and increases the phase error in the fringes of the interferogram.

The registration can be done after the generation of the SLC SAR images or it can be done simultaneously with the generation of the SLC images. This second approach results in a time reduction in the registration process, Fornaro et al. (1994), Fernandes et al. (1996).

In this work it is shown a process to simultaneously generate and register two SLC SAR images from spaceborne sensors and how this process can be used in a interferometric processor that can generate automatically the interferogram, the fringes and the coherence map.

## 2 SAR signal

A sample of a Real Aperture Radar (RAR) or a Synthetic Aperture Radar (SAR) image is generated by the backscattering of the transmitted signal within of a resolution cell. The dimension of a resolution cell is given by:

-for a RAR:

in range $$D_r = \frac{c_o T_p}{2} \quad [\text{m}] \qquad (2.1)$$

in azimuth $$D_a = \theta_a \, r \quad [\text{m}] \qquad (2.2)$$

$T_p$ is the transmitted signal pulsewidth, $c_o$ is the light speed, $\theta_a$ is the antenna beamwidth in azimuth and $r$ is the slant range between the radar antenna and the resolution cell center.

-for a SAR:

in range $$D_r = \frac{c_o}{2\,B_r} \quad [\text{m}] \qquad (2.3)$$

in azimuth $$D_a = \frac{v}{B_a} \quad [\text{m}] \qquad (2.4)$$

$B_r$ is the transmitted chirp bandwidth given by $B_r = \gamma . T_p$, where: $\gamma$ is the chirp rate, $v$ is the relative velocity between the scatter and the sensor platform. $B_a$ is the azimuth bandwidth given by: $B_a = \gamma_a . T_a$, where $\gamma_a$ is the azimuth chirp rate and $T_a$ is the illumination time:

$$\gamma_a = \frac{2.v^2}{\lambda . r} \quad [\text{Hz/s}] \qquad (2.5)$$

$$T_a = \frac{r.\theta_a}{v} \quad [\text{s}] \qquad (2.6)$$

$\lambda$ is the carrier frequency wavelength.

The pixel spacing gives the distance between two consecutive resolution cells. For the RAR or SAR systems it is given by:

in range $$d_r = \frac{c_o T_s}{2} \quad [\text{m}] \qquad (2.7)$$

in azimuth $$d_a = \frac{v}{prf} \quad [\text{m}] \qquad (2.8)$$

$T_s$ is the echo signal sample time and *prf* is the Radar pulse repetition frequency.

In the horizontal plane the range dimension of a resolution cell and the range pixel spacing must be divided by the factor:

$$f_h = sin(\alpha) \qquad (2.9)$$

where $\alpha$ is the incidence angle of the electromagnetic wave in the scene.

If two images have different values of $T_S$, $v$, $prf$ or $\alpha$, they have different pixel spacing, and therefore different scale factors. Consequently, they can not be registered only with a shift operation. In the interferometry process, the same scene is observed from different positions, therefore the images are observed with different incidence angles $\alpha$ and then even though they have the same parameter $T_S$, the images have different range scales.

For images with different values of $T_p$, $\theta_a$, $\gamma$, $v$, $\lambda$ or $\alpha$, the resolution cells of the two images are different and the resolution cells can not have a perfect superposition, therefore two registered pixels show a statistical decorrelation.

As an example, Figure 2.1 shows a cut in range and azimuth of two simulated ERS-1 SAR images with point targets. Image 1: $T_S$ = 52.72 ns (pixel space in range: 7.91m) , $prf$ = 1634.55 Hz (pixel spacing in azimuth: 4.34m) and sensor altitude equal to 800.0 km. Image 2: $T_S$ = 66.07 ns (pixel spacing in range: 9.91m), $prf$ = 1934.55 Hz (pixel spacing in azimuth: 3.67m) and sensor altitude equal to 800.2 km. The baseline between the SAR sensors is 538.52 m and the baseline inclination is 21.80°. The images have different scale factors and therefore the point targets are not registered.

A sample of a Synthetic Aperture Radar image, $s(r,x)$, can be represented approximately by:

$$s(r,x) = \iint h_r(r-r', x-x'; r').\gamma(r',x'). \times \exp\left\{-\frac{4.\pi}{\lambda} r'\right\} dx'.dr' \qquad (2.10)$$

where: $r$ and $x$ are, respectively, the radial and azimuth dimensions, $\gamma(r',x')$ is the scene complex reflectivity at $(r',x')$, $h_r(.,.;.)$ is the SAR Point Spread Function, range dependent, and $\exp\left\{-\frac{4\pi}{\lambda} r'\right\}$ is the phase due the round trip delay between the radar and the scatters. The complex reflectivity $\gamma(r,x)$ is a function of the backscattering coefficient $\sigma_o$:

$$|\gamma(r,x)|^2 = \sigma_o(r,x) \qquad (2.11)$$

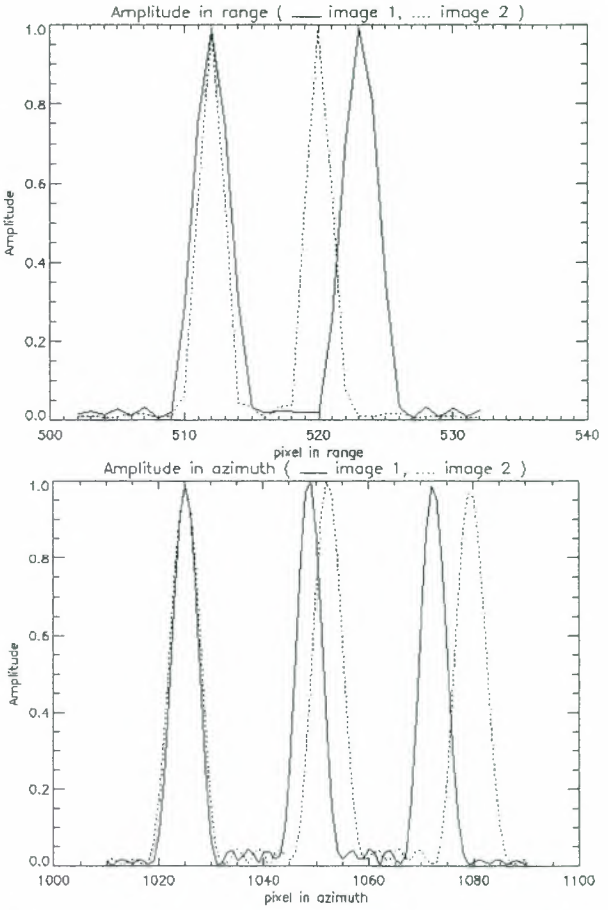


Figure 2.1: simulated point targets images with different scale factors.

An ideal point target at $(r_o, x_o)$, can be represented by a Dirac Function:

$$\gamma(r,x) = c\ \delta(r-r_o, x-x_o) \qquad (2.12)$$

where $c$ is a complex constant and $\delta(.,.)$ is the Dirac Function.

In this case, the SAR image is the Point Spread Function:

$$s(r,x) = c\ h_r(r-r_o, x-x_o; r_o) \exp\left\{-\frac{4.\pi}{\lambda} r_o\right\} \qquad (2.13)$$

If the SAR is ideal, its Point Spread Function is the Dirac Function:

$$h_r(r,x) = k\ \delta(r,x) \qquad (2.14)$$

where $k$ is a complex constant.

For this function, the SAR image is the complex reflectivity of the scene:

$$s(r,x) = k\ \gamma(r,x) \exp\left\{-\frac{4.\pi}{\lambda} r\right\} \qquad (2.15)$$

For a SAR sensor, the Punctual Spread Function can be approached by, Carrara et al. (1995):

$$h_r(r,x) = k\,\frac{\text{sen}(\pi.x/D_a)}{\pi.x/D_a}\,\frac{\text{sen}(\pi.r/D_r)}{\pi.r/D_r} \qquad (2.16)$$

## 3 Range and azimuth scaling

We will suppose that we have two SAR images to be registered. One of them is the reference image and the other will be registered with the former. We will also suppose that the central pixel of both images are registered and that the scale factor to be applied in azimuth and range in the second image to be registered are, respectively, $F_a$ and $F_r$. If the reference image is represented by $s_{ref}(\tau,t)$ the second registered image will be $s(\tau.F_r, t/F_a)$. The relationship between $(\tau,t)$ and *(r,x)* used in Section 2 is given by:

$$(\tau,\ t) = \left(\frac{2}{c_o}r,\ \frac{1}{v}x\right)$$

We will assume that the second image raw data is represented by $pp(\tau,t)$ in the range time ($\tau$) and azimuth time (t) domain.

### 3.1 Azimuth scaling

We will consider a point target at $(\tau_o,t_o)$, whose raw data due the second SAR sensor is represented by:

$$\begin{aligned} pp(\tau,t;\tau_o,t_o) &= a(t).s(\tau - 2.R(t;r_o,t_o)/c_o) \\ &\times \exp\left\{-j\pi\gamma(\tau - 2.R(t;r_o,t_o)/c_o)^2\right\} \\ &\times \exp\left\{-j4\pi R(t;r_o,t_o)/\lambda\right\} \end{aligned} \qquad (3.1)$$

with,

$$r_o = \frac{c_o}{2}\tau_o \qquad (3.2)$$

$$R(t;r_o,t_o) = \sqrt{r_o^2 + v_2^2(t-t_o)^2} \qquad (3.3)$$

where: a(.) is the antenna azimuth function, s(.) is the transmitted pulse amplitude, $\exp\left\{-\pi\gamma\tau^2\right\}$ is the range chirp and $\exp\left\{-j4\pi\sqrt{r_o^2 + v_2^2(t-t_o)^2}/\lambda\right\}$ is the azimuth phase modulation, $v_2$ is the relative velocity between the scatter and the second sensor platform and $t_o = 0$ is the scene azimuth center.

The azimuth scaling can be modified multiplying the raw data $pp(\tau,t;\tau_o,t_o)$ by:

$$\phi_0(t;r_o) = \exp\left\{-j\pi(F_a - 1)\gamma_a\, t^2\right\} \qquad (3.4)$$

with the azimuth scaling $F_a$ given by:

$$F_a = \frac{v_1\ prf_2}{v_2\ prf_1} \qquad (3.5)$$

where, $prf_1$ is the pulse repetition frequency of the reference SAR sensor, $v_1$ is the relative velocity between the scatter and the reference sensor platform, $prf_2$ is the pulse repetition frequency of the SAR which generated the raw data of the secondary image, and $\gamma_a$ is the azimuth chirp rate:

$$\gamma_a = \frac{2.v_2^2}{\lambda.r_o} \qquad (3.6)$$

After the multiplication:
$pp(\tau,t;\tau_o,t_o).\phi_o(t;r_o)$, the resulting signal has a new azimuth modulation term with azimuth phase center at $t_o/F_a$ instead $t_o$, Fernandes et al. (1996):

$$\exp\left\{-j4\pi\sqrt{r_o^2 + F_a v_2^2(t - t_o/F_a)^2}\right\},$$

and a new azimuth chirp rate given by:

$$\gamma_{a\,\text{mod}} = \gamma_a F_a \qquad (3.7)$$

With this new phase center and after the azimuth focus we obtain the azimuth scaling in the second SAR image.

### 3.2 Range scaling

The Chirp Scaling Algorithm, Raney et al. (1994), provides means to scale the SAR image, Moreira et al. (1996) and Fernandes et al. (1996).

The Fast Fourier Transform (FFT) applied in the azimuth direction of the SAR raw data, $pp(\tau,t)$, transforms the range time - azimuth time domain into the range time - azimuth Doppler domain.

$$pP(\tau,f) = FFT_{az}\{pp(\tau,t)\} \qquad (3.8)$$

where $pP(\tau,f)$ is the raw data in the range time ($\tau$) and azimuth Doppler (f) domain.

The range cell migration trajectory in the $pP(\tau,f)$ image is given by, Raney et al. (1994):

$$R_f(f;r) = r + r\,C_s(f) \qquad (3.9)$$

where $C_s(f)$ is the curvature factor:

$$C_s(f) = \frac{1}{\sqrt{1 - \left(\frac{\lambda.f}{2.v}\right)^2}} - 1 \qquad (3.10)$$

and $v$ is the relative velocity between the scatter and sensor platform.

Equation (3.9) shows that the range cell migration at range $r$ has a curvature given by $r\,C_s(f)$. This curvature is range dependent. To transform the range cell migration trajectory into a range independent trajectory, the $pP(\tau, f)$ image is multiplied by the chirp scaling phase given by, Raney et al. (1994):

$$\phi_1(\tau, f; r_{ref}) = \exp\left\{-j.\pi.K_s(f; r_{ref}).C_s(f)\left[\tau - \tau_{ref}(f)\right]^2\right\} \tag{3.11}$$

where: $r_{ref}$ is the reference range, it will be chosen in the center of the scene, and $K_s(f; r_{ref})$ is a function of $f$ with $r_{ref}$ as a parameter.

$$\tau = \frac{2.r}{c_o} \tag{3.12}$$

and

$$\tau_{ref}(f) = \frac{2}{c_o} r_{ref}\left[1 + C_s(f)\right] \tag{3.13}$$

After the multiplication:

$pP(\tau, f).\phi_1(\tau, f; r_{ref})$, the resulting image has a range cell migration trajectory given by:

$$R_f(f; r) = r + r_{ref}\,C_s(f) \tag{3.14}$$

The equation (3.14) shows that the range cell migration at range $r$ has a curvature given by $r_{ref}\,C_s(f)$. This curvature is range independent.

The property of the chirp scaling phase to equalize the range cell migration can be extended to provide a scale in range, Moreira et al. (1996) and Fernandes et al. (1996).

For a range scaling factor of $F_r$, it must be choose for the chirp scaling phase $\phi_1(\tau, f; r_{ref})$ a new curvature factor (the modified curvature factor) given by:

$$C_{scl}(f) = C_s(f) + (1 - F_r)\frac{1 + C_s(f)}{F_r} \tag{3.15}$$

If the scale factor is one, there is no scaling. This scaling is given by, Fernandes (1996):

$$F_r = \frac{T_{s2}.sin(\alpha_2)}{T_{s1}.sin(\alpha_1)} \tag{3.16}$$

where $\alpha_1$ and $\alpha_2$ are, respectively, the incidence angle in the center of the scene observed by the reference SAR sensor and the secondary SAR sensor. $T_{s1}$ and $T_{s2}$ are, respectively, the echo signal sample time of the reference and secondary SAR sensors.

With this new factor, the range cell migration will be equalized and scaled. The new range cell migration trajectory will be given by:

$$R_f(f; r) = r_{ref} + (r - r_{ref})\,F_r + r_{ref}\,C_s(f) \tag{3.17}$$

In (3.17) we note that the curvature is constant and given by $r_{ref}\,C_s(f)$, the range $r$ of (3.14) becomes $r_{ref} + (r - r_{ref})\,F_r$. This is equivalent to an expansion or contraction around the center point $r_{ref}$. For instance, if $r$ is a set of distances: [10, 20, 30, 40, *50*, 60, 70, 80] with $r_{ref} = 50$ and $F_r = 0.9$, we will have the new set of distances around $r_{ref} = 50$: [14, 23, 32, 41, *50*, 59, 68, 77].

If we suppose that the central pixel of this image is registered with the central pixel of another image (reference image), both images can be registered by the range focus.

The modified curvature factor introduces in the chirp scaling algorithm a phase error that can be compensated, Moreira et al. (1996), Fernandes et al. (1996).

### 3.3 The modified chirp scaling algorithm

The modified version of the chirp scaling algorithm takes into account the modification introduced in the previous sections. Another method for the azimuth scaling and a new configuration for the modified chirp scaling algorithm (the extended chirp scaling algorithm) is given by Moreira et al. (1996).

Figure 3.1 shows the point targets of Figure 2.1 registered in range and azimuth by the proposed modified version of the chirp scaling algorithm.

The chirp scaling and the modified chirp scaling block diagram are shown respectively in Figure 3.2.a and 3.2.b, Raney et al. (1994), Fernandes et al. (1996).

## 4 Interferometric processor

Using the scaling in range and azimuth discussed in the previous section, it was developed an interferometric processor. This processor simultaneously generates and registers two SLC SAR images, calculates the interferogram, the fringes with flat earth correction and the coherence map. The processor input are two sets of SAR raw data, the satellites orbits, velocities and the radar and signal parameters.

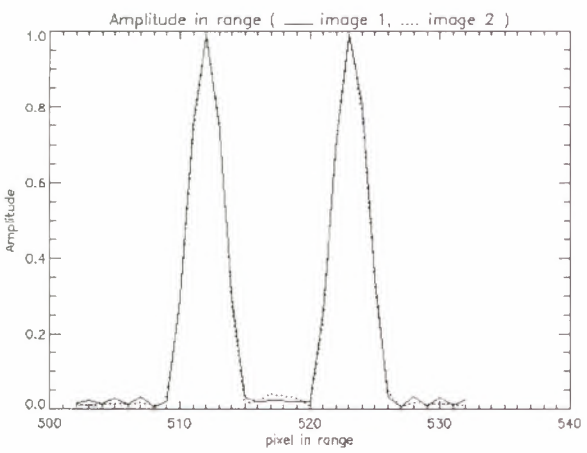


(range)

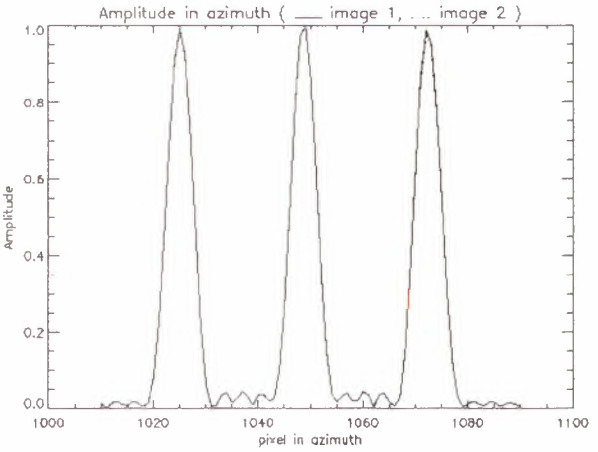


(azimuth)

Figure 3.1: registered points targets.

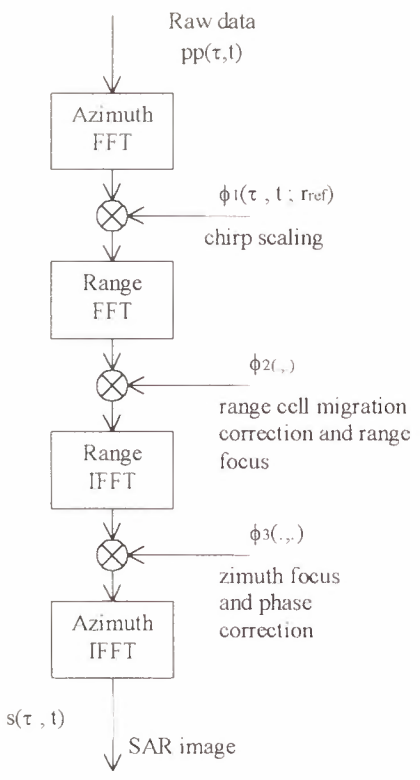


a) chirp scaling

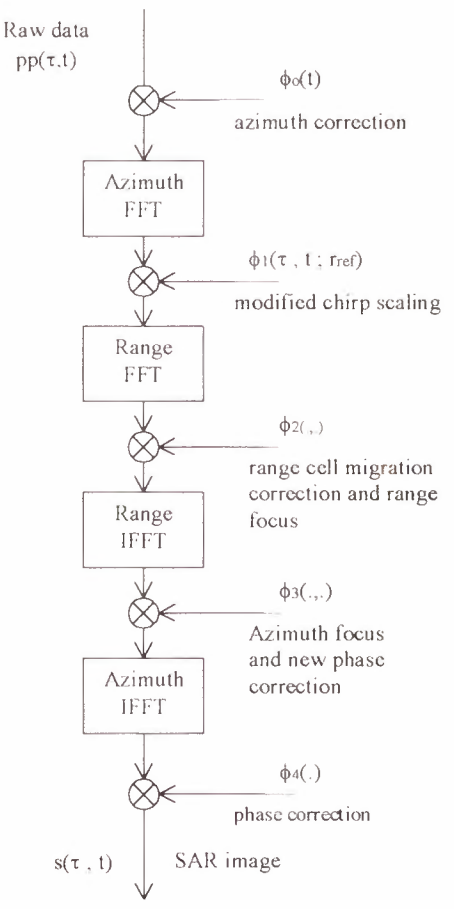


b) modified chirp scaling

Figure 3.2: chirp scaling algorithm.

Figure 4.1 shows the interferometric processor general block diagram.

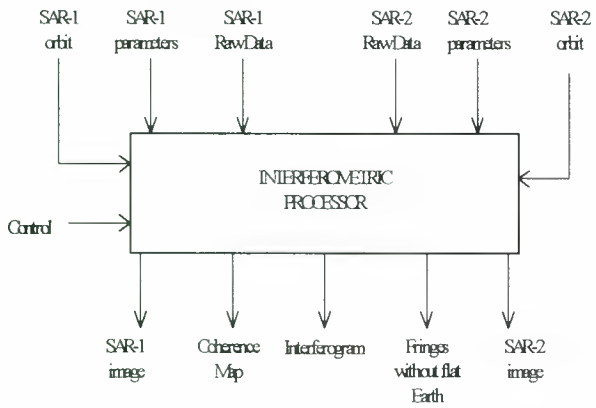


Figure 4.1: input/output of the interferometric processor

As an example, Figure 4.2 shows the interferogram and the fringes, with flat Earth correction, from two registered images obtained from the ERS-1 SAR sensor over Fayoum-Rayan area (35Km in range, 32 Km in azimuth) near Cairo City.

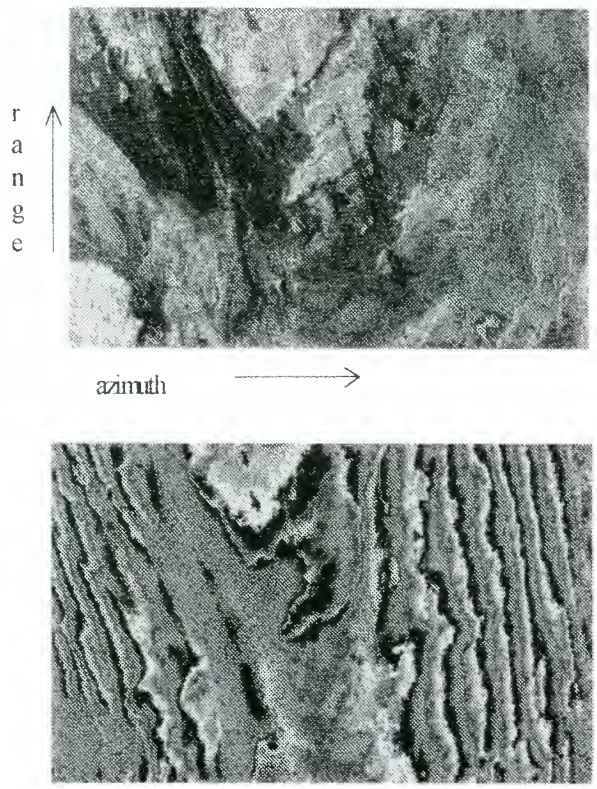


Figure 4.2: interferogram and fringes, with flat earth correction.

The processor selects one image as a reference image. The reference image is generated and the secondary image are simultaneously generated and registered with the former. If the SAR raw data are very big the processor divide the raw data in a small sets of data (2kB x 2kB or 4kB x 4kB blocks of data) and processes each set of data. The Figure 4.3 shows the block diagram of the interferometric processor for each set of raw data.

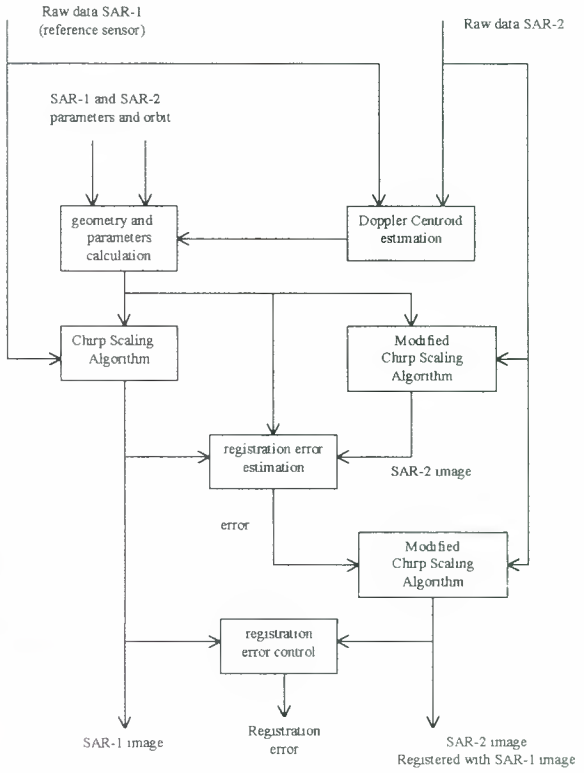


Figure 4.3: registration process.

Figure 4.4 shows the calculation of the interferogram, fringes and coherence map for two registered SLC SAR images, Mura (1993), Alenn, (1995).

As an example, Figure 4.5 shows a ERS-1 amplitude image of a pair of images and the coherence map of these images from Düsseldorf area in Germany.

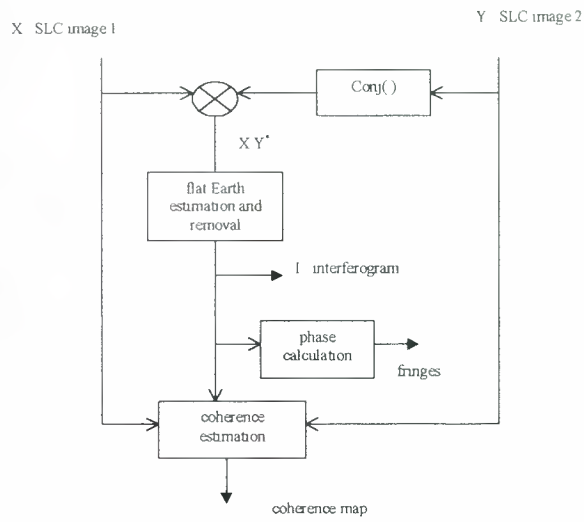


Figure 4.4: interferogram, fringes and coherence map calculation.

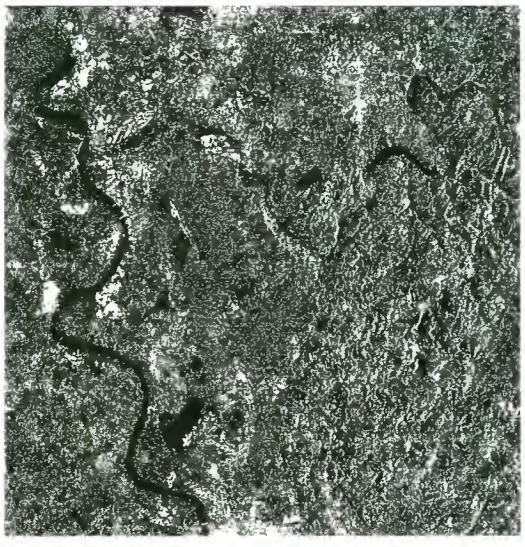

a) amplitude image

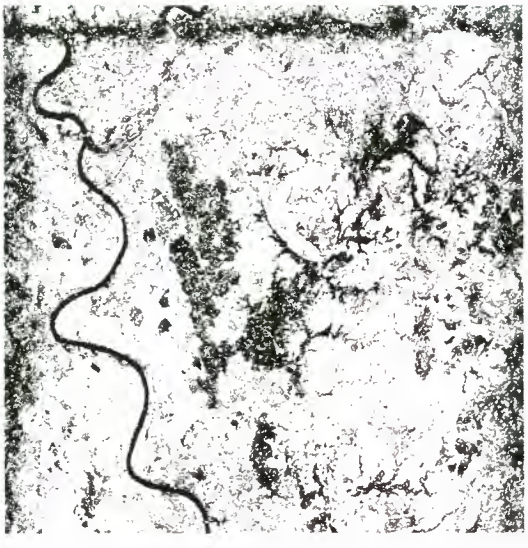

b) coherence map

Figure 4.5: a ERS amplitude image and the coherence map of two ERS-1 images from Düsseldorf area in Germany, Reigber (1997).

## 5 Conclusions

The proposed procedure combines the SAR images generation and registration. The integrated processes reduces the computing time and preserve the image quality. The developed procedure was used in a interferometric processor that calculates the interferogram, the fringes and the coherence map.

The performance of the processor has been tested by the registration of simulated point targets and by the interferometric processing of real ERS-1 raw data.

## Acknowledgments

The author wish to tanks the Institut für Hochfrequenztechnik (HF) - Deutsches Zentrum für Luft- und Raumfahrt (DLR) in Oberpfaffenhofen/Germany, the International Civil Aviation Organizaton (ICAO) Project BRA-95/802 Objective 6-ITA and the Fundação de Amparo à Pesquisa do Estado de São Paulo (FAPESP) for their support in this work.

## References

Allen, C. *Interferometry Synthetic Aperture Radar*. IEEE Geoscience and Remote Sensing Society Newsletter, Sept., 1995, pp. 6-13.

Carrara, W.; Goodman, R. S.; Majewski, M. *Spotlight Synthetic Aperture Radar: signal processing algorithms*. Artech House, Boston, 1995.

Fernandes, D.; Waller, G. Moreira, J. R. Registration of SAR images using the chirp scaling algorithm. International Geoscience and Remote Sensing Symposium *(IGARSS'96)*, Nebrasca, 1996, *Proceedings*, pp. 799-801.

Fornaro, G.; Franceschetti, G.; Marzouk, E. S. A new approach for image registration in interferometric processing. . *Proceedings, International Geoscience and Remote Sensing Symposium (IGARSS'94)*, Seatle, 1998, pp. 1983-1985.

Moreira, A.; Scheiber, R.; Mittermayer, J. Extended Chirp Scaling Algorithm for Air- and spaceborne SAR data processing Stripmap and ScanSAR. *IEEE Transactions on Geoscience and Remote Sensing*, V. 34, No. 5, pp. 1123-1136, September, 1996.

Mura, J. C. Performance and interferometric capabilities of the INPE/DLR SAR processor. Deutsche gesellschaft für Ortung und Navigation e. v. 8, Radarsymposium, sept., 1993, pp. 166-171.

Reigber, A. Multitemporale Analyse der Kohärenz von SAR-Daten. *Diplomarbeit*, Universität Konstanz / Institut für Hochfrequenztechnik (HF) der Deutsches Zentrum für Luft- und Raumfahrt (DLR), 1997.

Raney, R. K.; Runge, H.; Bamler, R.; Cumming, I. G.; Wong, F. H. Precision SAR processing using chirp scaling. *IEEE Transactions on Geoscience and Remote Sensing*, V. 32, No. 4, 1994, pp. 786-799.

# The use of textural features on the polarimetric SAR image classification*

SIDNEI JOÃO SIQUEIRA SANT'ANNA
CORINA DA COSTA FREITAS
CAMILO DALELES RENNÓ

INPE--Instituto Nacional de Pesquisas Espaciais
Caixa Postal 515, 12201-097 São José dos Campos, SP, Brazil
{sidnei,corina,camilo}@dpi.inpe.br

**Abstract.** In this work the potentiality of the textural information that polarimetric SIR-C data can provide to discriminate some types of land use is studied. That information is extracted from the data by using statistical and distributional measures. The Euclidean distance is used to select the best set of features for discriminating classes of interest. Features bands (textural bands) are built by filtering the images, and they are used as channels on ICM classification. The discriminatory power of the selected features is assessed by analyzing the classification results, which are evaluated using the confusion matrix and the Kappa coefficient of agreement. The results show that the textural information, as well as the tonal information provided by these images are very important to discriminate the land use under study.

## 1 Introduction

The Brazilian Amazonian Tropical Forest has been the object of several studies, particularly concerning the estimation of the extent and rate of gross deforestation. With an area of about 5 million square kilometers, 4 million of which covered by forest, a total of 517,069 square kilometers were deforested by 1996 (INPE, 1998). The knowledge and understanding of tropical deforestation process and its consequences are important aspects of global change, and they are necessary for the Brazilian Government to take actions for the sustainable use of the natural resources.

Besides the importance of mapping the deforested areas, the study of secondary succession is also important due to the impact that these areas have on the region carbon cycle balance, which might have consequences on the global clime change and on the carbon budget. Compared to primary formations, the secondary forest accumulate biomass more rapidly and therefore act as a net sink for atmospheric carbon (Brown and Lugo, 1990), but this net sink is still poorly quantified (Schimel, et al., 1995).

Many studies that have been done in Brazilian Amazonian still use LANDSAT-TM data to map and to monitor the changes in forests, deforested areas and regenerating forests. However, weather conditions strongly limit the data availability. The use of radar data is therefore the only way of overcoming this problem. In addition to the all weather capability of radar and the availability of currently systems (ERS, JERS, RADARSAT, airborne systems, etc), the use of radar data to monitor deforestation and regeneration is strongly motivated by the sensitivity of the radar backscatter to standing biomass (Le Toan et al., 1992; Ranson et al., 1995; Luckman et al., 1997b; Yanasse et al., 1997).

The number of studies in Amazon using radar data has increased for those reasons. Nevertheless, proper methods for extracting information from radar images are still object of study, and they are dependent of the type of application (estimation of above ground biomass, mapping of deforested areas, identification of different kind of crops, classification of specific land use, among others) and the sensor characteristics, as polarization (HH, HV, VH and VV), band (C, L, X, Ku, P, etc), angle of illumination, pixel resolution, etc.

The extraction of the information from images is usually derived from tonal analysis. However, only tonal information is not sufficient to gather all information provided by SAR images. Therefore, many researchers have used textural attributes to extract the complementary information (see, for instance, Luckman et al., 1997a; Sant'Anna et al., 1997; Soares, et al., 1997).

The objective of this paper is to analyze and to select several texture features (attributes) from radar images, for the discrimination of some land use classes (primary forest, different stages of secondary forest, bare soil and pasture). After a brief description in **Section 2** about the study area and the data used, the methodology is detailed in **Section 3**, pointing out the whole process of extraction and selection of features used for land cover classification. The results are presented in **Section 4**, and **Section 5** was reserved for the final conclusions of the work.

* This work was supported by grants from PPG-7 (0808/95 and 0816/95), Convênio FINEP (6.6.96.0473.00 and 6.6.96.0474.00).

## 2 Study area and data

The study area is located on Pará State, Brazil, in the Tapajós National Forest. Although this Forest is a reserved area, in the study site there are primary forest and deforested regions. Some deforested regions were abandoned and are presently under regeneration. Besides the importance of mapping these regions, another reason for choosing the Tapajós area is the availability of different remote sensing data and field work information. Among these data set, a multi-temporal LANDSAT/TM images from 1984 to 1995 (except 1994) are available, which were used to build a regeneration stage map of the area, as described in details in Sant'Anna et al.(1995).

Several radar data are also available for this area, such as JERS-1 (L-HH band polarization), RADARSAT (C-HH band polarization), SAREX (C-HH and C-VV band polarization), ERS-1 (C-VV band polarization), and SIR-C (L and C bands, HH and HV polarization). To reach the objectives of this work, the SIR-C data were chosen, because they have higher discrimination potentiality than the other radar sensors due to the possibility of combining different bands and polarization. The SIR-C images used in this paper are part (950 columns by 1400 lines) of the images obtained on October 1994, with approximately 8 nominal looks.

A color composite of the SIR-C images is shown in **Figure 1a**, with L-HH, L-HV and C-HH in the red, green and blue channels, respectively. In **Figure 1b** is depicted the regeneration stage map, where the classes are represented by colors as following: primary forest (Forest) in dark green, old regeneration (OldReg – secondary succession with more than or equal to 8 years old) in light green, new regeneration (NewReg – secondary succession with less than 8 years old) in yellow, recent activities (RecAct - bare soil, pasture and some agricultural crops) in magenta, clouds and shadows in black and regions without information in gray. The light and dark blue areas appearing on **Figure 1a** refer to deforested areas. There are not many areas of the OldReg class, and it is very difficult to see them on **Figure 1a** because they have a very similar pattern than those presented by the Forest class (reddish tone). In fact, the visual confusion between these two classes is apparently bigger than the confusion among others classes. Some most representative areas of the OldReg class are indicated by white arrows in **Figure 1b**.

## 3 Methodology

The regeneration map was used as a mask over SIR-C images, after registering the map to these images. In this registration process the SAR images were the base images and the map was the wrapping image, in order to not modify the SAR data properties. After the map had been registered, its regions (classes) could be associated with SAR data. To avoid errors such as register displacements and precise identification of the classes boundaries, a morphological operator, called erosion, was applied to the map using a 3x3 window.

The analysis was followed by features extraction. Two kind of measures denominated statistical (including first and second order statistical measures) and distributional (including parameters that characterize statistical distributions) were used as features. The former were computed in amplitude and intensity data and they are represented with subscript A and I, respectively, while the latter were computed only in amplitude data.

The statistical measures were defined by: mean ($\mu_A$ and $\mu_I$), mean in dB ($\mu_{dB}$), standard deviation ($\sigma_A$ and $\sigma_I$), coefficient of variation ($CV_A$), autocorrelation for lags (0,1), (1,0) and (1,1), represented by $\rho_A(0,1)$, $\rho_A(1,0)$ and $\rho_A(1,1)$, respectively, and coefficient of variation for the same lags, represented by $CV_A(0,1)$, $CV_A(1,0)$ and $CV_A(1,1)$. The definition of the coefficient of variation for lag $(s_x, s_y)$ is given by:

$$CV_A(s_x, s_y) = \frac{\sqrt{\hat{\gamma}(s_x, s_y)}}{\mu_A}$$

where $\hat{\gamma}(s_x, s_y)$ is the estimated autocovariance for lag $(s_x, s_y)$, with $s_x$ and $s_y$ representing the distances between pixels in the two orthogonal directions $x$ and $y$.

The distributional measures are estimated parameters from distributions that are widely used on SAR data modeling. The selection of the distributions was based on a $\chi^2$-goodness-of-fit test for the Gaussian ($N$), Log-Normal ($LN$), Weibull ($W$), Square Root of Gamma ($\Gamma^{1/2}$), K-Amplitude ($K_A$) and G0-Amplitude ($G_A^0$) distributions. Before doing the goodness-of-fit test the data were sub-sampled in a 1 to 4 ratio (only one pixel every 2x2 window was used), to reduce the effect of spatial correlation on test statistics. The $LN$, $\Gamma^{1/2}$, $K_A$ and $G_A^0$ were the best distributions fitted to sample data and their parameters were chosen as discriminant measures, except the parameter for the $\Gamma^{1/2}$ which is related to the mean value of the data, and it is already considered into the statistical measures. Therefore, the parameters used in the analysis were: mean and standard deviation of the $LN$ distribution ($\mu_{LN}$ and $\sigma_{LN}$), and the $\alpha$ parameter of the $K_A$ and $G_A^0$ distributions ($\alpha_{KA}$ and $\alpha_{GA0}$). For details about these distributions and their parameters' estimators, the reader is referred to Vieira (1996) and Frery et al. (1997a).

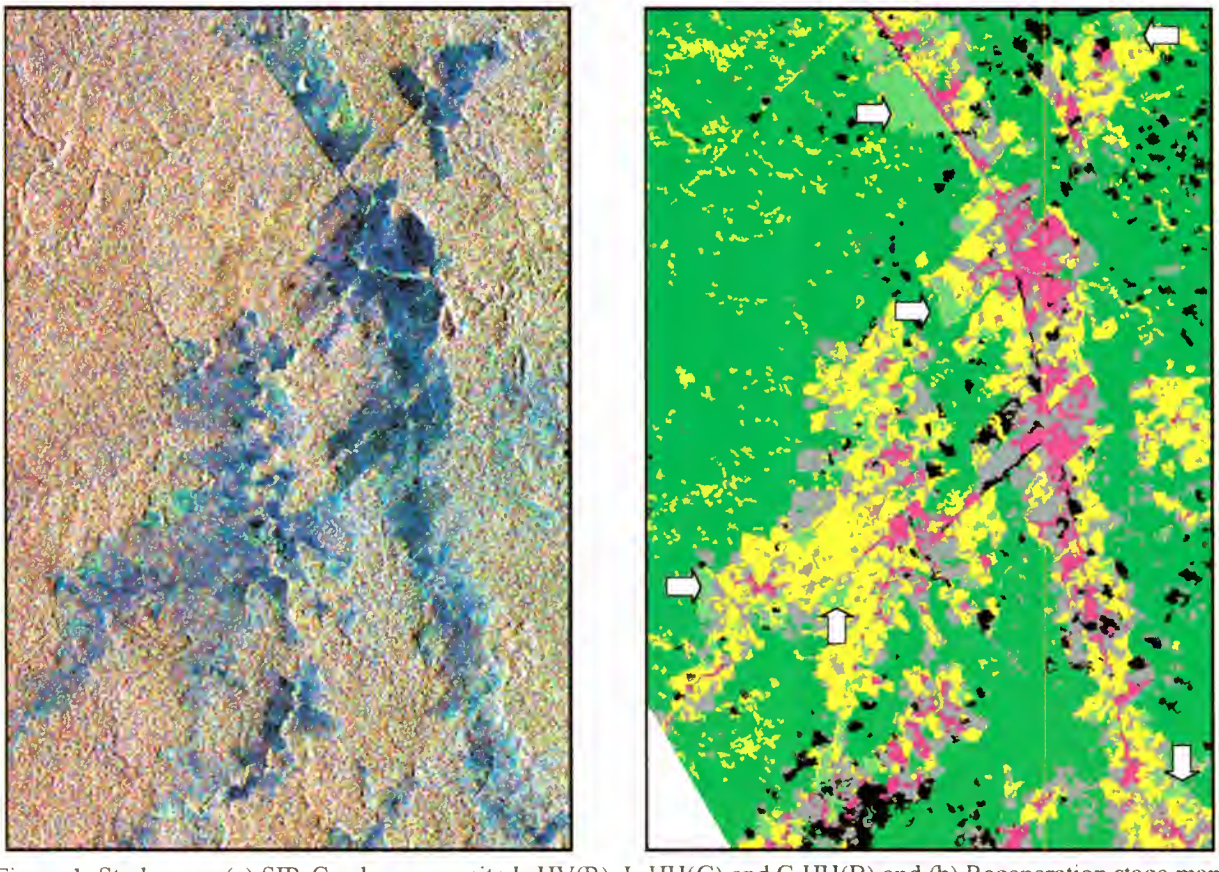

Figure 1: Study area: (a) SIR-C color composite L-HV(R), L-HH(G) and C-HH(B) and (b) Regeneration stage map

The estimators of the parameters for the $K_A$ and $G_A^0$ distributions involve the equivalent number of looks ($N$). The equivalent number of looks for SIR-C images was estimated from intensity data, using $\hat{N} = 1/CI^2$ for samples from homogeneous areas (recent activities class for C bands and old regeneration class for L bands). The estimated values of $\hat{N}$ for each pair of band/polarization and their mean are shown in **Table 1**. The mean value was used on the estimation of the $\alpha_{KA}$ and $\alpha_{GA0}$ parameters for all pair of band/polarization.

TABLE 1 - Estimated number of looks and overall mean, for SIR-C images.

| Band/ Polariz. | C HH | C HV | L HH | L HV | Overall Mean |
|---|---|---|---|---|---|
| $\hat{N}$ | 6.06806 | 6.28219 | 6.10203 | 5.33963 | 5.94798 |

The estimation of the sixteen measures (12 statistical and 4 distributional) was conducted for each class in the four original bands (with a total of sixty-four features), considering only regions which had the number of pixels greater than or equal to 100. **Table 2** gives the number of regions and the total number of pixels before and after sub-sampling. The sub-sampling was used only for the goodness-of-fit test. Parameters estimation was performed using the whole data sets to obtain more accurate values.

TABLE 2 - Number of regions and pixels used on the measures estimation.

| Classes | Regions | Pixels (after Sub-sampling) |
|---|---|---|
| **RecAct** | 75 | 47,689 (8,535) |
| **NewReg** | 358 | 177,753 (27,894) |
| **OldReg** | 114 | 55,923 (9,975) |
| **Forest** | 70 | 2,217,098 (433,076) |

The selection of the features with the highest discriminatory power for the classes of interest was based on the Euclidean distance for each pair of classes (RecAct-NewReg, RecAct-OldReg, RecAct-Forest, NewReg-OldReg, NewReg-Forest, and OldReg-Forest). All estimated features were standardized by taking the values and dividing them by its maximum value, so they would range from 0 to 1. The influence of outliers on the estimated features was minimized by trimming them on 10%. After the selection of the "best" discriminatory attributes, bands of these attributes were generated by a filtering process.

These bands of attributes and the original images were used to perform several classifications. The

Gaussian Multivariate Maximum Likelihood (ML) and the Multivariate Iterated Conditional Modes (ICM) were used as classifiers (Frery et al., 1997b and Vieira et al. 1997). The images resulting from the ML classification were used as one of the input for ICM classifier, which needs a contextual image to start the classification. The training and test samples were obtained from areas that had more than 250 pixels in the eroded regeneration stage map. The number of pixels utilized on both samples are presented in **Table 3**. In order to evaluate the classifications results, the confusion matrix and the Kappa coefficient of agreement were computed from the test samples. To verify the difference between two Kappa values a Z test was performed (Ma and Redmond, 1995).

TABLE 3 – Number of pixels for training and test samples.

| Classes | Training | Test |
|---|---|---|
| **RecAct** | 15,561 | 6,614 |
| **NewReg** | 58,315 | 28,553 |
| **OldReg** | 13,880 | 3,501 |
| **Forest** | 465,294 | 173,193 |

## 4 Results and Discussion

The Euclidean distance was computed for the trimmed and non-trimmed samples resulting in the same selected attributes. Therefore the analysis that follows is based on the non-trimmed samples. According to the analysis of Euclidean distance five attributes were selected to discriminate the six pairs of classes (**Table 4**). From the selected features it can be noted that only two bands (L-HH and L-HV) and four measures ($\mu_{LN}, \mu_A, \alpha_{KA}$ and $\mu_I$) were chosen. The C bands do not seem to carry any information with the measures used here to discriminate the classes under study, and L-HV band is the most important band for this purpose.

TABLE 4 – Selected features for discriminating pair of classes.

| Pair of Classes | Selected Features |
|---|---|
| RecAct-NewReg | $\mu_{LN}(lhv)$ |
| RecAct-OldReg | $\mu_{LN}$(lhv) |
| RecAct-Forest | $\mu_A(lhv)$ |
| NewReg-OldReg | $\alpha_{KA}(lhh)$ |
| NewReg-Forest | $\mu_I(lhv)$ |
| OldReg-Forest | $\alpha_{KA}(lhv)$ |

The filtered images with these measures were built using windows of size 7x7 pixels, except for the $\alpha$ parameter of K-Amplitude that a window size of 11x11 pixels was used. However, when building the filtered image with $\alpha_{KA}$(lhh) parameter, the estimation of this parameter presented problems and therefore this attribute was changed to $CV_A(lhh)$. This $CV_A$ measure was chosen, since it is highly correlated with $\alpha_{KA}$ and both measures seem to carry the same information (see Sant'Anna et al., 1997).

Five sets of images were generated and the ML/ICM classifications were performed for each set. These sets were:

- **Sirc2**: includes two original bands (L-HH and L-HV);
- **Sirc4**: includes the four original bands (C-HH, C-HV, L-HH and L-HV);
- **Sirc5**: includes the five bands generated by the selected attributes;
- **Sirc7**: includes the L-HH and L-HV original bands and the five attribute bands; and
- **Sirc9**: includes the four original bands and the five attribute bands.

The Sirc2 set includes only the L-HH and L-HV bands because they are the two bands appearing on the list of the five best selected features. These five sets were generated aiming at the comparison of the influence of the original and attribute bands on the classification results.

The ICM classifications for the sets described above are presented in **Figures 2** to **6**. In these figures the classes of RectAct, NewReg, OldReg and Forest are represented by magenta, yellow, light and dark green colors, respectively. The ML classification results are not presented here since the ML classification was used as one of the inputs of ICM classifier and the results of the latter is usually much better than those obtained with ML classifier.

The evaluation of the classifications was assessed from confusion matrices and the Kappa coefficients of agreement and their sample variances ($\hat{\kappa}$ and $\hat{\sigma}^2_{\hat{K}}$), which are given in **Tables 5** to **9**, for the aforementioned classifications.

From the classification of the Sirc2 and Sirc4 sets (**Figures 2** and **3**) and from **Tables 5** and **6** it can be noticed that the Forest class is better classified when all the original bands (C-HH, C-HV, L-HH and L-HV) are used, instead when only the L bands are used. The confusion between the Forest class and regeneration classes is greater on the Sirc2 set than the Sirc4 set. The addition of C bands improves the classification of Forest and OldReg classes, by decreasing the misclassification of Forest pixels as belonging to the regeneration classes, as well as the misclassification of OldReg pixels as belonging to the Forest class. The RecAct and NewReg classes do not suffered many changes on their classification results by including C bands in the Sirc2

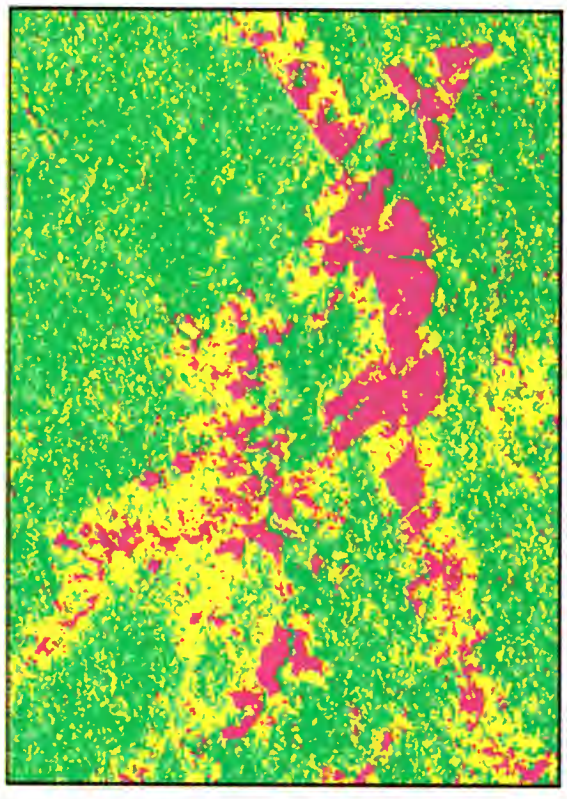

Figure 2: ICM classifications using Sirc2 set.

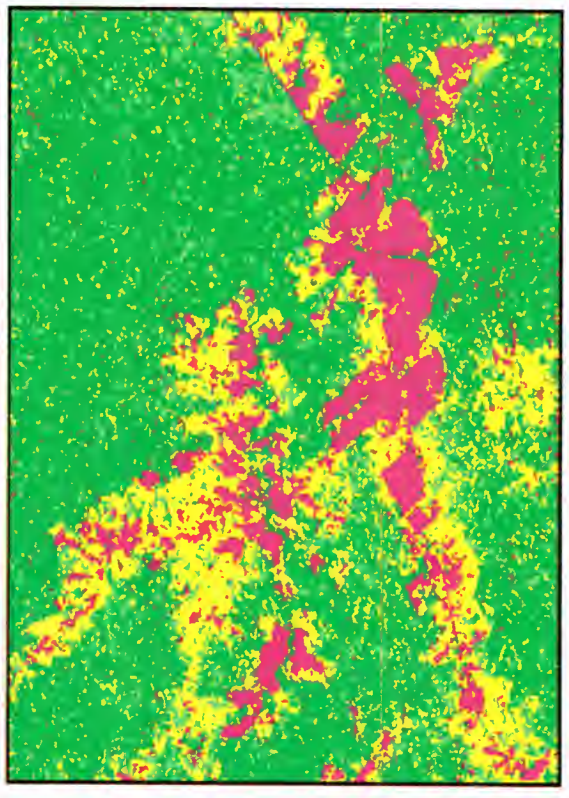

Figure 3: ICM classifications using Sirc4 set.

set. These facts evidence the influence of the C bands on the discrimination between Forest class and regeneration classes.

TABLE 5 – Confusion matrix for the Sirc2 set classification.

| Classes\ Classif | RecAct | NewReg | OldReg | Forest |
|---|---|---|---|---|
| **RecAct** | 91.0 | 7.6 | 0.2 | 1.2 |
| **NewReg** | 12.6 | 62.9 | 11.9 | 12.6 |
| **OldReg** | 8.6 | 52.3 | **25.4** | 13.7 |
| **Forest** | 1.3 | 22.0 | 20.7 | **56.0** |
| $\hat{K} = 0.2515$ | | $\hat{\sigma}^2_K = 1.4016 \times 10^{-5}$ | | |

TABLE 6 – Confusion matrix for the Sirc4 set classification.

| Classes\ Classif | RecAct | NewReg | OldReg | Forest |
|---|---|---|---|---|
| **RecAct** | 90.5 | 8.2 | 0.1 | 1.2 |
| **NewReg** | 12.3 | 64.6 | 13.5 | 9.6 |
| **OldReg** | 8.1 | 50.1 | **36.5** | 5.3 |
| **Forest** | 1.1 | 9.7 | 12.3 | **76.9** |
| $\hat{K} = 0.4404$ | | $\hat{\sigma}^2_K = 1.7398 \times 10^{-5}$ | | |

The classification results obtained using Sirc4 and Sirc5 sets (**Figures 3** and **4**) were used to compare the discriminatory power carried by textural and tonal information. It can be noticed that the classification of the RecAct class is about the same (see **Tables 6** and 7) when both types of information are used. The textural information contained in the selected features was important to improve the classification results of the Forest class. The results of classification using only features bands, presented in **Table 7**, show a significant decrease (close to 44%) of the OldReg pixels that were misclassified as NewReg class and a improvement (about 32%) of the pixels that were correctly classified as OldReg class. However, the misclassification of the OldReg pixels as Forest pixels increased when only features bands were used.

The classification results obtained for Sirc5 and Sirc7 sets (**Tables 7** and **8**) are very similar, meaning that the addition of the original L bands to the feature bands (Sirc5) did not improve the classification. This can be justified by the fact that $\mu_A(lhv)$ and $\mu_I(lhv)$ are included in the Sirc5 set, and they are features that gather tonal information. The result of Z test gives no evidence to reject the hypothesis that the two Kappa values are different, at a confidence level of 95%. It might indicate that the tonal information carried by L-HH band/polarization has no influence on the classification results.

When comparing the results from the sets that use only L bands (Sirc2 and Sirc5), the classification results

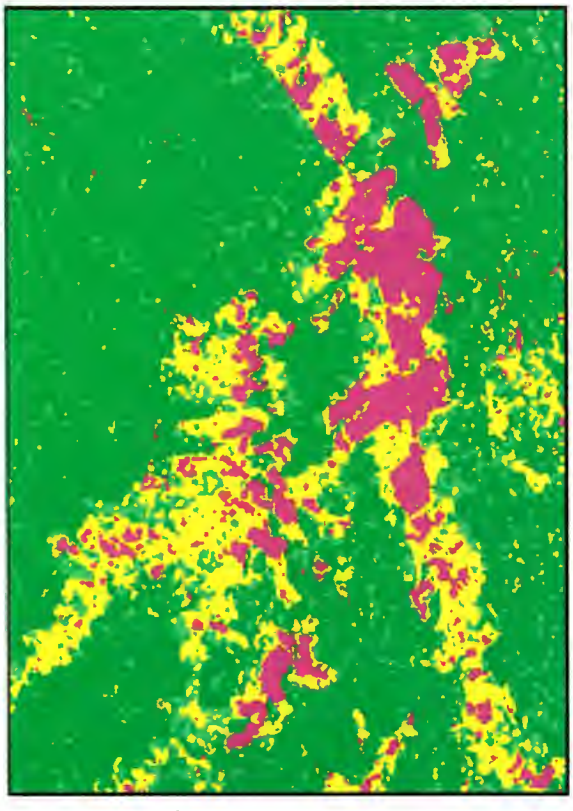

Figure 4: ICM classification using Sirc5 set.

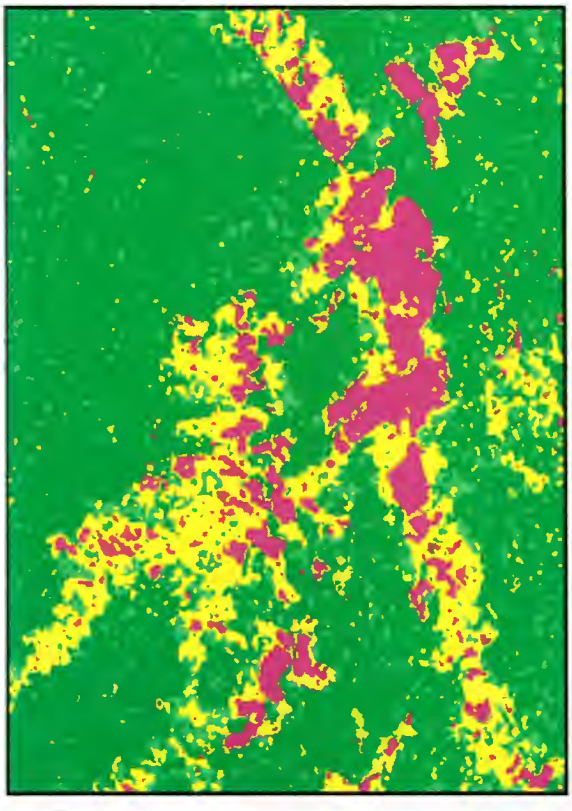

Figure 5: ICM classification using Sirc7 set.

for Sirc5 are better than those obtained for Sirc2, which means that the features information discriminate better than only tonal information.

TABLE 7 – Confusion matrix for the Sirc5 set classification.

| Classes\ Classif | RecAct | NewReg | OldReg | Forest |
|---|---|---|---|---|
| **RecAct** | 89.5 | 10.5 | 0.0 | 0.0 |
| **NewReg** | 7.1 | 50.7 | 19.5 | 22.7 |
| **OldReg** | 4.7 | 28.1 | 53.2 | 14.0 |
| **Forest** | 0.7 | 4.9 | 8.3 | 86.1 |
| $\hat{K} = 0.4952$ | | $\hat{\sigma}^2_{\hat{K}} = 2.3988 \times 10^{-5}$ | | |

TABLE 8 – Confusion matrix for the Sirc7 set classification

| Classes\ Classif | RecAct | NewReg | OldReg | Forest |
|---|---|---|---|---|
| **RecAct** | 89.5 | 10.5 | 0.0 | 0.0 |
| **NewReg** | 7.0 | 52.7 | 18.3 | 22.0 |
| **OldReg** | 5.5 | 28.5 | 53.9 | 12.1 |
| **Forest** | 0.6 | 5.1 | 8.7 | 85.6 |
| $\hat{K} = 0.4967$ | | $\hat{\sigma}^2_{\hat{K}} = 2.3355 \times 10^{-5}$ | | |

However, associating the textural information and the tonal information provided by four original bands (Sirc9 set) increase the percentage of pixels of the NewReg and OldReg classes that were correctly classified (**Table 9**), by decreasing the misclassification of pixels from these classes as belonging to the Forest class.

It can be seen from the classification results of the five sets that there is not a significant modification on the classification of the RecAct class. The use of the features bands or C bands on the classification decreases the misclassification of Forest pixels as regeneration classes, but the features bands seem to be better than C bands for this purpose. The Sirc5, Sirc7 and Sirc9 classifications (**Figures 4** to **6**) appear cleaner than those that only use the original bands (**Figures 2** and **3**). The areas of OldReg were better classified when the textural features and C bands are used.

The pixels of OldReg class misclassified as NewReg class is the largest error found on the classifications. It is of about 50% for Sirc2 and Sirc4 images and it is reduced by half for Sirc5, Sirc7 and Sirc9 images.

Using only the original bands (Sirc2 and Sirc4 sets) the RecAct was the class with the best classification (90% of the pixels), followed by Forest (66%), NewReg (64%) and OldReg (31%). When textural features are added, these percentages values are RecAct (89%), Forest (86%), OldReg (55%) and NewReg (53%). These results can be seen as good due to the complexity

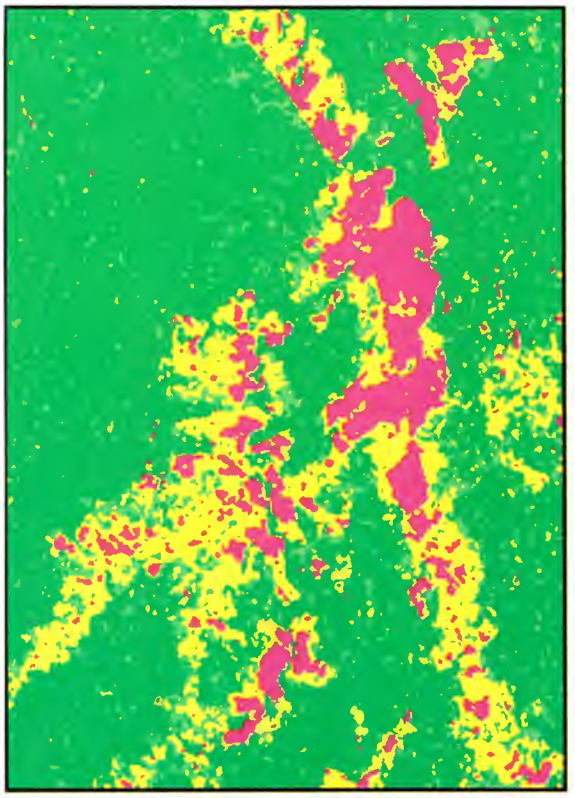

Figure 6: ICM classification using Sirc9 set.

of the study area and taking into account that the classification was done using only radar images.

The Z tests for all pairs of Kappa values were performed and they can be considered different at 95% confidence level, except for Sirc5 and Sirc7 sets. Therefore, the best classification result was obtained using Sirc9 set.

TABLE 9 – Confusion matrix for the Sirc9 set classification

| Classes\ Classif | RecAct | NewReg | OldReg | Forest |
|---|---|---|---|---|
| **RecAct** | **89.3** | 10.6 | 0.0 | 0.1 |
| **NewReg** | 7.0 | **56.8** | 18.0 | 18.2 |
| **OldReg** | 5.5 | 29.1 | **58.4** | 7.0 |
| **Forest** | 0.5 | 4.2 | 8.7 | **86.6** |
| $\hat{K} = \mathbf{0.5328}$ | | $\hat{\sigma}^2_{\hat{K}} = 2.2755 \times 10^{-5}$ | | |

## 5 Conclusions

This work showed a methodology for analysis and selection of attributes (features) for image classification. The methodology was applied to SIR-C images aiming at the discrimination of four types of land use on the Brazilian Amazonia. From the results it can be concluded that the SIR-C images have good discriminatory potential to separate the classes of interest. The results presented in this paper encourages further studies in this field of research.

From the five selected features it could be noted that the L band has, in general, more information than the C band to discriminate the classes used in this study. The L-HV band/polarization seems to be the best data to discriminate these classes. The selected features include textural and tonal information features showing that the both information are important for SAR image classification purposes. The $\alpha$ parameter of the K-Amplitude distribution shows gather some important textural information for discriminating regeneration classes from the others.

The best results were obtained for the classes of Recent Activities and Primary Forest, showing that is possible to map recent deforested areas using SIR-C data. The worst results of classification were obtained for New Regeneration and Old Regeneration. The task of discriminating these two classes is difficult even when using optical data (LANDSAT/TM images, for instance). The results showed that the Recent Activities class can be discriminated from the other classes using only tonal information, but textural attributes are necessary to discriminate the other classes. The C bands are important to discriminate Old Regeneration and Primary Forest classes. The use of features improves the classification of the Old Regeneration class by decreasing the misclassification of pixels from this class as New Regeneration class, but the confusion between these two classes are still large.

The distance measure used (Euclidean distance) to select the features with highest discriminatory power does not consider variations among and within classes. Thus other measures for selecting features may be used to improve the results. Other textural attributes (not only statistical and distributional) or another classification technique may be used to improve the classification results.

## References


Brown, S.; Lugo, A.. Tropical secondary forest. *Journal of Tropical Ecology*, 6, pp.1-32, 1990.

Frery, A.C.; Müller, H.J.; Yanasse, C.C.F.; Anna, S.J.S A model for extremely heterogeneous clutter. *IEEE Trans. Geosc. Rem. Sens.*, 35(3):1-12, 1997a.

Frery, A.C.; Yanasse, C.C.F.; Vieira, P.R.; Sant' Anna, S.J.S.; Rennó, C.D. A user-friendly system for synthetic aperture radar image classification based on grayscale distributional properties and context. Simpósio Brasileiro de Computação Gráfica e Processamento de Imagens, 10., 1997, p. 211-218. *SIBGRAPI 97*. Los Alamitos, CA, IEEE Computer Society, 1997b.

Instituto Nacional de Pesquisas Espaciais (INPE). INPE atualiza os dados do desflorestamento na Amazônia, de 1995 a 1997. INPE Notícias, N° 13, p. 1-2, jan-fev de 1998.

Le Toan, T.; Beaudoin, A.; Riom, J.; Guyon, D. Relating forest biomass to SAR data. *IEEE Trans. Geosc. Rem. Sens.*, 30:403-411, 1992.

Luckman, A.J.; Frery, A.C.; Yanasse, C.C.F.; Groom, G.B. Texture in airborne SAR imagery of tropical forest and its relationship to forest regeneration stage. *International Journal of Remote Sensing*, 18 (6): 1333-1349, 1997a.

Luckman, A.J.; Baker,J.; Kuplich, T.M.; Yanasse, C.C.F.; Frery, A.C. A study of the relationship between radar backscatter and regenerating tropical forest biomass for spaceborne SAR instruments. *Remote Sensing of Environment*, 60: 1-13, 1997b.

Ma Z. and Redmond, R.L. Tau coefficients for accuracy assessment of classification of remote sensing data. *Photogrammetric Engineering and Remote Sensing*, 61(4):435-439, April, 1995.

Ranson. K.J.; Saatchi, S.; Sun, G. Boreal forest ecosystem characterization with SIR-C/XSAR. *IEEE Transactions on Geoscience and Remote Sensing*, 33 (4): 867-876, July, 1995

Schimel, D.; Enting, I.G.; Heimann, M.; Wigley, T.M.L.; Raynaud, D.; Alves, D.; Siegenthaler, U. $CO_2$ and the carbon cycle. In: Climate Change 1994, Radiative Forcing of Climate Change and An Evaluation of the IPCC IS92 Emission Scenarios. Cambridge University Press, pp.35-71, 1995.

Sant'Anna, S.J.S.; Yanasse, C.C.F.; Hernandes, P.F.; Kuplich, T.M.; Dutra, L.V.; Frery, A.C.; Santos, P.P. Secondary forest age mapping in Amazonia using multi-temporal Landsat/TM imagery. In: 1995 International Geoscience and Remote Sensing Symposium, Italy, Jul. 10-14, 1995. *Quantitative remote sensing and applications*. Florence, Italy, IEEE, v. 1, p.323-325.

Sant'Anna, S.J.S.; Yanasse, C.C.F.; Frery, A.C. Estudo comparativo de alguns classificadores utilizando-se imagens RADARSAT da região de Tapajós. In: Primeras Jornadas Latinoamericanas de Percepción Remota por Radar: Técnicas de Procesamiento de Imágenes. Buenos Aires, Argentina, dez.~1996, *Workshop Proceedings*. ESA, 1997, p. 187-194. (ESA SP-407).

Soares, J.V.; Rennó, C.D.; Formaggio, A.R.; Yanasse, C.C.F.; Frery, A.C. An investigation of selection of texture features for crop discrimination using SAR image. *Remote Sensing of Environment*, 59 (2): 234-247, 1997.

Vieira, P.R. *Desenvolvimento de classificadores de máxima verossimilhança e ICM para imagens SAR*. (MSc in Remote Sensing) – Instituto Nacionsl de Pesquisas Espaciais. São José dos Campos, SP, Brazil, 1996. 251 p. (INPE-6124-TDI/585).

Vieira, P.R.; Yanasse, C.C.F.; Frery, A.C.; Sant' Anna, S.J.S. Um sistema de análise e classificação estatística para imagens SAR. In: Primeras Jornadas Latinoamericanas de Percepción Remota por Radar, Buenos Aires, Dez. 1996. *Técnicas de Processamiento de Imágenes*. Paris, ESA, 1997. p. 170-185.

Yanasse, C.C.F.; Sant' Anna, S.J.S.; Frery, A.C.; Rennó, C.D.; Soares, J.V.; Luckman, A.J. Exploratory study of the relationship between tropical forest regeneration stages and SIR-C L and C data. *Remote Sensing of Environment*, 59 (2): 180-190,1997.

# WINDOW SIZE SELECTION FOR TEXTURE IMAGE GENERATION FROM SAR DATA: A CASE STUDY FOR A BRAZILIAN AMAZON TEST SITE

Milton Cezar Ribeiro[1,2]; Diogenes Salas Alves[1]; Corina da Costa Freitas [1]
João Vianei Soares[1]; Fernando Mitsuo II[1]

[1]INPE—National Institute for Space Resource
P.O. 515, 12201- 097 - São José dos Campos, SP, Brazil
{milton,dalves,corina,fii}@dpi.inpe.br, {vianei}@ltid.inpe.br

[2] Science, Applications and Spatial Technology Foundation – FUNCATE
Av. Brigadeiro Faria Lima, 3305, Martin Cerere
12225-000 – São José dos Campos, SP, Brazil

**Abstract.** The goal of this paper is to test several window sizes for generation of SAR texture images. Two JERS-1 and one Radarsat images were used. A total of 69 known targets in Rondônia State, Brazilian Amazon were used and classified in six cover classes. Five window sizes - 5x5, 7x7, 9x9, 11x11 and 15x15 pixels - were tested. Fourteen texture images were generated for each window size, resulting in 210 texture images. For all these images Mahalanobis distances we computed for each paired cover classes. For JERS-1 the best window sizes were 7x7 and 11x11. Regarding the Radarsat image, the largest window size (15x15) used appears to be small, denoting that greater window sizes might be tested. The best discrimination, for JERS-1 images, was between recent deforestation and pasture, while Radarsat presented best discrimination between pasture and mature forest. JERS-1 showed to be better than Radarsat for land cover mapping.

**Keywords:** SAR, window size, texture measures, Amazonia

## 1. Introduction

The tropical rain forest plays an important role in the biogeochemical, hydrological and climatic cycles. A large amount of $CO_2$ is launched into atmosphere because of biomass burning, following deforestation (Schimel *et al.*, 1995) .

Since the 70's, optical remotely sensed data has been used for monitoring of natural areas. These data have been used for land cover/land change mapping, allowing the identification of several cover classes like crop fields, bare soil, pasture, secondary forest and mature forest. In some regions, the high cloud cover is a limitation for using optical data. An example is the last mapping of deforestation on the Brazilian Amazon Basin (INPE, 1998), where the Amapá State could not be mapped due to the absence of low cloud cover images.

Synthetic Aperture Radar (SAR) images have been used as an alternative source of data for land cover mapping. Luckman *et al.* (1997) studied the relationship between backscatter and regenerating forest biomass and found that these data could provide useful information for above-ground biomass estimation. Rennó and Soares (1996), using SIR-C/X-SAR for crop discrimination at Pernambuco State, Brazil, found that the classification accuracy assessed by the *Kappa* coefficient of agreement reached up to *0.9* when several texture measures were used. Rignot *et al.* (1996) used SIR-C and Landsat TM data for deforestation and secondary growth mapping in Rondônia/Brazil and found that multi-band cross-polarized SAR data were important for classification. Yanasse *et al.* (1996) tested the relationship between regenerating stages and SIR-C (L-band, C-band, cross-polarized) data, and noticed that the coefficient of variation for L-HH and L-HV data presented an inverse relationship with regeneration stages.

Tonal and textural information have been used for explore better SAR data. Sant'Anna *et al.* (1996) used the Frost filter, Coefficient of variation and the $\alpha$ parameter of $\kappa$-amplitude distribution. They classified a subset of a Radarsat image using three different algorithms: a) maximum likelihood, b) Interacted Conditional Modes (ICM) and c) region growing segmentation/Bhattacharya. The authors concluded that, for mapping bare soil/pasture, secondary forest and mature forest the best *kappa* value were found when Frost and $\alpha$ parameter filtered images were classified by ICM algorithms.

From the above, it is evident that the importance of using textural measures for SAR classification. These measures may be obtained using filtered images with a moving window of a certain size. However the proper size of the window is dependent on the used measure, on type of application and on the used data.

In this work five window sizes are investigated and used on the generation of Haralich's texture images, from two JERS-1 (L-band, HH) and one Radarsat (C-band, HH) data, in order to SAR classification and land cover mapping.

## 2. Test site and ground truth

The test site is located at Rondônia State, western Brazilian Amazon, with central coordinates S09°30'/W62°50' (**Figure 1**). The region presents a slightly undulated terrain, with an average annual rainfall of about 2,200mm, mean annual temperature of 23,6°C (H.Schimitz, unpublished data), and a dry season from late April to late August.

After the 70's decade the settlement of small farmers began along the BR-364 highway. As a consequence forest has been clear cut to allow crop fields and pasture establishment. Deforested land is used for some years and when soil looses its fertility the areas are sometimes abandoned, leading to forest regeneration (Uhl *et al.*, 1988).

Aerial reconnaissance was performed during the first survey on July/96 and about a hundred aerial photos at 1:15,000 scale were taken. During September/96, several targets of interest were visited, GPS coordinates along the roads were taken, and the land cover for each target was analyzed. Interviews with local people have been made, asking about the age of secondary forest areas and management techniques.

## 3. Land cover and regeneration stages map generation

A Regeneration-stage map was built using multi-temporal series of Landsat images from 1985 to 1996. These images were registered using the Landsat 1995 image as the reference. The ENVI (Environment for Visualizing Image) system was used to perform this task. Target contours were digitized on the screen, over a subregion of 24x18 km and cover classes were assigned to each region defined by the contours. The cover classes of interest were: a) RD: recent deforestation, b) PA: pasture/bare soil, c) YSF: young secondary forest (2-4 years), d) ISF: intermediate secondary forest (5-8 years), e) OSF: old secondary forest (9-13 years) and f) MF: mature forest. Aerial photos and GPS coordinates were also helpful in the map generation. **Figure 2** shows the target contours superimposed on Landsat TM5 1996 imagery, as well as their cover classes. **Table 1** presents a list of the cover classes, their number of targets and total area per class.

## 4. SAR data set

In this work, two JERS-1 (L-band, HH-polarized) and one Radarsat (C-band, HH-polarized) amplitude images were used. The imaging date were May 28 and July 11, 1996 for JERS-1 images and August 19/1996 for the Radarsat image. These images presents 12.5m of pixel spacing, and are on 16 bits format. JERS-1 was generated by National Space Development Agency of Japan (NASDA) and Radarsat was generated by Canadian Center for Remote Sensing (CCRS).

## 5. Image processing

JERS-1 and Radarsat data were read using ENVI and PCI systems, respectively. Both images were firstly converted from 16 to 8 bits to save disk space and to turn computer processing easier. SAR images were registered using the Landsat 1995 image as the reference. As Landsat images presents 30m resolution, all three SAR images were also converted to this same resolution, using a linear transformation and nearest neighbor resampling. A subset image of 800x600 pixels was selected for each SAR data, containing 69 targets.

## 6. Texture image generation

For each SAR image fourteen Haralick's texture images were generated, based on the Gray Level Co-occurrence Matrices (GLCM). Soares *et al.* (1997) presented a review for the used textures here. Five window sizes were used: 5x5, 7x7, 9x9, 11x11 and 15x15 pixels. It were generated 14 (textures) x 5 (window sizes) x 3 (SAR image), with a total of 210 texture images. These 210 texture images were normalized to have mean zero and unitary standard deviation. **Table 2** presents a list with all texture measures and the average value calculated per cover classes, using July 11/JERS-1 data and the 11x11 moving window. Results presented on **Table 2** will be discussed on future works. **Figure 3** shows some illustrative color composition of texture images for JERS-1 (July 11) and Radarsat (August 19) data.

## 7. Results

The Mahalanobis distances (D2) were computed for all two-by-two cover classes combination for each window size and texture measures. The SAS (Statistical Analysis System) software was used to compute all D2 values. Small values of D2 denote that two classes are similar, or can not be discriminated, and large values of D2 mean that the pair of classes are dissimilar or well discriminated. **Figures 4** and **5** show D2 values obtained for some paired cover classes for JERS-1 data recorded on May 28 and July 11, respectively, and **Figure 6** presents the same results obtained for Radarsat data. Paired cover classes with D2 less than 2.0 were not presented here.

Observing the Mahalanobis distances for the JERS-1 image collected on May 28 (**Figure 4**), a general tendency of 7x7 window to present the best results can be noticed. Note that windows greater than 7x7 pixels show a decline of their D2 for many of texture measures and paired cover classes. One could

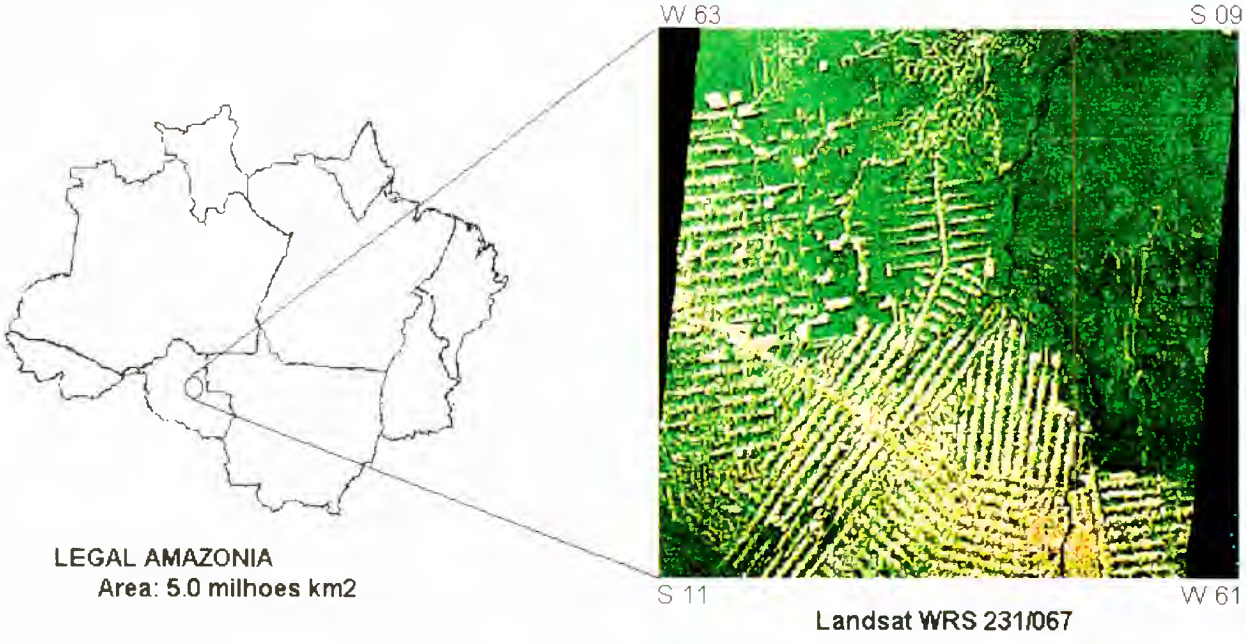


Figura 1: Site test Location and Landsat TM 5 (WRS 231/067) image.

Figure 2: Target contours superimposed on Landsat TM5 band (1996) image. Legend: •-RD (Recent Deforestation), •-PA (Pasture), •-YSF (Young Secondary Forest), •-ISF (Intermediate secondary Forest), •-OSF (Old Secondary Forest), •-MF (Mature Forest)

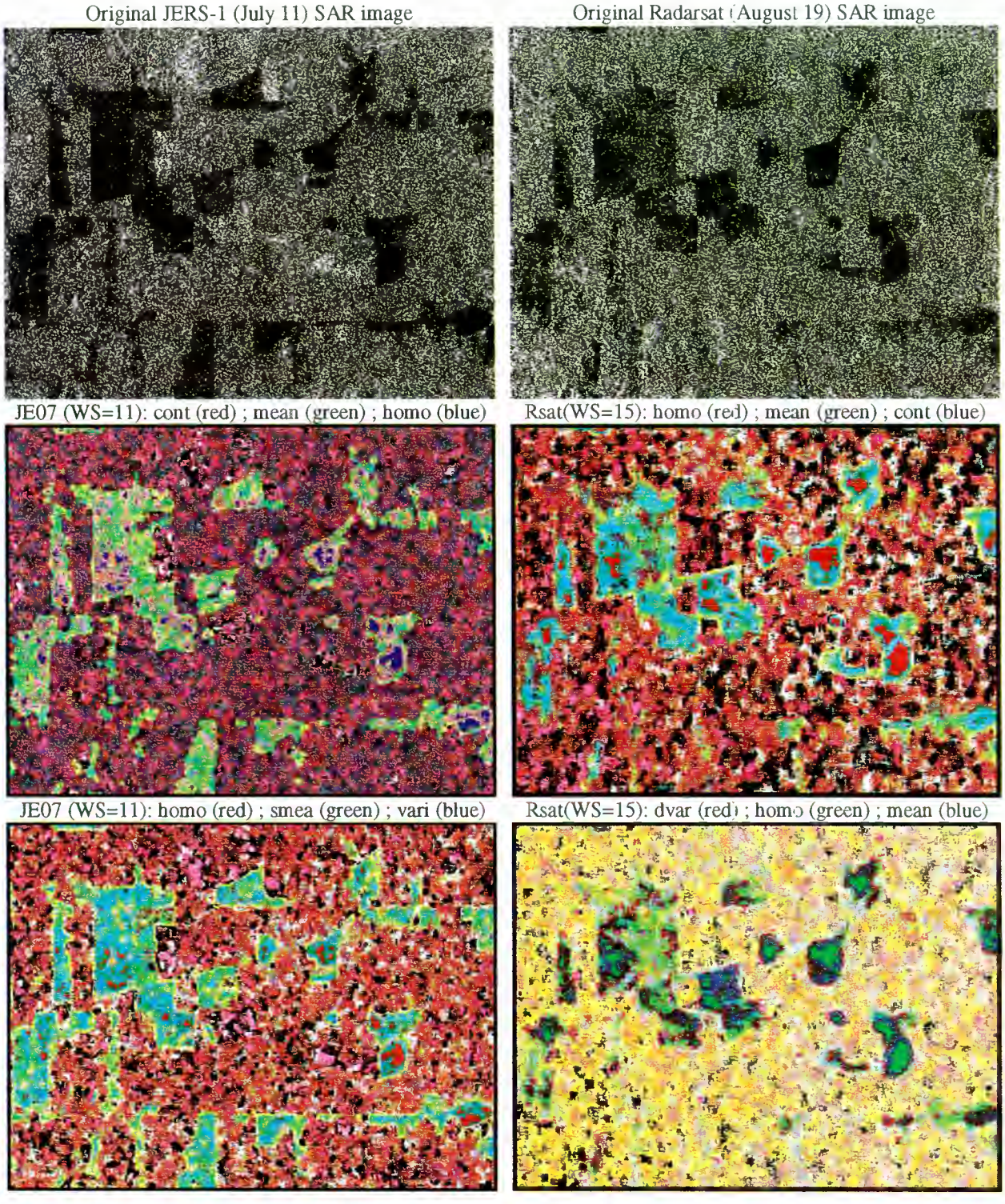


Figure 3: Color composition for original and texture SAR images. Legend: Rsat (Radarsat, August 19) ; JE07 (JERS-1, July 11) ; cont (Contrast) ; mean (Mean) ; homo (Local Homogeneity) ; smea (Mean of Sum Vector) ; vari (Variance) ; dvar (Variance of Difference Vector) ; WS (window size)

also verify that the biggest D2 value was obtained when comparing RD and PA cover classes.

**Figure 5** (JERS-1 for July) shows the same behavior observed in **Figure 4**, but in this case the selected window size was 11x11 and not 7x7 pixels. Possibly it may be related to changes in vegetation phenology and associated water content in forest area along the dry season of region.

Comparing **Figure 4** and **Figure 5** for JERS-1 texture images, it can be noticed that, for May, the RD class was only well discriminated from PA and for July it can be noticed a good discrimination between RD and all other cover classes. In fact, when Landsat images for May and July/1996 were checked, it was observed that when JERS-1 image was collected on May 28, some targets appear on clear cut process, with part of their area still covered by MF class. On July 11, all targets selected as belonging to RD class were completely deforested.

Analyzing D2 values for Radarsat imagery (**Figure 6**), one could verify that an ascendant tendency is showed when larger window sizes are used. Unfortunately it is difficult to say, for our study case, what is the best window size for Radarsat because no result for windows greater than 15x15 pixels were computed. Looking at the D2 values for both JERS-1 and Radarsat images, one could find that RD-PA, PA-YSF, PA-ISF, PA-OSF and PA-MF are even better discriminated. In other words, the pasture (PA) class presents a high level of discrimination and if one has interest on this particular class both JERS-1 and Radarsat images could provide good information.

In general terms, the JERS-1 image presented better discrimination between classes when compared to Radarsat. It is interesting to notice that RD and PA were poorly discriminated with Radarsat, but they were the best separable classes in JERS-1 data. Possibly it is related to the band that each sensor operates, where Radasat (C-HH) is more sensitive to canopy cover, while JERS-1 presents good response to vegetation components such as trunk and steam. For JERS-1 the remaining ground cover just after the clear cut process (unburned slash trunks and steams) could contribute with the best discrimination between RD and PA cover classes.

**Conclusions**

For the Radarsat image it was noticed that the five herein tested window sizes were still small, denoting that on future studies windows greater than 15x15 pixels should be tested. For texture measures classification purpose, the presented results lead us to choose 7x7 and 11x11 for JERS-1 (May, July) and 15x15 for and Radarsat images.

**References**


Instituto Nacional de Pesquisas e Estudos Espaciais (INPE). INPE atualiza os dados de desflorestamento na Amazônia, de 95 a 97. INPE notícias. No. 13, p.1-2, Jan.-Fev. de 1998.

Luckman, A.; Baker, J.; Kuplich, T.M.; Yanasse, C.C.F.; Frery, A.C. A study of the relationship between radar backscatter and regenerating tropical forest biomass for spaceborne SAR instruments. Remote Sensing of Environment, 60, pp.1-13. 1997.

Rennó, C.D.; Soares, J.V. Utilização de medidas texturais na discriminação de classes de uso do solo do perímetro irrigado de Bebedouro, Pernambuco, Brasil, utilizando-se imagens SAR. In: Proceeding of the first Latino-American Seminar on Radar Remote Sensing – Image Processing Techniques, Buenos Aires, Argentina, 2-4 Dec., 1996, pp.171-177. 1996.

Rignot, E.; Salas, W.A.; Skole, D.L. Mapping deforestation and secondary growth in Rondonia, Brazil, using imaging radar and thematic mapper data. Remote Sensing of Environment, 59, pp.167-179. 1997.

Sant'Anna, S.J.S.; Yanasse, C.C.F.; Frery, A.C. Estudo comparativo de alguns classificadores utilizando-se imagens Radarsat da região de Tapajós. In: Proceeding of the first Latino-American Seminar on Radar Remote Sensing – Image Processing Techniques, Buenos Aires, Argentina, 2-4 Dec., 1996, pp.187-194. 1996.

Schimel, D.; Enting, I.G.; Meimann, M.; Wigley, T.M.L.; Raynand, D.; Alves, D.; Seigenthaler, U. $CO_2$ and the carbon cycle. In. J.T. Houghton, L.G.; Meira Filho, J.; Bruce, B.A.; Lee, H.; Callander, E.; Haites, N.; Harris; Maskell, K., editors, Climate change 1994: radiactive forcing of climate change and an evaluation of the IPCC 1992 emission scenaries, pp.35-71. Cambridge University Press, 1995.

Soares, J.V.; Rennó, C.D.; Formaggio, A.R.; Yanasse, C.C.F.; Frery, A.C. An investigation of selection of texture features for crop discrimination using SAR image. Remote Sensing of Environment, 59, pp.234-247. 1997.

Uhl, C.; Buschbacker, R.; Serrão, E.A.S. Abandoned pastures in eastern Amazonia: I-patterns of plant succession, Journal of Ecology, 76, pp.663-681. 1988.

Yanasse, C.C.F.; Sant'Anna, S.J.S.; Frery, A.C.; Rennó, C.D.; Soares, J.V.; Luckman, A.J. Exploratory study of the relationship between tropical forest regeneration stages and SIR-C L and C data. Remote Sensing of Environment, 59, pp.180-190. 1996.

Table 1: Survey fields summary for six studied cover classes

| COVER CLASS | # of targets | # of pixels | Area (ha) |
|---|---|---|---|
| 1) Recent Deforestation (RD) | 5 | 6,448 | 580.32 |
| 2) Pasture or bare soil (PA) | 17 | 12,883 | 1,159.47 |
| 3) Young Secondary Forest (YSF) | 11 | 5,109 | 459.81 |
| 4) Intermediate Secondary Forest (ISF) | 9 | 4,872 | 438.48 |
| 5) Old Secondary Forest (OSF) | 23 | 12,927 | 1,163.43 |
| 6) Mature Forest (MF) | 4 | 30,557 | 2,750.13 |
| **Total** | 69 | 72,796 | 6,551.64 |

Table 2: Average texture measures for each cover class, computed using 11x11 window size and the JERS-1 image obtained on July 11, 1996.

| Haralick's Texture Measures | COVER CLASSES | | | | | |
|---|---|---|---|---|---|---|
| | RD | PA | YSF | ISF | OSF | MF |
| 1) Mean (mean) | 1.23 | -1.33 | 0.02 | 0.20 | 0.26 | 0.53 |
| 2) Variance (vari) | 0.70 | -1.28 | -0.01 | 0.20 | 0.12 | 0.36 |
| 3) Energy (ener) | 2.25 | 0.17 | -0.03 | 0.20 | -0.02 | 0.04 |
| 4) Correlation (corr) | -0.36 | 0.93 | -0.03 | -0.04 | -0.21 | -0.45 |
| 5) Entropy (entr) | 0.05 | 0.17 | 0.20 | 0.18 | 0.20 | 0.19 |
| 6) Contrast (cont) | 0.78 | -1.35 | -0.01 | 0.18 | 0.16 | 0.50 |
| 7) Homogeneity (homo) | 1.63 | 0.75 | -0.02 | 0.24 | -0.09 | -0.10 |
| 8) Dissimilarity (diss) | 0.65 | -1.06 | 0.07 | 0.20 | 0.21 | 0.46 |
| 9) Mean of sum vector (smea) | 1.13 | -1.34 | 0.03 | 0.20 | 0.27 | 0.53 |
| 10) Variance of sum Vector (svar) | 0.37 | -1.09 | 0.02 | 0.19 | 0.09 | 0.21 |
| 11) Entropy sum vector (sent) | 0.14 | -0.02 | 0.18 | 0.18 | 0.19 | 0.20 |
| 12) Mean of difference Vector (dmea) | 0.65 | -1.06 | 0.07 | 0.20 | 0.21 | 0.46 |
| 13) Variance difference Vector (dvar) | 0.69 | -1.27 | 0.02 | 0.20 | 0.16 | 0.44 |
| 14) Entropy difference Vector (dent) | 0.23 | -0.12 | 0.17 | 0.19 | 0.20 | 0.24 |

RD=Recent Deforestation PA=Pasture or bare soil YSF=Young Secondary Forest
ISF=Intermediate Secondary Forest OSF = Old Secondary Forest MF = Mature Forest

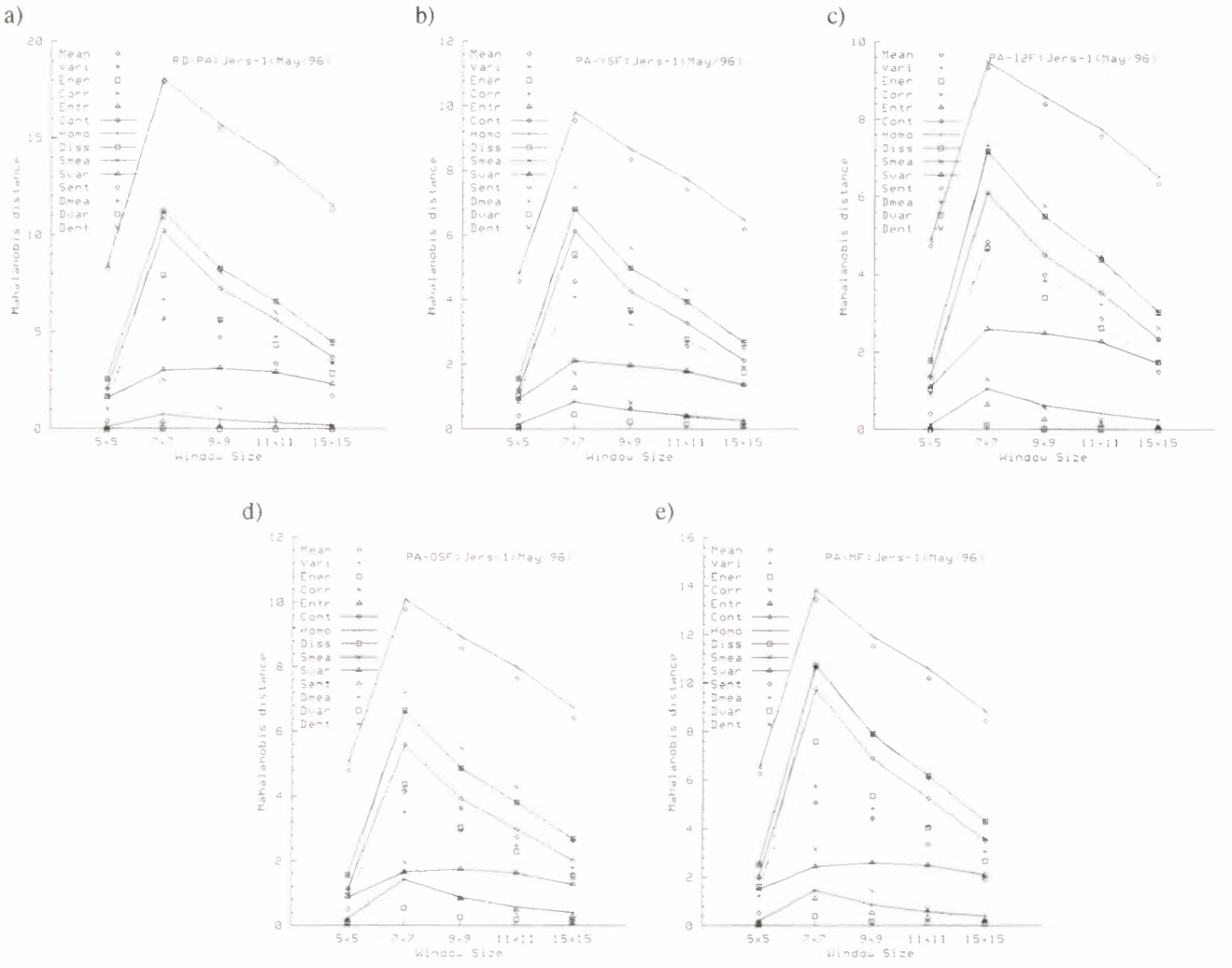


Figure 4: Mahalanobis distances obtained for paired cover classes comparisons, using Haralick's texture measures computed for JERS-1 (May 28, 1996) image. a) RD-PA b) PA-YSF c) PA-ISF d) PA-OSF e) PA-MF

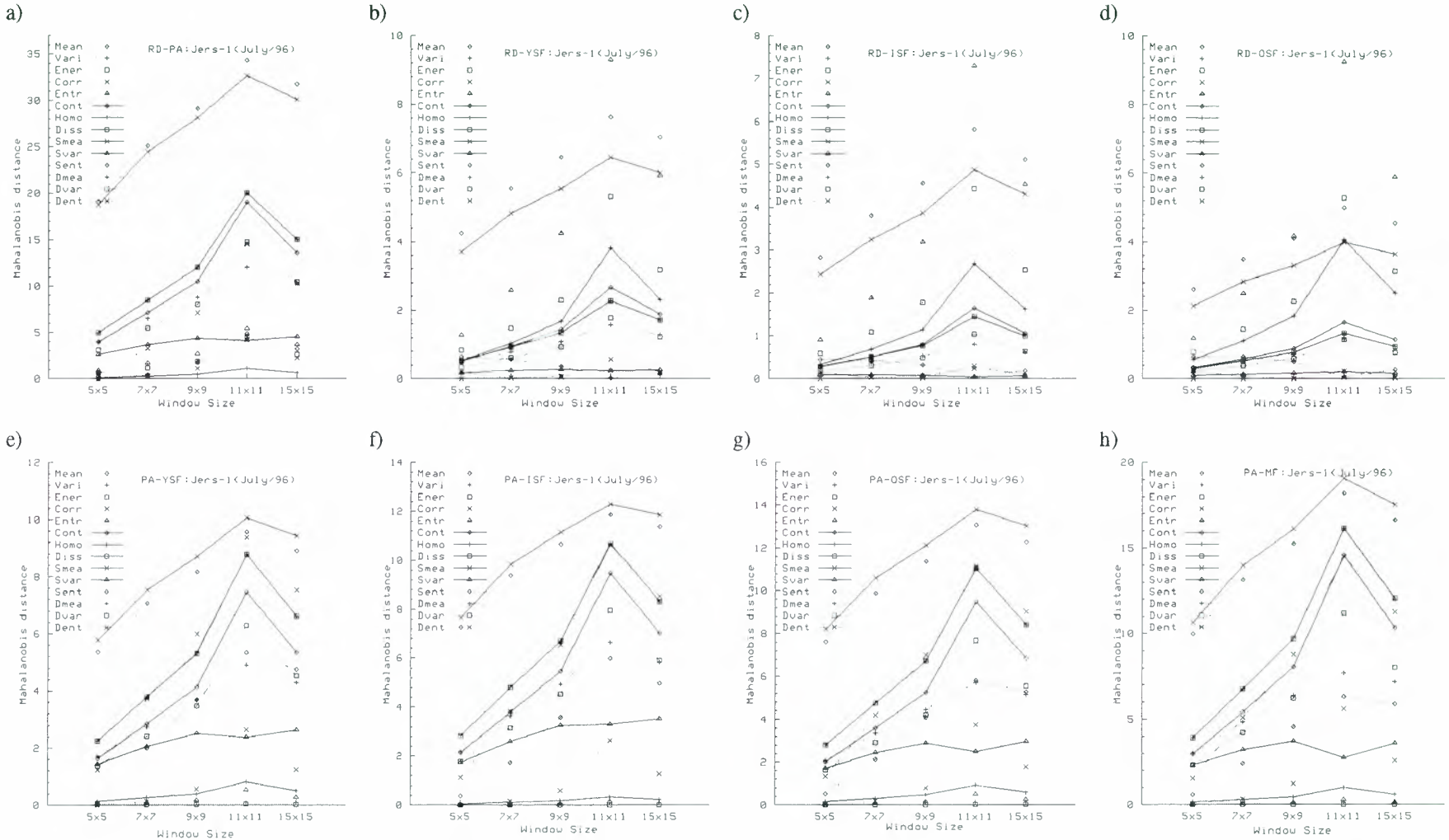


Figure 5: Mahalanobis distances obtained for paired cover classes comparisons, using Haralick's texture measures computed for JERS-1 (July 11, 1996) image. a) RD-PA b) RD-YSF c) RD-ISF d) RD-OSF e) PA-YSF f) PA-ISF g) PA-OSF h) PA-MF

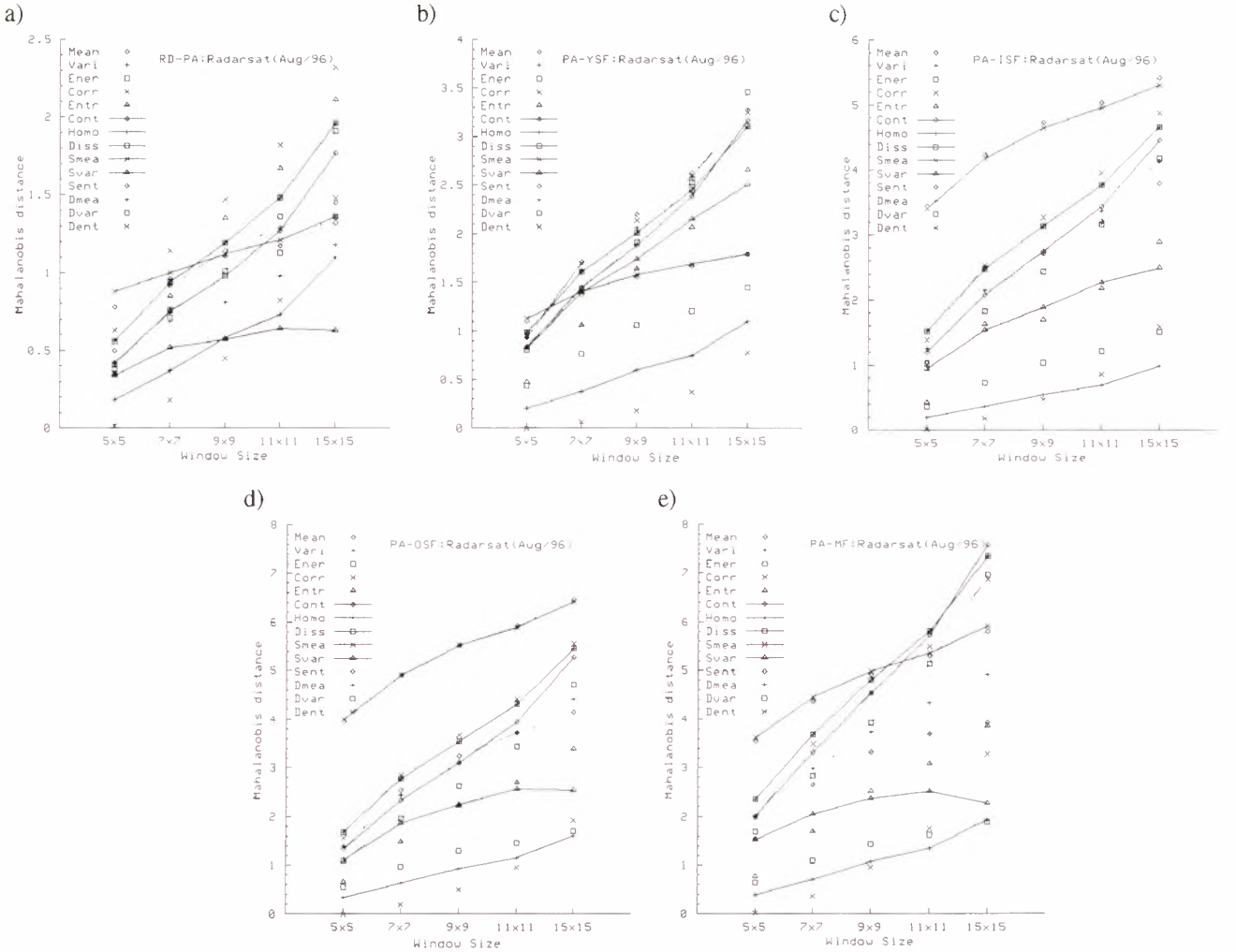


Figure 6: Mahalanobis distances obtained for paired cover classes comparisons, using Haralick's texture measures computed for Radarsat image (August 19, 1996). a) RD-PA b) PA-YSF c) PA-ISF d) PA-OSF e) PA-MF

# SEGMENTATION OF SAR IMAGES USING QUADTREE AND POTTS MODEL

*Olimpia Arellano Neri, Miguel Moctezuma Flores and *Flavio Parmiggiani*

Faculty of Engineering, DEPFI-UNAM, Cd. Universitaria, Apdo. Postal 70-256, Mexico,D.F., Mexico.
Fax: (52 5) 616.10.73, email:olimpia@verona.fi-p.unam.mx.
*Istituto per lo Studio delle Metodologie Geofisiche Ambientali, IMGA-CNR.
Via Gobetti 101, 40129, Bologna, Italy.

**Abstract**: This paper presents a contextual classifier based on quadtree structures and Markov random fields theory. The initial classification is realized by a clustering algorithm, then for each level of the tree, boundary regions are found. Pixels of boundary regions are classified by using a combination of nearest class mean criterion, Mahalanobis distance criterion and finally a Markov model. Our scheme is simple to implement and performs well, giving satisfactory results for SAR images.

## Introduction

The use of synthetic aperture radar (SAR) images instead of visible range images is becoming more popular, because of their capacity of imaging even in case of adverse meteorological conditions. Unfortunately the poor quality of some SAR images makes it difficult to extract information and even more to guarantee a good positioning of the detection. For this reason, it is necessary to define general parameter estimation methods which must be robust to radiometrical variations and to degradations introduced by speckle.

We propose a semiautomatic scheme of segmentation which is applied to SAR images. This method consist on three main steps. The first two steps concern quadtree structures in order to obtain low resolution estimation of boundaries. Hierarchical approaches are well adapted to the processing of high resolution data. The last step concerns segmentation of boundary regions at high resolution. The tested data consist on ERS-1 images with a spatial resolution of 12.5 m per pixel.

## 1 Quadtree Structures

Consider an N x N image d(i,j) defined for $0 < (i,j) < N$ and $N=2^m$ (m is the number of the tree's levels). The quadtree of this image is defined as [Schneier (1979)]:

$$q(i,j,k) = \frac{1}{4}\left[ q(2i,2j,k-1) + q(2i+1,2j,k-1) + q(2i,2j+1,k-1) + q(2i+1,2j+1,k-1) \right]$$

where: $0 < k \le m$, $0 \le (i,j) < 2^{m-k}$, and

$q(i,j,0) = d(i,j)$

Hence a quadtree is based on 2 x 2 block averaging. The level just above the base consists of nodes representing non-overlapping 2 x 2 blocks of pixels in the original image so that the size of this level is $2^{m-1} \times 2^{m-1}$. This process can be repeated until the root node is reached, its value is the mean gray level of the entire image.

**Figure 1.1** shows a SAR image with its gray level histogram. **Figure 1.2(a)-(c)** represents level 3 of the smoothing. Also shown are the histograms, indicating an increase in class. Quadtrees are useful in image segmentation because the averaging process reduces the variance of the signal within a single homogeneous region. However, the smoothing procedure also introduces a bias due to merging of data from different regions [Spann and Wilson (1985)].

In the last stage of the process we will obtain an image of only one pixel; then the structure has to be truncated in an optimal level. The election of such level is important because is from here where the first classification takes place. The optimal level is selected subjectively by observing the sequence of the histograms in the smoothing process.

Figure 1.1. Image ERS-1 (Precision Image-PRI, ©ESA) and its histogram. Size of the scene: 256 x 256 pixels, pixel resolution: 12.5 x 12.5 m.

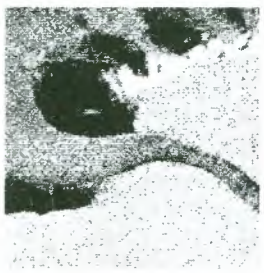

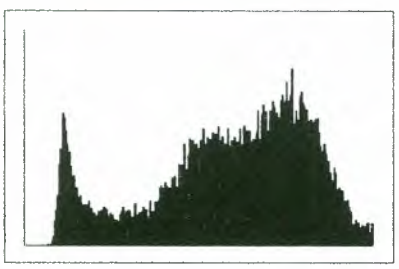

(a) Size:128 x 128 pixels

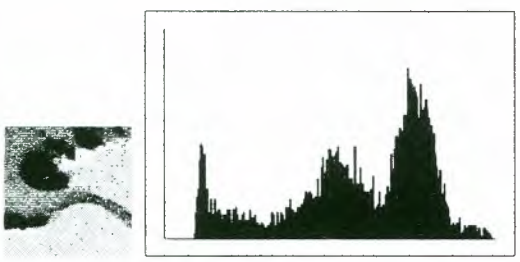

(b) Size:64 x 64 pixels

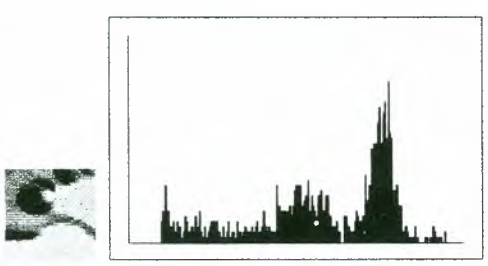

(c) Size:32 x 32 pixels

Figure 1.2(a)-(c). Effects of quadtree smoothing.

For the next stage of processing we consider the level whose histogram shows a reduction in variance at the modes associated to homogeneous regions, and where the bias due to merging of data from different regions is minimum. For the sequence of **Figure 1.2**, the selected level is shown in **Figure 1.2(b)**.

## 2 Low Resolution Classification

In order to define a local centroid, consider a probability density p(x). The local centroid defined at each point x in class space is given by:

$$\mu(x) = x + \frac{\int_{-w}^{w} x' p(x+x')dx'}{\int_{-w}^{w} p(x+x')dx'}$$

This equation states that the local centroid at point x is just the center of mass of the probability distribution calculated over a window of size 2w and centered on x. Since the global probability distribution of an image can not be written as a sum of a set of non-overlapping local distributions, an iterative scheme can be used [Spann and Wilson (1988)].

Let h(x) be the histogram value for position x in the class space. The algorithm works by continually updating the histogram by moving probability masses to the position of their local centroid until no change in the histogram is observed. Hence, if $h^n(x)$ is the updated histogram on the nth iteration, the algorithm proceeds as follows:

$$h^0(x) = h(x)$$

$$\downarrow$$

$$h^n(x) = \sum_{y \in \Omega^n(x)} h^{n-1}(y)$$

where $\Omega^n(\cdot)$ defines the domain of configurations at iteration $n$.

$y \in \Omega^n(x)$ iff

$$x = y + \frac{\sum_{y'=-m}^{m} y' h^{n-1}(y+y')}{\sum_{y'=-m}^{m} h^{n-1}(y+y')}$$

$$\downarrow$$

if

$$h^n(x) = h^{n-1}(x), \quad \forall x$$

$$n = n+1 \leftarrow\leftarrow no \leftarrow\leftarrow \downarrow \rightarrow\rightarrow yes \rightarrow\rightarrow stop$$

In this case the local centroids are computed within a window of width 2m+1. While the convergence properties of the algorithm are hard to determine, it has been observed in practice [Arellano (1997)] that it converges in a small number of iterations (typically 5-15). The number of classes found depends both on the window size and the histogram of the image. By applying the centroid algorithm to the image of **Figure 1.2(b)**, we used a window of 30, so then we obtained a

classified image in 3 classes. **Figure 2(a)-(g)** illustrates the process.

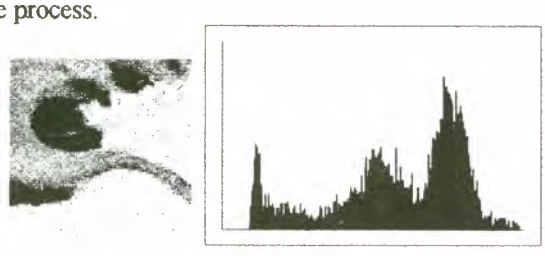

(a) Iteration 0

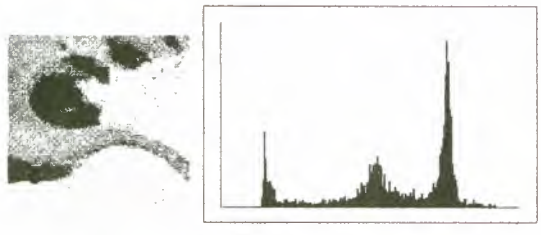

(b) Iteration 1

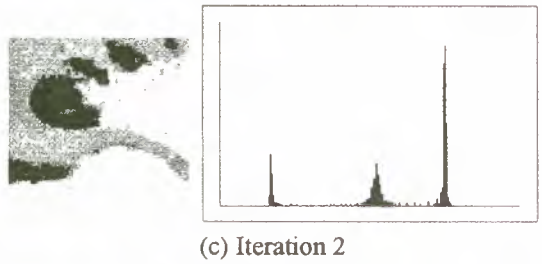

(c) Iteration 2

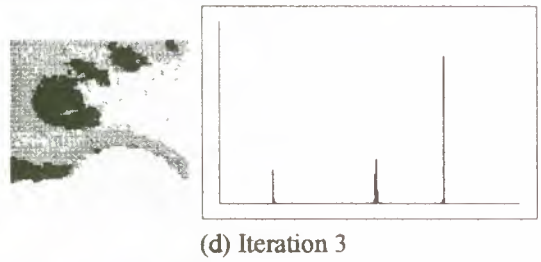

(d) Iteration 3

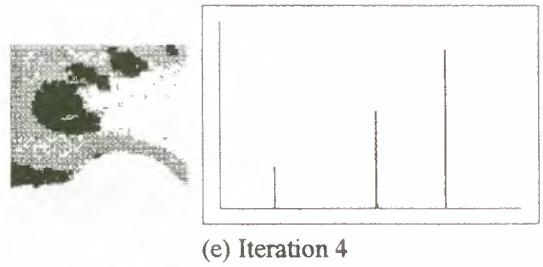

(e) Iteration 4

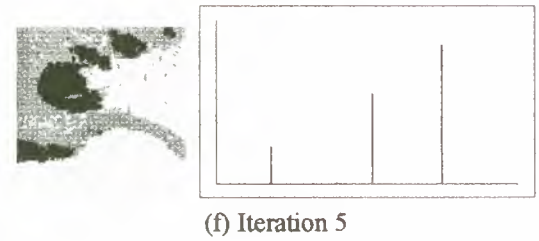

(f) Iteration 5

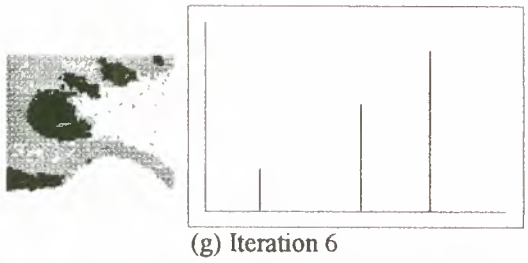

(g) Iteration 6

Figure 2(a)-(g). Local Centroid Clustering Process.

### 3 Boundary Estimation

The quadtree smoothing is a means of trading off resolution in class space with spatial resolution. Hence, following the clustering procedure at the highest quadtree level, each boundary node at this level defines an L x L block of pixels at the lowest quadtree level (highest spatial resolution) with $L= 2^k$, k being the quadtree height. The problem now is restoring the full spatial resolution.

A solution can be found by making an additional assumption. That is that the classification introduced at the highest level of the quadtree is valid at lower levels [Wilson (1985)]. Thus a boundary region is defined; nodes not in the boundary region are given the same class as their father; nodes in the boundary region are classified in such a way that the boundary region width is reduced by a factor of 2 on each step down the quadtree. The result is a boundary between pixels at the lowest level of the tree and thus at full spatial resolution.

A more precise description of the boundary estimation procedure is as follows. The classification is made at level k where a classification at level k+1 has already taken place. Define $q(i,j,k)$ as the $(i,j)$ th node at level k and *c(q(i,j,k))* as the class of this node. At the beginning each node is assigned with the class of its father: $c(q(i,j,k)) = c\left(q\left(\frac{i}{2},\frac{j}{2},k+1\right)\right)$.

From this classification, the boundary region $\Lambda_b(k)$ is defined as:

$(i,j,k) \in \Lambda_b(k) \Leftrightarrow c(q(i,j,k)) \neq c(q(i',j',k'))$,

where $(i',j') \in N_8(i,j)$, the 8-neighbor set of $(i,j)$.

Once $\Lambda_b(k)$ is determined, it is augmented by the set $\Lambda_1(k)$ of nodes which have an 8-neighbor in $\Lambda_b(k)$.

$(i,j) \in \Lambda_1(k) \Leftrightarrow (i',j') \in \Lambda_b(k)$, and $(i',j') \in N_8(i,j)$.

This gives a region of uncertainty defined by the index set $\Lambda_c(k) = \Lambda_b(k) + \Lambda_1(k)$. Since this region of uncertainty is going to be the boundary between pixels at the lowest level of the tree, the classification of pixels of this region should be made with a minimum of errors. In this paper a combination of three criteria was applied in order to define high resolution estimations: nearest

class criterion, Mahalanobis distance and the Potts model.

### 3.1 Nearest Class Mean Criterion

This criterion is applied initially to the region of uncertainty of the image whose size is 64 x 64. This region is smoothed with a filter whose spatial width depends on the estimated signal-noise ratio between regions $\rho_k$ for level k :

$$\Lambda_2(k) = h(i, j, \rho_k) * \Lambda_c(k), \quad \text{where} \quad \rho_k = \frac{(\mu_1 - \mu_2)}{\sigma_k}, \quad \mu_1$$

and $\mu_2$ are the means found by means of the local centroid clustering algorithm and * denotes convolution.

Variance is computed by:

$$\sigma_k^2 = \frac{1}{N(\Lambda'_c(k))} \sum_{(i,j)\in\Lambda'_c(k)} \left[q(i, j, k) - \mu(i, j, k)\right]^2,$$

where $\Lambda'_c(k)$ is the set of non-boundary nodes, $\mu(i, j, k)$ is the mean value, $q(i, j, k)$ is the gray level of pixel $(i, j, k)$, $\mu(i, j, k) = \mu_{c[q(i,j,k)]}$, and $N(\cdot)$ is the number of points inside the region $(\cdot)$.

The filter $h(i, j, \rho)$ of function $\Lambda_2(k)$ is formed by convolution using a *(3x3)* filter.

In the first iteration $h_1(i, j, \rho) = \lambda(\rho), \quad (i, j) = 0,$

then $h_1(i, j, \rho) = \frac{1 - \lambda(\rho)}{8}, \quad -1 \le (i, j) \le 1, \quad (i, j) \ne (0,0).$

The function $\lambda(\rho)$ is a linear function of $\rho$. It was fixed by experimentation, giving maximum smoothing for $\rho < 2$ and no smoothing for $\rho > 8$ . After smoothing, a decision in made on all the nodes in the boundary region using a nearest class criterion. Define $i$ as the number of classes in the image and $\mu_i$ as the means of the classes. For each pair of classes a threshold $\Theta_{i,i+1} = \frac{|\mu_i - \mu_{i+1}|}{2}$ is found. Then a class $\mu_{p(x)}$ is assigned to the pixels of the region of uncertainty which are in the interval $\mu_{i+1} \ge p(x) \ge \mu_i$,

$$\mu_{p(x)} = \begin{cases} \mu_i & \mu_i \le p(x) \le \mu_i + \Theta_{i,i+1} \\ \mu_{i+1} & \mu_i + \Theta_{i,i+1} < p(x) \le \mu_{i+1} \end{cases}$$

### 3.2 Mahalanobis Distance Criterion

Once that the nearest class mean criterion is applied, a second classification is made to those pixels by using Mahalanobis distance criterion [Devijver (1983)]. After removal of all resulting isolated nodes, the process is repeated at level k-1.

### 3.3 Potts Model

The boundary found at level k-1 (128 x 128) is projected at level k = 0 (256 x 256), where a new region of uncertainty is created and classified by a Potts model [Descombes *et al* (1996)] based in Markov Random Fields theory (MRFs). A MRF is a discrete stochastic process whose global properties are controlled by means of local properties. They are defined by local conditional probabilities.

The goal of the segmentation process is associate to each pixel of the data a label from a finite set. In a probabilistic framework, this approach consists if defining a MRF model through clique potentials and selecting the most likely labeling by a Maximum A Posteriori (MAP) approach.

Denote by X the image corresponding to the data and by Y the segmented image. The segmentation process consists of maximizing the conditional probability P(Y/X) which, from Bayes' rule, is proportional to P(X/Y)P(Y). P(Y) is referred as the *a priori* model whereas P(X/Y) is referred as the data-driven term.

The energy function associated to Potts model is written

$$U(Y) = \sum_{c=\{i,j\}} \beta \delta_{y_i = y_j}.$$

The $\beta$ coefficient defines the homogeneity properties of the solution, that is, the greater this term, the more likely two adjacent pixels will have the same label. In this study the data-driven term is defined by cost functions depending on the label $l$ and denoted $f^l$. The induced parameters are directly extracted from the data. The associated potential, applied to first-order cliques is then

$$U(X / Y) = \sum_{c=\{i\}} \sum_{l} f^l(x_i) \delta_{y_i = l},$$

where $x_i$ and $y_i$ are the data and label values respectively in site $y$.

The segmentation problem thus consists in minimizing the global energy:

$$U(X / Y) + U(Y).$$

In the MAP framework, the minimization process was performed by a stochastic technique (simulated annealing) [Geman and Geman (1984)].

Regarding the cooling schedule, the final temperature $\lim_{k\to\infty} T_k = 0$, is approximated by the geometrical decreasing rule $T_{k+1} = \tau T_k$, where $k$ denotes the *kth* transition and $\tau$ is the decrease ratio. As it was pointed out in [Kirkpatrick *et al* (1983)], in order to estimate the global minimum of energy functions, $\tau$ must be close to *1*. In this study $\tau = 0.95$. **Figure 3** shows the final result of the segmentation.

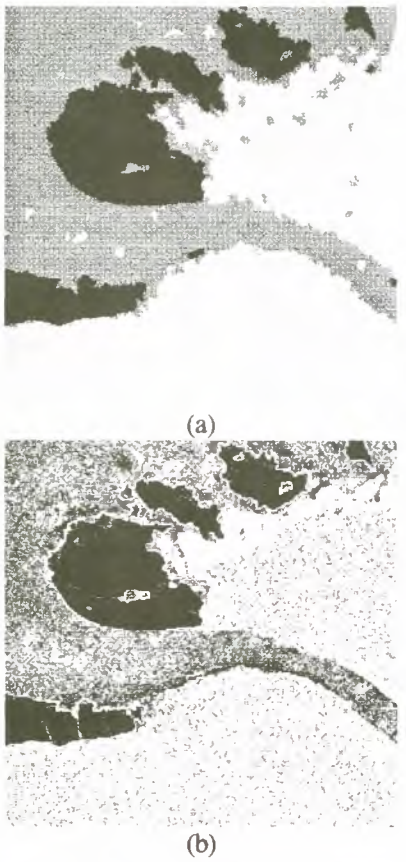

Figure 3. (a) Final result of the segmentation, (b) Original image with boundary line.

**4 Conclusions**

A scheme for image segmentation has been described, in which an attempt is made to use spatial information to overcome the weaknesses of purely statistical methods. This method consists in three main steps: quadtree smoothing, centroid clustering and boundary estimation.

The segmentation process depends on the boundary shape and downward propagation of errors. The low resolution classification is statistical but is based on a local centroid algorithm, which do not requires *a priori* information. To assure a minimum of errors in the lowest level and in order to prevent the propagation of errors, we classify the pixels of the boundary by using three differents criteria: the nearest class mean, Mahalanobis distance and Potts model.

Markov random fields theory offers an opportunity to overcome signal-to-noise ratio conditions typical of SAR images. Experimental results have been presented which bear out theoretical expectations and demonstrate the power of the method. Some of the perspectives to continue this study are: a) To apply a probabilistic relaxation in order to obtain low resolution segmentations; b) In the highest level, classifications can be made by using an binary scheme (Markovian Ising model). Extensions to texture segmentation are foreseen.

**References**


Arellano O. *Método de estructuras de árbol (quadtree) para la segmentación de imágenes de percepción remota*, Thesis of Master, México, 1997.

Descombes X.; Moctezuma M.; Maitre H.; Rudant J-P. *Coastline detection by a Markov segmentation on SAR images*, Signal Processing No. 55, 1996, pp. 123-132.

Devijver, P.A.; Kittler, J. *Pattern Recognition: A Statistical Approach*, London, Prentice Hall, 1983.

Geman S.; Geman D. *Stochastic relaxation, Gibbs distribution and the Bayesian restoration of images*, IEEE Trans. Pattern Anal. Machine Intell., vol. 6, No. 6, 1984, pp. 721-741.

Kirkpatrick S.; Gellat C.; Vecchi M. *Optimization by simulated annealing*, Science, No. 220, 1983, pp. 671-680.

Schneier M. *Linear time calculations of geometric properties using quadtrees*, TR-770 Computer Science Center, University of Maryland, 1979.

Spann M.; Wilson R. *A quadtree Approach to Image Segmentation that Combines Statistical and Spatial Information*, Patt. Rec. 18, 1985, pp. 257-269.

Wilson R. *From Signals to Symbols- the Inferential Structure of Perception*, Proc. IEEE COMPINT-85, Montreal, 1985, pp. 221-225.

Wilson R.; Spann M. *Image Segmentation and Uncertainty*, Research Studies Press LTD, England, 1988.

# COMPARISON OF SAR SEGMENTATION ALGORITHMS

Eduardo V. D. Lucca[1], Corina da C. Freitas[1], Alejandro C. Frery[2], Sidnei J. S. Sant'Anna[1]

[1]INPE-DPI
Av. dos Astronautas 1758
12227-010 São José dos Campos, SP, Brazil
Tel: 55-12-3456475, Fax: 55-12-3456468
lucca@dpi.inpe.br; corina@dpi.inpe.br; sidnei@dpi.inpe.br

[2]UFPE-DI
CP 7851
50732-970 Recife, PE, Brazil
Tel: 55-81-2718430, Fax: 55-81-2718438
frery@di.ufpe.br

## ABSTRACT

This paper aims at comparing the performance of two segmentation algorithms, the MUM (Merge Using Moments) and RWSEG, from simulated data, containing regions with differents homogeneity degrees, for land use aplications. The process for obtaining simulated images consists of criating a phantom (class idealized image) which summarizes the main geometric and topologic characteristics of targets. Then a statistical modelling of observations from each class through a particular distribution is proposed. The performance of the algorithms in study is evaluated from qualitative and quantitative analysis of the acquired results. The quantitative analysis is done from empiric evaluation methods of a segmentation. In order to reduce the influence of particular images on the performance assesment, a Monte Carlo experience is performed.

**Keywords:** SAR segmentation; MUM; RWSEG; Segmentation evaluation

## INTRODUCTION

In the last years there has been an increasing interest in data obtained from synthetic aperture radar (SAR) systems and its remote sensing applications. The importance of these systems derives from its capability of generating high resolution images regardless the availability of solar illumination or meteorological conditions.

The increasing demand as well as current and future availability of SAR data produce a strong need of automatic techniques for image processing and analysis. However, the proposal and implementation of these techniques are complex tasks, since SAR images employ coherent radiation and the resulting images are corrupted by a form of multiplicative signal-dependent noise known as *speckle*.

One of the first steps in image analysis consists of decomposing the input data into a collection of uniform, continuous and disjoints regions. This process is known as *segmentation*. Segmentation is one of the most critical tasks in the image analysis, and its importance has boosted the development of a great variety of algorithms for this purpose. The objective of segmentation algorithms is to provide an automatic way to obtain an image decomposition. Nevertheless, such algorithms can not be applied to all types of images, and besides that, they depend on the type of application in mind. Thus, the performance evaluation and the comparison among such algorithms represent an important issue.

The evaluation and comparison methods for segmentation algorithms aim at determining its limitations, advantages and applications. They can be divided into two categories: analytical and empirical. The analytical methods directly examine and assess the segmentation algorithms themselves by analysing their principles and properties, whereas the empirical methods evaluates them indirectly through their results (Zang, 1996). Several methods have been proposed in order to evaluate and compare the segmentation algorithms performance. Some examples found in the literature concerning this subject are Caves et al. (1996), Delves et al. (1992), Zhang, (1996) and Quegan et al. (1988).

The purpose of this paper is to compare quantitatively two distinct segmentation algorithms available in the software CAESAR (version 2.1): the MUM and the RWSEG. These algorithms are developed specifically for SAR data, and they are applied to simulated SAR images with 3 and 8 looks. These simulated images contain regions with different homogeneity degrees, in order to simulate distinct types of targets. This evaluation is performed employing empirical discrepancy methods. This work represents one step

towards mastering segmentation techniques for SAR images.

## SAR DATA MODELLING

SAR data posses distinctive statistical properties and its knowledge is very important for developing processing techniques and for image understanding. These properties can be used to discriminate different types of land by using some particular distributions for data modelling (Frery et al., 1997).

The multiplicative model has been widely used in the modelling, processing and analysis of SAR images. This model assumes that the observed return $Z$ is a random variable defined as the product between random variables $X$ and $Y$, where $X$ models the terrain backscatter and $Y$ models the speckle noise (Yanasse et al.,1995). Different distributions for $X$ and $Y$ yield to different models for the observed data $Z$.

Different types of region, number of looks ($n$), and kind of detection (intensity or amplitude format) can be associated to different distributions. This information is shown in **Table 1**. Regarding to region types, the homogeneous (agricultural fields, bare soil and pasture areas, for example), heterogeneous (primary forest, for example), and the extremely heterogeneous (urban areas, for example) are considered. Only amplitude format case is considered (variables with subscript "A" dente this fact). It is interesting to point out that the considered homogeneity degrees are dependent of sensor parameters such as wavelength, angle of incidence, polarization, etc.

**Table 1** shows that backscatter for homogeneous, heterogeneous, and extremely heterogeneous areas can be modelled as a Constant, as Square Root of Gamma distributed, and as Reciprocal of a Square root of Gamma distributed, respectively. The speckle is modelled by a Square Root of Gamma distributed random variable. Thus, the return $Z$ in amplitude case is modelled by a Square Root of Gamma, a $K$-Amplitude, and a $G^0$-Amplitude distributed random variable for homogeneous, heterogeneous, and extremely heterogeneous areas, respectively. For more details about these distributions, the reader may refer to (Frery et al., 1997).

## THE SEGMENTATION ALGORITHMS

The segmentations algorithms evaluated in this paper are: the MUM (Cook et al., 1994) and the RWSEG (White, 1986). These algorithms are implemented in CAESAR software (version 2.1) and were developed specifically for SAR data. They produce cartoon images, i.e., each region in the resulting segmentation is represented with the mean of the data values in that region (NASoftware, 1994). A segmentation algorithm using this cartoon model endeavours to find regions of constant backscatter by examining the pattern of values found in the input images. Besides that, both algorithms produce segmentations based on intensity and assume the multiplicative model for the image formation. They also assume that the pixel values in an image are uncorrelated.

### MUM (MERGE USING MOMENTS)

This algorithm starts with a very fine segmentation (it can be assumed that each pixel is a region, for instance) and proceeds by comparing neighbouring regions. The regions that are "significantly different" are left aside, and those regions that are "similar" are tagged. The tagged regions are then sorted out and as many as possible are merged. This process of tagging, sorting and merging continues on until there are no more regions to be merged (Cook et al., 1994).

The termination criterion is controlled by the user via the $p$ parameter ($0 < p < 18$). If the probability that two neighbouring regions are taken from the same backscatter exceeds $10^{-p}$ then they are merged. Two other parameters have to be defined: $i$ and $l$. The first allows the specification of the format of the input data (amplitude or intensity) whereas the second allows the specification of the number of looks of the input image (NASoftware, 1994).

### RWSEG

This algorithm segments an image by successive edge detecting and region growing. At the end of this iterative process, a region merging stage is used to produce the final segmentation. During the iterative process of edge detection and region growing, detected edges are used to limit region growing and the resulting segmentation is used to generate an improved edge map (White, 1986).

After each iteration, the average contrast of segments is measured, and iteration continues until the average contrast decreases. The final stage checks if adjacent segments are statistically distinct and merges segments which are not.

There are three parameters that control the algorithm: $i$, $j$ and $e$ (NASoftware, 1994). The parameter $i$ allows the specification of the format of the input data (amplitude or intensity). The parameter $j$ controls the probability for region merging and the parameter $e$ controls the probability for edge detection, which is related to the probability of false alarms.

## QUANTITATIVE MEASURES OVER SEGMENTATIONS

The quantitative measures used in this paper to evaluate segmentations produced by MUM and RWSEG are those reported in Delves et al. (1992), which are helpful when using empirical discrepancy methods. These methods take into account the difference between

segmented and reference images and can be used to assess the performance of the algorithms. The reference image can be obtained from manual segmentation of the original image (real or simulated) used as input data.

According to Delves et al. (1992), a first step to evaluate a segmented image consists of comparing the regions detected in the segmented image with those in the reference image. This method is based on a fitting process of these regions, by matching segmented and reference images. For each region of the reference image, there will be one in the segmented image which is selected to better represent it. This region in the segmented image is called *fitted region*. The best fit between each region of reference image and its fitted region can be evaluated and measured by criteria of position, number of pixels, mean intensity, and shape of fitted regions.

Let the original image and its segmentations (reference and segmented images) with dimensions *xpix* columns by *ypix* lines be matched up and referenced to X-Y plane. A region in a reference and segmented image is refered by $i$ and $f$ respectively, and is assumed that $N$ and $M$ are the numbers of regions of these images respectively. The notation $< g_i >$ and $< g_f >$ is used to denote averages of $g$ over a simple region in the reference and segmented images and $N(i)$ and $N(f)$ for the number of pixels in region $i$ and $f$ respectively. From matching reference and segmented images, two matrices of $N$ by $M$ elements, denoted $Gf$ and $Fit$ are constructed with components definided by:

$$Gf(i,f) = \frac{N(i \cap f)}{N(i \cup f)} \text{ and}$$

$$Fit(i,f) = \frac{\left[ xd + yd + \left( \frac{pd + id}{2} \right) \right]}{Gf(i,f)}$$

where

$$xd = \frac{\left| \langle x_i \rangle - \langle x_f \rangle \right|}{xpix}, \qquad yd = \frac{\left| \langle y_i \rangle - \langle y_f \rangle \right|}{ypix},$$

$$pd = \frac{\left| N(i) - N(f) \right|}{\left| N(i) + N(f) \right|}, \qquad id = \frac{\left| \langle I_i \rangle - \langle I_f \rangle \right|}{\left| \langle I_i \rangle + \langle I_f \rangle \right|} \quad \text{with}$$

$i = 1, \ldots, N$ and $f = 1, \ldots, M$. The values $< x_k >, < y_k >$ and $< I_k >$ represent, respectively, the abscissas, ordinates and return means in region $k$.

The $Gf$ matrix describes pairs of regions $(i,f)$ which have common pixels and gives a relation measure between the number of intersection pixels and the total number of pixels for each pair of regions. The values in $Fit$ matrix represent a fit success measure between regions $i$ and $f$ taking into account size, shape, position, and data mean intensity of regions. For each region $i$ in the reference image its corresponding fitted region $f$ is taken to be at the minimum value of $Fit\ (i,f)$.

Once defined the fitted region for each region of reference image, the fit success can be evaluated through quantitative measures that take into consideration relative aspects of position, mean intensity, size, and shape of fitted regions.

- SUCCESS OF POSITION FIT(*Fitxy*)

$$Fitxy = 1 - \frac{(xd + yd)}{2}$$

- SUCCESS OF INTENSITY FIT(*Fiti*)

$$Fiti = 1 - \left( \frac{\left| \langle I_i \rangle - \langle I_f \rangle \right|}{\left( \langle I_i \rangle + \langle I_f \rangle \right)} \right)$$

- SUCCESS OF SIZE FIT(*Fitn*)

$$Fitn = 1 - \left( \frac{N(i) - N(f)}{N(i) + N(f)} \right)$$

- SUCCESS OF SHAPE FIT(*Gshape*)

$$Gshape = \frac{N(i \cap f)}{N(i \cup f)}$$

Note that these measures vary between 0 and 1 values, where value equal 1 represents the best fit.

Thus, for each par of fitted regions there is a value of *Fitxy*, *Fiti*, *Fitn* and *Gshape*. For the $N$ regions of the reference segmentation there is a set of $N$ values for each success measures. The tested segmentation (segmented image) can be quantitatively measured through the mean value of *Fitxy*, *Fiti*, *Fitn* and *Gshape* obtained from $N$ regions, or through a single value denoted by general mean fit, which is obtained by computing the mean value of these success measures over the $N$ regions.

## OBTAINING SIMULATED IMAGES

The simulated images used in this paper were generated using a phantom image. The phantom is an idealized class image created from interest class observation in real SAR images, that summarizes the main geometric and topologic characteristics in these images. However, these characteristics are related to the application type required by the user. The application type determines the result of manual segmentation which is necessary to obtain the reference segmentation used when applying empirical discrepancy methods.

The application type defined in this paper is soil occupation and use studies. The most frequent regions in this applications are agricultural fields, bare soil, pasture areas, urban areas, forests, etc. These regions

can be described through their homogeneity degree, and can be classified in homogeneous, heterogeneous, and extremely heterogeneous (for some sensor parameters).
The next step consists of modelling observations from each class present in the phantom through a particular distribution. The spatial correlation between pixels values is not taken into consideration due to computational cost. Moreover, the MUM and RWSEG assume that the pixel values in the image are uncorrelated. The model proposed (phantom and statistical data modelling) has three important and desirable characteristics: representativeness, controllability and repeatability.
A JERS-1 real image (3 looks amplitude) was used to attain representativeness in terms of scale, topology and spatial distribution. A 480x480 pixels subimage, with the classes of interest, was selected and then its manual segmentation was performed (see **Figure 1-a**). To classify the regions obtained in manual segmentation, eight distinct classes were defined: three homogeneous types (light, medium, and dark blue), three heterogeneous types (yellow, light brown, and dark brown) and two extremely heterogeneous types (red and magenta). It is important to point out that the difference among same homogeneity type class is obtained through different parameters that characterise the distribution defined for each class. Each segment present in the manual segmentation was classified as one of these class resulting in a classified image (phantom) with 36 segments (**Figure 1-b**).
The observations from each class were modelled with a certain distribution, shown in **Table2**. The $\mu$ value denotes the true mean of the return random variable $Z$.
After the phantom regions were stochastically modelled, the 3 and 8 looks simulated images (amplitude format) were obtained in a number suited for the Monte Carlo experience. **Figure 1** shows the resulting manual segmentation, the phantom and one resulting 8 look simulated image.

## APPLYING THE SEGMENTATION ALGORITHMS

The MUM and RWSEG algorithms were applied for the 3 and 8 looks simulated images obtained by simulation. Each algorithm has specific parameters that must be selected by the user and they affect the final resulting. Thus, these specific parameters were selected in order to obtain a good deal of combinations, and to determine how the selected parameters affect the final resulting segmentation. None pre-processing was applied in input data.
The purpose in this stage is to determine from qualitative (visual inspection) and quantitative (success measures) analysis which parameters from each algorithm give the best 3 and 8 looks simulated image segmentation and, from these selected parameters, perform the Monte Carlo experience.

The MUM algorithm was performed using the parameter $i$ for amplitude data, the parameter $l$=3 for the 3 looks simulated image and $l$=8 for the 8 looks simulated image, and the parameter $p$ with 17 possible values (1 to 17). At the end of this process 34 segmentations were obtained.
The RWSEG algorithm was performed using the parameter $i$ for amplitude data, the parameter $e$ with values 1.65, 1.96, 2.33, 2.58, 2.81, 3.09, 3.29, 3.48, 3.72, 3.89, 4.06, 4.27, 4.42, 4.57, 4.77, and 4.91, and the parameter $j$ with values 0, 2, 4, 6, 8 and 10. The $e$ (16 values) and $j$ (6 values) possibles arrangements for each input data (3 and 8 looks simulated images) resulted in a total of 192 segmentations.
After qualitative and quantitative analysis of all obtained segmentations, the best segmentation for each input data and each algorithm was selected. The best MUM segmentations were obtained with $p$=5 for the 3 looks image and $p$=10 for the 8 looks image. The best RWSEG segmentations were obtained with $e$=2.58 and $j$= 2 for the 3 looks image and with $e$=3.29 and $j$=2 for the 8 looks image.

## MONTE CARLO EXPERIENCE

In order to reduce the influence of a particular image over the quantitative performance assesment, a Monte Carlo experience was performed. The Monte Carlo methodology is based on image replications with the same statistical properties. After many replication images, there will be a measures vector set for each segmentation algorithm, which can be compared through measure set analysis.
In order to obtain representative results, the replication number must not be lower than 30. In some reported experiences in literature concerning this subject (Bustos and Frery, 1992), thousands of replications are necessary to obtain acceptable quality levels. However, due to computational cost required, the methodology was applied in 30 replications for each input data.
The images were segmented by both algorithms using the parameters which yielded to the best result for 3 and 8 looks images. Once the segmentations were obtained, the quantitative success measures were applied for all the obtained ones.

## EXPERIMENTAL RESULTS

The general means fit obtained for quantitative success measures applied over the MUM (represented by blue line) and RWSEG (represented by red line) replication image segmentations (3 and 8 looks) are presented in **Figure 2**.
The analysis of **Figure 2** suggests that, for most of the 3 looks and 8 looks (2/3 of each) replications, the MUM general mean fit is better than the RWSEG one. Besides that, the general mean fit obtained for each 8 looks

replication images is better than that obtained for each 3 looks replication images.

In order to summarize the performance for each algorithm in the Monte Carlo experience through a single value, the mean and variance of these general means fit were calculated by computing their obtained values for all replications of each image set. These measures were denoted by total mean fit and total variance fit. The obtained MUM total mean values were 0,82964 and 0,85445 for 3 and 8 looks image set, respectively. For the RWSEG, 0,820022 and 0,84548 were obtained, for 3 and 8 looks image set, respectively. The total variances for MUM and RWSEG were 0,000130 and 0,000134 for the 3 looks replications. For the 8 looks replications, the obtained values were 0,000147 and 0,000127. The comparison between these total means shows that, for both image sets, the MUM total mean is better than that of RWSEG at confidence level of at least 99%.

To compare both algorithms from each success fit measures, the mean ($\hat{\mu}$) and variance ($\hat{\sigma}^2$) of each one was calculated computing the values obtained for these fit measures for each 3 and 8 looks replication image. These measures were denoted by global mean fit and global variance fit. The resulting global mean and global variance for each fit measure are shown in **Table 3**.

From **Table 3** values and through **Figures 3, 4, 5,** and **6**, which show each MUM (represented by blue line) and RWSEG (represented by red line) fit measures values obtained for each 3 and 8 looks replication, it is possible to compare the algorithms from each success fit measure point of view.

**Table 3** analysis shows that, according to position and shape fit, the global means obtained for MUM are better than those obtained for RWSEG for both image sets with confidence level of 99%. The MUM supremacy in these cases are shown clearly in **Figures 3** and **6** respectively. The size fit global means obtained for both algorithms are statistically equal with confidence level of 95% for both image sets (**Figure 5**). For the intensity fit in the 3 looks image set, the RWSEG attained better global mean than that obtained by MUM, at the 95% level of confidence, but the difference between these global means is not significant with at the 99% level of confidence (**Figure 4**). However, these global means are equal for 8 looks image set at the 95% level of confidence.

## CONCLUSIONS

The anaysis of the MUM and RWSEG general means obtained for each replicated image in Monte Carlo experience allows to conclude that, for the proposed image set, the MUM algorithm produces quantitatively better segmentations than those produced by the RWSEG. This result is confirmed when comparing the total mean obtained for both algorithms.

The MUM is more skillful than RWSEG at producing segments at the correct position and with the correct shape. However, both algorithms are equivalent in terms of size and intensity of the produced segments. Thus, for the aplication type defined to compare both algorithms, the MUM is more appropriate to perform the image segmentations.

The comparison of the quantitative measures and visual analysis result over the produced segmentations reveals that even visually different segmentations have very close quantitative values. However, the quantitative measures confirm the qualitative analysis results.

## ACKNOWLEDGMENTS

This work was supported by grants from PPG-7 (0808/95 and 0816/95), Convênio FINEP (6.6.96.0473.00 and 6.6.96.0474.00), CNPq (Proc. 523469/96-9) and FACEPE (APQ 0707-1.03/97).

## REFERENCES

Bustos, O.H.; Frery, A.C. **Simulação estocástica: teoria e algoritmos**. Rio de Janeiro, IMPA, 1992.

Caves, R.; Quegan, S.; White, R.G. Quantitative comparison of the performance of SAR segmentation algorithms. **IEEE Transactions IP**, (submitted), 1996.

Cook, R.; McConnell, I.; Oliver, C.J. MUM (Merge Using Moments) segmentation for SAR images. In: Proc. SPIE, 2316, 92-103, 1994.

Delves, L.M.; Wilkinson, R.; Oliver, C.J.; White, R.G. Comparing the performance of SAR segmentation algoritms. **International Journal of Remote Sensing**, 13:21221-2149, 1992.

Frery, A.C.; Müller, H.J.; Yanasse, C.C.F.; Sant'Anna, S.J.S. A model for extremely heterogeneous clutter. *IEEE Trans. Geosc. Rem. Sens.*, 35(3):1-12, 1997.

NASoftware. Caesar: user guide. Version 2.1. Liverpool, 1994.

Quegan,S.; Rye,A.J.; Hendry,A.; Skingley,J.; Oddy,C.J. Automatic interpretation strategies for synthetic aperture radar images. **Phil. Trans. R. Soc. Lond**. A 324, 409-421, 1988.

White, R.G. **Low-Level segmentation of noise imagery.** Technical Report 3900, DRA, St Andrews Road, Malvern, Works, 1986.

Yanasse, C.C.F. **Statistical analysis of synthetic aperture radar images and its applications to system analysis and change detection**. (PhD Thesis) Sheffield, UK, University of Sheffield, 1991.

Yanasse, C.C.F.; Frery, A.C.; Sant'Anna, S.J.S. Stochastic distribuitions and the multiplicative model: relations, properties, estimators and applications to SAR image analysis. São José dos Campos, INPE, 1995. (INPE-56630-NTC/318).

Zhang, Y.J. A survey on evaluation methods for image segmentation. **Pattern Recognition**, 29:1335-1346, 1996.

**TABLE 1 - DISTRIBUTIONS WITHIN THE MULTIPLICATIVE MODEL FOR DIFFERENT DEGREES OF HOMOGENEITY**

| Regions Type | Backscatter | Speckle | Return |
|---|---|---|---|
| | $X_A$ | $Y_A$ | $Z_A = X_A Y_A$ |
| Homogeneous | $C(\sqrt{\beta})$ | $\Gamma^{1/2}(n,n)$ | $\Gamma^{1/2}(n,n\beta^{-1})$ |
| Heterogeneous | $\Gamma^{1/2}(\alpha,\lambda)$ | $\Gamma^{1/2}(n,n)$ | $K_A(\alpha,\lambda,n)$ |
| Extremely Heterogeneous | $\Gamma^{-1/2}(\alpha,\lambda)$ | $\Gamma^{1/2}(n,n)$ | $G_A^0(\alpha,\gamma,n)$ |

**TABLE 2- DISTRIBUTIONS AND PARAMETERS ASSUME FOR EACH REGION TYPE**

| | | | | 3 Looks ($n$=3) | | | 8 Looks ($n$=8) | | |
|---|---|---|---|---|---|---|---|---|---|
| REGION TYPE | DISTRIB | $\mu$ | $\alpha$ | $\beta$ | $\lambda$ | $\gamma$ | $\beta$ | $\lambda$ | $\gamma$ |
| Homogeneous 1 | $\Gamma^{1/2}(n,n\beta^{-1})$ | 70 | - | 126,3 | - | - | 201,1 | - | - |
| Homogeneous 2 | $\Gamma^{1/2}(n,n\beta^{-1})$ | 80 | - | 144,4 | - | - | 229,8 | - | - |
| Homogeneous 3 | $\Gamma^{1/2}(n,n\beta^{-1})$ | 150 | - | 270,8 | - | - | 430,9 | - | - |
| Heterogeneous 1 | $K_A(\alpha,\lambda,n)$ | 90 | 2,0 | - | $2,0\times10^{-4}$ | - | - | $2,1\times10^{-4}$ | - |
| Heterogeneous 2 | $K_A(\alpha,\lambda,n)$ | 170 | 5,0 | - | $1,5\times10^{-4}$ | - | - | $9,4\times10^{-4}$ | - |
| Heterogeneous 3 | $K_A(\alpha,\lambda,n)$ | 130 | 3,0 | - | $1,5\times10^{-4}$ | | - | $1,5\times10^{-4}$ | - |
| Extremely Het 1 | $G_A^0(\alpha,\gamma,n)$ | 220 | -7,0 | - | - | $8,5\times10^{5}$ | - | - | $8,1\times10^{5}$ |
| Extremely Het 2 | $G_A^0(\alpha,\gamma,n)$ | 160 | -4,0 | - | - | $9,0\times10^{4}$ | - | - | $8,6\times10^{4}$ |

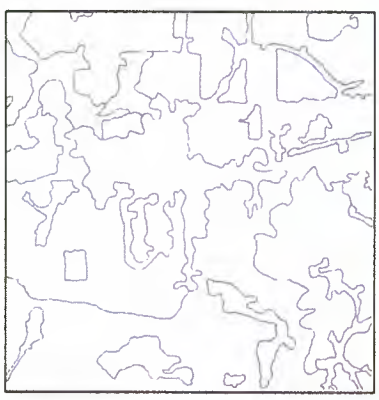

(a)

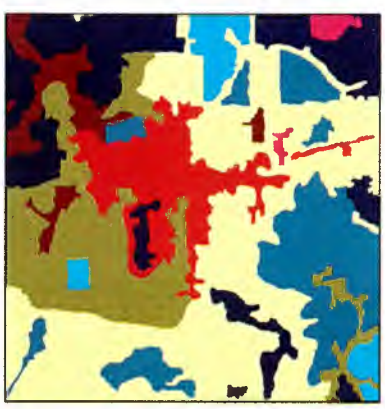

(b)

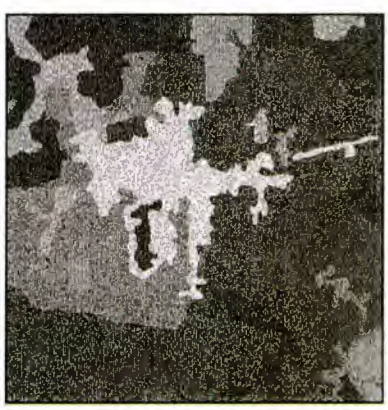

(c)

Figure 1 - (a) Manual segmentation, (b) phantom (c) simulated 8 looks image.

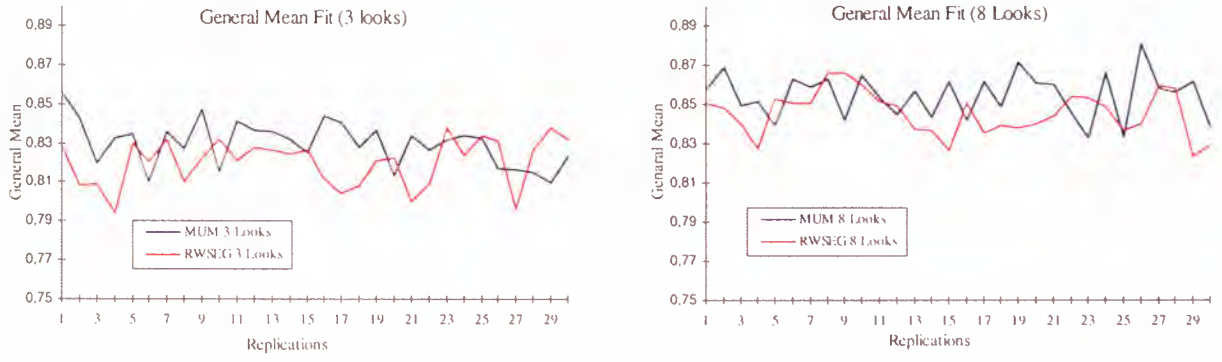


Figure 2 - MUM and RWSEG general mean fit variation for each 3 and 8 looks replication image.

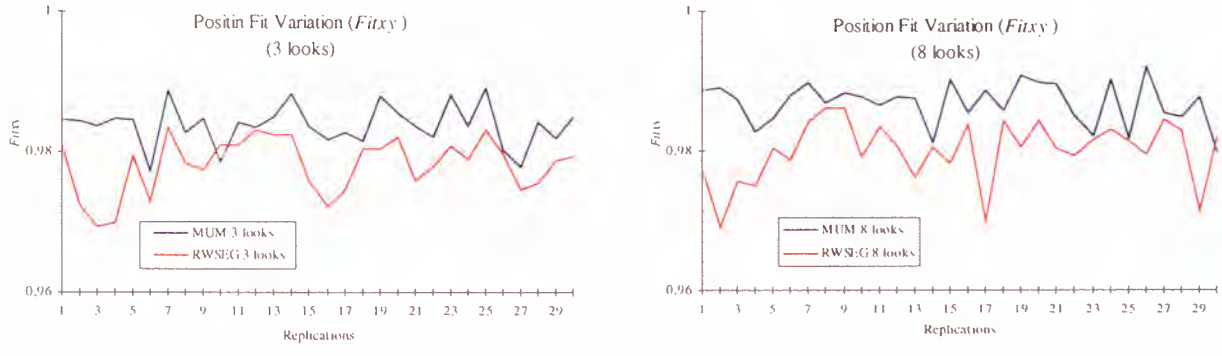


Figure 3 - MUM and RWSEG position fit variation for each 3 and 8 looks replication image.

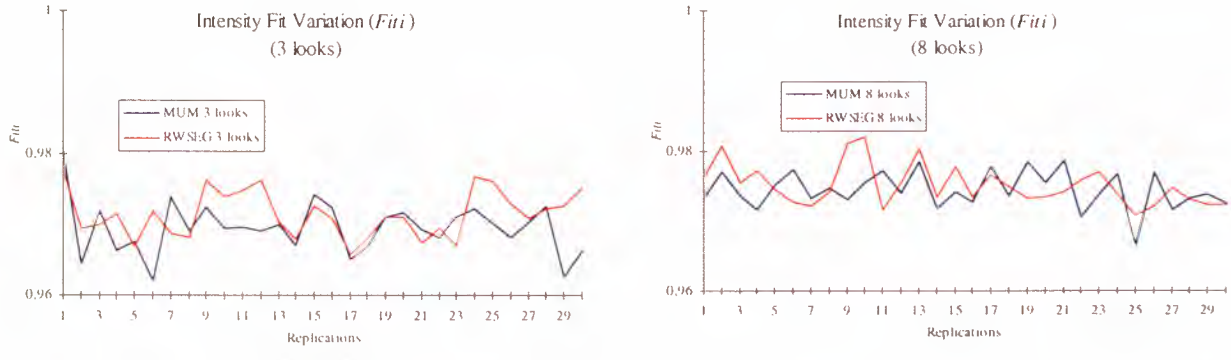


Figure 4 - MUM and RWSEG intensity fit variation for each 3 and 8 looks replication image.

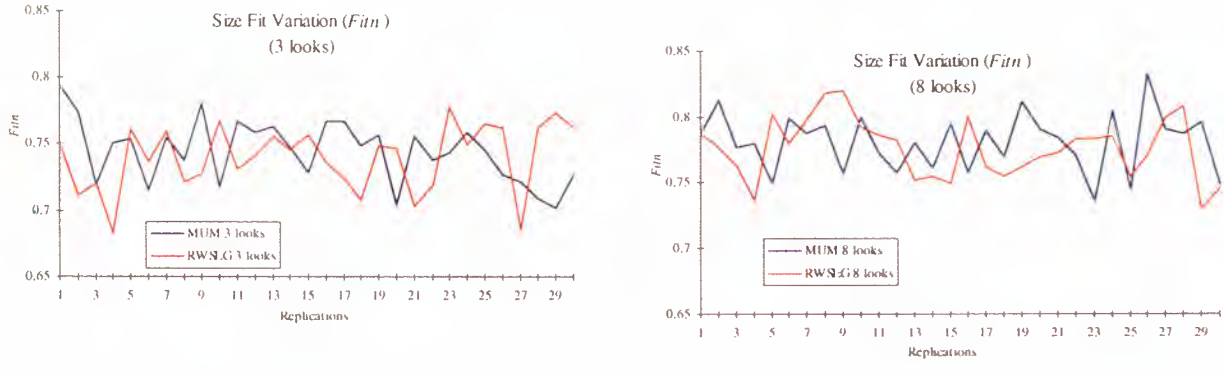

Figure 5 - MUM and RWSEG size fit variation for each 3 and 8 looks replication image.

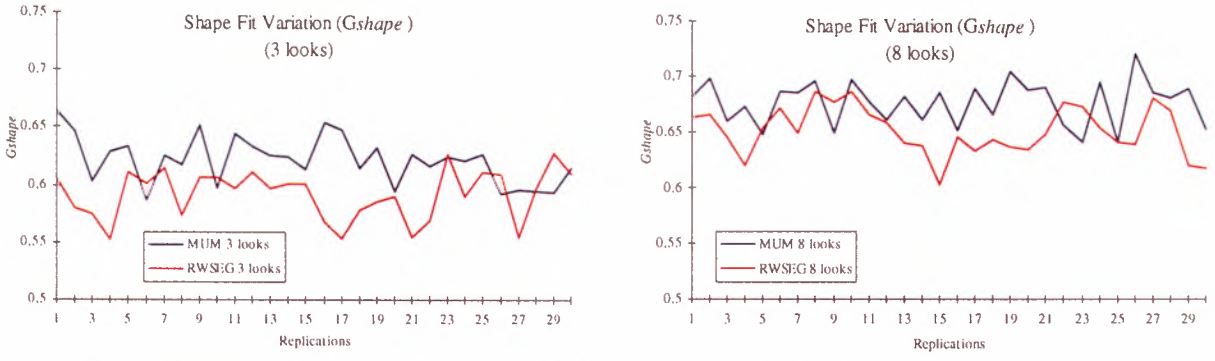


Figure 6 - MUM and RWSEG shape fit variation for each 3 and 8 looks replication image.

# Radar 4

*Coordinators:* David Fernandes, *ITA* &
Maurizio Fea, *ESA/ESRIN*

# CLASSIFICAÇÃO TEXTURAL DE FEIÇÕES GEOLÓGICAS POR VARIOGRAMAS NA PROVÍNCIA MINERAL DO TAPAJÓS A PARTIR DE IMAGENS JERS-1 / SAR.

ENRICO CAMPOS PEDROSO[1]
ALVARO PENTEADO CRÓSTA[1]
CARLOS ROBERTO DE SOUZA FILHO[1]

[1]UNICAMP – Instituto de Geociências da Universidade de Campinas
Caixa Postal 6152, 13.083-970, Campinas – SP, Brasil
Tel. (019) 788-7352 / Fax: (019) 289-1562 / E-mail:{enrico,alvaro,beto}@ige.unicamp.br

Abstract. Texture analysis is playing an increasingly important role in digital image processing techniques to derive physical information about geologic surfaces and processes. The use of traditional reconnaissance mapping tools such as optical remote sensing is severely constrained in tropical regions by almost permanent cloud coverage. The use of radar remote sensing is therefore a preferable means to assess the geology and structural framework of those areas. This paper evaluates the potential use of JERS-1 / SAR data to map a geologically complex region such as the Tapajos Mineral Province. We employ variogram textural analysis to automatically identify textural domains that can be correlated to both Archaean-Proterozoic bedrock and Quaternary gold-mineralized placers. The semivariogram classifier proved to be a powerful feature recognition technique that can be successfully applied for regional geologic and mineral exploration studies.

## 1. Aspectos Gerais

Grande parte da produção de ouro, cassiterita e diamantes da região amazônica brasileira, venezuelana e colombiana é oriunda de depósitos sedimentares do tipo placer. Esses depósitos possuem ampla distribuição areal na superfície terrestre, pois são formados por processos superficiais ativos com poder dinâmico de dispersão de seus produtos. Os placers aluvionares ocorrem geralmente próximos à superfície e, em sua maioria, de forma inconsolidada, fazendo com que os custos de pesquisa e exploração sejam relativamente reduzidos.

A região do Tapajós, situada nos estados do Amazonas e Pará, compreende unidades com idades que variam desde o Arqueano até o Cenozóico e representa a mais importante província aurífera aluvionar do país. Entretanto, o nível de conhecimento geológico disponível sobre estes depósitos é limitado, provavelmente devido à pouca ênfase dada aos estudos sobre ambientes supergênicos. Outro fator que impede o avanço sistemático dos estudos nesta região é a logística. Problemas típicos de regiões tropicais, tais como: a densa cobertura vegetal, a inexistência de estradas e acessos, a presença de estações climáticas bem definidas com períodos chuvosos severos, o espesso capeamento de solos e o elevado grau de alteração intempérica das rochas dificultam e encarecem a realização de quaisquer atividades de pesquisa na região.

O sensoriamento remoto orbital vem sendo intensamente aplicado ao estudo de recursos naturais. Os sistemas de sensoriamento remoto imageadores produzem imagens sinópticas cobrindo os aspectos espectrais e texturais da superfície terrestre, possibilitando desta forma a obtenção de informações sobre a geologia e a geomorfologia das áreas imageadas. Os sistemas imageadores de radar e as informações por eles geradas são distintas daquelas adquiridas pelos sistemas sensores convencionais, que operam na parte óptica do espectro eletromagnético, como o LANDSAT–5 / TM, SPOT / HVR, JERS-1 / OPS, entre outros. Por se tratar de um sistema ativo, o radar possui sua própria fonte de energia (iluminação) e portanto, opera independentemente da presença de luz solar. As radiações de microondas emitidas por este sistema podem ser controladas pela geometria de aquisição, o que é impossível para a radiação solar utilizada pelos sistemas óticos. A faixa das microondas do espectro eletromagnético está situada em uma janela de transmissão atmosférica, o que torna estes sistemas capazes de operar em condições atmosféricas adversas (nuvens, precipitações pluviométricas, brumas). Outras características dos sistemas de radar incluem: (i) maior sensibilidade a variações de rugosidade superficial (microtopografia) e da morfologia de superfície (macrotopografia); (ii) maior penetração na superfície, especialmente para o JERS-1 / SAR, que apresenta o maior comprimento de onda (23cm) entre os sistemas de microondas orbitais em operação; (iii) sensibilidade a propriedades elétricas (constante dielétrica dos materiais), relacionadas à umidade e, (iv) possibilidade de estereoscopia. Essas características fazem com que a utilização de sistemas de radar em regiões tropicais seja altamente benéfica. As informações observadas nas imagens SAR estão relacionadas à rugosidade da superfície (textura), topografia (estruturas), condições de umidade e vegetação.

Este trabalho descreve um método para o processamento de imagens de radar direcionado para

**Image Processing Techniques** *Proceedings of the 2nd Latino-American Seminar on Radar Remote Sensing held at Santos, Sao Paulo, Brazil, 11-12 September 1998* (ESA SP-434, October 1998).

análise e classificação textural de domínios geológico-metalogenéticos, através de métodos estatísticos de análise textural por variogramas. A metodologia aplicada se baseou em técnicas potencialmente aplicáveis em atividades de mapeamento geológico e exploração mineral em regiões tropicais com intensa cobertura vegetal, como suporte a trabalhos de pesquisa básica.

A área de estudo localiza-se no interior da Província Mineral do Tapajós (PMT), a oeste da Reserva Garimpeira do Tapajós, na porção nordeste da folha Jacareacanga (escala 1:250.000), extremidade sudoeste do Estado do Pará. A mesma contém aproximadamente 1283 $Km^2$ e está limitada entre os paralelos 06°02' e 06°11' de latitude Sul e meridianos 57°14' e 57°37' de longitude Oeste (Figura 1).

Os dados utilizados neste trabalho compreendem (i) imagens de radar JERS-1 / SAR[1] (Path 408/Row 311) adquiridas em 22/12/1996, (ii) mapa geológico na escala de 1:250.000 (Pessoa et al. 1977) e (iii) bases cartográficas do IBGE e DSG nas escalas 1:250.000 e 1:100.000. ER Mapper / ER Radar, GSLIB (Deutsch & Journel, 1992) e USTC (Miranda et al. 1997) foram os principais programas empregados neste estudo.

## 2. Aspectos Geológicos

A Província Mineral do Tapajós está inserida no contexto da Plataforma Amazônica (Cráton Amazônico), que atuou como área estável durante o desenvolvimento da orogênese Brasiliana, sendo constituída por um embasamento de rochas magmáticas e metamórficas e por uma cobertura sedimentar-magmática. Sobre esse embasamento, passaram a se constituir as coberturas representadas pelas grandes bacias sedimentares paleozóicas. As coberturas jurássicas e mais novas transcendem os limites dessas bacias.

A compartimentação tectono-estratigráfica regional da PMT compreende sequências que vão do Arqueano ao Fanerozóico. O cenário geológico regional é composto por: (i) Embasamento Arqueano-Paleoproterozóico (3,1 a 1,9 Ga); (ii) Magmatismo ácido a intermediário Mesoproterozóico (1,7 a 1,5 Ga); (iii) Coberturas sedimentares Proterozóicas e Magmatismo básico Mesoproterozóico (1,6 a 1,5 Ga); (iv) Magmatismo básico Meso/Neoproterozóico (1,0 Ga); (v) Coberturas Sedimentares Fanerozóicas (<600 Ma) e (vi) Coberturas sedimentares e lateríticas Cenozóicas (<65 Ma), (SUDAM-GEOMITEC, 1972, 1976; Pessoa et al. 1977; Bizinella et al. 1980; Faraco et al. 1996; Klein et al. 1997, Coutinho et al. 1997, entre outros).

A geologia da área de estudo, representada na Figura 2, compreende as litologias pertencentes à Suíte Metamórfica Cuiú-Cuiú, Suíte Intrusiva Parauari, Suíte Intrusiva Maloquinha, Granito Cumaru e os depósitos quaternários auríferos subrecentes e recentes.

## 3. Análise Textural por Variogramas

As imagens de sensoriamento remoto apresentam propriedades espaciais distintas que se quantificadas podem ser utilizadas em diversas aplicações no estudo de recursos naturais (e.g., Curlander, 1984; Farr, 1984; Haralick et al. 1973; Rubin, 1989). A técnica de análise textural por variogramas é indicada para a análise de todos os fenômenos observáveis em imagens de sensoriamento remoto pois esta se baseia nas características espaciais da população amostral, fundamentada na teoria das variáveis regionalizadas (Matheron, 1963). Em termos práticos, o variograma é uma função geoestatística simétrica no espaço, o qual possibilita o estudo da dispersão natural das variáves regionalizadas em função de um espaço e direção amostral. Uma variação da função semi-variograma tradicional proposta inicialmente por Matheron (op. cit.), denominada função semi-variograma circular (Miranda et al., 1997), foi utilizada nos procedimentos de variografia utilizados (Equação 1).

$$\gamma(x_0 + h) = \frac{1}{2n}\sum_{i=1}^{n}[(DN(x_0 + r) - \mu H(x_0)]^2$$

onde:

* $\gamma_{(x0+h)}$ representa a função semi-variograma em um pixel localizado em $x_0$ e passo radial h.
* $DN(x_0+r)$ representa o valor do nível de cinza em um passo com distância radial r a partir de $x_0$ (raio h, ângulo $\theta$).
* $\mu_H(x_0)$ representa o valor médio de uma vizinhança circular de raio H e centro $x_0$.
* H representa o máximo número de passos (lag distance) necessário para a descrição do dado.
* n representa o número de pixels da vizinhança em uma distância h radial.

A metodologia utilizada no processamento digital das imagens de radar consiste basicamente de uma fase de pré-processamento e outra de processamento, conforme ilustra o fluxograma da Figura 3. A fase de pré-processamento dos dados SAR envolve os procedimentos de correção radiométrica (ruído speckle) (Pedroso et al. 1997), correção geométrica, segmentação por textura e sub-amostragem. Esta etapa precede a aquela de classificação textural propriamente dita. A

[1] O JERS-1 / SAR é um sistema de radar de abertura sintética que opera na banda L ($\lambda \sim 23,5$ cm - 1275 MHz), com polarização paralela HH e ângulo de incidência de 35° 21'. Os dados SAR foram obtidos com o nível de processamento 2.1 - NASDA *Standard Process* (*i.e.* Reamostragem a partir do sistema de projeção UTM). A iluminação do SAR possui direção de leste para oeste.

segmentação por textura constitui em uma etapa de fundamental importância na caracterização geoestatística dos domínios texturais investigados. Nesta fase, os domínios texturais são analisados qualitativa e quantitativamente através da análise de variabilidade realizada mediante as rotinas do GSLIB (Deutsch & Journel, 1989). A classificação textural por variogramas foi empregada na imagem JERS – 1 / SAR subamostrada em 25% (592 x 942 pixels), apresentando célula de resolução de aproximadamente 50 metros. Nesta etapa, o semi-variograma médio de uma determinada classe textural foi obtido a partir de semi-variogramas omnidirecionais. Estes foram calculados em três áreas de treinamento localizadas em posições distintas onde esta determinada classe ocorre na imagem.

Posteriormente, os semi-variogramas omnidirecionais médios das classes texturais estudadas foram plotados em um único gráfico, o qual expressa a assinatura geoestatística dos domínios texturais investigados (Figura 5). Desta forma, a análise do comportamento das curvas nos diferentes passos possibilita a determinação dos valores de passos que melhor distingüem as classes texturais investigadas. Esta etapa assume um importante papel no processo de classificação textural, pois as imagens relativas aos passos selecionados servirão de dados de entrada para o método de classificação não-supervisionada ISOCLASS (ISODATA) posteriormente utilizado.

A determinação dos domínios texturais baseia-se em dados obtidos a partir da análise das imagens de radar, mapa geológico e informações de trabalhos de campo. As classes em questão estão representadas na Figura 4, sendo Classe 01 – Área de influência da Suíte Intrusiva Maloquinha (PMm), representada por uma textura suavizada e arredondada, típica de terrenos graníticos; Classe 02 – Área de influência da Suíte Metamórfica Cuiú-Cuiú (Acc), com rugosidade média, representante do embasamento Arqueano da Província; Classe 03 – Área de influência dos placers mineralizados em Au (Garimpo de Porto Rico), evidenciada por uma textura plana (terraços), com as drenagens bastante dissecadas devido à atividade antrópica da explotação mineral desenvolvida na região; Classe 04 – Área de influência do Granito Cumaru (PMc), marcada por uma textura com rugosidade grosseira, caracterizada por um relevo mais acidentado que os adjacentes, representado por áreas com áreas de sombras periódicas, delimitando as cristas do relevo granítico; Classe 05 – Área de influência dos Aluviões Recentes (Qr), representada por uma textura granular bastante fina e homogênea e Classe 06 – Área de influência do Rio Tapajós (água), representada por uma textura escura (muito baixo valor de DN), consequência da reflexão essencialmente especular, típica da água. delimitando as cristas do relevo granítico; Classe 05 – Área de influência dos Aluviões Recentes (Qr), representada por uma textura granular bastante fina e homogênea e Classe 06 – Área de influência do Rio Tapajós (água), representada por uma textura escura (muito baixo valor de DN), consequência da reflexão essencialmente especular, típica da água.

Na análise variográfica, o valor do patamar depende exclusivamente da variabilidade estatística do dado, enquanto que o valor do alcance está relacionado à continuidade espacial do mesmo. No entanto, a assinatura geoestatística, particular para cada domínio textural investigado, caracteriza-se não só pelos valores de variância e continuidade da população, mas principalmente pelo comportamento da função semi-variograma nos passos considerados. A análise pormenorizada do comportamento da função semi-variograma e a determinação dos passos ótimos a diferenciação das classes investigadas antecedem os processos de classificação textural por variogramas.

O primeiro passo dos semi-variogramas mostra um grau de separabilidade bastante incipiente entre as classes estudadas. Observa-se porém que as classes representadas em vermelho (Suíte Intrusiva Maloquinha) e em amarelo (Aluviões Recentes) são coincidentes. O mesmo acontece entre as classes Suíte Metamórfica Cuiú-Cuiú (magenta) e Granito Cumaru (laranja), que apresentam um valor de semi-variância bastante semelhante. A título de ilustração, o passo 2 pode ser utilizado na diferenciação entre as classes 1 e 3; 2 e 3 e 4 e 5, ao passo que as classes 2 e 4 e 5 e 6 apresentam variâncias semelhantes, fazendo com que este valor de Lag Distance não seja diagnóstico para a discriminação entre estas últimas classes. No passo 5, apenas as classes 1 e 5 podem ser discriminadas entre si ou em relação as classes 2,3,4 e 6 que apresentam valores de variância semelhantes. No passo 10, observa-se três famílias de classes texturais que podem ser discriminadas, sendo estas as classes 1; 5; 6 e 2,3,4. Os passos que melhor distinguem os domínios texturais em investigação foram então utilizados como bandas de entrada para a classificação não-supervisionada. Após a obtenção do produto da classificação, esta análise interpretativa dos passos pode também auxiliar vantajosamente as etapas de edição e atribuição de cores às classes estudadas.

É importante ressaltar que, devido à complexidade do processo, o resultado final não apresenta domínios texturais compostos de uma única cor, mas sim de arranjos de cores. A superposição da geologia da área nos mapas temáticos gerados a partir dos processos de classificação mostra que os domínios texturais apresentam um padrão de composição e disposição de cores bastante particular.

A Figura 6 corresponde ao mapa temático obtido através da classificação textural gerada pelo algoritmo ISOCLASS. A classificação produzida a partir dos canais texturais calculados das imagens JERS-1 / SAR sub-amostrada e filtrada, pelo algoritmo USTC, caracterizou as classes texturais de forma eficaz. Comparando o mapa temático da Figura 6 com a

geologia da área de estudo (Figura 2), observa-se que as áreas de a, b, c, d, e e f (correspondentes às classes aqui consideradas) apresentam uma boa correlação com as unidades litológicas e regiões mineralizadas.

As áreas g e h, não diretamente estudadas neste trabalho, apresentaram uma assinatura textural semelhante à observada em c (terraços mineralizados em ouro). Tal coincidência corrobora a eficiência do método no reconhecimento de feições texturais de interesse, visto que g e h representam depósitos secundários, do tipo placers auríferos, atualmente em exploração (garimpos São José e das Tropas, respectivamente). Partindo desta premissa, i consiste em uma área interessante para uma verificação detalhada visto a sua semelhança textural com as áreas mineralizadas supracitadas.

Observa-se ainda na Figura 6 a homogeneidade da classe 05 (aluviões recentes), representada em f pela cor azul. A separação inequívoca desta classe é importante, principalmente pelo fato de que estes aluviões também hospedam mineralizações de ouro.

## 4. Conclusões

A análise dos resultados obtidos permite afirmar que os domínios texturais estudados possuem assinaturas geoestatísticas particulares (semivariogram signatures). As etapas de pré-processamento dos dados SAR são indispensáveis para o sucesso das etapas posteriores de classificação textural por variogramas. No pré-processamanto, destaca-se aqui a importância da (i) supressão do speckle, o qual, se não atenuado, é capaz de mascarar as propriedades texturais presentes nas imagens; e (ii) a subamostragem da cena, que permite uma caracterização variográfica aprimorada da classe textural que se pretende quantificar.

A classificação textural por variogramas consiste em um método eficaz na caracterização espacial das feições geológicas estudadas. As classes texturais 01, 03 e 05, representadas respectivamente pela Suíte Intrusiva Maloquinha, Placers Mineralizados e Aluviões Recentes, foram discriminadas satisfatoriamente.

Estudos mais abrangentes do que o aqui reportado demonstram ainda que o método de classificação textural por variogramas tem uma excelente aplicabilidade no reconhecimento e caracterização de feições relacionadas a recursos naturais.

## 5. Agradecimentos

À FAPESP (Processo nº 96/07518-8) e CNPq pelas bolsas concedidas e auxílio ao projeto de pesquisa, à CPRM pelo fornecimento do mapa geológico da folha Jacareacanga (Escala 1:250.000) e ao Sr. Takashi Nishidai (Earth Remote Sensing Data Analysis Center – ERSDAC e JAPEX Geoscience Institute) pelo fornecimento dos dados digitais JERS-1/SAR. Este trabalho foi desenvolvido no Laboratório de Processamento de Informações Geo-Referenciadas (LAPIG) do Instituto de Geociências da UNICAMP.

## 6. Referências Bibliográficas

Bizinela, G.A.; Santiago, A.F.; Melo, A.F.F. de; Santos, A. dos; Borges, F.R.; Godoy, H.K.; Yamaguti, H.S.; Oliveira, J.R. de; Carmona, J.R.M.; D'antona R. de J.G. e Oliveira, R.L. Projeto Tapajós – Sucunduri, Relatório Final. Manaus, Convênio DNPM/CPRM, 1980, v. 2 e v. 3, mapa.

Coutinho, M.G. da N.; Liverton, T. e Souza, E.C. de. Granitic magmatism and related gold mineralization in the Tapajós Mineral Province, Amazonian Area, Brazil. 2nd International Symposium on Granites and Associated Mineralizations, Salvador–BA, 1997, p.46-7.

Curlander, J.C. Utilization of spaceborne SAR data for mapping. IEEE Transactions on Geoscience and Remote Sensing, Vol.GE-22, No. 2, 1984, p.106-12.

Deutsch, C.V. e Journel, A. G. GSLIB: Geostatistical Software Library and User's Guide. Oxford University Press, 1992, 340p.

Faraco, M.T.L.; Carvalho, J.M. de A. e Klein, E.L. Carta Metalogenética da Província Aurífera do Tapajós, escala 1:5000.000, nota explicativa, Ministério de Minas e Energia, Secretaria de Minas e Metalurgia, CPRM, Serviço Geológico do Brasil, SUREG Belém, 1996, 18p.

Farr, T.G. Recent advances in geologic mapping by radar. Jet Propulsion Laboratory, California Institute of Technology, Pasadena, CA., 1984, p.199-215.

Haralick, R.M.; Shanmugam, K. e Dinstein, I. Textural features for image classification. IEEE Transactions on Systems, Man, and Cybernetics, Vol. SMC-3, No. 6, 1973, p.610-21.

Klein, E.L.; Vasquez, M.L.; Santos, A. dos e Martins, R.C. Structural elements of the Maloquinha intrusive suite in the Tapajós mineral province, northern Brazil, and the emplacement of the plutons. Second International Symposium on Granites and Associated Mineralizations. Salvador – BA, 1997, p. 313-314.

Matheron, G. Principles of Geostatistics. Economic Geology, El Paso - TX, Vol. 58, n. 8, 1963, p.1246-66.

Miranda, F.P; Fonseca, L.E.N.; Beisl, C.H.; Rosenqvist, A. e Figueiredo, M.D.M.A.M. Seasonal mapping of flooding extent in the vincinity of the balbina dam (Central Amazonia) using RADARSAT-1 and JERS-1 SAR data. International Symposium: Geomatics in the era of radarsat – GER '97, Otawa, Canada, 1997.

Pedroso, E.C.; Crósta, A.P. e de Souza Filho, C.R. Avaliação da habilidade de algorítmos na redução do speckle de imagens JERS-1 SAR. In: SBG,

Congr. Bras. Geol., 38, Salvador – BA, vol 7, 1996, pp. 26-29.

Pessoa, M.R.; Santiago, A.F.; Andrade, A.F. de; Nascimento, J.O. do; Santos, J.O.S.; Oliveira; J.R. de; Lopes, R. da C. e Prazeres, W.V. Projeto Jamanxim, Relatório Final. Manaus, Convênio DNPM/CPRM, 8 v. il., mapa, bibliogr., 1977.

SUDAM/GEOMITEC. Projeto Tapajós – Jamanxim: Mapeamento geológico em semi-detalhe, prospecção geoquímica por concentrado de batéia de minerais pesados em áreas da bacia do rio Jamanxim, Belém, 1972, 214p.

SUDAM/GEOMITEC. Projeto Tapajós – Maués: Geologia, prospecção geoquímica e por concentrado de batéia, Belém, 1976, Vol. I a IV.

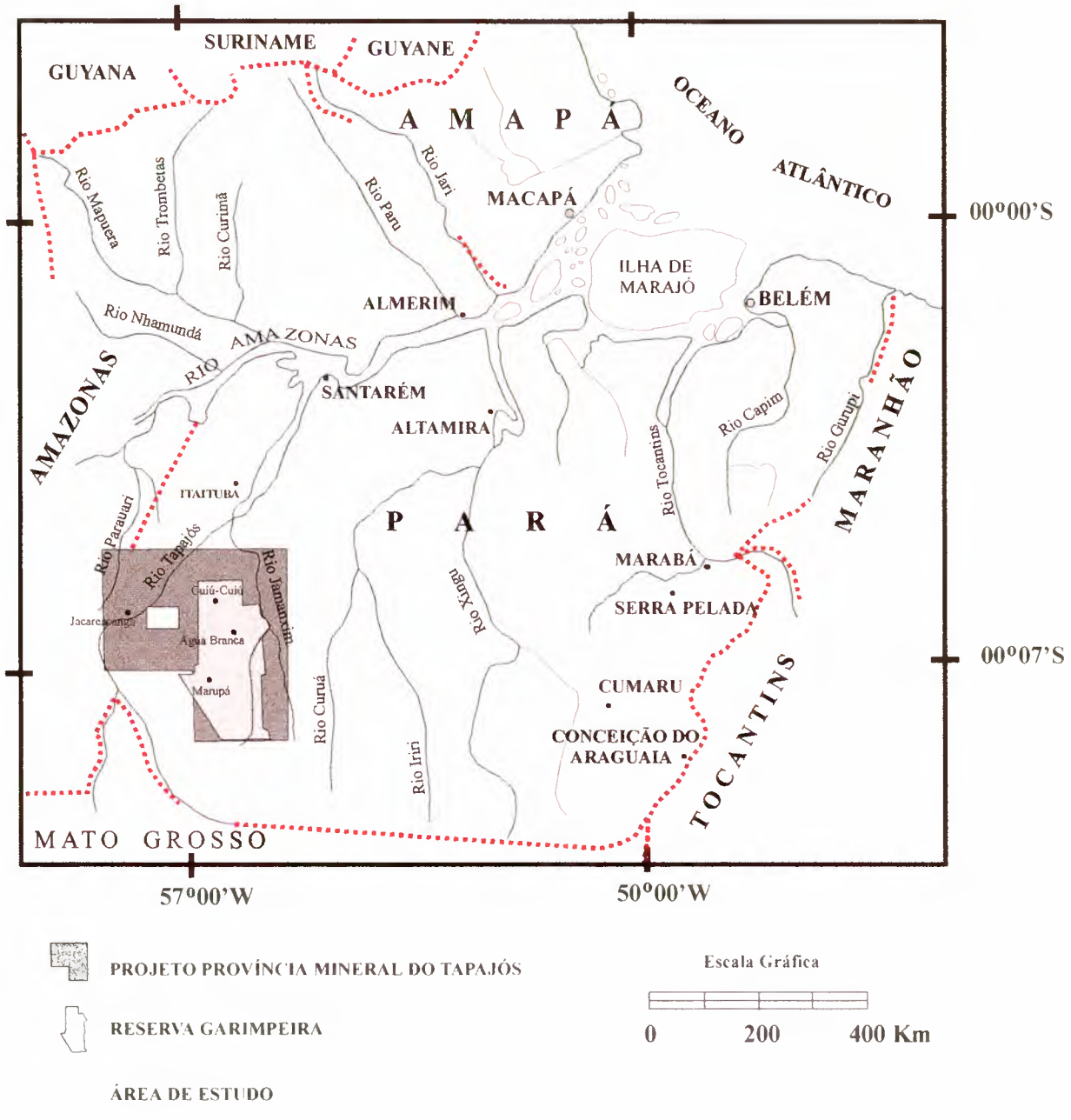


Figura 1. Mapa de localização da área de estudo.

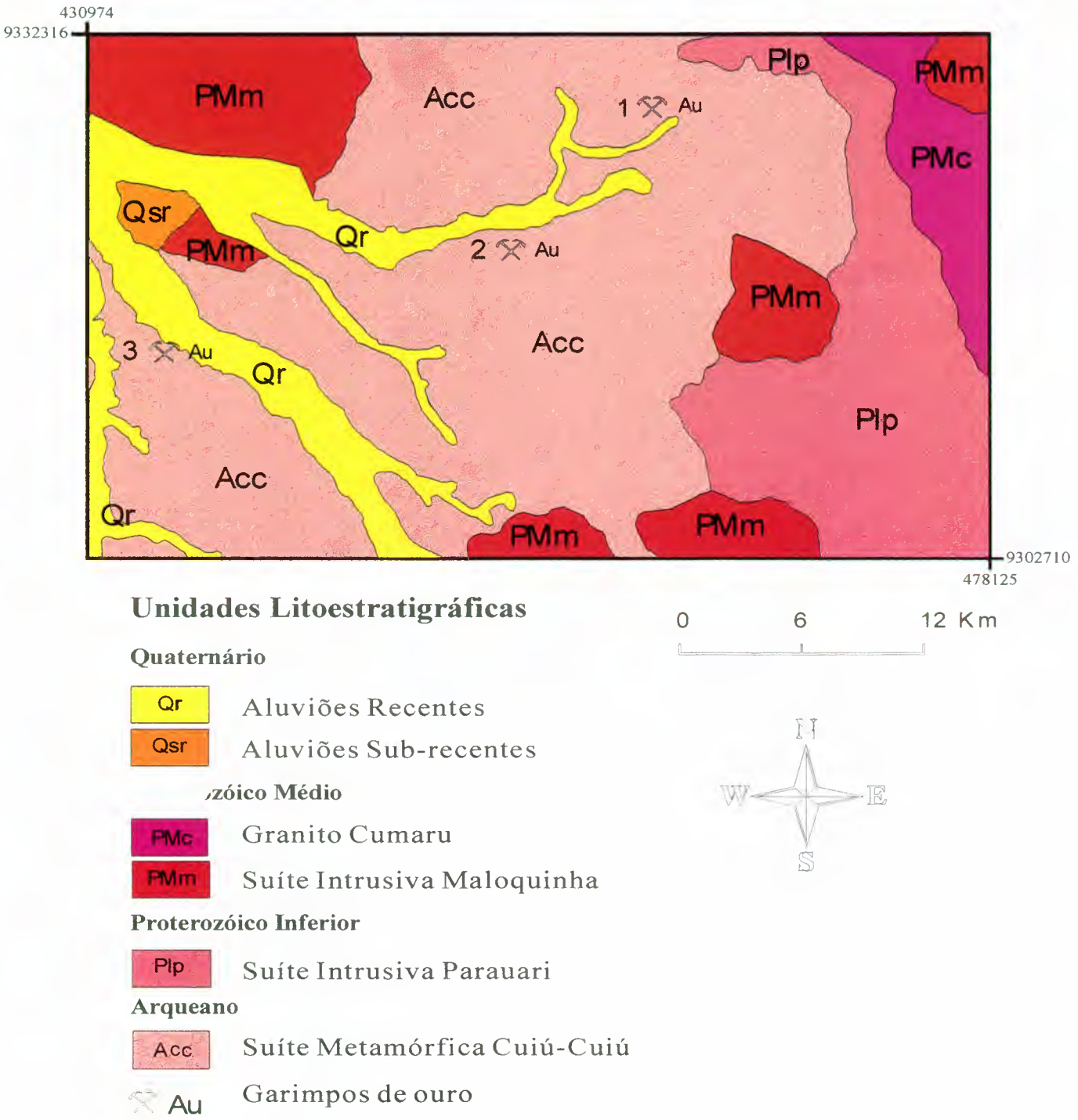


Figura 2. Mapa geológico da área de estudo com a localização aproximada dos principais garimpos da região: 1. Garimpo de Porto Rico, 2. Garimpo de São José e 3. Garimpo das Tropas.

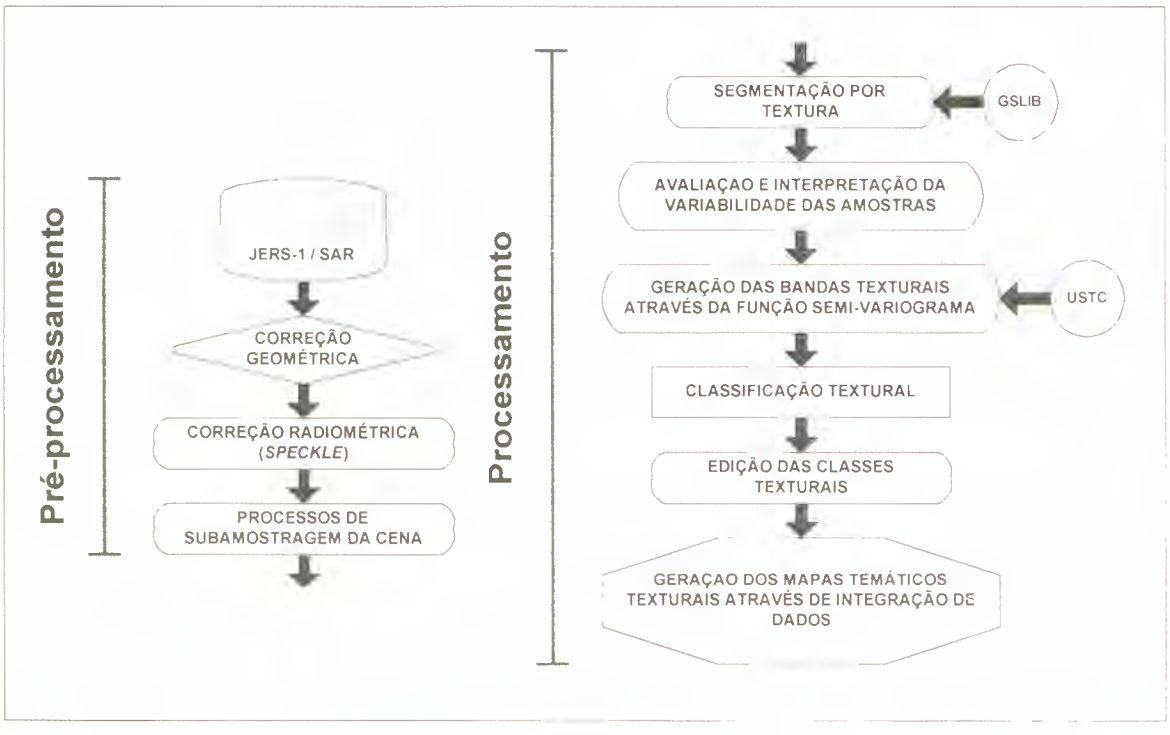


Figura 3. Fluxograma de atividades do processamento realizado nas imagens de radar JERS-1 / SAR.


Figura 4. Imagens JERS-1 / SAR (592 x 942 pixels), sub-amostrada em 25%, com a localização das áreas de treinamento de dimensões 30 x 30 pixels, identificadas na legenda.

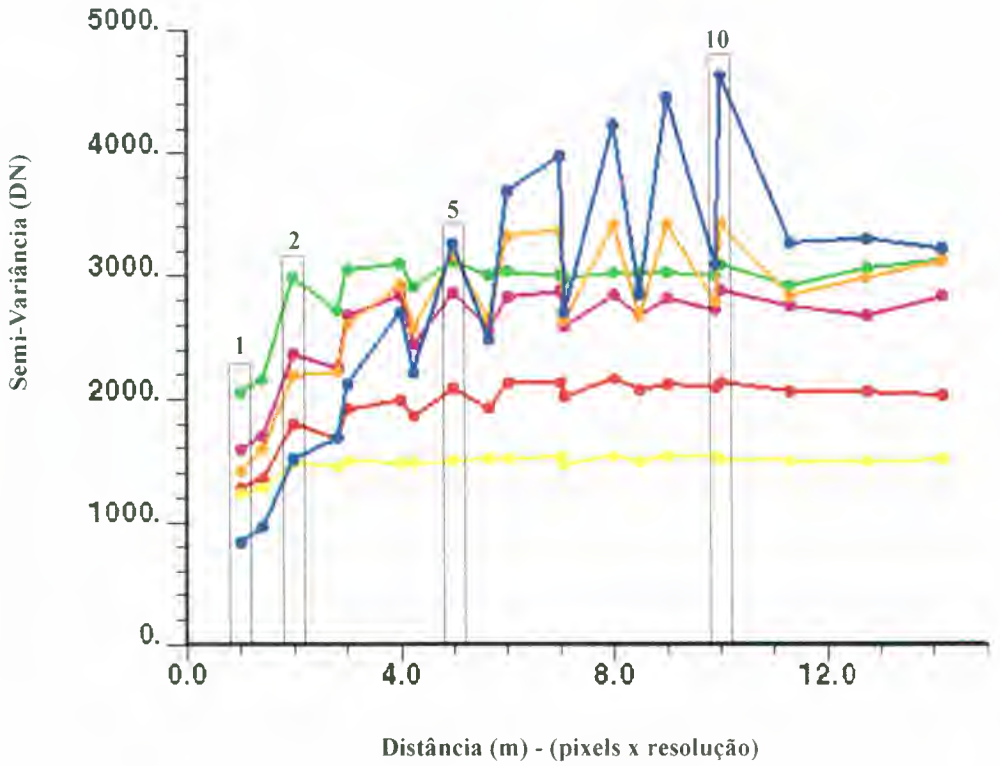


Figura 5. Semi-variograma médio das classes texturais calculadas a partir das três áreas de treinamento calculadas para cada domínio textural investigado (Imagem JERS-1 / SAR, 592 X 942, subamostrada em 25%, janela amostral de 30 x 30 pixels, 10 passos (Lag Distance).

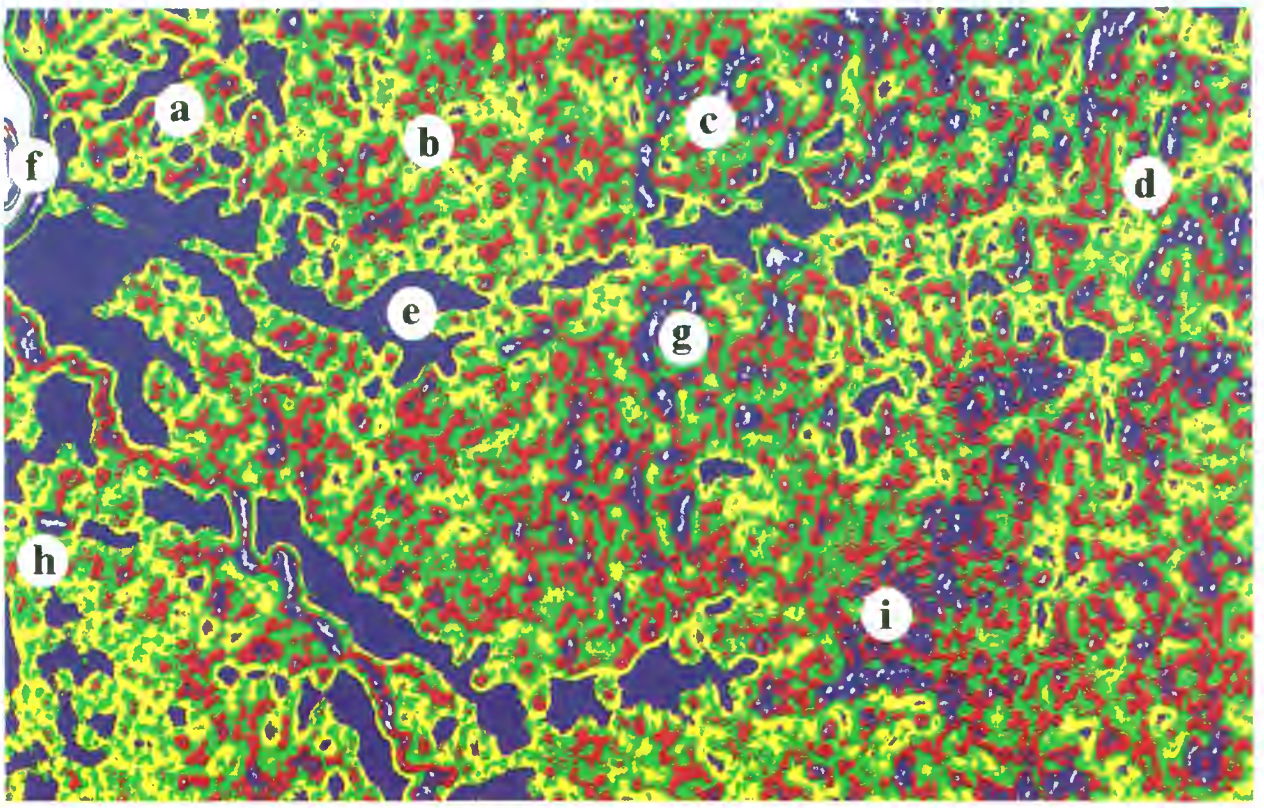


Figura 6. Classificação não-supervisionada da imagem sub-amostrada (592 x 942 pixels) filtrada. Esta imagem apresenta dez classes texturais, em escala aproximada de 1:320.000.

# A SYSTEM FOR MULTILOOK POLARIMETRIC SAR IMAGE STATISTICAL CLASSIFICATION

Corina da C. Freitas[1], Antonio H. Correia[1], Alejandro C. Frery[2], Sidnei J. S. Sant'Anna[1]

[1]INPE-DPI
Av. dos Astronautas 1758
12227-010 São José dos Campos, SP, Brazil
Tel: 55-12-3456475, Fax: 55-12-3456468
corina@dpi.inpe.br; correia@dpi.inpe.br; sidnei@dpi.inpe.br

[2]UFPE-DI
CP 7851
50732-970 Recife, PE, Brazil
Tel: 55-81-2718430, Fax: 55-81-2718438
frery@di.ufpe.br

## ABSTRACT

This paper presents a system for the statistical classification of multilook polarimetric SAR images. The methods used are the pointwise Maximum Likelihood (ML), as initial solution, and the contextual ICM (*Iterated Conditional Modes*) algorithm. The multilook SAR data are modelled from the multivariate complex Wishart distribution, and the densities for several important transformations are derived. The system is user-friendly, since it is based upon interactive graphic user interfaces. With this approach, the statistical modelling is hidden to the user. Examples of classifications of SIR-C/X-SAR images is presented.

## INTRODUCTION

The intensification of remote sensing studies in the field of Synthetic Aperture Radar (SAR) imaging sensors is leading towards a better understanding of the scattering mechanisms of terrestrial targets in the microwaves spectrum. Besides this, it has led to more dependable applications of SAR imagery and products to geology, cartography, and other fields of knowledge.

One of the most useful products of digital images is the result of automatic or semiautomatic data classification. This product is becoming more and more precise since the Gaussian hypothesis was weakened, and since better suited distributions were incorporated into the process (Nezry et al., 1996; Frery et al., 1997a).

In Vieira (1996) this improvement becomes evident: it is shown that the simultaneous use of proper distribution for each class, along with contextual information, leads to better classifications than those obtained either by Gaussian fitting and/or pointwise classification. On the other hand, the use of single-band SAR data has its limitations.

The number of studies and applications involving polarimetric SAR data is increasing steadily. These data are formed by sending and receiving the electromagnetic signal in both horizontal and vertical polarisation and, thus, they may carry a larger amount of information than that available from a single band. Though there is currently no sensor operating in different bands and polarisations, studies in this area are useful.

Several works are devoted to the statistical characterisation of single-look polarimetric SAR data. The reader is referred to DeGrandi et al. (1992), Kong, (1988), Lim et al. (1989), Quegan and Rhodes (1995), Yueh et al. (1989), to name a few.

The potential of multilook polarimetric data, where each value is the mean over several observations, is notorious as presented in Lee and Grunes (1994) and in Lee et al. (1995), for instance. The statistical properties of this kind of data have not been fully exploited yet. They have the advantage of exhibiting a speckle noise reduction as well as data reduction.

A system for multilook polarimetric SAR image classification was developed, in order to assess the potential of this kind of data. It is strongly based on the statistical properties of the data, and it uses a ML classification as the initial configuration for a contextual Markovian classification technique: the ICM, presented in Vieira (1996). In this work an extension of this system is presented, which allows the analysis of intensity, phase difference, ratio of intensities and intensity-phase data. These data formats are derived from multilook polarimetric SAR imagery, and their distributional properties are here recalled. The system if based on graphic user interfaces, and was developed as an extension of the ENVI image processing system.

## POLARIMETRIC SAR SYSTEMS

Conventional SAR systems operate in a single frequency, with a single antenna of fixed polarisation for both the transmitted and received signals. Either the intensity or the amplitude of the returned signal is recorded and, as a consequence, any information carried in the phase of the complex electromagnetic signal is lost.

When polarimetric SAR sensors are used, the full complex signal is recorded and, thus, the return in all the configurations (HH, HV, VH and VV) are fully recorded (intensities and relative phases). In order to accomplish this for every resolution cell the complex scattering matrix, denoted as

$$\mathbf{S} = \begin{pmatrix} S_{VV} & S_{VH} \\ S_{HV} & S_{HH} \end{pmatrix} \tag{1}$$

is measured. Subscripts $p,q \in \{H,V\}$ denote the transmission and emission components of the signal, respectively, and elements $S_{pq}$ are called complex scattering amplitude. Sarabandi (1992) shows that

$$S_{pq} = |S_{pq}| e^{i\phi_{pq}} = \sum_{n=1}^{N} |s_{pq}^{n}| e^{i\phi_{pq}^{n}} \tag{2}$$

where $N$ is the number of scatterers of each resolution element, each having amplitude $|s_{pq}^{n}|$ and phase $\phi_{pq}^{n}$.

Other ways of representing polarimetric data are the Stokes matrix, the modified Stokes matrix, the covariance matrix and the Mueller matrix (Ulaby and Elachi, 1990).

## STATISTICAL PROPERTIES OF POLARIMETRIC SAR DATA

Data obtained with coherent illumination, as is the case of SAR data, are corrupted by a signal-dependent noise called *speckle*. A usual model for the signal and this noise is the Multiplicative Model. It states that, under certain conditions (Tur et al., 1982) the observed value in every pixel is the outcome of the random variable $Z = XY$, where $X$ is the random variable that models the *backscatter* and $Y$ is the one that models the *speckle* noise, and these last two are independent.

Statistical models for multilook polarimetric data are derived from the covariance matrix, which exhibits a complex Wishart distribution (Lee and Grunes, 1992; Du and Lee,1996).

Ulaby and Elachy (1990) show that, for satellites that transmit and receive through the same antenna (which is the usual case), it is possible to suppose that $S_{HV} = S_{VH}$. Therefore, the matrix presented in eq. (1) can be reduced, without loss of information to

$$\mathbf{Z} = \begin{bmatrix} S_1 \\ S_2 \\ S_3 \end{bmatrix} \tag{3}$$

where $S_i$, $1 \le i \le 3$ denotes $S_{HH}$, $S_{HV}$ and $S_{VV}$ in any convenient order.

When the number of elementary backscatterers (denoted $N$ in eq. (2)) is very large, it can be assumed that the vector $\mathbf{Z}$ in eq. (3) obeys a multivariate complex Gaussian distribution (Goodman, 1963). This is true if the backscatter $X$ is constant, independently of the imaged area, since the speckle $Y$ is assumed to obey a multivariate complex Gaussian law.

In this work multilook data are considered and, in order to derive their distributional properties, vector $\mathbf{Z}$ in eq. (3) will be, thus, considered the $k$-th single-look observation and denoted $\mathbf{Z}(k)$. A fixed number, $n$, of independent outcomes of $\mathbf{Z}$ are averaged to form the $n$-looks covariance matrix, given by (Lee et al., 1995).

$$\mathbf{Z}^{(n)} = \frac{1}{n} \sum_{k=1}^{n} \mathbf{Z}(k) \mathbf{Z}^{*}(k)^{T} \tag{4}$$

where $\mathbf{Z}^{*}(k)^{T}$ denotes the transposed conjugate of $\mathbf{Z}(k)$.

The advantage of working with the covariance matrix, defined as $\mathbf{A} = n\mathbf{Z}^{(n)}$, is that it exhibits a multivariate complex Wishart distribution (Srivastava, 1963). Its density is given by

$$p_{\mathbf{Z}^{(n)}}(\mathbf{z}) = \frac{n^{qn} |\mathbf{z}|^{(n-q)} \exp[-n\mathrm{Tr}(\mathbf{C}^{-1}\mathbf{z})]}{K(n,q)|\mathbf{C}|^{n}} \tag{5}$$

where $q$ denotes the dimension of the vector $\mathbf{Z}$, $K(n,q) = \pi^{q(q-1)/2}\Gamma(n)\cdots\Gamma(n-q+1)$, Tr denotes the trace of the matrix, $\mathbf{C} = \mathrm{E}[\mathbf{Z}\mathbf{Z}^{*T}]$, and $\Gamma$ is the Euler Gamma function (DeGroot, 1968).

Using eq. (5) it is possible to derive the densities for situations of particular interest, as presented in Lee et al. (1995). The following situations were implemented in the system here considered: a pair of intensities, phase difference, ratio of intensities and pair intensity-phase.

## THE SYSTEM

The system behaves as an extension of the ENVI v. 2.5 (*Environment for Visualisation of Images*) system, and it uses its functions and others from IDL (*Interactive Data Language*). In this manner, several functions such as those for data management, processing and analysis were reused.

Both classifications implemented are supervised and, thus, require the specification of training sets for parameter estimation. These sets are informed through *regions of interest*, previously defined by the used with

ENVI utilities. The equivalent number of looks ($n$ in eqs. (4) and (5)) is also an input parameter; it can be estimated within the system as presented in Vieira (1996).

The ICM classification method is a contextual procedure that, in order to classify every pixel, uses both the observed value in the corresponding coordinate and the classification of the surrounding sites. In order to incorporate this context within a statistical framework, a Markovian model is incorporated for the classes. This model is known in the literature as Potts-Strauss (Frery et al. 1997b; Vieira, 1996; Vieira et al. 1997).

The system here presented uses an inference technique called *pseudolikelihood*, in order to estimate the required parameters of the Markovian model without the need of intervention of the user. Details are available in Vieira (1996), Vieira et al. (1997) and in Frery et al. (1997b). The current implementation uses any existing classification as starting point, being the ML the preferred one.

The following subsections describe the functionality of the system, in every case for $n$ looks intensity data. The densities and parameter estimators are presented in Lee et al. (1994).

## ICM INTENSITY BIVARIATE SAR

This option applies the ML and ICM classifications to a pair of intensity images, either two polarimetric components or the result of two passages of the same monospectral sensor (such as JERS-1, ERS-1, etc.).

After the input of the initial data the interface shown in Figure 1 is presented. It exhibits the 2-D histogram of the pair of bands, along with the 2-D estimated density, both in perspective and in contour plot. The estimated parameters are presented at the bottom of the plots.

As every interface presented in this work, that presented in Figure 1 is fully interactive with the user. The user can specify the interval the plots will be drawn, any desirable rotation, the number of levels to be used, etc. This feature greatly stimulates the interaction of the user with the data. The input values affect all the sub-windows, since they are connected in order to help the visualisation.

This interface has to be used for every class of interest. Once this is performed, the ML classification is performed, and the interface shown in Figure 2 is presented to the user. The user can interactively choose the classes for which the estimated densities are presented (in perspective and in isolines). The user can specify the viewpoint and number of slices. Each class is associated to a unique colour.

The ML classification is produced, and used as initial configuration by the ICM algorithm. This iterative technique stops according to the number of coordinates whose classification changes from one iteration to the next (Vieira, 1996).

Denoting as $R_1, R_2$ the pair of intensities, their joint density under the model characterised by eq. (5) is

$$p(R_1,R_2)=\frac{n^{n+1}(R_1R_2)^{\frac{(n-1)}{2}}\exp\left(-\frac{n\left(\frac{R_1}{H_{11}}+\frac{R_2}{H_{22}}\right)}{1-|\rho_c|^2}\right)}{(H_{11}H_{22})^{\frac{(n+1)}{2}}\Gamma(n)(1-|\rho_c|^2)|\rho_c|^{n-1}}I_{n-1}\left(\frac{2n|\rho_c|}{1-|\rho_c|^2}\sqrt{\frac{R_1R_2}{H_{11}H_{22}}}\right)$$

where $H_{11}=\mathrm{E}[R_1]$ and $H_{22}=\mathrm{E}[R_2]$, $I_{n-1}$ denotes the modified Bessel function of order $n-1$, and

$$\rho_c=\frac{\mathrm{E}[S_iS_j^*]}{\sqrt{\mathrm{E}[|S_i|^2]\mathrm{E}[|S_j|^2]}}=|\rho_c|e^{i\theta}$$

The parameter $|\rho_c|$ can be estimated by

$$\hat{\rho}=\frac{\mathrm{E}[(R_1-\overline{R}_1)(R_2-\overline{R}_2)]}{\sqrt{\mathrm{E}[(R_1-\overline{R}_1)^2]\mathrm{E}[(R_2-\overline{R}_2)^2]}}$$

where $\overline{R}_1$ and $\overline{R}_2$ denote the mean of $R_1$ and $R_2$, respectively.

$$\Psi=Arg\left|\overbrace{\frac{1}{n}\sum_{k=1}^{n}S_i(k)S_j^*(k)}^{R_{ij}^{(n)}}\right|=\tan^{-1}\left[\frac{\Im\left[R_{ij}^{(n)}\right]}{\Re\left[R_{ij}^{(n)}\right]}\right] \qquad (4)$$

where $\Re$ and $\Im$ denote, respectively, real and imaginary parts.

After the required parameters have been introduced, Figure 3 is presented, with the histogram of the data, the fitted density and estimated phase difference parameters. When every class has been checked with this interface, Figure 4 is shown. This interface presents the estimated densities of the phase difference for every considered class, allowing the visual assessment of their separability throughout this feature.

The density of the quantity defined above, under the aforementioned model, is given by

$$p_\Psi^{(n)}(\psi)=\frac{\Gamma(n+1/2)(1-|\rho_c|^2)^n\beta}{2\sqrt{\pi}\,\Gamma(n)(1-\beta^2)^{n+1/2}}+\frac{(1-|\rho_c|^2)^n}{2\pi}F(n,1;1/2;\beta^2)$$

where $-\pi<\psi\le\pi$, $\beta=|\rho_c|\cos(\psi-\theta)$, $\theta$ is the phase of the complex coefficient of correlation and $F(n,1;1/2;\beta^2)={}_2F_1(n,1;1/2;\beta^2)$ is the Gaussian hypergeometric function (Abramowitz and Stegun, 1964).

## ICM PHASE DIFFERENCE SAR

This option applies the ML and ICM classifications to $\Psi$, the difference between the phases of two complex images. These images are derived from two components $S_i(k)$ and $S_j(k)$ of single-look images (eq. (2)) in the following manner:

## ICM RATIO OF INTENSITIES

Both the ML and ICM classification are obtained, derived from the ratio between two multilook intensity bands, i.e., using data of the form $R_i/R_j$ .

Analogously to the previous situation, namely for the classification using phase difference, after the required inputs the histogram, fitted densities and estimated parameters are shown for every class. Once the fittings have been checked for every class, the whole set of fitted densities is shown.

The density that characterises this data is

$$p^{(n)}(w) = \frac{\tau^n \Gamma(2n)(1-|\rho_c|^2)^n (\tau+w) w^{n-1}}{\Gamma(n)\Gamma(n)[(\tau+w)^2 - 4\tau|\rho_c|^2 w]^{(2n+1)/2}}$$

where $\tau = H_{11}/H_{22}$ and $w = R_1/R_2$ .

## INTENSITY AND PHASE ICM SAR

This option calculates both the ML and ICM classification, using a multilook intensity image $R_i$ and a phase difference $\Psi$. The input data for this processing are two multilook bands $R_i$ and $R_j$, and the corresponding multilook complex image $R_{ij}^{(n)}$ (see eq. (6)).

The rest of the process is as presented in previous sections, namely for classification using a pair of intensities.

In order to derive the joint density of $R_I$ and $\Psi$, intensity and phase difference data obtained from two components $S_i$ and $S_j$ of the scattering matrix, consider the image

$$B_1 = \frac{nR_1}{H_{11}} = \frac{\sum_{k=1}^{n} |S_i(k)|^2}{H_{11}}$$

The joint density of $B_I$ and $\Psi$ is given by

$$p(B_I,\psi) = \frac{B_I^{n-1}\exp\left(-\frac{B_I}{1-|\rho_c|^2}\right)}{2\pi\Gamma(n)} {}_1F_1\left[1;\ \frac{1}{2};\ \frac{\beta^2}{1-|\rho_c|^2}B_I\right] + \frac{\beta B_I^{n-\frac{1}{2}}\exp\left(-\frac{B_I(1-\beta^2)}{1-|\rho_c|^2}\right)}{2\pi\Gamma(n)\sqrt{1-|\rho_c|^2}}$$

where ${}_1F_1$ is the Confluent hypergeometric function (Abramowitz and Stegun, 1964).

## EXPERIMENTAL RESULTS

In Correia (1998) applications of all the aforementioned classifications are presented, aiming at the assessment of the feasibility of the proposed system and methodology.

The results here presented are obtained using a space shuttle SIR-C/X-SAR image, bands L and C, type MLC (Multi-Look Complex), with 4.7854018 as its nominal number of looks. Its pixel spacing is of 12.5×12.5 meters. It was obtained the 14th of April, 1996, over the region of Petrolina, PE, Brazil, an agricultural area exhibiting several crops. The image has 407x370 pixels, and was taken at 09°07' S, 40°18' W.

The classes of interest for this study are river (blue), caatinga (green), prepared soil (red), soy (magenta), tillage (cyan) and corn (yellow). Samples of each class were obtained, of sizes 4949, 5177, 3221, 2609, 635 and 3505, respectively.

Figure 5 shows two colour composites of the original data. To the right, C-band data is shown with the HH polarisation in the red channel, the HV in the green and the VV in the blue. To the left, L-band with the same colour coding.

The equivalent number of looks (ENL) was estimated as 2.97479. This value is the mean of the ENLs for each component, as presented in Table 1. As expected, this value is below the nominal number of looks due to, among other factors, the lack of independence between individual elements in eq. (3).

TABLE 1 - ESTIMATED ENLs FOR ALL THE AVAILABLE BANDS AND POLARISATION, AND OVERALL MEAN

| | Band | |
|---|---|---|
| **Polarisation** | **L** | **C** |
| **HH** | 2.6688 | 2.67133 |
| **HV** | 3.18357 | 2.97230 |
| **VV** | 3.53396 | 2.81879 |
| **Mean** | 2.97479 | |

Large samples were collected over homogeneous areas, in order to be able to apply a decorrelation algorithm. This method first estimates the autocorrelation function,

in order to define the most suited lags for subsampling in both horizontal and vertical directions. All samples passed the $\chi^2$ goodness of fit test at the 1% level of significance, revealing no significant departure from the hypothesised distribution.

All four types of classifications were obtained, and the best one, for both L and C bands, was obtained when two intensity images were used. In particular, the pairs HV-VV and HH-HV were the most successful in bands L and C, respectively, for either ML or ICM classifications.

The comparison among classifications was performed using the coefficient of agreement $\kappa$, in order to assess quantitatively the significance of the differences. Using this criterion, for the considered image it was possible to conclude that

1. In band L, with intensity pair HV-VV, the ML (ICM, respectively) classification performed, in mean, 111.09% (67.22%, resp.) better than the other classifications.
2. In band C, with the intensity pair HH-HV, the ML (ICM, resp.) classification performed, in mean, 246.95% (180.04%, resp.) better than the other classifications.

Table 2 presents the estimated coefficients of agreement ($\hat{\kappa}$) and their sample variances ($\hat{\sigma}^2_{\kappa}$) for the best classifications obtained using band C and L intensity pairs, and both ML and ICM algorithms. The sample sizes used to calculate the values presented in Table 2 are 3844 (river), 3585 (caatinga), 2101 (prepared soil), 2128 (soy), 360 (tillage) and 1946 (corn).

In this way, it can be concluded that, for the current SIR-C image in intensity pairs:

1. The ICM applied to the L band yields to results 28.14% better than the ML, both using the HV-VV components.
2. The ICM applied to the C band yields to results 20.38% better than the ML, both using the HH-HV components.

TABLE 2 - ESTIMATED COEFFICIENTS OF AGREEMENT ($\hat{\kappa}$) AND THEIR SAMPLE VARIANCE ($\hat{\sigma}^2_{\kappa}$) FOR ALL THE INTENSITY PAIRS CLASSIFICATIONS.

| Image | $\hat{\kappa}$ | $\hat{\sigma}^2_{\kappa}\left(\times 10^{-5}\right)$ |
|---|---|---|
| **ML/L–HV-VV** | 0.606424 | 2.35719 |
| **ML/C–HH-HV** | 0.575344 | 2.50954 |
| **ICM/L–HV-VV** | 0.777114 | 1.64955 |
| **ICM/C–HH-HV** | 0.692635 | 2.10982 |

Figure 6 shows the best results of the ML classifications for the L (left) and C (right) bands data, when using two intensity images. Figure 7 shows the best results of the ICM classifications, when using the same bands data. From these figures and from Table 2 it is possible to conclude that the ICM classification scheme is superior to the ML.

## CONCLUSIONS

In this paper a system for pointwise and contextual polarimetric multilook SAR image classification was presented. It functions as and add-in to the ENVI system, and it was developed in IDL. The system was built with the interactivity and user-friendliness in mind. It is also goal-driven, so users not familiar to it can learn it easily.

The system proved being efficient for the classification of a SIR-C/X-SAR image, though the modelling of data from all the observed classes was restricted, in the sense that only a model for homogeneous areas was considered.

According to Landis and Koch (1977), the classifications obtained with this system qualify as "very good", using the coefficient of agreement $\kappa$ as a measure of quality.

For the considered data, the use of contextual information (incorporated through the ICM classification algorithm) yields to a significant classification improvement, of the order of 24%. This improvement is not so dramatic as those obtained for single band amplitude data (Vieira, 1996), which is a somewhat expected result due to the larger amount of information potentially present in polarimetric data sets.

## ACKNOWLEDGMENTS

This work was supported by grants from PPG-7 (0808/95 and 0816/95), Convênio FINEP (6.6.96.0473.00 and 6.6.96.0474.00), CNPq (Proc. 523469/96-9) and FACEPE (APQ 0707-1.03/97).

## REFERENCES

Abramowitz, M.; Stegun, I. *Handbook of mathematical functions: with formulas, graphs, and mathematical tables.* New York, Dover, 1964.

Correia, A.H. *Desenvolvimento de classificadores de máxima verossimilhança e ICM para imagens SAR polarimétricas.* (MSc in Remote Sensing) – Instituto Nacional de Pesquisas Espaciais. São José dos Campos, SP, Brazil, 1998. To be presented.

DeGrandi, G.; Lemoine, G.; Sieber, A. Supervised fully polarimetric classification: an experimental study on the MAESTRO-1 Freiburg data set. In: IGARSS'92 International Geoscience and Remote Sensing Symposium'92, Houston, May. 26-29, 1992. *International Space Year: space remote sensing.* IEEE, 1992. v. I, p. 782–785.

DeGroot, M.H. *Probability and statistics*. Menlo Park, Addison-Wesley, 1975. 607 p.

Du, L.J.; Lee, J.S. Polarimetric SAR image classification based on target decomposition theorem and complex Wishart distribution. In: IGARSS'96 International Geoscience and Remote Sensing Symposium'96, Lincoln, May. 27-31, 1996. *Remote Sensing for a Sustainable Future*. IEEE, 1996. v. I, p. 439–441.

Frery, A.C.; Müller, H.J.; Yanasse, C.C.F; Sant'Anna, S.J.S. A model for extremely heterogeneous clutter. *IEEE Trans. Geosc. Rem. Sens.*, 35(3):1–12, 1997a.

Frery, A.C.; Yanasse, C.C.F.; Vieira, P.R.; Sant'Anna, S.J.S.; Rennó, C.D. A user-friendly system for synthetic aperture radar image classification based on grayscale distributional properties and context. Simpósio Brasileiro de Computação Gráfica e Processamento de Imagens, 10., 1997, p. 211–218. *SIBGRAPI 97*. Los Alamitos, CA, IEEE Computer Society, 1997b.

Goodman, N. R. Statistical analysis based on a certain multivariate complex Gaussian distribution. *Ann. Math. Stat.*, 34(1):152–177, 1963.

Kong, J.A. Identification of terrain cover using the optimal polarimetric classifier. *J. Electrom. Waves Appl.*, 2(2):171–194, 1988.

Landis, J.; Koch, G.G. The measurements of observer agreement for categorical data. *Biometrics*, 33(3):159–174, 1977.

Lee, J.S.; Hoppel, K.W.; Mango, S.A. Intensity and phase statistics of multi-look polarimetric and interferometric SAR imagery. *IEEE Trans. Geosc. Rem. Sens,*. 32(5):1017–1028, 1994.

Lee, J.S.; Du, L.; Schuler, D.L.; Grunes, M.R. Statistical analysis and segmentation of multi-look SAR imagery using partial polarimetric data. In: IGARSS'95 International Geoscience and Remote Sensing Symposium'95, Firenze, Jul. 10–14, 1995. *Quantitative Remote Sensing for Science and Applications*. Piscataway, IEEE, 1995. v. III, p. 1422–1424.

Lee, J.S.; Grunes, M.R. Classification of multilook polarimetric SAR imagery based on complex Wishart distribution. *Int. J. Rem. Sens.*, 15(11):2299–2311, 1994.

Lim, H.H; Swartz, A.A.; Yueh, H.A.; Kong, J.A.; Shin, R.T.; Van Zyl, J.J. Classifications of earth terrain using polarimetric SAR images. *J. Geophys. Res.*, 94(B6):7049–7057, 1989.

Nezry, E.; Lopés, A.; Ducrot-Gambart, D.; Nezry, C.; Lee, J.S. Supervised classification of K-distributed SAR images of natural targets and probability of error estimation. *IEEE Trans. Geosc. Rem. Sens.*, 34(5):1233–1242, 1996.

Quegan, S.; Rhodes, I. Statistical models for polarimetric data: consequences, testing and validity. *Int. J. Rem. Sens.*, 16(7):1183–1210, 1995.

Sarabandi, K. Derivations of phase statistics from the Mueller matrix. *Radio Science*, 27(5):553-560, 1992.

Srivastava, M.S. On the complex Wishart distribution. *Ann. Math. Stat.*, 36(1):313–315, 1963.

Tur, M.; Chin, K.C.; Goodman, J.W. When is speckle noise multiplicative? *Appl. Opt.*, 21:1157–1159, 1982.

Ulaby, F. T.; Elachi, C. *Radar polarimetric for geoscience applications*. Norwood, Artech House, 1990. 364p.

Vieira, P.R. *Desenvolvimento de classificadores de maxima verossimilhança e ICM para imagens SAR*. (MSc in Remote Sensing) – Instituto de Nacional de Pesquisas Espaciais. São José dos Campos, SP, Brazil, 1996. 251 p. (INPE-6124-TDI/585).

Vieira, P.R.; Yanasse, C.C.F.; Frery, A.C; Sant'Anna, S.J.S. Um sistema de análise e classificação estatísticas para imagens SAR. In: Primeras Jornadas Latinoamericanas de Percepción Remota por Radar, Buenos Aires, Dez. 1996. *Técnicas de Processamiento de Imágenes*. Paris, ESA, 1996. p. 170–185.

Yueh, S.H.; Kong, J.A.; Jao, J.K.; Shin, R.T.; Novak, L.M. K-distributition and polarimetric terrain radar clustter. *J. Electrom. Waves Appl.*, 3(8):747–768, 1989.

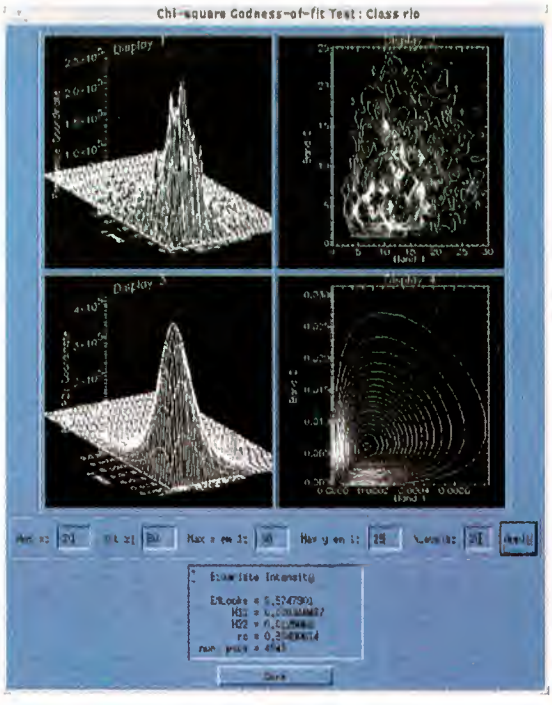


Fig. 1 - Density, 2-D histogram, contour plot and estimated parameters of two multilook intensity bands.

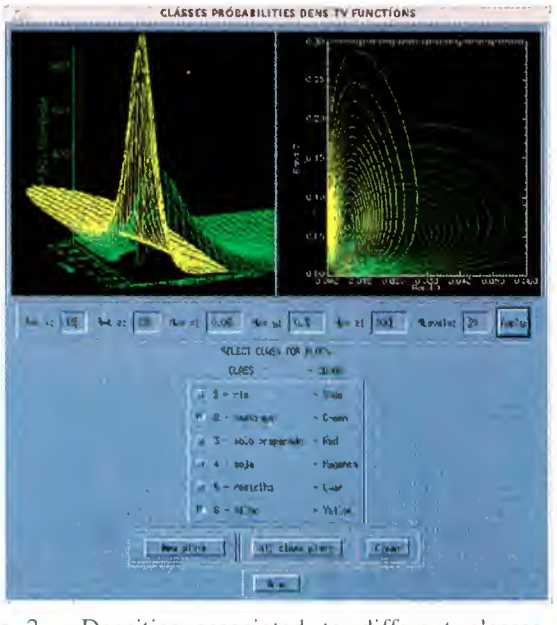


Fig. 2 - Densities associated to different classes of interest.

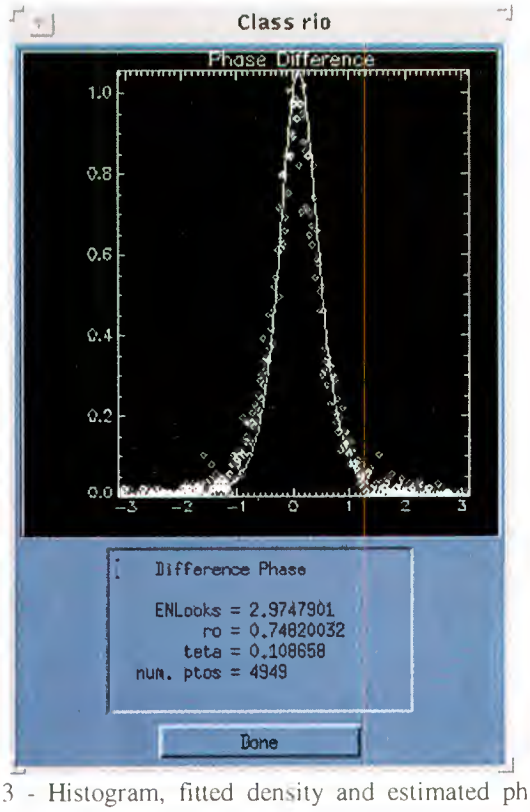


Fig 3 - Histogram, fitted density and estimated phase difference parameters.

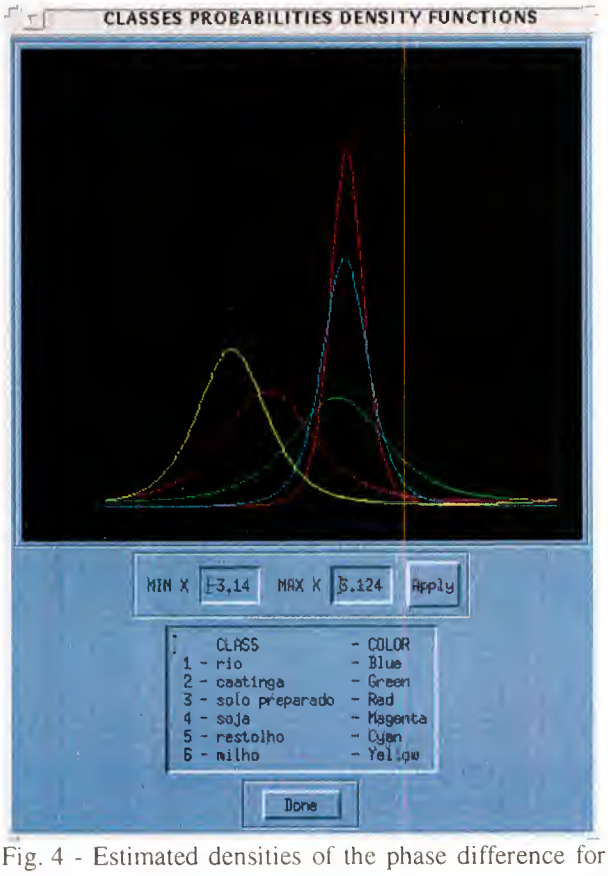


Fig. 4 - Estimated densities of the phase difference for every considered class.

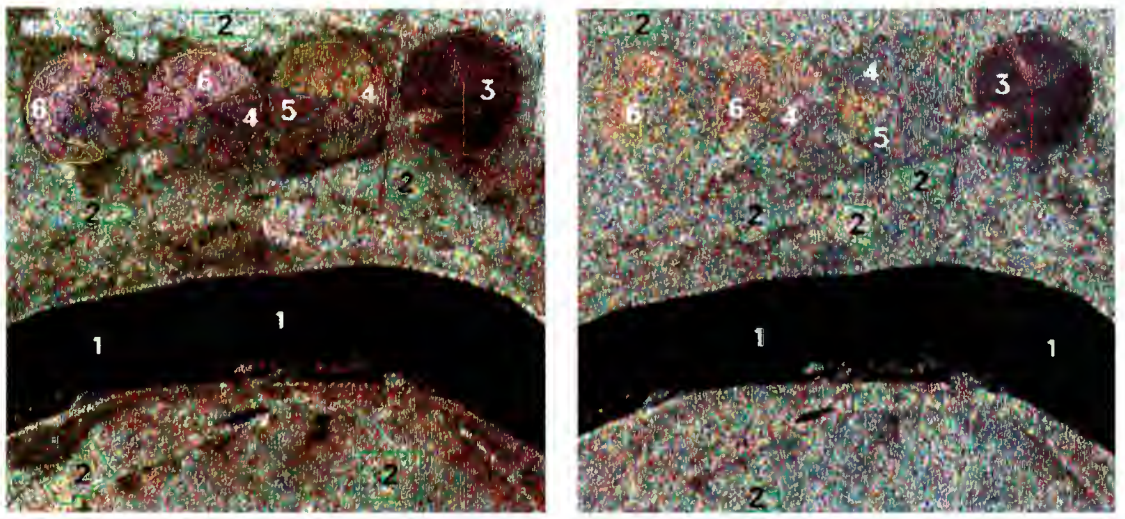


Fig. 5 - Colour compositions (original data) R-HH, G-HV, B-VV, bands L (l) with training sets and C (r) with test sets.

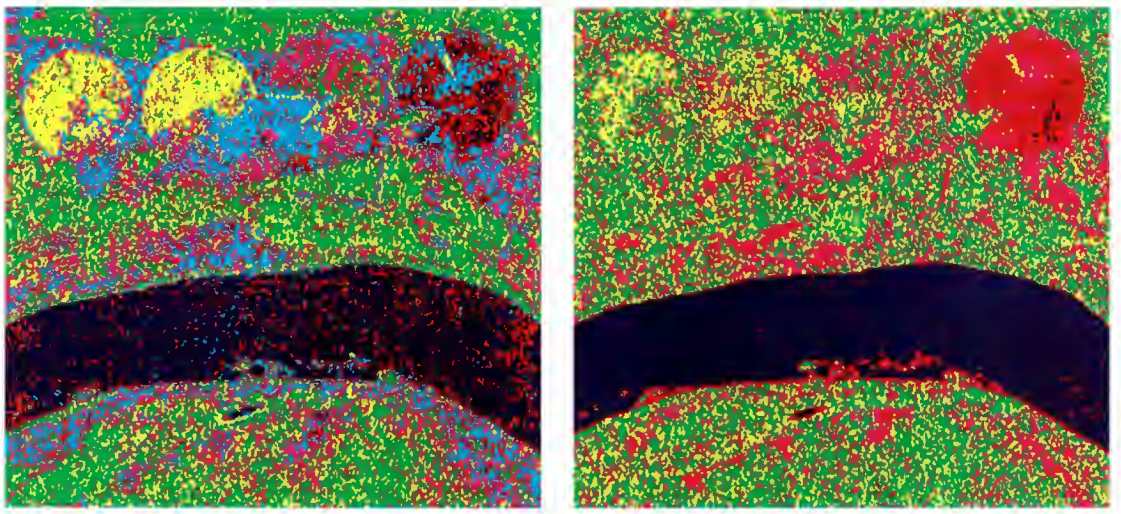

Fig. 6 - ML classifications of the L (l, using HV and VV components) and C (r, HH and HV components) data sets.

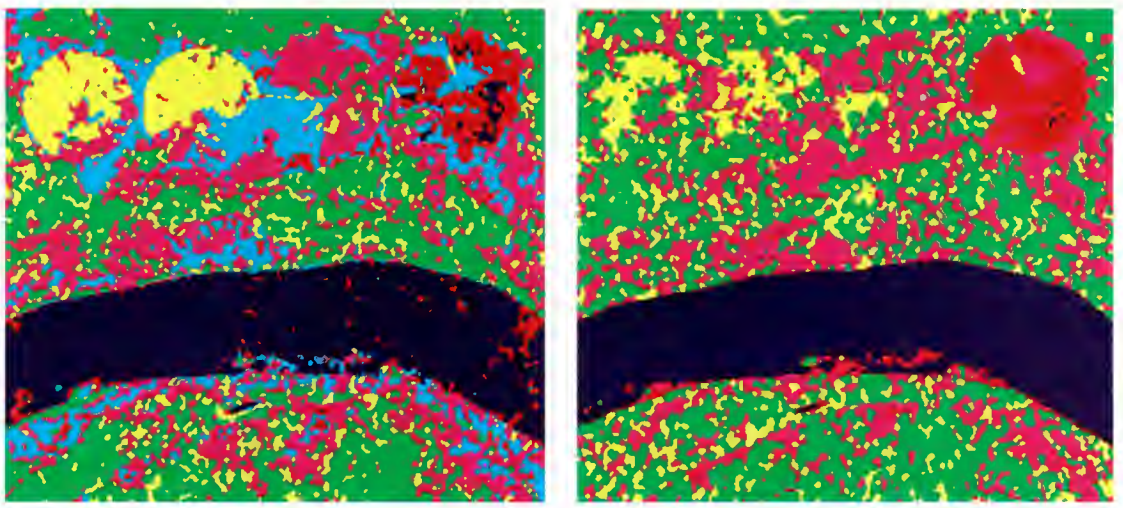

Fig. 7 - ICM classifications of the L (l, using HV and VV components) and C (right, HH and HV components) data sets.

# SYNTHETIC APERTURE RADAR TEXTURE CLASSIFICATION BY AUTORREGRESSIVE MODELLING

*Sérgio Monteiro Soares, Luciano Vieira Dutra, *Waldecir João Perrela*

Instituto Nacional de Pesquisas Espaciais, INPE, Caixa Postal 515, 12201-097, São José dos Campos, SP Brasil. Fax:55-12-345 6468, email (msoares, dutra)@dpi.inpe.br.
*Instituto Tecnológico da Acronáutica, CTA/ITA, Praça Marechal Eduardo Gomes, 50, Vila das Acácias, CEP 12228-900, São José dos Campos, SP, Brasil, email waldecir@ele.ita.cta.br

**Abstract.** A texture feature extraction method using autorregressive modeling is presented and used for rain forest classification. The method was tested using a JERS-1 (L band) SAR image from "Floresta Nacional do Tapajós", Pará State, Brazil. The identified classes were Dense Primary Forest and Undulate Primary Forest. A Landsat TM color composition and field data from the same area was used as reference. A set of filtered (using inverse autorregressive filters) bands, obtained from the original SAR image, was used to classify a scene composed by typical samples of primary forests. The results were analyzed using the confusion matrix, and showed a Kappa coefficient of 96.1 %, instead of a Kappa of 36.1 % using the original channel only.

## 1 Introduction

Texture, as is widely known, is a key feature to use SAR imagery for digital classification purposes. Several methods have been presented in the literature with limited success. In this text we present a methodology based on two-dimensional autorregressive modeling for texture feature extraction and classification of primary forest classes as observed in JERS-1 imagery.

## 2 Autorregressive Models.

The Autorregressive (AR) models are a particular case of the Autorregressive and Moving Average models, (ARMA) which assume time series as being generated by a linear filter (figure 2.1) excited by a white noise. The input of this filter, called *shocks*, is a time sequence of independent random variables, identically distributed with null average and variance $\sigma^2$, IID(0, $\sigma^2$).

| White Noise($a_t$) → | LINEAR FILTER | → Time Series ($Z_t$) |
|---|---|---|

Figure 2.1 - Time serie $Z_t$ as output of linear filter, excited by white noise $a_t$.

The ARMA filter can be described as a weighted addition of observation and previous inputs - the so called difference equation. This addition, with finite or infinite number of coefficients, will be convergent for stationary processes, and the filter will be *stable*. The ARMA model is described by the equation 2.1 (Marple, 1988).

$$Z_t = \sum_{k=1}^{p} \phi_t . Z_{t-k} - \sum_{k=0}^{q} \theta_t . a_{t-k} + \mu \qquad (2.1a)$$

or

$$Z_t^* = \phi_1 . Z_{t-1}^* + \ldots + \phi_p . Z_{t-p}^* + a_t - \theta_1 . a_{t-1} - \ldots - \theta_q . a_{t-q} \qquad (2.1b)$$

where: $Z_t^* = Z_t - \mu$

The coefficients $\phi_t$ are the autorregressive parameters and $\theta_t$, the moving average. This is the ARMA(p, q) model, of order p and q, where $\theta_0 = -1$, without loss of generality.

From equations 2.1a and 2.1b, the purely autorregressive model (q=0) can be stated as below:

$$Z_t = \sum_{k=1}^{p} \phi_t . Z_{t-k} + a_t + \mu \qquad (2.2a)$$

$$Z_t^* = \phi_1 . Z_{t-1}^* + \ldots + \phi_p . Z_{t-p}^* + a_t \qquad (2.2b)$$

where, again, $Z_t^* = Z_t - \mu$

The parameters $\phi_t$, in the equations 2.2a and 2.2b, can be estimated by the Yule-Walker equations, using the recursive Levinson-Durbin algorithm, as described in Kay (1988), pages 170 and 171.

Extension of the AR model for the two-dimensional case is straightforward and estimation of model parameters for the quarter plane support is easily obtained. (Maple, 1998). Here an alternative method is used, where two-dimensional samples of image classes are transformed into one-dimensional time series by concatenating segments of line. Then autorregressive parameters are estimated for this one dimensional time series of concatenated segments. The concatenation operation of line segments generates a mapping that later will be used to re-map the estimated coefficients back to the plane, establishing, this way, the two-dimensional autorregressive model (AR-2D) (Dutra, 1990).

## 3 Methodology

The methodology for textural feature extraction and classification is summarized by the following steps

(Soares,1998):

- Stage 1: Autorregressive model estimation.

An AR2D model is fitted for each textural class of interest (section 2) . In this work rectangular areas were used for data collection and were also used for training the classifier in a later stage.

- Stage 2: Definition of Autorregressive Inverse Filters

Parameters that are within confidence levels for the null hypothesis (Brockwell & Davis, 1987, pages 231-238) are excluded from the models of each class. This will define a finite length two-dimensional filter that is matched to each texture. From equation 2.2 $a_t$ can be obtained relative to each estimated texture class filter. These are called inverse filters because they estimate the *shocks* that gave origin to each texture field, as depicted in figure 2.1.

- Stage 3: Inverse AR Filtering, Whitenning and Energy

Matched inverse autorregressive filters, relative to each class, are applied sequentially to the original image. When a region is filtered by its matched correspondent filter, the resulting field is expected to yield minimum energy (eq. 3.2) when compared all other non matched filters. This field will also be an approximately white noise field. To measure the whitening of the output of the inverse filters the following operator, who acts in a neighborhood of a point of coordinate l=(i,j), is defined:

$$b_L = \sum_{m,n \in W} \frac{(x_{m,n} - \bar{x})(x_{m,n+1} - \bar{x})}{\#W} + \sum_{m,n \in W}^{*} \frac{(x_{m,n} - \bar{x}).(x_{m+1,n} - \bar{x})}{\#W} \qquad (3.1)$$

where $b_L$ is the whitening coefficient that will substitute the central pixel of a window W; #W is the cardinality of the window. $b_L$ is the addition of the autocorrelations of lag 1, and presents values next to zero for white noise random fields. The energy filter is given by:

$$FEn(i,j) = \sqrt{\frac{\sum_{m,n \in W}^{n} (x_{m,n})^2}{\#W}} \qquad (3.2)$$

where $x_{m,n}$ is the value of the pixel in position $(m,n)$.

As a result a set of M bands of filtered images, where M is equal of number of classes multiplied by three, are obtained form the original image:

- The raw output of the inverse filters.

- The whitening coefficient calculated from the outputs of the inverse filters.

-The energy bands, also calculated from the outputs of the inverse filters.

- Stage 4: Classification of Máximum Likelihood

The set of filtered bands of the original image is then classified by the Maximum Likelihood classifier with the same training samples that had generated the AR parameters (Soares, 1998).

**4 Results**

To test the method, a mosaic of JERS-1 sub-images containing representative textures of two types of forests: dense flat forest and undulated (dissected) forest was chosen. The mosaic, shown in **figure 4.1,** is relative to the National Forest of the Tapajós, in the State of Pará, Brazil.

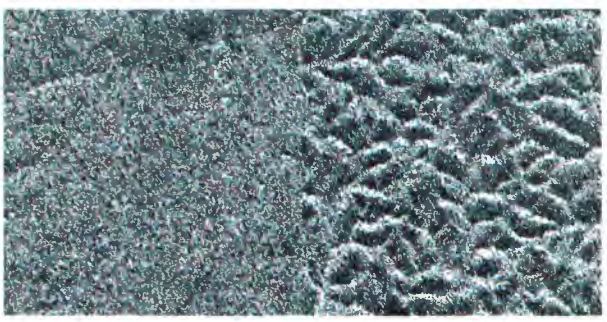

Figure 4.1 - Mosaic of JERS-1 images with dense flat forest (right) and undulated forest (left) - National Forest of the Tapajós, Pará, Brazil.

On the mosaic, samples of each class, as in figure 4.2, have been collected.

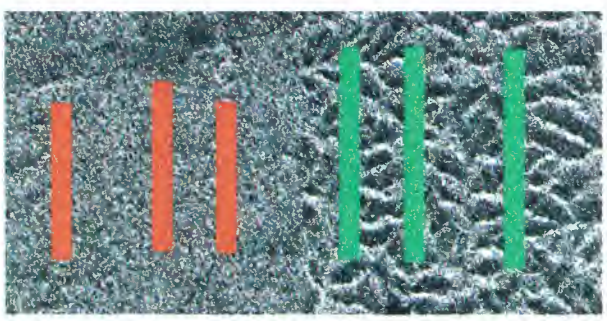

Figure 4.2 - Samples of two Classes of Forests.

Applying the maximum likelihood classification (mlc), in the six band set, the result of figure 4.3 was produced.

Figure 4.3 - Classification on the set of all the bands

generated in the stage-4.

A confusion matrix for this classification, produced using test samples, in shown in table 4.1:

Table 4.1 - Confusion Matrix of the Maximum Likelihood Classification of all six bands generated in stage-3.

| Classes /Classification | Non Classified | Dense Forest | Undulated Forest | Σ |
|---|---|---|---|---|
| Non Classified | 0 / 0% | 0 / 0% | 0 / 0% | 0 |
| Dense | 0 / 0% | 35655 / 98% | 633 / 2% | 36288 |
| Undulated | 0 / 0% | 789 / 2% | 34691 / 98% | 36480 |
| Σ | 0 | 36444 | 36424 | 72768 |
| | **Kappa:** 0.960917 | | $\sigma_k^2$ : 1.05332E-06 | |

For comparison, the Maximum Likelihood Classification using only the original channel is presented in figure 4.4.

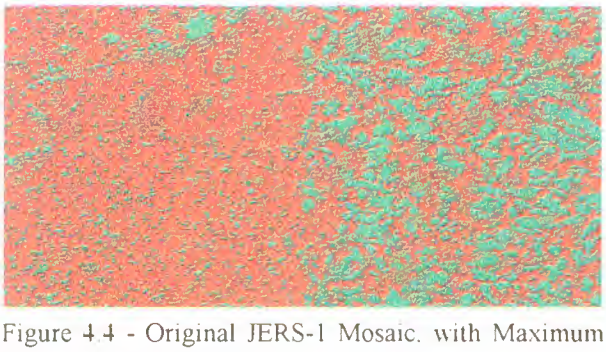

Figure 4.4 - Original JERS-1 Mosaic, with Maximum Likelihood Classification.

The same test samples used in table 4.1 were used to calculate the confusion matrix as shown in table 4.2.

Table 4.2 - Confusion Matrix for the Classification based on the original JERS-1 Mosaic.

| Classes /Classification | Non Classified | Flat Forest | Undulated Forest | Σ |
|---|---|---|---|---|
| Non Classified | 0 / 0% | 0 / 0% | 0 / 0% | 0 |
| Dense | 0 / 0% | 30943 / 85% | 5345 / 15% | 36288 |
| Undulated | 0 / 0% | 17723 / 49% | 18757 / 51% | 36480 |
| Σ | 0 | 48666 | 24102 | 72768 |
| | Kappa: 0.366549 | | $\sigma_k^2$ : 2.6728E-05 | |

## 5 Conclusion.

The proposed methodology for texture feature extraction showed good potential for JERS-1 texture discrimination, and the authors will continue the studies, examining the applicability for other types of textures and sensors.

## 6 Acknowledgements

The authors of this work are grateful to the following researchers of the INPE: Dra Corina da Costa Freitas, MsC Sidnei João Siqueira Sant'anna and MsC Camilo Daleles Renó.

## References

Brockwell, P.J.; Davis, R. A. *Times series:theory and methods.* Berlin, Springer-Verlag, 1987.

Dutra, L. *Classificação de Texturas usando Modelos ARMA e Distâncias da Função de Autocorrelação.* (Tese de Doutorado em Computação Aplicada). Instituto Nacional de Pesquisas Espaciais, São José dos Campos, Abril 1990, 162 p. (INPE-5067-TDL/406).

Kay,S.M. *Modern Spectral Estimation: Theory & Application.*New Jersey, Englewood Cliffs, 1988, 543p.

Marple, S. L. *Digital spectral analysis.* Englewood Cliffs, NJ, Prentice-Hall, 1987

Soares, S.M. Classificação textural de imagens de radar por modelagem estatística autorregressiva. Dissertação de Mestrado em Sensoriamento Remoto. Instituto Nacional de Pesquisas Espaciais, São José dos Campos, SP, 1998.

# A Supervised Classifier for Multispectral and Textured Images Based on an Automated Region Growing Algorithm*

**Jorge Lira and Gabriela Maletti**

Instituto de Geofísica-UNAM
Circuito Institutos, Cd. Universitaria
04510 México D.F., México
labpr@tonatiuh.igeofcu.unam.mx

**Abstract**

A couple of supervised classifiers to segment optical multispectral images and textured radar images have been developed. In both classifiers, an automated region-growing algorithm delineates the training sets. Optimum statistics for defined classes are derived from the training sets. This algorithm handles three parameters: an initial pixel seed, a window and a threshold for each class. A suitable pixel seed is manually implanted through visual inspection of the image classes. The optimum value for the window and the threshold are obtained from spectral or texture distances. These distances are calculated from mathematical models of spectral and textural separabilities. A pixel is incorporated into a region if a spectral or texture homogeneity criterion is satisfied in the pixel-centered window for a given threshold. In this scheme, a region grows as much as possible but maintains the overlap with other regions in a minimum. The homogeneity criterion is obtained from the models of spectral and texture distances. The set of pixels forming a region represents a statistically valid sample of a defined class signaled by the initial pixel seed. The grown regions constitute therefore optimum training sets for each class. The statistical behavior of these training sets is used to classify the pixels of the image in one member of a set of classes. Comparing the statistical behavior of a sliding window with that of each class does the classification. The size of this window is the same as the one employed in the region-growing algorithm. The centered pixel of the sliding window is labeled as belonging to a class if its spectral or texture distance is a minimum to the class. Such distance is evaluated using the statistical content of the class and the sliding window as input to the model of spectral or textural separability. A series of examples, employing synthetic and natural images, are presented to show the value of this classifier. The goodness of the segmentation is evaluated by means of the Kappa coefficient and a matrix of distances derived from the mentioned model.

## 1.- Introduction

A digital multispectral image, such as that gathered by satellite sensors, contains spectral, contextual and textural information related to the scene of interest. For optical images, the detail of information depends upon a series of factors, such as: number of spectral bands, size of the pixel, number of quantization levels, and signal to noise ratio. For radar images the factors are: pixel size, polarization, wavelength, geometric aspect, and signal to noise ratio. A given pixel in the image carries information of the related instantaneous field of view (IFOV). A pixel in the image is a numerical characterization of the average radiometric properties of the IFOV. Hence, a pixel is a statistical sample of the average response to the incoming radiation of the IFOV. In addition, a pixel is embedded in a certain spatial context. To derive the location and spatial organization of image objects a segmentation is required. A model of the scene is constructed by means of a segmentation of the image. By means of this model, some valuable aspects of scene behavior may be obtained.

Segmentation is a partition of the image in a number of regions, each region related to a spatial pattern of the scene. The regions may be labeled as pertaining to a certain class of objects, hence generating a classification. The final product is therefore a thematic map useful for scene understanding. The first classifiers labeled the pixels of the image in a class using only its spectral properties and ignoring the context. This approach named per-pixel classification, proved to be limited in nature and applicable only to well spectral differentiated cases. In the last years, efforts (Gong and Howarth, 1992; Arai, 1993; Kontos and Rokos, 1996) have been devoted to context classifiers. In this approach, a pixel is labeled to a class taking into account its spectral properties and the context of location. On the other hand, a texture is a spatial organization of pixel values; therefore, a texture classifier must be contextual by nature. A contextual classifier consistently produces higher classification accuracies than the per-pixel classifier.

A supervised classifier employs a-priori information of each determined class; this is usually done by means of training sets. These training sets are defined through

* Work supported by project IN102797 of DGAPA-UNAM

closed polygons outlined by some interactive procedure on the image. In this definition, there is not a clear criterion to assume that the training sets are valid statistical samples of the classes. Therefore, as a basic premise to a classifier, a procedure should be established to assure that the training sets are representative samples of the classes. A second premise is that the classification of a pixel should be performed by direct comparison between the statistical behavior of the classes and that of the pixel neighborhood.

In this work, a new contextual classifier is proposed that determine statistical samples of defined classes as a result of an automated region-growing algorithm. A pixel is then classified by comparing the shape of the density function associated to the pixel neighborhood and that of the classes. The comparison is done by means of a measure of similarity between density functions both: for spectral response and for texture content. As explained in the next sections, this scheme of classification is valid for both classifiers described in the present paper.

## 2 Contextual Classifier

### 2.1 Region growing scheme

The contextual classifier uses the training sets determined by an optimized region-growing algorithm (Lira and Frulla, 1998). The sets are statistical representations of defined classes, being these spectral or textural. This algorithm begins by seeding pixels in suitable places of the image where the existence of a class is known. This task is done manually by visual inspection of the image with the support of ancillary data such as ground truth. Once the seeds are determined, one per class, the growing of the class regions starts. The growing is performed by pixel aggregation satisfying a homogeneity criterion. The criterion is evaluated in a window with optimum size. A pixel is aggregated into the region provided the difference between the homogeneity value of the seed centered window and the pixel-centered window does not exceed a certain threshold. The growing of a region is terminated when this homogeneity criterion is no longer satisfied. The homogeneity criterion and the threshold are both derived from a measure of separability. The above may be formally established as follows

Let $g(\mathbf{r})$ be the image and $\mathbf{p}_{ij}^0 \in g$, and let $R_0 = \{\mathbf{p}_{ij}^0\}$ be the initial sub-region signaling a class. The pixel $\mathbf{p}_{ij}^0$ is known as the seed related to $R_0$. Let $R_0^{'}$ be the set of pixels that do not belong to $R_0$ but having at least a neighbor with $R_0$ under certain connectivity. Let $E(R_0)_v$ the value of the homogeneity criterion applied to the neighborhood $v$ of $R_0$. The set $R_1$ is the region jointly formed by $R_0$ and the pixels $\mathbf{p}_{kl}^1 \in R_0^1$ for which $E(\mathbf{p}_{kl}^1)_v$ differs from $E(\mathbf{p}_{ij}^0)_v$ in less than a threshold $\varepsilon$. In other words, $R_1$ is the following set

$$R_1 \equiv [\mathbf{p}_{kl}^1 : |E(\mathbf{p}_{kl}^1)_v - E(\mathbf{p}_{ij}^0)_v| \le \varepsilon] \qquad (1)$$

The real number $\varepsilon$ is known as the parameter of uniformity. Once $R_1$ is been determined the previous step is repeated, so in general the region $R_m$ is given by

$$R_m \equiv [\mathbf{p}_{kl}^m : |E(\mathbf{p}_{kl}^m)_v - E(\mathbf{p}_{ij}^0)_v| \le \varepsilon] \qquad (2)$$

The homogeneity criterion is always tested against the original neighbor $R_0$. The growing of a region continues until $R_{k+1} = R_k$. The above is easily generalized for a number of initial regions. Thus, the labeling of a tested pixel is carried out as

$$\mathbf{p}_{kl} \rightarrow \text{class } t\text{: } |E(\mathbf{p}_{kl})_v' - E(\mathbf{p}_{ij}^0)_v'| \le \varepsilon \qquad (3)$$

Where $E(\mathbf{p}_{kl})_v'$ is the homogeneity criterion applied to the tested pixel.

### 2.2 Estimation of optimum parameters for region growing

The optimum value for the window $v$ and the threshold $\varepsilon$ are obtained as follows. An odd sized window neighborhood is assumed for each seeded pixel. Begining from $v = 3$, the windows are systematically incremented in size. Only squared windows are considered. For multispectral images, the density function is estimated, for radar images the joint density function is derived by means of the co-occurrence matrix. Let $\mathcal{S}_v^a(i)$ be the density function in a window of $v$ x $v$ pixels for spectral class $a$. Let $\mathcal{T}_v^s(i,j)$ be the joint density function in a window of $v$ x $v$ pixels for texture class $s$. These functions are normalized

$$\sum_{i=1}^{256} \mathcal{S}_v^a(i) = 1 \text{ and } \sum_{j=1}^{256}\sum_{i=1}^{256} \mathcal{T}_v^s(i,j) = 1 \qquad (4)$$

The above is assuming 256 quantization levels in the image, and $\mathcal{S}_v^a(i)$ is a k – dimensional vector where k is the number of bands. The joint density function $\mathcal{T}_v^s(i,j)$ is obtained by means of the co-occurrence matrix evaluated in the window $v$ for directions 0°, 45°, 90° and 135° of the Freeman code. The optimum window size $v$ is estimated when

$$\sum_{i=1}^{256} |\mathcal{S}_v^a(i) - \mathcal{S}_{v+1}^a(i)| \le 0.03 \text{ or}$$

$$\sum_{j=1}^{256}\sum_{i=1}^{256} \Im_v^s(i,j) - \Im_{v+1}^s(i,j) \le 0.03 \quad (5)$$

In this sense, the window size is adjusted according to class heterogeneity. A smooth class requires a small window size; a heterogeneous class requires a greater window size. Equation (5) means the existence of an optimum window size for each class. The 3% indicated in equation (5) is derived from heuristic tests.

The third parameter handled in the region-growing algorithm is a threshold ε named the uniformity parameter. To estimate the value of this parameter $\varepsilon_S$ for a multispectral image, let $d_{ab} = \sum_i \Im_{v_a}^a(i) - \Im_{v_b}^b(i)$, $\forall\ a \neq b$, be the minimum distance between spectral class-*a* and any other spectral class-*b*. Then, a pixel *p* is incorporated into the region class *a* if

$$\Im_{v_a}^a - \Im_{v_a}^p < \%d_{ab} \quad (6a)$$

and if

$$0.75\sigma_a < \sigma_p < 1.25\sigma_a \quad (6b)$$

The heterogeneity $\in_a = \sigma_a/\mu_a$, of the initial optimum window for class *a*, and $\in_p = \sigma_p/\mu_p$, the heterogeneity of the pixel window might be used as well in (6b). The quantities μ and σ are the mean and the standard deviation respectively. The threshold $\varepsilon_S$ is determined by expression (6a) with the restriction provided by (6b).

The estimate of the threshold $\varepsilon_T$ for a textured radar image is as follows: a pixel *p* is incorporated into the region class s if

$$\Im_{v_s}^s - \Im_{v_s}^p < \%d_{st}$$

and if (7)

$$0.75\,\sigma_x^s < \sigma_x^p < 1.25\,\sigma_x^s \text{ and } 0.75\,\sigma_y^s < \sigma_y^p < 1.25\,\sigma_y^s$$

Where $d_{st} = \sum_i \Im_{v_s}^s(i,j) - \Im_{v_t}^t(i,j)$ is the minimum distance between texture class-*s* and any other texture class-*t*. The threshold $\varepsilon_T$ is determined by expression (7).

### 2.3 Rationale of spectral classifier

The basic steps of the spectral classifier are the following:

i. - The bands selected for classification are loaded into RAM memory. Decorrelated bands are usually employed in this step.

ii. - Pixels are seeded in selected places of each spectral class defined for segmentation.

iii. - The optimum window and uniformity spectral parameter values are derived for each defined class according to equation (5) and (6).

iv. - The optimized region-growing algorithm is applied to the selected pixels, employing optimum parameters according to the previous step.

v. - For each region grown, the normalized density function is obtained. Each region represents a spectral class and is a valid statistical sample of the spectral behavior of the class.

vi. - A set of pixel centered neighborhoods formed by the optimum window sizes of the classes is considered to classify the pixels of the image. For each pixel neighborhood, the density function is obtained.

vii. - A pixel $\mathbf{p}_{kl}$ of the multispectral image is classified according to the following

$$\mathbf{p}_{kl} \rightarrow \text{class } k\text{: } \sum_i \Im_{v_k}^k(i) - \Im_{v_k}^p(i) \text{ , minimum, } \forall\ v_k \in \mu \quad (8)$$

Where $\mathbf{p}_{kl}$ is a vector pixel with coordinates (k,l) and $\mu \equiv \{v_a, v_b, \ldots v_m\}$ is the set of optimum windows for m spectral classes.

### 2.4 Rationale of texture classifier

The rationale for the texture classifier is similar as the spectral classifier:

i. - The textured image is loaded into RAM memory. This image is usually a speckle filtered radar image.

ii. - Pixels are seeded in selected places of each texture class defined for segmentation.

iii. - The optimum window and uniformity texture parameter values are derived for each defined class according to equation (5) and (7).

iv. - The optimized region-growing algorithm is applied to the selected pixels, employing optimum parameters according to the previous step.

v. - For each region grown, a normalized co-occurrence matrix is obtained. This is the joint density function of the class. Each region is considered a statistically valid sample for the defined texture classes.

vi. - A set of pixel centered neighborhoods formed by the optimum window sizes of the classes is considered to classify the pixels of the image. For each pixel neighborhood the joint density function is obtained

vii. - A pixel $p_{kl}$ of the texture image is classified according to the following

$$p_{kl} \rightarrow \text{class } u\text{: } \sum_i \Im_{v_u}^u(i,j) - \Im_{v_u}^p(i,j) \text{ , minimum, } \forall\ v_u \in \eta \quad (9)$$

Where $p_{kl}$ is a pixel with coordinates (k,l) and $\eta \equiv \{v_q, v_r, \ldots v_w\}$ is the set of optimum windows for *w* texture classes.

### 3 Results and discussion

Three examples are presented in this work. These examples are worked out on the grounds of: a). - A set of 36 synthetic images with well known statistical parameters for each class. The images in this set are singled band and contain six classes each. The dimension of these images is 192 x 256 pixels. The density function of such classes is Rayleigh-like, with varying mean and standard deviation. b). - A multispectral SPOT image for which principal components were applied. The dimension of this image is 512 x 512 pixels, with a pixel size of 20 x 20 $m^2$, and covering a portion of central México. c). - A speckle filtered SEASAT radar image, gathered in the L band with four looks. The dimension of this image is 998 x 998 pixels, with a pixel size of 25 x 25 $m^2$, and covering a portion of northern México. The series of images shown below resumes these results.

From the set of synthetic images, a multiband image of decorrelated bands was generated

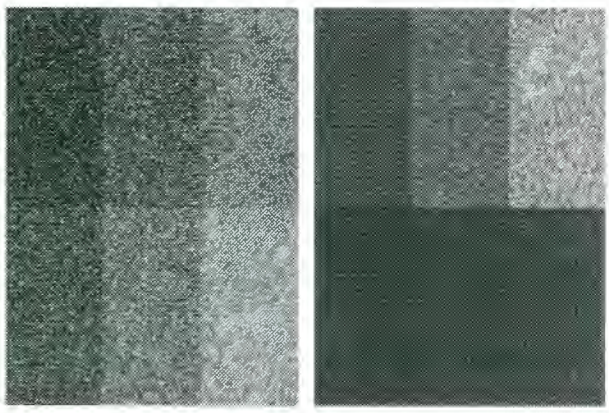

The region growing and the classification are shown in the following images

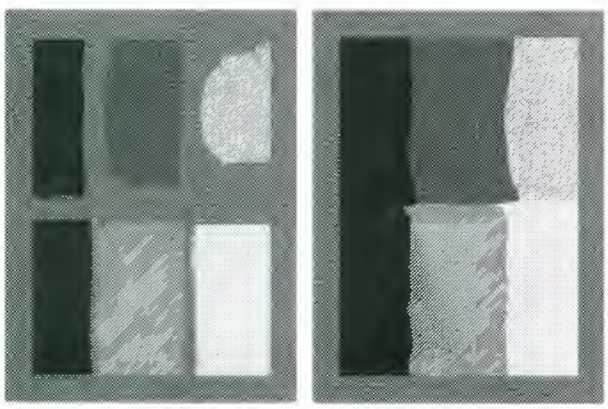

In the vertex of the four classes the density function is a class mixture generating a missclassification of some pixels. Both, for region growing and for classification, the window should be entirely contained in the image, hence the frame in the above two images.

The first two principal components of the SPOT image are the following:

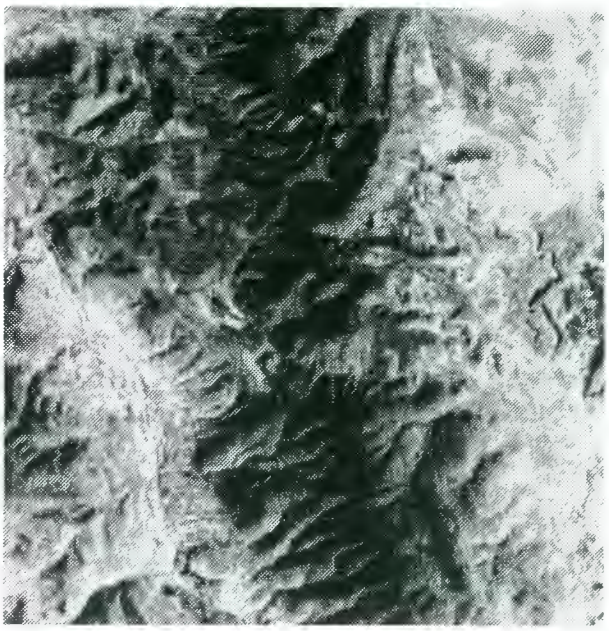

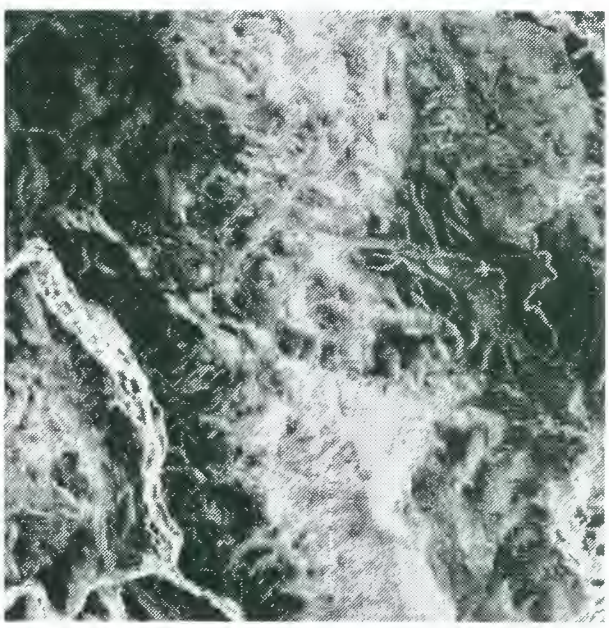

This two-band image depicts a mountainous range (center) covered by heavy vegetation, a stream of a river (lower left), and soil mixed with spare vegetation (right). On this image, six pixels were seeded signaling six spectral classes.

The following images show the result of the region growing and the spectral classification employing the difference of histogram's mean.

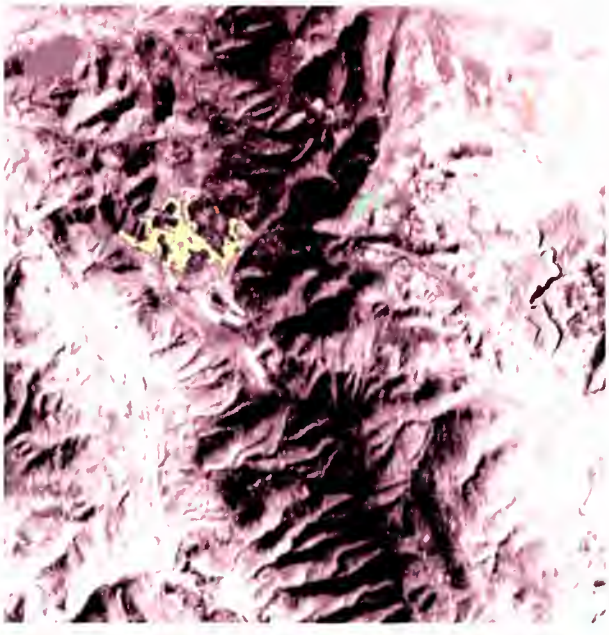

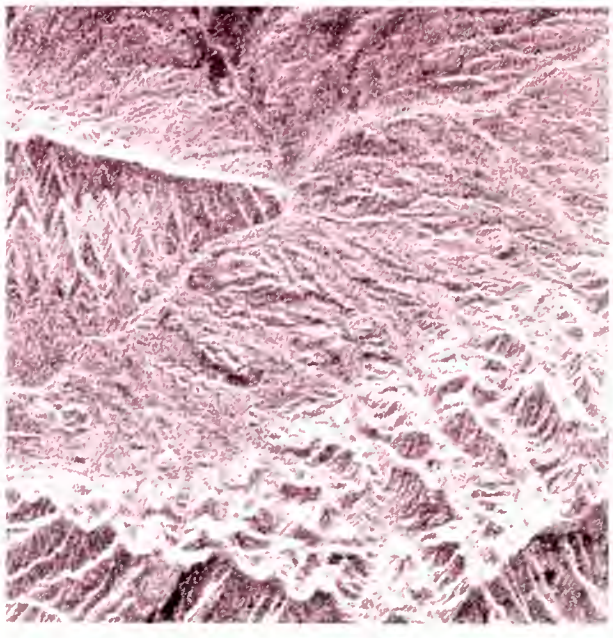

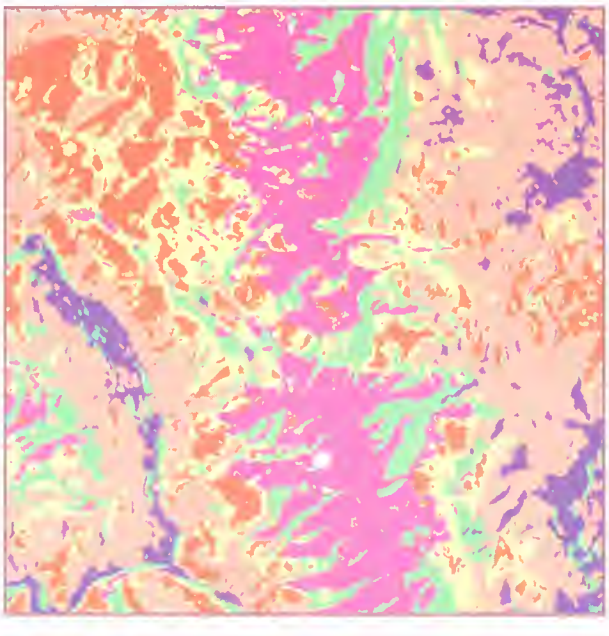

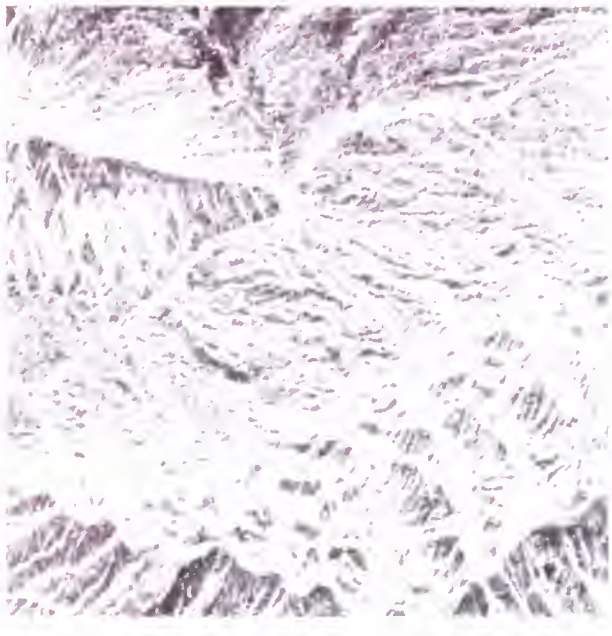

Those pixels whose associated density function have no intersection with the density function of any class are left unclassified.

The SEASAT radar image, speckled and filtered are the following:

The speckle was filtered by means of a geometric filter (Lira and Frulla, 1998). On the speckle free image, six pixels were seeded signaling six texture classes.

The following images show the result of the region growing and the texture classification

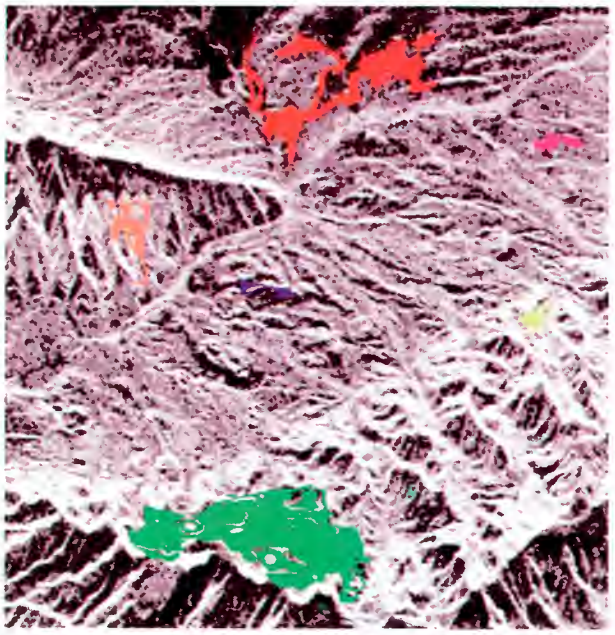

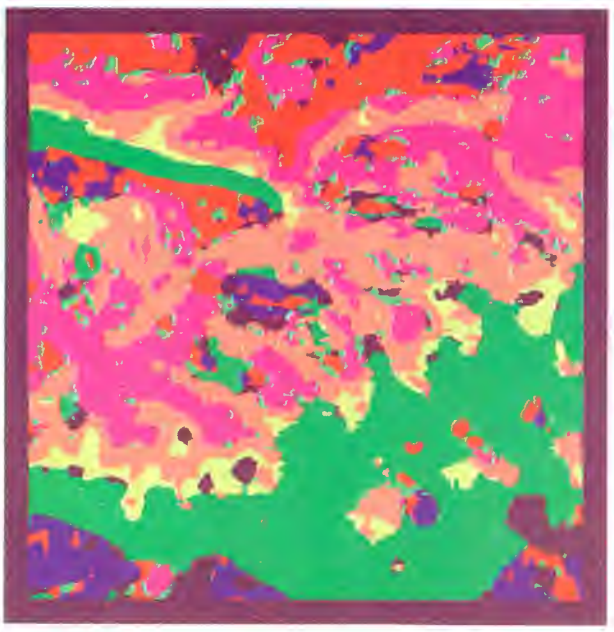

Four regions are shown as initial textures classes. The segmentation depicts four classes plus a non-classified pixels class (medium gray). The non-classified class includes the border of the image and parts of the image, this might be a fifht texture class.

## 4 Conclusions

A new contextual classifier based upon an automated region-growing algorithm has been developed and tested. This algorithm provides valid statistical samples of defined classes as input into a contextual classifier, both spectral and textural. The classification and growing of the regions are performed employing optimum windows for each class. No a-priori assumptions are made concerning the density functions of the classes. This is a basic premise since, based on experimentation, some classes show a gaussian behavior and some a Rayleigh like. The results are encouraging, although more research is needed, in particular the model for spectral and texture distance might be revised. However the rationale of classification is of general nature and might be adapted to new models of texture and spectral separabilities. In the present step of the research, no attempts have been made to identify the segmented classes with natural objects in the scene.

## 5 References

Arai, K. A Classification Method with a Spatial-Spectral Variability, *International Journal of Remote Sensing*, **14**, pp. 699-709, 1993.

Gong, P. And Howarth, P.J. Frequency-Based Contextual Classification and Gray-Level Vector Reduction for Land-Use Identification, *Photogrammetric Engineering & Remote Sensing*, **58**. pp. 423-437, 1992.

Kontoes, C.C. and Rokos, D. The Integration of Spatial Context Information in an Experimental Knowledge-Based System and the Supervised Relaxation Algorithm - Two Succesful Approaches to Improving SPOT-XS Classification, *International Journal of Remote Sensing*, **17**, pp. 3093-3106, 1996.

Lira, J and Frulla, L. An Automated Region Growing Algorithm for Segmentation of Texture Regions in SAR Images, *International Journal of Remote Sensing*, in press, 1998.

# A system for region image classification based on textural measures

CAMILO DALELES RENNÓ
CORINA DA COSTA FREITAS
SIDNEI JOÃO SIQUEIRA SANT'ANNA

INPE - Instituto Nacional de Pesquisas Espaciais
C. P. 515, 12201- 097 São José dos Campos, SP, Brasil
{camilo, corina, sidnei}@dpi.inpe.br

**Abstract.** This work presents a system for region classification using textural measures. The user can extract and analyze any kind of textural measures provide by this system and thus classify a group of region samples based on a set of selected measures. The system was developed using IDL and resources from ENVI, providing a user-friendly environment. An example of application of this system for a JERS-1 image is presented in this paper.

**Keywords:** classification, SAR image, texture

## 1 Introduction

The satellite images are powerful tools to improve the knowledge of world's natural resources. It is known that these resources are finite and are already being expended at a fast rate, which will increase with the world's rapidly expanding population. In Brazil, several studies have been done to try understanding the Amazonian Forest, with a special interest in the study of secondary succession and its role on the carbon cycle. For many years, Brazilian Amazon Deforestation Survey Project (PRODES) has mapped the deforestation and has estimated the extension and rates of deforestation. This mapping is based on optical images from sensor TM/LANDSAT. But the weather conditions in some regions limit the usefulness of these images. Non-optical sensors can be used to minimize this problem; particularly Synthetic Aperture Radar (SAR) images have been showed to be useful on helping the solution of weather conditions problem. In order to extract the information from these images, it is necessary to develop special tools for processing and analyzing them.

Usually the systems for analyzing images have used only tonal information in the classification process. Yanasse et al. (1993) and Yanasse et al. (1997) showed that tonal average was inadequate to discriminate old stage of regeneration from primary forest areas using C-band SAR data. However, the same authors obtained improvements in the discrimination between these classes when the coefficient of variation was used (Luckman et al., 1997; Yanasse et al., 1993). Texture is an important characteristic for the analysis of many types of images, in special, for SAR images. Unfortunately, there is not a formal approach or precise definition of textures. Nevertheless, various authors have tried to quantify it. Methods for textural analysis have been developed using spatial frequency patterns (Chen, 1990), first order statistics (Hsu, 1978, Irons and Petersen, 1981) and second order statistics (Haralick et al., 1973, Welch et al., 1990). Some textural measures do not make assumptions about the statistical distribution of the data and thus they could be taken from either radar or optical data. Yanasse et al. (1993) and Frery et al. (1997) studied some statistical distributions from radar data and concluded that some parameters of these distributions was related with textural information and could be used to discriminate land use classes.

This work presents a system developed at the National Institute for Space Research (INPE) for region classification using textural measures. The description of the system is presented on Section 2. The classification of a georeferenced JERS-1 image is presented as an example of the use of the system (Section 3).

## 2 The system

The system provides a user-friendly environment to extract and analyze textural measures from images, and classifies regions based on pre-selected measures. It was developed using IDL (Interactive Data Language) and functions from ENVI (Environment for Visualizing Images) system. The procedures were developed using a windows system where the user can easily find the functions of interest (**Figure 1**).

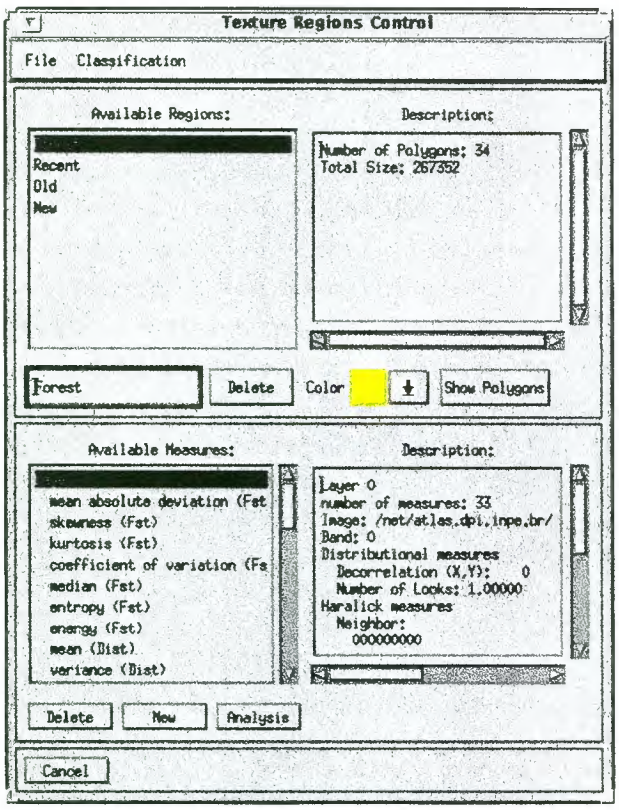


Figure 1: Main interface

Initially, the user must select samples from each class of interest. In fact, each sample is a polygon formed by one or more pixels from the image. A "region" is formed by joining samples from the same class. The regions can be taken by selecting image subsets drawn by the user (using ENVI's resources) or from segmented images. A segmented image can be defined as an image where each area or polygon is identified by one gray level, different from its neighbors.

The regions must have some samples in order to characterize the dispersion of textural measures. A "layer" is defined as a group of textural measures extracted from the same image and having the same neighborhood configuration pattern. In this form, the system can compare different textural measures from the same image or the same textural measure from different images.

### 2.1 Textural measures

A set of measures implemented in this system can be split on four groups: first order, distributional, Haralick's and autocorrelation measures.

The first order measures are calculated without considering spatial distribution of pixels. Seven of these measures are included in this system: mean absolute deviation, skewness, kurtosis, coefficient of variation, median, entropy and energy.

The distributional measures are parameters of statistical distributions, some of them specific for radar data. Eight distributional measures are calculated by this system: estimated mean, variance and standard deviation of Normal and Log-Normal distributions; and estimated $\alpha$ parameter of the K-Intensity and K-Amplitude distributions. For an overview about $\alpha$ parameter estimators, the interested reader can see Yanasse et al. (1993), Frery et al. (1997) and Yanasse et al. (1997) among others.

The Haralick's measures are based on the Gray Level Co-occurrence Matrix (GLCM). The GLCM describes probabilities of the co-occurrence of two specific gray-levels given specific pixel locations in terms of relative direction and distance. More details about these measures can be found on Haralick et al. (1973), Haralick (1979), Unser (1986) and Welch at al. (1990). Eighteen measures are included in this system: contrast, entropy, energy, homogeneity, correlation, dissimilarity, chi-square, cluster shade and cluster prominence; mean, variance, entropy and energy of the sum and difference vectors; and contrast of the difference vector.

In this system, the autocorrelation spatial measures can be defined from lags –4 to 4, in row and column directions. Also, the system permits to calculate ratios between two different autocorrelations.

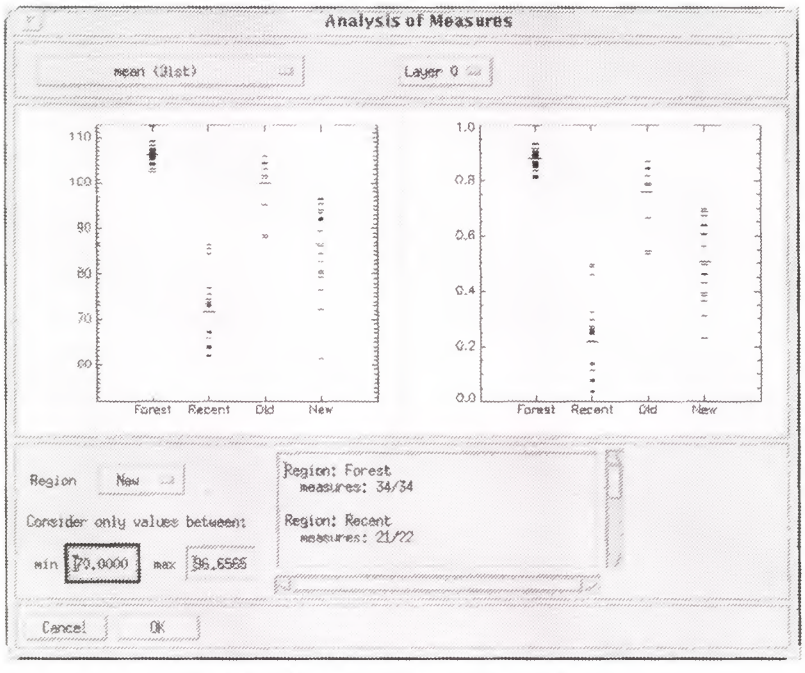


Figure 2: Interface for measure analysis.

## 2.2 Analysis of textural measures

The textural measures have a variable range of values and thus it is necessary to standard each one of them. Thereby the measures are linearly stretched, ranging from zero (minimum value) to one (maximum value), considering all classes of interest. It is important to pay attention to the presence of outlier values that must be eliminated before standardization. The user can analyze each measure and redefine its range in order to discard outlier values. The interface for making this analysis is shown in **Figure 2**, for the particular case of the data mean. The abscissas refer to the classes of interest, and the ordinates to the measure values (original on the left plot and standardized on the right plot).

## 2.3 Selection of textural measures

It is evident that a large number of measures can be extracted and become impracticable to use all of them in the image classification. The decision rule to choose one or more measures can be based on discriminant factor, which evaluates the separability between classes. The discriminant factor adopted in this system is calculated using the variation within and between two classes and given by:

$$DF_{AB} = \frac{n_A \cdot \sum_{i=1}^{n_A}\left(X_{Ai} - \overline{X}_A\right)^2 + n_B \cdot \sum_{i=1}^{n_B}\left(X_{Bi} - \overline{X}_B\right)^2}{n_A \cdot \sum_{i=1}^{n_A}\left(X_{Ai} - \overline{X}_B\right)^2 + n_B \cdot \sum_{i=1}^{n_B}\left(X_{Bi} - \overline{X}_A\right)^2}$$

where, $X_{\omega i}$ is the $i^{th}$ sample of class $\omega$, $\overline{X}_{\omega}$ is mean value of class $\omega$, $n_{\omega}$ is number of samples of class $\omega$. Thereby there will be one measure with maximum discriminant factor for each combination of classes. For example, if there are 4 classes, there will be until 6 selected measures. The window of the system that shows the pairs of classes and its selected discriminant factor is illustrated in **Figure 3**.

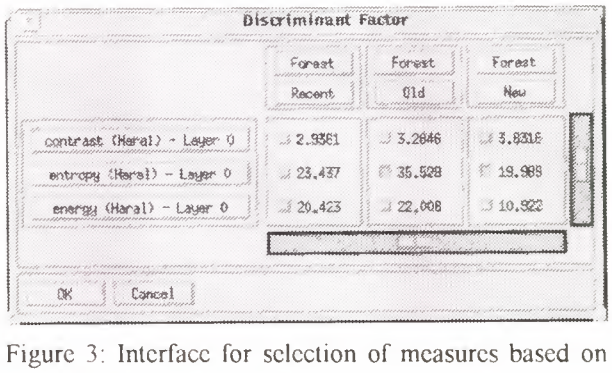


Figure 3: Interface for selection of measures based on discriminant factor.

After selecting the textural measures, the mean vector, the covariance matrix and some characteristics of each class and of standardization process are saved in

a file (called training file) which will be used on the classification process.

### 2.4 Classification

The classification initiates by selecting the training file. If one of the selected textural measures would not have been extracted, the system will do it before the classification. Each polygon of each region will be classified as belonging to the class of interest that minimizes the Mahalanobis distance.

After classifying all polygons, the system will build an image, by painting the pixels from each polygon with the color of the class designed to it. The visualization as well as the evaluation of the classified image can be done using ENVI's resources.

## 3 An example of application on JERS-1 image

The potentiality of system is demonstrated by using a georeferenced JERS-1 image from 06/26/1993, L band, HH polarization and amplitude data. The size of this image is 903 samples per 1980 lines and the pixel resolution is 30 m. **Figure 4a** illustrates a piece (400x400 pixels) of this image. This image surrounds the Tapajós National Forest (FLONA), Pará State, Brazil (54°01'48" to 55°49'33" WGr, 02°56'37" to 03°23'30" S). The FLONA region has large areas of tropical forest that have been cleared and converted into pasture and agricultural fields. Some of these areas were abandoned, becoming a secondary succession.

Four classes of interest were established in this work: primary forest (PF), areas without anthropogenic action; old secondary forest (OSF), areas abandoned for more than 7 years old; new secondary forest (NSF), areas abandoned for less than 7 years old; and recent activities (RA), others land uses, e.g., bare soil, pasture and agricultural fields.

Samples for each class of interest were chosen based on a land use map (**Figure 4b**), built from a multi-temporal LANDSAT/TM images from 1984 to 1993. The methodology used for building this map is describe in Sant'Anna et al. (1995). The number of collected samples and total number of pixels belonging to each class are shown in **Table 1**

Table 1: Information about training samples.

| Class of interest | Number of polygons | Total number of pixels |
|---|---|---|
| PF | 34 | 267,352 |
| OSF | 11 | 3,561 |
| NSF | 20 | 13,102 |
| RA | 22 | 11,566 |

All first order measures, all distributional measures (except $\alpha$ parameter of the K-intensity distribution), all Haralick's measures (using the 8 nearest neighbors to calculate the co-occurrence matrix), the autocorrelations with Lags (1,0) and (1,1), and the ratio of these two autocorrelations (Lag (1,1)/Lag (1,0)) were extracted for each sample.

**Table 2** shows the 3 best measures according to the discriminant factor for each pair of classes. It can be observed that the largest discrimination occurred between PF and OSF classes using Haralick's entropy. This result is very important because these classes are not separable when using only mean value (Yanasse et al., 1993; Yanasse et al., 1997). The PF and RA classes are also well discriminated, showing a large discriminant factor value. The smallest discriminant factor value was found for the pairs OSF/NSF and

Table 2: Discriminant factor for each pair of classes of interest.

| | PAIR OF CLASSES OF INTEREST* | | | | | |
|---|---|---|---|---|---|---|
| | PF/OSF | PF/NSF | PF/RA | OSF/NSF | OSF/RA | NSF/RA |
| Median | 7.09 | 14.66 | **33.19** | 2.29 | **7.20** | **3.13** |
| Haralick's entropy | **35.53** | **19.99** | 23.44 | 2.28 | 1.59 | 1.17 |
| Haralick's correlation | 1.12 | 4.40 | 4.14 | **2.69** | 2.31 | 1.04 |

*The marked values indicate the measure selected for pair of class.

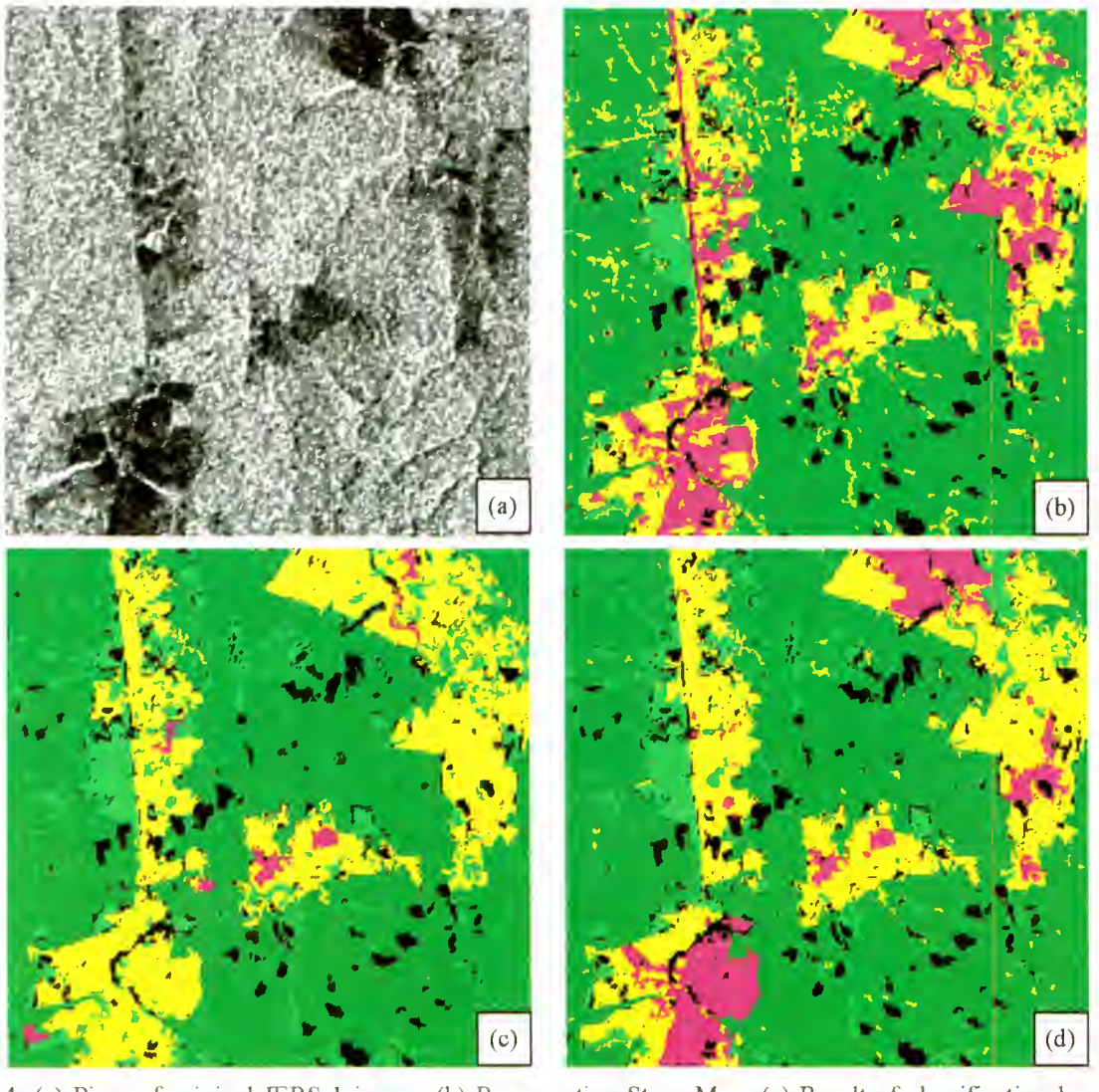


Figure 4: (a) Piece of original JERS-1 image; (b) Regeneration Stage Map; (c) Result of classification based on 3 textural measures (median, Haralick's entropy and Haralick's correlation); (d) Result of classification based on 2 textural measures (median and Haralick's entropy) performed in 2 parts. Dark green is primary forest (PF), light green is old secondary forest (OSF), yellow is new secondary forest (NSF) and magenta is recent activities (RA).

NSF/RA, indicating that these classes are poorly separable.

The result of the classification using the 3 best selected measures is shown in **Figure 4c**. It can be noted that many polygons of RA were misclassified as NSF and a large number of little polygons was classified as OSF when, in fact, should be classified as NSF.

To improve this result, the selection of measures and classification was done in 2 steps. In the first one, PF was joined to OSF and NSF was joined to RA, creating 2 groups. The median was chosen in the selection process as the best textural measure to discriminate among these groups, with a discriminant factor of 10.10. A classification was performed to separate these 2 groups. In second step, the polygons from each group were classified on one of the classes that forms the group using the measure selected for that pair (Haralick's entropy to PF/OSF and median to NSF/RA). The result is shown in **Figure 4d**. A visually improvement on the classification can be seen, when comparing the two classified images with the land use map.

## 4 Conclusion and further work

This work presented a system for region classification using textural measures. The system gives to the user the possibility of extracting and analyzing many types

and configurations of textural measures. The user may test the discriminatory power of a measure and study the variation of this discriminatory power when any characteristic is changed (polygon size, image type, etc).

The textural information carried on images are very important to the comprehension of its complexity and must not be ignored on the classification process. This importance can be indicated by the results obtained in this work.

The inclusion of new measures into the system is possible due to the simple computer language used on its implementation. Other methods for measure selection may also be implemented. Finally, the system can be adapted to permit the use of textural filters. In other words, this system can be easily upgraded.

**Acknowledgements**

The authors thank CNPq for the support through project PROTEM-CC GEOTEC (Process 680.061-94-0).

**References**

Chen, C.H. Texture unit, texture spectrum, and texture analysis. *IEEE Trans. Geosc. Rem. Sens.*, 28(4):509-512, July 1990.

Frery, A.C.; Müller, H.J.; Yanasse, C.C.F.; Sant'Anna, S.J.S. A model for extremely heterogeneous clutter. *IEEE Trans. Geosc. Rem. Sens.*, 35(3):1-12, May 1997.

Haralick, R.M. Statistical and structural approaches to texture. *Proc. IEEE*, 67(5):786-804, May 1979.

Haralick, R.M.; Shanmugan, K.; Dinstein, I. Texture features for image classification. *IEEE Trans. Systems, Man and Cybernetics*, SMC-3(6):610-621, Nov. 1973.

Hsu, S.Y. Texture-tone analysis for automated land-use mapping. *Photogram. Eng. Rem. Sens.*, 44(11):1393-1404, Nov. 1978.

Irons, J.R.; Petersen, G.W. Texture transforms of remote sensing data. *Rem. Sens. Environ.*, 11(5):359-370, Nov. 1981.

Luckman, A.J.; Frery, A.C.; Yanasse, C.C.F.; Groom, G.B. Texture in airborne SAR imagery of tropical forest and its relationship to forest regeneration stage. *Intern. Journal Rem. Sens.*, 18(6):1333-1349, 1997.

Sant'Anna, S.J.S.; Yanasse, C.C.F.; Hernandez Filho, P.; Kuplich, T.M.; Dutra, L.V.; Frery, A.C.; Santos, P.P. Secondary forest age mapping in Amazônia using multi-temporal Landsat/TM imagery. In: IGARSS, Italy, July 10-14 1995, *Quantitative remote sensing for science and applications.*, v.1, pages 323-325, Florence, Italy. IEEE

Unser, M. Sum and difference histograms for texture classification. *IEEE Trans. Pattern Anal. Mach. Intell.*, PAMI-8(1):118-125. Jan. 1986.

Welch, R.M.; Kuo, K-S; Sengupta, S.K. Cloud and surface textural features in polar regions. *IEEE Trans. Geosc. Rem. Sensing*, 28(4):520-528. July 1990.

Yanasse, C.C.F.; Frery, A.C.; Sant'Anna, S.J.S.; Hernandez Filho, P.; Dutra, L.V. Statistical analysis of SAREX data over Tapajós – Brazil. In: M. Wooding and E. Attema, editors, *SAREX-92: South American Radar Experiment*, pages 25-40, Paris, 1993. ESA.

Yanasse, C.C.F.; Sant'Anna, S.J.S.; Frery, A.C.; Rennó, C.D.; Soares, J.V.; Luckman, A.J. Exploratory study of the relationship between tropical forest regeneration stages and SIR-C L and C data. *Rem. Sens. Environ.*, 59(2):180-190, 1997.

# METODOLOGIAS DE PRE-PROCESAMIENTO Y PROCESAMIENTO UTILIZADAS EN EL TRATAMIENTO CUANTITATIVO DE DATOS SAR PARA EL ESTUDIO DE AMBIENTES EN EL BAJO DELTA DEL RIO PARANA, ARGENTINA

L. A. Frulla[1], J. A. Milovich[1], H. Karszenbaum[1], P. Kandus[2]

[1]Consejo Nacional de Investigaciones Científicas y Técnicas (CONICET)
Julián Alvarez 1218
(1414) Buenos Aires, Argentina
Phone (54-1) 772-1471 Fax: (54-1) 776-0410
e-mail: laura@caerce.edu.ar

[2]Laboratorio de Ecología Regional, Departamento de Biología - Facultad de Ciencias Exactas y Naturales Universidad de Buenos Aires (UBA)

## ABSTRACT

From SAR point of view, the Delta of Paraná's river (Argentina), a major fresh water wetland, represents a complex area where the radar backscattered signal has the influence of the structural properties of the landscape elements as well as of the dielectric properties due to the different flooding conditions of the land cover categories. To understand the different mechanisms that take place in the interaction between the sensor and the scene charcteristics and to assist in the extraction of quatitative information, a metholodology approach for pre-processing and processing SAR data (obtained in different operational modes) is presented. Radarsat/SAR images were used to illustrate the methods as well as auxiliary data (Lansat/TM data, thematic maps, field work) to support the analysis and to validate the procedures. Even though these procedures were designed specifically for the purpose of the present paper, the same framework can be applied to other environments with similar charcteristics.

## 1. INTRODUCCION

En la última década ha habido un esfuerzo sostenido con el fin de colocar en órbita sistemas satelitales de observación terrestre con radares de apertura sintética (SAR/ERS, SAR/JERS, Radarsat). Estos esfuerzos realizados en tan pequeño período de tiempo pueden considerarse como un indicador de la importancia de estas observaciones. Por otra parte, las diferencias existentes entre cada sensor, unido al hecho de que existe una disponibilidad creciente de este tipo de información, sugiere el desarrollo de técnicas que permitan el aprovechamiento de las características distintivas de cada sistema y la utilización de este tipo de datos individualmente o combinados a fin de estudiar el medio ambiente terrestre.

La zona de estudio, el Bajo Delta del Río Paraná (Argentina) constituye un importante humedal situado muy próximo a la Ciudad de Buenos Aires del cual no sólo es de gran interés su estudio y monitoreo como ecosistema natural sino también como área productiva, ya que contiene grandes plantaciones de sauce y álamo [1]. A los fines del radar, se trata de una zona compleja donde la señal retrodispersada contiene tanto elementos estructurales del paisaje como eléctricos debido a la presencia permanente de agua.

Si bien las imágenes SAR han demostrado su utilidad en aplicaciones hidrológicas, cuando se trata de estudiar vegetación con diferentes niveles de inundabilidad, la literatura presenta resultados que, en algunos casos, son contradictorios debido a las diferencias en la estructura de la vegetación y en el grado de inundabilidad de la misma y al sistema utilizado (banda, polarización, ángulo de incidencia) [2]. Por consiguiente, para facilitar la interpretación de las imágenes SAR del Bajo Delta del Río Paraná se planteó un enfoque metodológico a fin de comprender, en la señal de radar retrodispersada, los efectos debido a las características del sistema y de su tratamiento (distorsiones radiométricas y geométricas), y los de la información propia del objeto de estudio.

Este enfoque incluye el análisis de las correcciones radiométricas y geométricas aplicadas a las imágenes y la extracción de información cuantitativa de la zona de estudio. Si bien algunos de estos procedimientos, como por ejemplo, las correcciones por efectos de pérdidas de potencia en rango y por modelo de antena son transparantes al usuario ya que están incluídas en el procesamiento original de las imágenes, otros efectos tales como posibles cambios en la ganancia de la antena, saturación de la señal y ruido *speckle* deben ser corregidos por el usuario para lograr mejores resultados. Además, a fin de llevar a cabo análisis multitemporales y/o multi-modo, los datos deben calibrarse para poder relacionar los valores digitales de cada pixel con los correspondientes valores de coeficiente de *backscattering sigma nought*.

**Image Processing Techniques** *Proceedings of the 2nd Latino-American Seminar on Radar Remote Sensing held at Santos, Sao Paulo, Brazil, 11-12 September 1998* (ESA SP-434, October 1998).

Una vez que las imágenes se corrigen por efecto de las distorsiones radiométricas y geométricas, es posible aplicar distintos procedimientos de procesamiento (análisis e interpretación). Sin embargo, es sabido, que estas dos etapas no son completamente independientes, es decir, determinados procedimientos de pre-procesamiento modifican los datos y esta modificación en algunos casos puede facilitar la posterior utilización de los mismos y en otros casos agregar artefactos o producir una disminución de la resolución y de la calidad radiométrica de las imágenes. Tomado estos elementos en consideración, este trabajo tiene por objetivos: 1) describir y analizar las variables de entrada y salida de rutinas básicas de preprocesamiento (calibración, reducción de ruido *speckle* y geolocalización) y los efectos principales que resultan de aplicarlas a imágenes SAR del sistema Radarsat correspondientes a la zona de estudio, 2) analizar mediante estadísticas de primer orden, los mecanismos de interacción sensor/escena para estructuras específicas de vegetación del Delta del Río Paraná y para distintos modos de observación del sistema Radarsat. La metodología propuesta se ilustra con imágenes Radarsat/SAR adquiridas para distintos ángulos de incidencia y en distintas fechas. Además se utilizaron imágenes Landsat 5/TM de fechas próximas a la de las imágenes SAR, mapas temáticos pre-existentes y muestras de campo, como apoyo para el análisis de los resultados y validación de los procedimientos. Las secciones siguientes presentan en primer término los procedimientos de pre-procesamiento utilizados y su análisis, a continuación los procedimientos empleados para analizar los mecanismos de interacción entre la señal y los elementos estructurales de la escena, para finalizar con la discusión de resultados y conclusiones.

## 2. MEDICIONES QUE REALIZA EL RADAR

La relación fundamental entre las características del radar, el objeto y la señal recibida está dada por la ecuación del radar [3]. En este sentido, la potencia ( $P$ ) que recibe la antena (y que es la magnitud directamente medida por el sensor) está relacionada con el coeficiente de *backscattering sigma nought* ( $\sigma^0$ ). Por otra parte la teoría electromagnética de la luz explica que la intensidad de una onda electromagnética ( $I$ ) es proporcional al flujo promedio de energía por unidad de tiempo (potencia), o sea al valor cuadrático medio del campo eléctrico. Entonces la potencia es proporcional al cuadrado de la amplitud de la onda ( $A^2$ ). Además, las antenas de radar detectan la intensidad del brillo que los objetos reflejan en una longitud de onda particular. Por lo tanto la potencia recibida es proporcional al brillo del objeto ( $\beta^0$ ), quien además está relacionado con $\sigma^0$ y $\gamma^0$. Las relaciones radiométricas que vinculan estas magnitudes son:

$$P \propto I \propto A^2 \propto \beta^0 = \frac{\sigma^0}{\sin(\alpha)} = \frac{\gamma^0}{\tan(\alpha)} \qquad (1)$$

donde $\alpha$ es el ángulo de incidencia local.

Es muy importante considerar la diferencia que existe entre $\beta^0$, $\gamma^0$ y $\sigma^0$. La primer magnitud representa la observación del radar en su forma más pura. Es decir $\beta^0$ está relacionada con la reflectividad promedio de centros dispersores distribuidos por unidad de área del plano de rango oblicuo y para su cálculo no se requiere información acerca del ángulo de incidencia local. La segunda magnitud, $\gamma^0$, es la reflectividad media de centros dispersores distribuidos por unidad de área del frente de onda incidente y tiene la ventaja que mantiene relativamente constante la reflectividad en un amplio rango de ángulos de incidencia en el caso de superficies rugosas, pero requiere del conocimiento del ángulo de incidencia local para su cálculo. La tercera magnitud, $\sigma^0$, describe la reflectividad promedio de centros dispersores distribuidos por unidad de área en el plano local de la superficie observada. Se trata de la propiedad intrínseca a ser observada y también para su cálculo requiere del conocimiento del ángulo de incidencia local. Lo descripto se representa en la Figura 1, donde el incremento de área utilizado para normalizar cada magnitud se representa como un segmento contenido en el plano. La otra dirección que define dicho incremento corresponde a la dirección de acimut, que obviamente es la misma para las tres magnitudes. Desde el punto de vista geométrico, en general los contajes de amplitud de productos estándar multi-vista están proyectados en la dirección de rango horizontal. En este caso, las magnitudes obtenidas a partir de estos contajes, dado que sólo involucran operaciones radiométricas, quedarán también proyectadas en rango horizontal.

La ecuación (1) indica que el coeficiente de *backscattering* $\sigma^0$ es proporcional a la potencia $P$, y se lo conoce comunmente como la representación de $\sigma^0$ en potencia. La raíz cuadrada de $\sigma^0$ es proporcional a la amplitud $A$, y esta magnitud se conoce como la

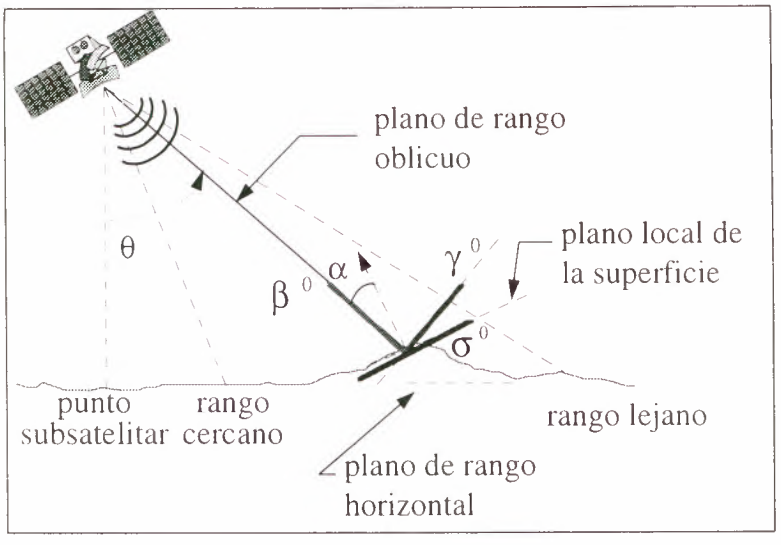


*Figura 1: Magnitudes radiométricas medidas por el radar y sus derivadas. Los segmentos indican la dirección en el plano de la figura del incremento de área utilizado para normalizar la magnitud correspondiente. (θ es el ángulo de observación del sensor).*

representación de $\sigma^0$ en amplitud ($\sigma^0_A$). Además $\sigma^0$ se puede expresar en forma logarítmica, i.e. en decibeles ($\sigma^0|_{dB}$). Esta última representación es útil puesto que la reflectividad del radar tiene un rango dinámico que puede alcanzar varios órdenes de magnitud en potencias de diez. Sin embargo, es importante tener en cuenta que cada etapa de preprocesamiento requiere de una representación específica de $\sigma^0$. La relación entre las magnitude mencionadas es:

$$\sigma^0|_{dB} = \begin{cases} 10 \log_{10}(\sigma^0) \\ 20 \log_{10}(\sigma^0_A) \end{cases} \qquad (2)$$

## 3. CONJUNTO DE DATOS UTILIZADOS

Este trabajo se ha desarrollado dentro del marco de los proyectos GLOBESAR 2 y se ha contado con imágenes SAR/Radarsat de los modos S1, S6 correspondientes al verano del año 1997 y una imagen S1 de invierno del mismo año. En forma adicional a las imágenes de radar se dispuso de imágenes Landsat 5-Thematic Mapper facilitadas por la Comisión Nacional de Actividades Espaciales (CONAE) y de fotos aéreas pancromáticas. Además, se contó con datos de altura del nivel del agua del Puerto de Buenos Aires provenientes de los registros del Servicio de Hidrografía Naval. Estos fueron utilizados como indicadores del estado de las condiciones de marea durante la fecha de la toma de imágenes. También se obtuvieron datos sobre vientos (intensidad y dirección) y cantidad de precipitación caída para las mismas fechas. Se utilizó esta información para evaluar la influencia de las condiciones climáticas sobre la señal de radar retrodispersada para cada uno de los ambientes considerados y de la imagen en conjunto.

## 4. CARACTERISTICAS DE LA ZONA DE ESTUDIO

Los patrones de paisaje del Bajo Delta del Río Paraná están definidos por la coexistencia de elementos naturales con otros derivados de la intervención del hombre. Todos estos ambientes son inundables en mayor o menor medida. Entre los ambientes naturales pueden mencionarse bosques correspondientes a altos relativos o medias lomas y, en situaciones de bajo, pajonales y juncales donde el sustrato se encuentra saturado o inundado por prolongados períodos de tiempo o en forma permanente. Aproximadamente el 30% de la superficie representada originalmente por estos ambientes está ocupada en la actualidad por plantaciones de sauce y álamo las cuales constituyen la principal actividad productiva del delta. Teniendo en cuenta estas características, se definió un esquema conceptual de clasificación propio, basado en rasgos estructurales y funcionales. Este esquema, si bien particular es comparable con esquemas elaborados para otros humedales y fue utilizado satisfactoriamente para la realización de un mapa temático de uso y cobertura a partir de imágenes multitemporales Landsat/TM [1], utilizado en este trabajo como mapa de referencia. Para facilitar la interpretación y análisis de las imágenes de radar de esta zona, el esquema mencionado se simplificó y se redujo a tres situaciones estructurales: bosque, pajonal y juncal, con sus correspondientes categorías [4].

## 5. PREPROCESAMIENTO, PROCESAMIENTO Y MANEJO DE DATOS SAR

La Figura 2 resume la línea metodológica planteada para el pre-procesamiento y procesamiento de datos SAR teniendo en cuenta las características de las imágenes Radarsat, la zona de estudio y los objetivos de este trabajo. Se indica, además, la magnitud requerida como entrada a cada procedimiento.

### 5.1. Calibración

Este tipo de procedimientos dependen del procesador del sistema satelital considerado (en este caso para datos Radarsat) y además, a nivel del usuario, se utilizan especialmente para ajustar posibles cambios temporales en la ganancia de la antena y en las condiciones de saturación de la señal y a fin de convertir los valores de amplitud de cada pixel (expresados en contajes digitales) a valores de coeficiente de *backscattering* o de brillo [5]. Se trata de un procedimiento necesario para estudios multitemporales y/o multiángulo (como en este caso). La ecuación utilizada para el sistema Radarsat es:

$$\sigma^0 = [(DN^2 + A_0)/A] \sin\alpha \qquad (3)$$

donde DN son los valores de la imagen de amplitud expresados en contajes digitales, $A_0$ es una constante y A es una tabla de reescalado que depende de la distancia de rango. Los archivos de encabezamiento de las imágenes contienen estos valores o datos adecuados de los cuales se pueden obtener. Si bien es posible calcular $\sigma^0$ para cada pixel, su significado físico cobra sentido cuando este valor se promedia sobre un grupo de pixeles correspondientes a un blanco distribuido en la imagen. Se utilizó el *software* PCI para llevar a cabo este procedimiento.

### 5.2. Reducción de *speckle*

Es posible reducir el efecto del ruido *speckle* aplicando técnicas de filtrado a las imágenes SAR de varios *looks*. Si bien existen distintos tipos de filtros [6]-[7], el mayor problema de los métodos se encuentra en la estimación de los valores de los parámetros de entrada de los distintos algoritmos: el tamaño de la ventana móvil, el desvío estándar del *speckle* y el factor de *damping* . La selección de estos parámetros depende en gran medida de las características del área de estudio. Regiones con grandes variaciones en los tonos de gris, muestran detalles finos en la imagen, por lo tanto es preferible que la ventana sea pequeña. Por el contrario, para zonas homogéneas, donde casi no existen variaciones en los tonos de gris, una ventana de mayor tamaño es preferible a fin de mantener la homogeneidad de la imagen [8]-[9]. Por otro lado, la textura de regiones homogéneas proviene del ruido *speckle* y por lo tanto, contiene información relacionada con el desvío estándar del mismo.

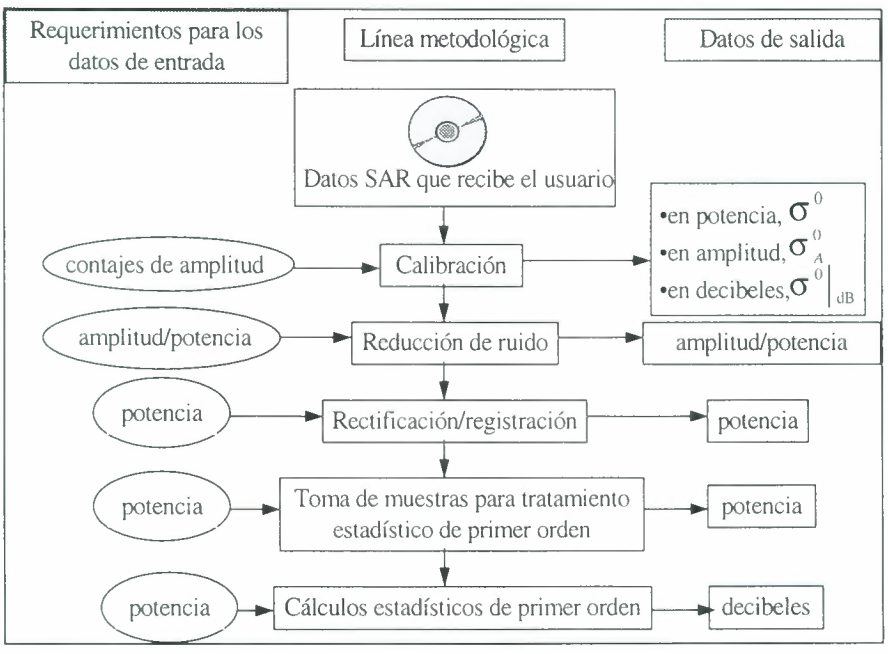


***Figura 2:*** *Línea metodológica desarrollada para el preprocesamiento y procesamiento de datos SAR.*

La identificación, en la imagen original, de este tipo de regiones es el primer paso para estimar el desvío estándar del *speckle*. Finalmente, aquellos filtros que incluyen el factor de damping, permitan garantizar características adaptivas. Sin embargo, el uso de valores de dumping grandes, preserva los bordes mejor, pero

reduce el efecto de suavizado. Por el contrario, la utilización de valores pequeños de damping aumenta el efecto de suavizado, pero no mantiene los bordes de forma correcta [10]. Como se indica en la Figura 2, el tipo de representación de $\sigma^0$ para la entrada/salida del filtro puede ser en amplitud o en potencia dependiendo del tipo de filtro y del diseño del *software*.

Se evaluó el comportamiento, para la zona de estudio, de cuatro filtros específicos para reducción de *speckle*: Enhanced Frost, Gamma Map, Kuan y Frost. Se utilizaron criterios cualitativos tales como la comparación visual de las imágenes filtradas con respecto a la original y el análisis de transectas para la evaluación de la degradación de las pendientes. Por otro lado se utilizaron criterios cuantitativos basados en la estadística de las imágenes filtradas y original, tales como la conservación del valor medio, la reducción de la desviación estándar y el valor medio de la diferencia absoluta entre la imagen original y las filtradas. La Figura 3 muestra la diferencia entre el valor medio de la imagen filtrada y el valor medio de la imagen original para cada uno de los cuatro filtros, la Figura 4 muestra el desvío estándar correspondiente a cada filtro y la Figura 5 el valor medio de la diferencia absoluta entre la imagen original y la resultante de cada filtro.

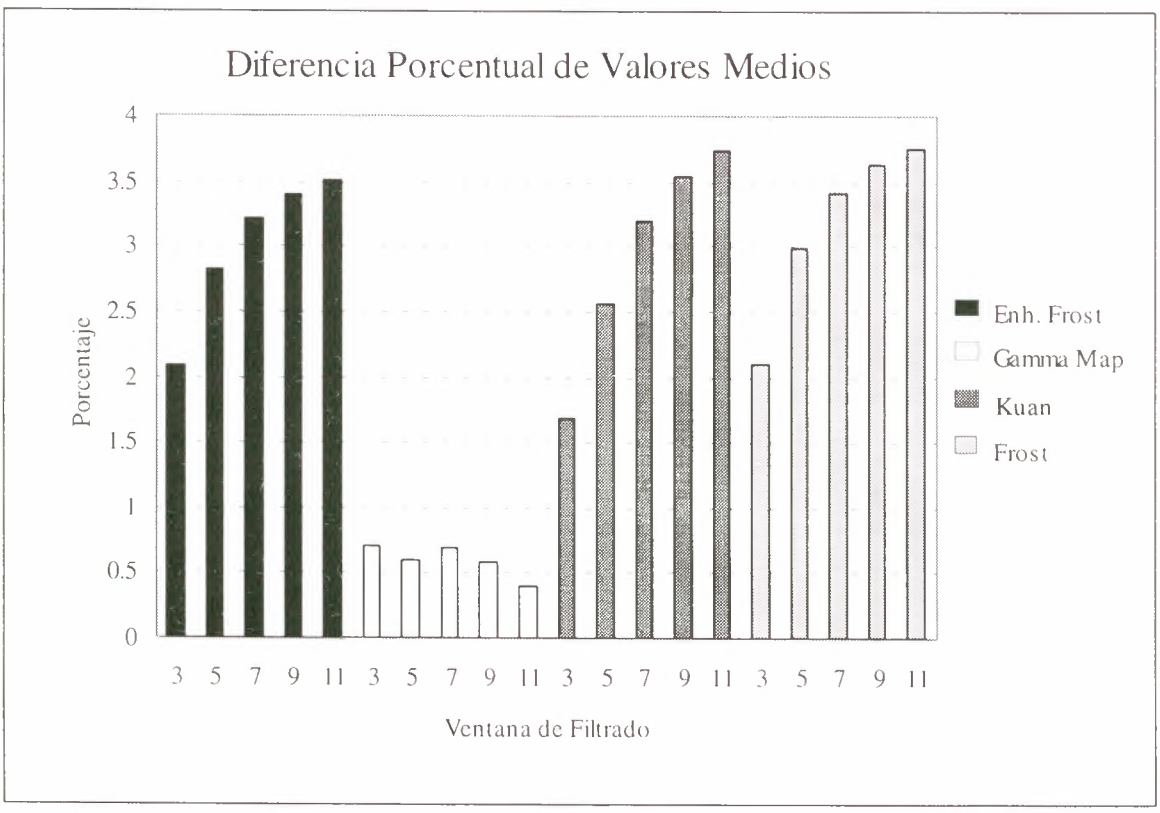


*Figura 3: Diferencia porcentual del valor medio de la imagen filtrada relativo al valor medio de la imagen original para cada uno de los filtros analizados y para tamaños de ventanas variando de 3x3 a 11x11.*

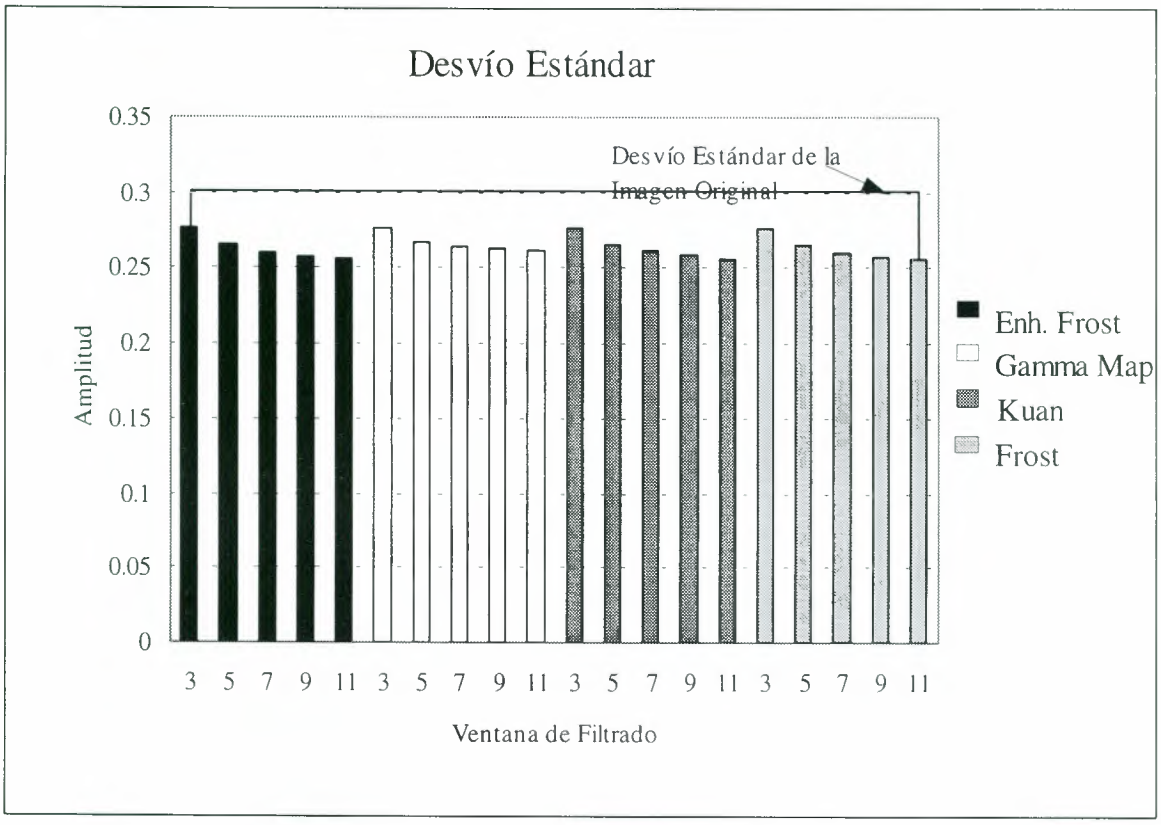


*Figura 4: Desvío estándar de las imágenes filtradas para cada uno de los filtros analizados y para tamaños de ventanas variando de 3x3 a 11x11. La recta constante en negro indica el desvío de la imagen original.*

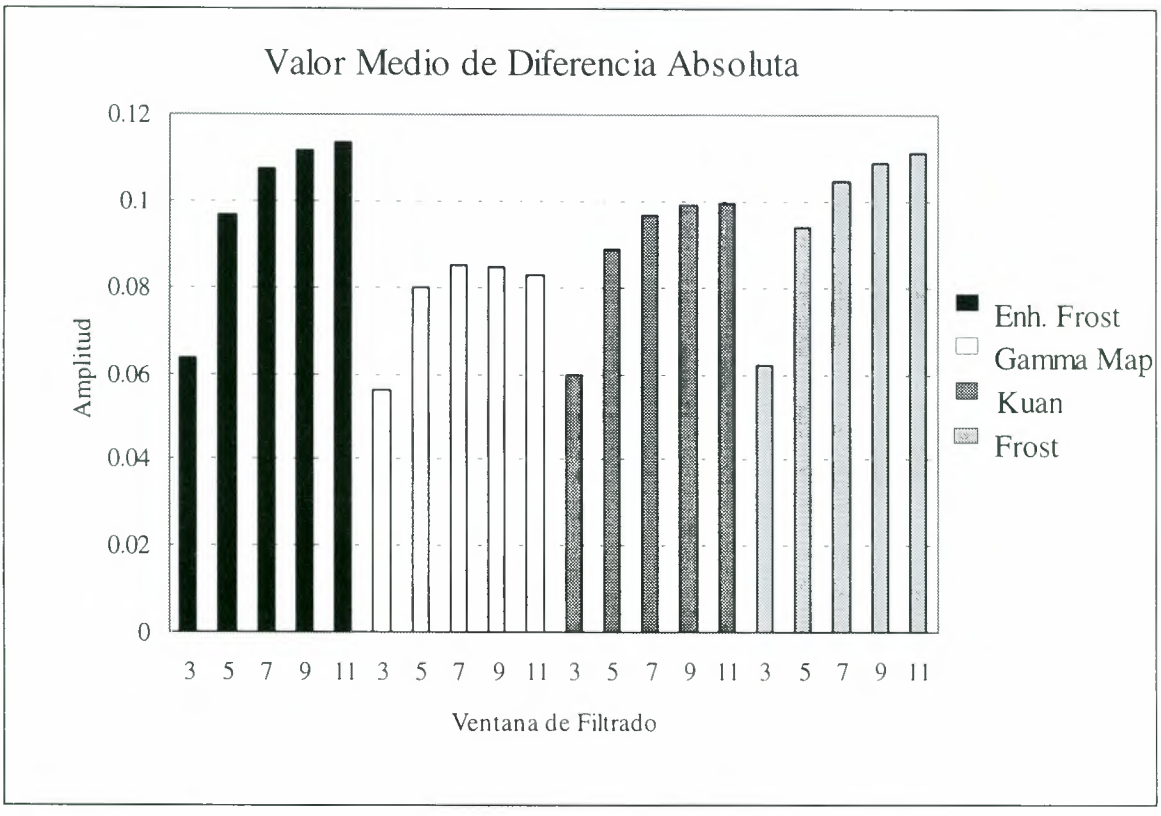


*Figura 5: Valor medio de la diferencia absoluta* entre *la imagen original y las filtradas para cada uno de los filtros analizados y para tamaños de ventanas variando de 3x3 a 11x11.*

### 5.3. Correcciones geométricas

Las correcciones geométricas, ya sea utilizando un modelo digital de terreno a fin de obtener una orto-imagen o una corrección polinomial asumiendo una superficie plana, involucran la utilización de técnicas de reemuestreo que a su vez incluyen la aplicación de interpolaciones radiométricas entre píxeles vecinos. La ecuación de radar generalizada para blancos extendidos calcula la potencia recibida mediante la suma pesada (en el límite, una integral) incluyendo valores $\sigma^0$ en incrementos de área relevantes. Si se amplía este concepto, la magnitud más adecuada para la interpolación radiométrica en el procedimiento de reemuestreo es $\sigma^0$ en potencia. Resulta obvio que si el método de interpolación utilizado es el del vecino más próximo, el resultado será el mismo cualquiera sea el tipo de representación utilizada para $\sigma^0$. En relación con los métodos de reemuestreo, es conveniente considerar lo siguiente: 1) el método del vecino más próximo mantiene la estadística global pero cambia la textura local, 2) la interpolación bilineal degrada la resolución, y 3) la convolución cúbica o un *kernel sinc* tienden a mantener la fidelidad en los valores locales y texturas. Por lo tanto, se recomienda este último método. Previamente a la extracción cuantitativa de información de las imágenes, es necesario corregirlas geométricamente a una dada proyección geográfica. De esa manera es posible la superposición de las distintas imágenes entre sí y la ubicación en las mismas de muestras tomadas en el terreno. La zona de estudio no posee diferencias importantes de elevación por lo que no es necesario la utilización de un modelo de terreno para realizar una ortorectificación. Por lo tanto, se empleó una corrección mediante remuestreo por convolución cúbica de la imagen calibrada en potencia mediante una transformación polinómica obtenida a partir de la toma de puntos de control. Se utilizó como referencia una imagen TM georeferenciada a una proyección Gauss-Kruger con un tamaño de pixel de 28.5 metros. Las imágenes se rectificaron con un tamaño de pixel de 14.5 metros para los modos *standard* y de 7.125 metros para el modo *fine*. Los errores *r.m.s.* obtenidos estuvieron comprendidos entre 20 y 40 metros.

Para las imágenes en modo estándar (S1 y S6), el análisis de las amplitudes y gráficos de dispersión de los vectores de errores residuales para los puntos de control mostró una distribución prioritaria en el sentido del rango cuando se suponía polinomios de grado 1. Esto indica una deformación residual en la dirección del rango mayor que en la dirección de azimut. Este efecto desaparece cuando se selecciona un polinomio de grado 2. El análisis de los valores de posicionamiento geográfico presentes en el *header* de las imágenes muestra iguales resultados, siendo más importante el efecto para el modo S1, lo cual concuerda con lo esperado.

### 5.4. Extracción de información cuantitativa de las imágenes de radar

Como se ha señalado en el párrafo anterior, resulta difícil (sin datos adicionales y/o modelos) separar la contribución de las características eléctricas de las geométricas en las imágenes de radar. A fin de extraer información cuantitativa acerca de los mecanismos de interacción del sensor con los elmentos seleccionados (pajonal, bosque, juncal), se llevó a cabo un análisis del contenido textural de los mismos. La textura contiene importante información acerca del arreglo estructural de la superficie y de la relación de éste arreglo con el entorno. En este trabajo se han utilizado estadísticas de primer orden para analizar la textura que esta zona, dadas sus características, ofrece al radar. Para llevar a cabo el objetivo propuesto, se extrajeron de las imágenes preprocesandas, entre 50 y 100 muestras de aproximadamente 50 pixeles cada una para cada uno de los ambientes seleccionados. Este paso se llevó a cabo sobre imágenes de potencia, según se indica en la Figura 2. Como datos de referencia se utilizaron fotos aéreas y datos de campo existentes. A fin de asegurar que las muestras obtenidas correspondían a cada uno de los ambientes seleccionados, se trabajó sobre una imagen TM geolocalizada de marzo de 1997 (fecha de verano próxima a los modos S1 y S6) y se obtuvieron los perfiles espectrales de todas las muestras. Este análisis confirmó la pertinencia de las muestras.

A fin de utilizar las estadísticas de primer orden para determinar la textura característica, se calcularon medias $\mu$, desvíos estándar $\sigma$ y coeficientes de variación $\sigma/\mu$ (indicador del grado de heterogeneidad). Es decir, se tomaron $m$ regiones como muestras de un ambiente dado, cada una de estas $m$ regiones posee valores estadísticos. Es decir, para la región $i$ se conocen: $\mu_i$: valor medio, $\sigma_i$: desvío estándar y $\mathbf{n}_i$: número de píxeles correspondientes a la región y también los valores máximo y mínimo alcanzados en cada muestra. Los valores estadísticos analizados se calcularon considerando dos situaciones diferentes:

- Caso 1: Se calcularon los valores medios y los desvíos estándar de cada ambiente correspondientes al conjunto de "todos los pixeles" de "todas las muestras". Es decir, el valor promedio resultante de cada ambiente contiene la influencia del ruido *speckle*.

- Caso 2: Se calcularon los valores medios y los desvíos estándar de cada ambiente a partir del conjunto de muestras. En este caso cada muestra es un individuo, definido por un valor medio. Los valores resultantes contendrán muy poca información debida al ruido

*speckle* (ya que éste se encuentra reducido por la operación "promedio").

Para poder analizar los resultados y a fin de poder compararlos con los obtenidos por otros autores, los valores promedio y desvío para los dos casos se convirtieron de potencia a $\sigma^0$ (decibeles). Finalmente, para cada muestra de cada ambiente, se calcularon también los coeficientes de variación. Estos valores se promediaron y se obtuvo un único valor medio para cada ambiente y el desvío estándar correspondiente. Las Figuras 6 y 7 muestran este análisis.

## 6. RESULTADOS Y CONCLUSIONES

De la Figura 3 se observa que el filtro que mejor conserva el valor medio es el Gamma Map, presentando diferencias menores al 0.75 % con respecto al valor medio de la imagen original para cualquier tamaño de ventana. Los demás filtros presentan diferencias que oscilan aproximadamente entre el 1.75 % y el 3.75%, aumentando con el tamaño de la ventana. El desvío estándar de las imágenes filtradas (Figura 4) disminuye a medida que aumenta el tamaño de la ventana de filtrado, indicando una disminución en el contenido de información. Si bien para una dada dimensión de ventana, todos los filtros producen valores equivalentes de desvío estándar, la imagen filtrada mediante el algoritmo Gamma Map presenta valores levemente superiores, indicando una pequeña pero mayor conservación del contenido de información original. La Figura 5 presenta una cuantificación de las imágenes de diferencia absoluta. El filtro Gamma Map produce las menores diferencias, y por lo tanto la menor pérdida de información. Por otra parte, el análisis de transectas mostró para el filtro Gamma Map una muy buena conservación de las pendientes.

Los resultados obtenidos llevaron a la elección del filtro Gamma Map para el tratamiento posterior de las imágenes. Debe tenerse en cuenta que esto significa que este filtro es el que mejor se comporta en el área de estudio analizada y no puede extrapolarse esta conclusión a otras regiones.

La zona de estudio carece de topografía, por lo que no es necesario utilizar un modelo de terreno para su corrección. Teniendo en cuenta este hecho y el resultado de los análisis, las imágenes se corrigieron utilizando polinomios de orden 2 y remuestreo por convolución cúbica.

Las Figura 6 muestra las estadísticas correspondientes a los distintos ambientes según lo descripto en la metodología como caso 2. En términos generales, se observa que los tres tipos de fisonomías propuestas tienen valores medios muy semejantes. Existe poca diferencia entre los valores de $\sigma^0$ correspondientes a los modos S1 y S6 siendo mayores los del modo S1. A su vez, el rango de valores de $\sigma^0$ de todos los ambientes para ambos modos es muy similar.

En particular, los ambientes de bosque y pajonal no son diferenciables entre sí en ninguno de los modos utilizados y los valores de $\sigma^0$ oscilan entre -5 y -10 decibeles. A diferencia de éstos, los ambientes de juncal presentan valores más elevados de $\sigma^0$ para el modo S1 probablemente debido a que, al tratarse de juncos en agua quieta, estos actúan como *corner reflectors* (efecto esquina) naturales. En el caso de las lagunas, la porción central de la misma presenta valores bajos de $\sigma^0$ debido a que la presencia de una película de agua quieta actúa como un reflector especular. El borde de las lagunas, al presentar mayor densidad de vegetación, tiene una respuesta similar a la de los otros ambientes.

Con respecto al modo S1 los valores de marzo son mayores (mayor cantidad de biomasa verde en pie) que los de agosto. En cuanto al rango de dispersión, este varía poco entre ambas fechas. Sin embargo, cabe señalar que en el caso de las plantaciones de sauce, estas presentan mayor variabilidad en agosto, probablemente debido a que al estar los árboles sin hojas, existe una mayor influencia del sotobosque en la señal retrodispersada.

Al considerar los mismos ambientes pero de acuerdo a las estadísticas calculadas según el caso 1, se observó que el efecto del ruido *speckle* aparece bien marcado ya que aumenta de manera significativa la dispersión de los datos. Sin embargo los valores medios de $\sigma^0$ son similares a los del caso 2.

Finalmente, se representaron los valores del coeficiente de variación para todos los ambientes y los modos considerados. La Figura 7 muestra los resultados obtenidos. Esta figura también presenta el coeficiente de variación correspondiente a zonas homogéneas para una imagen de potencia de 4 *looks*. Los valores de coeficiente de variación de todos los ambientes, tanto para el modo S1 como S6, se encuentran muy próximos al valor teórico calculado para zonas homogéneas, que es de 0,5. En aquellos casos donde se registraron valores del coeficiente de variación mayores (entre 0,6 y 0,8) éstos son indicadores de una heterogeneidad propia de cada ambiente. Sin embargo los mismos presentan una gran dispersión lo que imposibilita atribuirles una textura particular. A fin de verificar estos resultados, se procedió a calcular el coeficiente de variación para toda la imagen del modo S1 y para distintos tamaños de ventanas (5, 7 y 11) y se observó una gran homogeneidad en las imágenes resultantes. Si bien el

coeficiente de variación constituye un indicador de texturas muy utilizado, en este caso, los resultados no son satisfactorios, es decir, este método de textura aporta poco a la separabilidad de los ambientes.

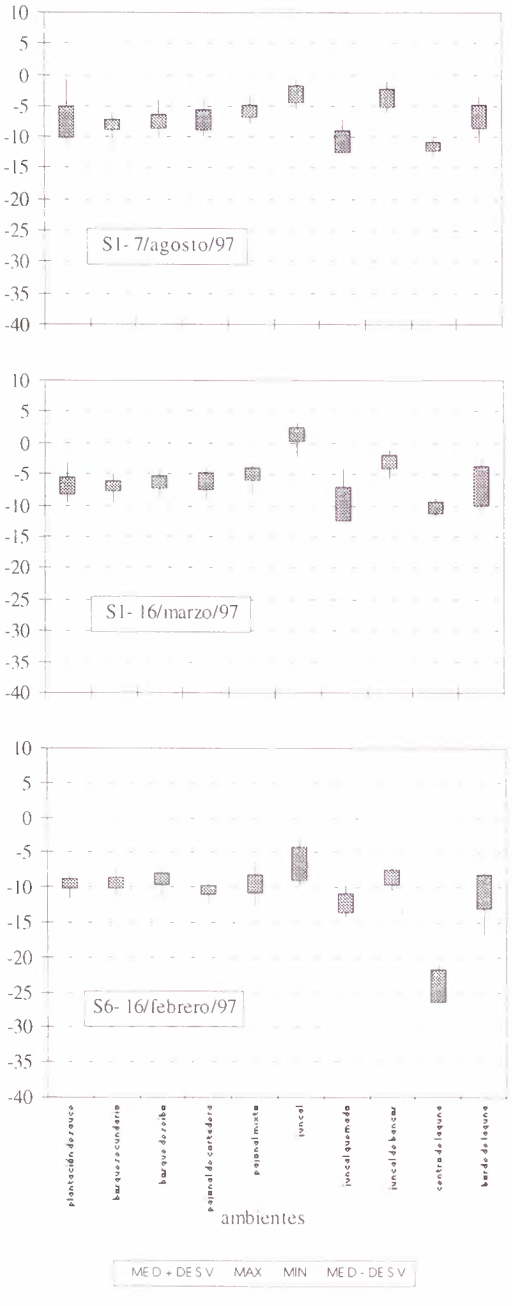


*Figura 6: Valores estadísticos en decibeles [dB] (máximo, mínimo, media y desvío estándar, correspondientes a cada ambiente) obtenidos mediante el cálculo según el Caso 2.*

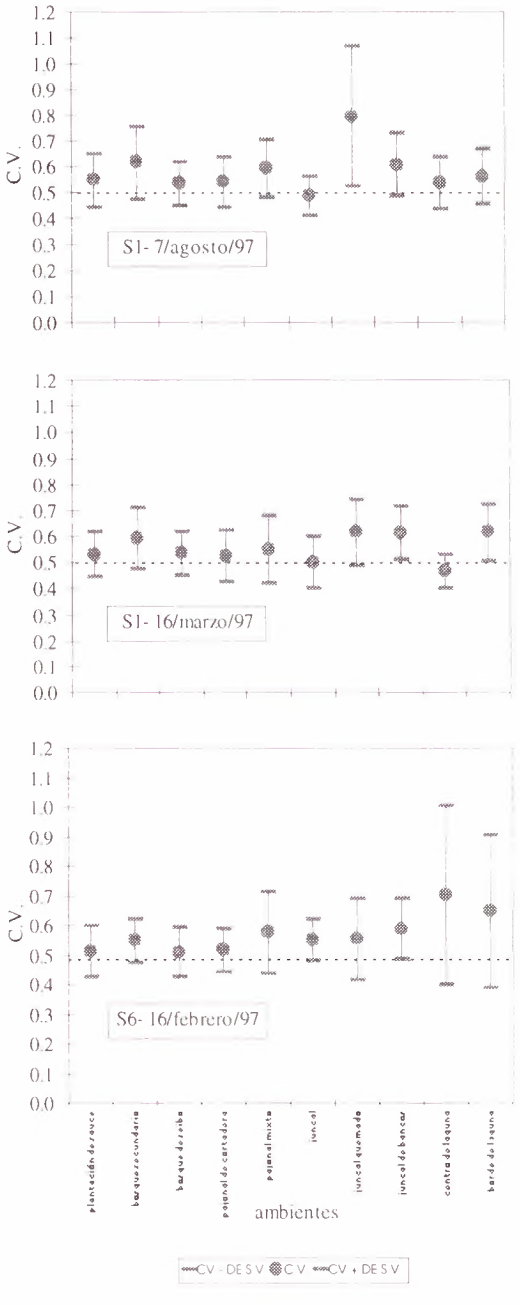


*Figura 7: Valores de la media y el desvío estándar del coeficiente de variación (CV) para cada ambiente. La línea de puntos indica el valor teórico correspondiente a zonas homogéneas.*

## AGRADECIMIENTOS

Se agradece al Dr. D. A. Gagliardini por su contínuo apoyo; al CONICET, a la Universidad e Buenos Aires y a la Agencia Nacional de Promoción Científica y Tecnológica por los subsidios que permitieron realizar esta investigación; a CONAE por los datos TM y a CCRS/RADARSAT por las imágenes de radar y el apoyo recibido.

## REFERENCIAS

[1] P. Kandus, H. Karszenbaum, L.A. Frulla, "Land cover classification system for the Lower Delta of the Paraná River (Argentina): Its relationship with Landsat Thematic Mapper spectral classes", Aceptado para su publicación en *Journal of Coastal Research* (USA).

[2] M. Pereira de Farias Costa, E.M.L.M. Novo, F.J. Ahern, "Integraçao de dados de radar adquiridos com diferentes ângulos de incidência para estudos de recervatório na Amazônia", *ESA Publications* SP-407, 125-131, 1997.

[3] T. Ulaby, R.K. Moore, A.K. Fund, "Microwave remote sensing. Active and passive", Vol. 1 and 2 (New York: Addison-Wesley Publishing Company), 1982.

[4] H. Karszenbaum, P. Kandus, L.A. Frulla, J.A. Milovich, "Contribution of Optical and SAR Imagery in the Identification and Distribution of Land Cover Features in the Lower Delta of Parana's River, Argentina", *Proceedings* del IEEE International Geoscience and Remote Sensing Symposium, IGARSS'98, Seattle, USA, 6-10 Julio 1998.

[5] H. Laur, P. Bally, P. Meadows, J. Sanchez, B. Schaettler, E. Lopinto, "Derivation of the Backscattered coefficient $\sigma^0$ in ESA ERS SAR PRI products", *ESA publication*, Document N°ES-TN-RS-PM-HL09, Issue 2, Rev. 2, 1996, pp. 41.

[6] V.S. Frost, J.A. Stiles, K.S. Shanmugan, J.C. Holtzman, "A model for radar images and its application to adaptive digital filtering of multiplicative noise". *IEEE Transaction on Pattern Analysis and Machine Intelligence*, PAMI-4, 157-165, 1982.

[7] D.T. Kuan, A.A. Sawchuck, T.C. Strand, P. Chavel, "Adaptive restoration of images with speckle", *IEEE Transactions on Acoustics, Speech, and Signal Processing*, ASSP-35, 373-383, 1987.

[8] Ch. Li, "Two adaptive filters for speckle reduction in SAR images by using the variance ratio", *International Journal of Remote Sensing*, Vol. 9, 641-653, 1988.

[9] A. Cortese, L.A. Frulla, J. Jacobo-Berlles, M. Mejail, A. Frery, "On the optimization of speckle filtering techniques for ERS-1 SAR images over Argentina", *Proceedings of the International Society for Photogrammetry and Remote Sensing*. Symposium on Resource and Environment Monitoring, Rio de Janeiro, Brazil, 26-30 Septiembre 1994, Vol. 30, Part 7a, 95-99.

[10] G. Schreier, (Editor). "SAR Geocoding: Data and systems", (Germany: Wichmann), 1993, pp. 437.

# THE USE OF SAR/TM SYNERGY FOR ESTIMATING SOIL MOISTURE CONTENT OVER A SEMI-ARID RANGELAND

Edson E. Sano[1], Jiaguo Qi[2], Alfredo R. Huete[3], M. Susan Moran[2]

[1] EMBRAPA – Empresa Brasileira de Pesquisa Agropecuária
CPAC – Centro de Pesquisa Agropecuária dos Cerrados
BR-020 Km 18 Cx. Postal 08223
73301-970 Planaltina, DF Brazil
E-mail: sano@cpac.embrapa.br

[2] USDA – U.S. Department of Agriculture
U.S. Water Conservation Laboratory
Phoenix, AZ 85040 USA

[3] University of Arizona
Department of Soil, Water, and Environmental Science
Tucson, AZ 85721 USA

**Abstract.** The C-band ERS-1 SAR data were combined with the Landsat TM data to improve the soil moisture estimates in a semiarid region. The SAR data were compared with the soil moisture measurements at three conditions: a) without any correction for soil roughness and vegetation effects; b) corrected for soil roughness effects; and c) corrected for both soil roughness and vegetation effects. The soil roughness effects were taken into account by using a dry season SAR image. The vegetation influence was considered by using an empirical relationship between SAR and leaf area index data, the latter being derived from TM images. Results indicated that the contribution of soil roughness and vegetation in the radar backscatter were significant and they must be taken into account to obtain accurate soil moisture estimations.

**Keywords**: Radar Remote Sensing; Soil Moisture; SAR/TM synergy.

## 1 Introduction

Soil moisture content needs to be measured consistently on a spatially distributed basis because it plays a critical role in hydrologic processes and energy fluxes at local, regional, and global scales by controlling the distribution of rainfall into runoff, evapotranspiration and infiltration (Benallegue et al., 1995; Dubois et al., 1995). Although ground-based techniques to measure soil moisture such as the gravimmetric method, neutron probe, and Time Domain Reflectrometry present accurate measurements, they are labor-intensive and represent point-based information of a terrain. As a result, this variable is often neglected in hydroclimatical and agricultural models.

Attempts have been made to derive spatially-based soil moisture content information from synthetic aperture radar (SAR) data. Many studies (Bernard et al., 1982; Benallegue et al., 1994; Cognard et al., 1995, among others) have obtained a simple linear correlation between soil moisture content and SAR data in long wavelengths (e.g., C-band at 5 cm or L-band at 21 cm). However, these and other promising results were obtained either from bare soil fields or from agricultural fields with flat surfaces and wide ranges of surface soil moisture contents. When sites of variable vegetation cover and soil roughness are included in the regression, we often find a considerable dispersion in the regression. The primary objective of this study was to develop a practical approach to account for both soil roughness and vegetation effects in the C-band SAR data to improve the estimation of rocky soil moisture content over a semiarid rangeland.

## 2 Experiment

The study area is located at the Walnut Gulch Experimental Watershed (31.72° N, 110.00° W), a representative site of shrub- and grass-dominated rangelands found in the southwestern part of the United States (**Figure 1**). The surface soils (0-5 cm) are predominantly sandy loams and gravelly loamy sands, with a rock content around 30% (Gelderman, 1970; Kustas and Goodrich, 1994). The vegetation is a mixed shrub/grass rangeland; that is, shrub-dominated in the western part of the watershed, and grass-dominated in the estearn part.

Seven European Remote Sensing (ERS-1) SAR images were acquired in 1992 as part of the Walnut Gulch Watershed remote sensing (WG'92) experiment conducted by the U.S. Department of Agriculture (Moran et al., 1996) and another single image was obtained in 1994 during the wet season (Day of Year –

DOY 206, **Table 1**). These images, obtained at a 30 m nominal spatial resolution and 12 m pixel spacing, were georreferenced to the Universal Transverse Mercator coordinate system (Zone 12, 1927 North American Datum, Clarke 1866), and calibrated, that is, corrected for topographic effects by accounting for the real backscatter area of each pixel using a digital elevation model (Beaudoin et al., 1994). Radar backscatter coefficients ($\sigma^{o}$; units = dB) were extracted from these preprocessed images using the equation proposed by Laur (1992):

$$\sigma^{\circ} = 10\log\left[\frac{\overline{DN}^{2} + STD^{2}}{K}\right]$$

where $\overline{DN}$ = average digital number of the site (average of at least 50 pixels per site);

$STD$ = standard deviation of DN; and

$K$ = sensor calibration constant.

Regarding the Landsat TM data, eight images obtained during the WG'92 experiment were analyzed (**Table 1**). The TM digital numbers were transformed to surface reflectance values in three steps (Moran et al.,1992, 1996; Washburne, 1994): a) acquisition of the incident solar illumination data from sunrise to solar noon in the same day of the Landsat overpasses, using a solar radiometer, to account for the atmospheric effects in the TM digital numbers; b) generation of at-satellite radiance values for a given series of surface reflectance values by using the Herman-Browning radiative transfer code; and c) generation of TM reflectance images from values derived from the radiative transfer code and from Landsat TM sensor calibrations. All TM images were also georeferenced to the UTM coordinate system.

Leaf area index ($LAI$) values were calculated from all Landsat TM scenes by using the following relationship proposed by Baret (1995):

$$LAI = -\frac{\log[(A - MSAVI)/B]}{K}$$

where $MSAVI$ is defined as (Qi et al., 1994):

$$MSAVI = (2\rho_{NIR} + 1 - [(2\ \rho_{NIR} + 1) * 2 - 8\ (\rho_{NIR} - \rho_{RED})] * 0.5) / 2$$

where $\rho_{NIR}$ and $\rho_{RED}$ are the surface reflectances in the near infrared and red spectral regions, respectively. For arid and semiarid regions, Qi et al. (1994) found the following values for $K$, $A$, and $B$: 0.67, 0.82, and 0.78, respectively.

Gravimetric samples for soil moisture content were collected at the Meteorological-Energy flux (MF) stations 1, 3, 5, and 6 in 1992 (**Table 1**). Six replicates of each sample were averaged to one reading. Volumetric soil moisture contents were derived using previously measured bulk densities (1.44 ~1.83 g/cm$^3$) (Troufleau et al., 1997). Soil moisture measurements were also made on the same day of the ERS-1 SAR overpass in 1994 at 21 validation sites in the shrub-dominated part of the watershed (three replicates). Dry bulk density data were obtained for each site by the excavation method (Blake and Hartge, 1986), allowing the calculation of volumetric soil moisture contents.

## 3 Approach

### Investigation Sites

The MF sites 1, 2, 3, 7, and 8, located in the shrub-dominated part of the watershed (**Figure 1**), were selected to investigate the use of SAR/TM synergism to correct the effects of vegetation in the SAR data, in order to obtain an improved estimation of soil moisture content from radar data in the watershed. The MF sites 4, 5, and 6, located in the eastern, grass-dominated side of the watershed, were not included in the analysis because of the limited number of available SAR images. The analysis was performed in four steps:

1) analysis of relationship between SAR and TM data, by comparing the multitemporal values of $\sigma^{\circ}$ and LAI simultaneously;
2) correction of the topographic effects in the radar backscattering signals. The technique involved a subtraction ($\sigma^{\circ} - \sigma^{\circ}_{dry}$); that is, the $\sigma^{\circ}$ from a given image was subtracted by the $\sigma^{\circ}$ from a dry season image. The assumption in this step was that the soil roughness is the only important parameter in the backscattering process in a dry season image. The coefficients derived from this subtraction is referred as $\sigma^{\circ}_{1}$ hereafter.
3) finding of an empirical relationship between $\sigma^{\circ}_{1}$ and LAI. This relation corresponds to the linear regression equation obtained by considering the $\sigma^{\circ}_{1}$ and LAI from four MF sites above mentioned; and
4) correction of the vegetation effects on $\sigma^{\circ}_{1}$ In this step, we calculated the residuals of radar backscattering coefficients ($\sigma^{\circ}_{2}$) for the MF sites by subtracting the measured and the estimated $\sigma^{\circ}_{1}$ values. The measured $\sigma^{\circ}_{1}$ values refer to the SAR signals obtained from the subtraction of $\sigma^{\circ}$ from a dry season image (step 2), while the estimated $\sigma^{\circ}_{1}$ values refer to the SAR signals calculated from the empirical $\sigma^{\circ}_{1}$ –LAI relation.

### Validation Sites

To validate the approach described above, the SAR and soil moisture data acquired in 1994 in the shrub-dominated part of the watershed by Sano et al. (1998) were analyzed applying the same methodology used for the investigation sites. In other words, the soil moisture contents measured during the 1994 ERS-1 SAR overpass were compared with the radar backscattering coefficients at three steps: 1) without any correction; 2) partially corrected for soil roughness; and 3) fully corrected for soil roughness and vegetation effects. The $\sigma^\circ_t$-LAI relation obtained from the investigation sites were applied to account for the vegetation effects. The LAI value for each validation site was derived by linearly interpolating the LAI values obtained in DOYs 194 and 226 (1992). These 1992 dates were the two closest days in relation to the 1994 overpass (**Table 1**).

## 4 Results

### Investigation Sites

**Figure 2** shows a temporal pattern (from April to November, 1992) of both LAI and $\sigma^\circ$ at MF sites 1, 2, 3, 7, and 8. Because the ERS-1 and Landsat satellite overpasses were not coincident, LAI values were linearly interpolated at the ERS-1 overpasses by using two adjacent LAI values. The assumption was that the soil drying was uniform and that there was no rain during the two TM overpasses. For MF sites 1, 2, and 7, we can notice a good degree of similarity between LAI and $\sigma^\circ$, particularly from DOY 160 to DOY 290. The reason for the small temporal $\sigma^\circ$ variation of MF sites 3 and 8 needs to be investigated.

Therefore, we used the $\sigma^\circ$ values from MF sites 1, 2, and 7 to derive the empirical LAI and $\sigma^\circ_t$ relation for the investigation sites (**Figure 3**). All multitemporal $\sigma^\circ$ values (from DOY 135 to DOY 291) were subtracted from the DOY 170 $\sigma^\circ$, since the lowest backscattering coefficients for all MF sites were found on this date. **Figure 3** also shows a consistently higher $\sigma^\circ_t$ values for MF 2, in comparison with MF 1 and MF 7 with similar LAI values. This suggests a higher soil moisture contents for the MF 2, so that this site was not included in the derivation of $\sigma^\circ_t$ –LAI relation. The obtained linear regression equation was:

$$\sigma^\circ_t \text{ (dB)} = -10.69 + 148.58 \text{ LAI}$$

### Validation Sites

The SAR and field data from 21 investigation sites in the shrub-dominated part of the watershed is shown in **Table 2**. **Figure 4a** shows the linear relationship between SAR backscattering coefficients and volumetric soil moisture content for the validation sites, without any correction for soil roughness and vegetation effects. The correlation was poor ($r^2 = 0.09$). When only soil roughness is corrected by using the subtraction technique, the soil moisture and SAR backscattering correlation was worse ($r^2 = 0.06$, **Figure 4b**). Consequently, correction for soil roughness without considering vegetation effects may not improve soil moisture estimation in arid and semiarid regions.

When both soil roughness and vegetation effects were corrected for, the soil moisture and SAR backscatter correlation was substantially improved (**Figure 4c**). The relatively high $r^2$ and slope values ( 0.66 and 0.30, respectively, if we do not include Sites 3, 4, and 5, which probably presented some laboratory or field experimental error) indicate that the techniques used in this study to account for roughness and vegetation effects were successful. However, the correlation is still lower than expected or lower than those obtained from other regions such as in agricultural areas or in temperate regions ($r^2 > 0.80$, e.g., Bernard et al., 1992). The reason for this low correlation can be the spatial variability of soil moisture in the study area, which was discussed in details by Sano et al. (1998).

## 5 Concluding Remarks

In this study, we used a microwave and optical synergism to improve the soil moisture content estimation using C-band ERS-1 SAR data in a semiarid region. The following were the major findings:

a) the C-band radar backscattering coefficients were highly, positively correlated with leaf area index derived from Landsat TM data. This indicates that the sparse vegetation in semiarid regions does contribute significantly to the radar backscatter observed with SAR systems. This was mainly due to low soil moisture contents in the semiarid regions (< 20%). In other words, the contribution from soil moisture in the backscattering process in semiarid regions is not significantly higher than that from vegetation, so that the influence of vegetation becomes significant in a multitemporal radar data analysis.

b) the techniques used in this study to account for soil roughness and vegetation effects allowed us to obtain improved soil moisture estimates and, upon validation, it may become an easy way to correct for effects of these two parameters without using multipolarization or multifrequency SAR data.

c) the $\sigma^\circ$-LAI relation obtained from the investigation sites (MF sites) performed well for some of the validation sites; nevertheless, future research involving more multitemporal data and more vegetation types needs to be conducted to obtain a more generical relationship.

## 6 Acknowledgments

Special thanks are due to Steve Land of EOSAT Corp., who provided the Landsat TM images at no cost. Drs. Alain Vidal and Denis Troufleau did the SAR image processing at the CEMAGREF/ENGREF, Montpellier, France. This research was partially supported by VEGETATION project at the USDA-ARS Water Conservation Laboratory, NASA EOS Program (NASA Ref. Num. NAG-W2425), NASA-EOS Interdisciplinary Research Program in Earth Sciences (NASA-IDP-88-086), National Science Foundation Grant # BSC-8920851, and NASA Landsat Team grant (# S-41396-F). The assistance and cooperation of personnel at USDA ARS Southwest Watershed Research Center in Tucson and at USDA ARS Tombstone facility were also greatly appreciated.

## 7 References

Baret, F. (1995). Use of spectral reflectance variation to retrieve canopy biophysical characteristics. In: Danson, M. (ed.), *Advances in Environmental Remote Sensing*, John Wiley, New York.

Beaudoin, A.; Deshayes, M.; Piet, L.; Stussi, N.; and Le Toan, T. (1994). Retrieval and analysis of temperate forest backscatter signatures from multitemporal ERS-1 data over hilly terrain. *1st Symp. ERS-1 Pilot Project*, Toledo, Spain, 23-25 June 1994, pp. 283-289.

Benallegue, M.; Normand, N.; Galle, S.; Dechambre, M.; Taconet, D.; Vidal-Madjar, D.; and Prevot, L. (1994). Soil moisture assessment at a basin scale using active microwave remote sensing: the AGRISCATT'88 airborne campaign on the Orgeval watershed. *Int. J. Remote Sens.*, vol. 15, n. 3, pp. 645-656.

Benallegue, M.; Taconet, O.; Vidal-Madjar, D.; and Normand, M. (1995). The use of radar backscattering signals for measuring soil moisture and surface roughness. *Remote Sens. Envir.*, vol. 53, pp. 61-68.

Bernard, R.; Martin, P.; Thony, J.; Vauclin, M.; and Vidal-Madjar, D. (1982). C-band radar for determining surface soil moisture. *Remote Sens. Environ.*, vol. 12, pp. 189-200.

Blake, G.R.; and Hartge, K.H. (1986). Bulk density. In: *Methods of Soil Analysis*, Part 1, Physical and Mineralogical Methods (A. Klute, ed.), Ed. Madison, WN:ASA/SSA, Chap. 13, pp. 363-375, 2nd ed.

Cognard, A.L.; Loumagne, C.; Normand, M.; Olivier, P.; Ottle, C.; Vidal-Madjar, D.; Louahala, S.; and Vidal, A. (1995). Evaluation of the ERS1/synthetic aperture radar capacity to estimate surface soil moisture: two-year results over the Naizin watershed. *Water Resour. Res.*, vol. 31, n. 4, pp. 975-982.

Dubois, P.C.; van Zyl, J.; and Engman, T. (1995). Measuring soil moisture with imaging radars. *IEEE Trans. Geosci. Remote Sens.*, vol. 33, n. 4, pp. 915-926.

Gelderman, F.W. (1970). *Soil survey of Walnut Gulch Experimental Watershed, Arizona.* Report, Soil Conserv. Serv. and Agric. Res. Serv., USDA.

Kustas, W.P.; and Goodrich, D.C. (1994). Preface. *Water Resour. Res.*, vol. 30, n. 5, pp. 1211-1225.

Laur, H. (1992). *Derivation of backscattering coefficients* $\sigma^o$. In: ERS-1 SAR.PRI Products, European Space Agency Publication, Nevilly, France.

Moran, M.S.; Jackson, R.D.; Slater, P.N.; and Teillet, P.M. (1992). Evaluation of simplified procedures for retrieval of land surface reflectance factors from satellite sensor output. *Remote Sens. Environ.*, vol. 41, pp. 169-184.

Moran, M.S.; Rahman, A.F.; Washburne, J.C.; Goodrich, D.C.; Weltz, M.A.; and Kustas, W.P. (1996). Combining the Penman-Monteith equation with measurements of surface temperature and reflectance to estimate evaporation rates of semiarid grassland. *Agr. For. Meteorol.*, vol. 80, pp. 87-109.

Qi, J.; Chehbouni, A.; Huete, A.R.; Kerr, Y.H.; and Sorooshian, S. (1994). A modified soil adjusted vegetation index. *Remote Sen. Environ.*, vol. 48, pp. 119-126.

Sano, E.E.; Huete, A.R.; Troufleau, D.; Moran, M.S.; and Vidal, A. (1998). Relation between ERS-1 synthetic aperture radar data and measurements of surface roughness and moisture content of rocky soils in a semiarid rangeland. *Water Resour. Res. (in press).*

Troufleau, D.; Vidal, A.; Beaudoin, A.; Moran, M.S.; Weltz, M.A.; Goodrich, D.C.; Washburn, J.; and Rahman, A.F. (1997). Optical-microwave synergy for estimating surface sensible heat flux over a semiarid rangeland. *Remote Sens. Reviews*. vol. 15, pp. 113-132.

Washburne, J.C. (1994). *A distributed surface temperature and energy balance model for a semiarid watershed.* University of Arizona, Department of Hydrology and Water Resources, 412 pp. (Ph.D. Dissertation).

Table 1. Dates for the Acquisition of Remotely Sensed and Soil Moisture Data for the WG'92 Experiment.

| Day of Year, 1992 | Landsat TM | ERS-1 SAR | Soil Moisture Sampling |
|---|---|---|---|
| 114 | yes | | yes |
| 116 | | yes | |
| 130 | | | yes |
| 135 | | yes | |
| 146 | | | yes |
| 162 | yes | | yes |
| 170 | | yes | |
| 178 | yes | | yes |
| 194 | yes | | |
| 210 | | | yes |
| 226 | yes | | yes |
| 240 | | yes | |
| 258 | | | yes |
| 274 | yes | | yes |
| 275 | | yes | |
| 290 | | | yes |
| 291 | | yes | |
| 306 | yes | | |
| 310 | | yes | |
| 326 | yes | | |
| 206[a] | | yes | yes |

[a] Image acquired in 1994

Table 2. Synthetic Aperture Radar and Field Data from the 21 Validation Sites Located in the Shrub-dominated Part of the Walnut Gulch Experimental Watershed (1994 data).

| Sampling Point | UTM (East-West) | UTM (North-South) | Backscattering Coefficient (dB) | Soil Moisture ($cm^3/cm^3$) |
|---|---|---|---|---|
| 1 | 3512550 | 585919 | -9.39 | 8.13 |
| 2 | 3511915 | 586178 | -8.56 | 9.58 |
| 3 | 3511214 | 586882 | -8.67 | 7.74 |
| 4 | 3509980 | 586177 | -9.18 | 3.93 |
| 5 | 3510284 | 585769 | -8.29 | 6.25 |
| 6 | 3505697 | 593802 | -9.99 | 10.00 |
| 7 | 3506746 | 594404 | -8.97 | 8.01 |
| 8 | 3507806 | 593359 | -8.99 | 5.41 |
| 9 | 3507567 | 592558 | -8.19 | 7.90 |
| 10 | 3511154 | 588333 | -7.86 | 9.30 |
| 11 | 3513025 | 588458 | -7.92 | 18.78 |
| 12 | 3512517 | 588488 | -8.11 | 15.90 |
| 13 | 3512751 | 589841 | -7.78 | 15.11 |
| 14 | 3511811 | 589109 | -8.73 | 11.59 |
| 15 | 3512092 | 589711 | -9.47 | 11.67 |
| 16 | 3511383 | 589706 | -8.88 | 9.51 |
| 17 | 3511000 | 589044 | -9.29 | 11.58 |
| 18 | 3512040 | 590393 | -9.61 | 11.15 |
| 19 | 3511716 | 590388 | -8.49 | 9.31 |
| 20 | 3510398 | 592299 | -10.08 | 10.94 |
| 21 | 3508993 | 592309 | -9.00 | 7.77 |

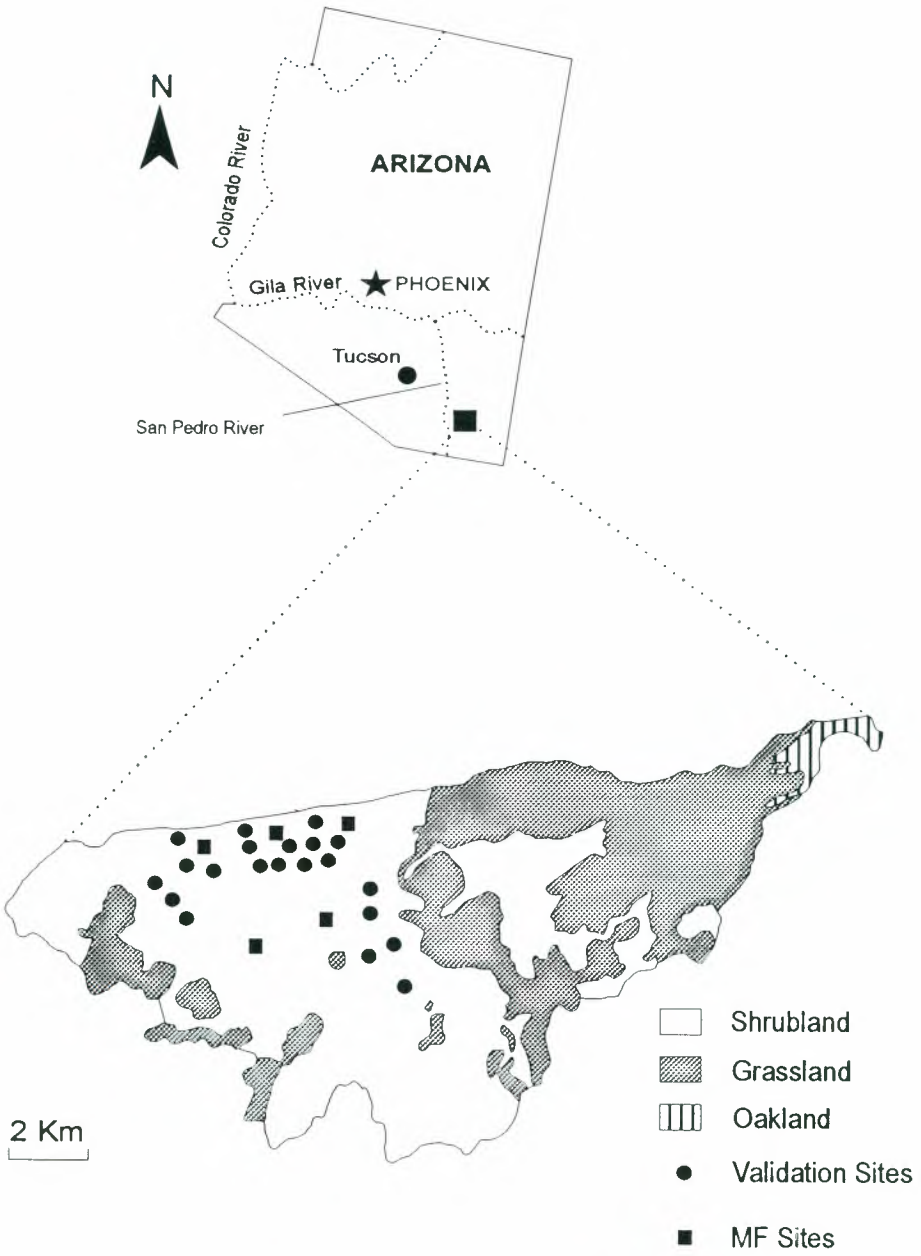


Fig. 1 – Map of the Walnut Gulch Experimental Watershed showing its location in the State of Arizona.

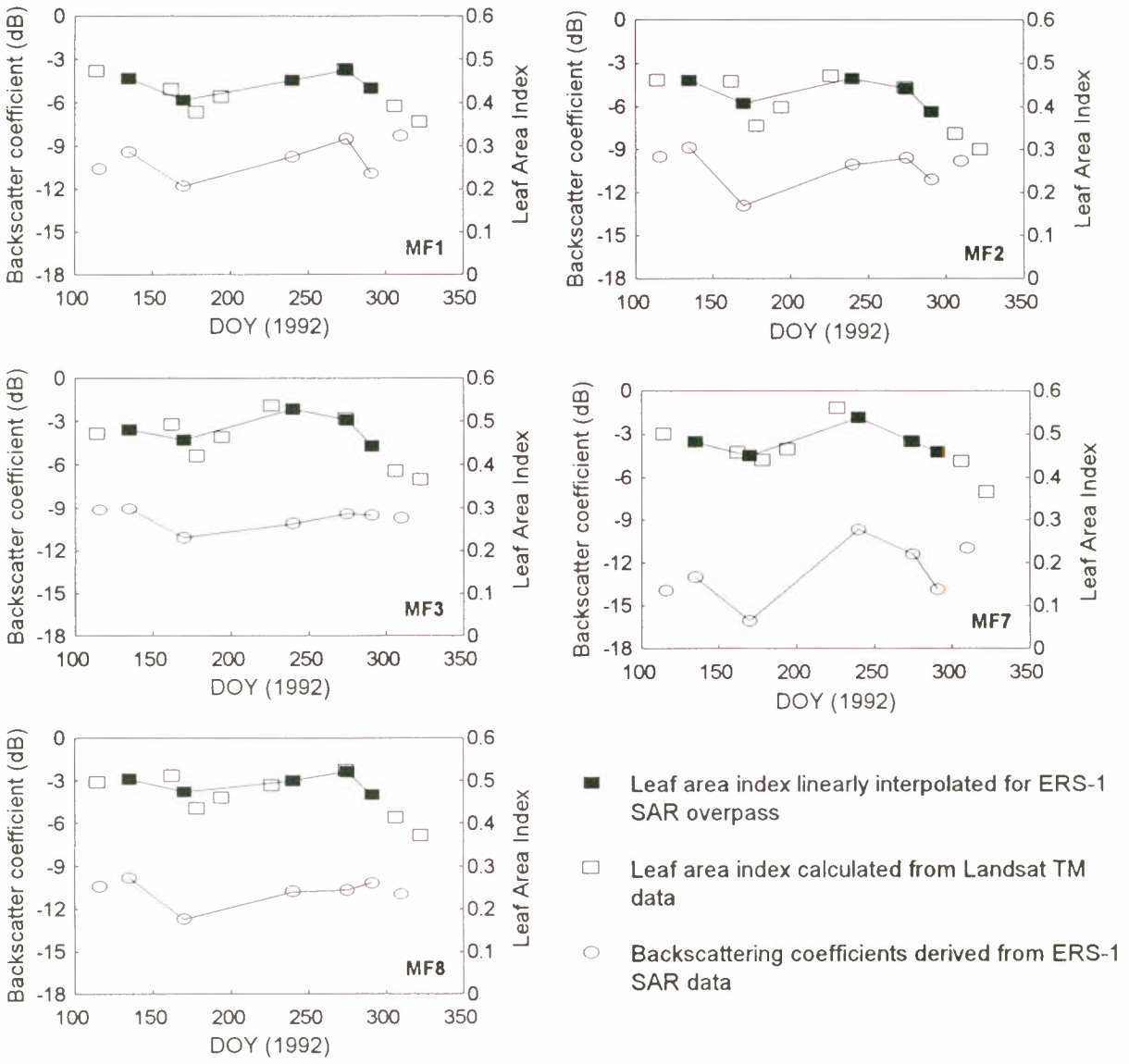


Fig. 2 – Temporal patterns of the backscattering coefficients and leaf area indices for Metflux stations 1, 2, 3, 7, and 8.

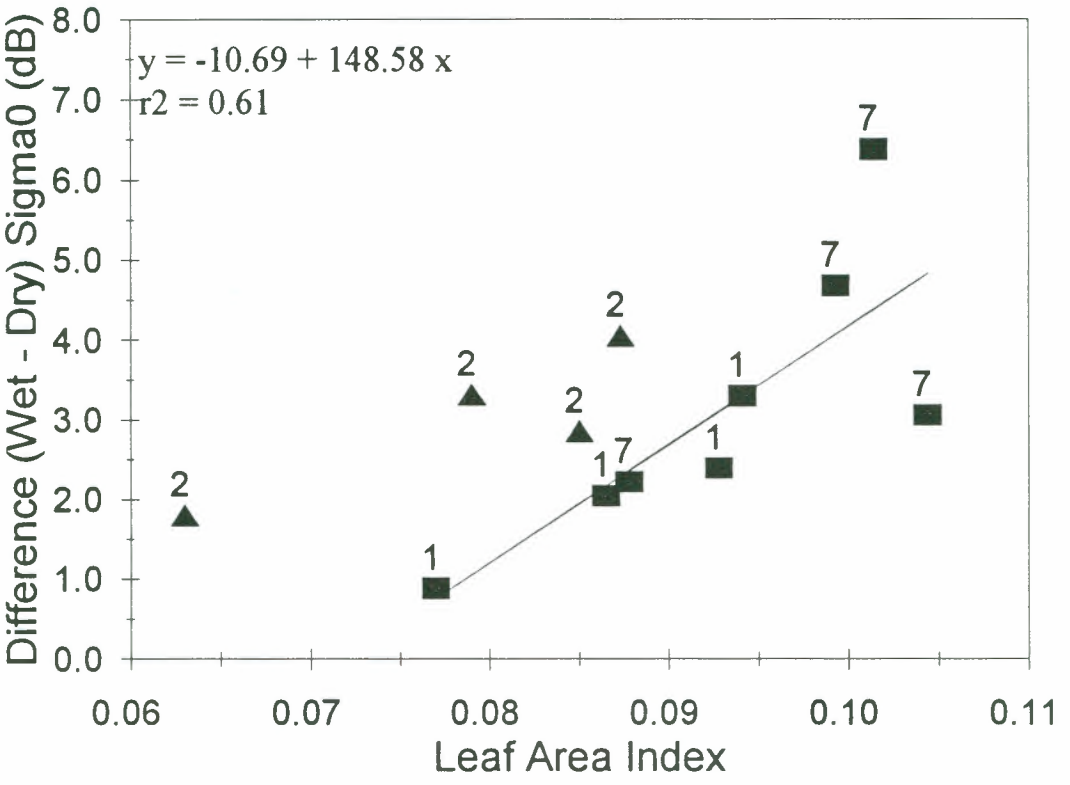


Fig. 3 – Scatterplot between radar backscattering coefficients and leaf area indices for MF stations 1, 2 and 7. Numbers above symbols represent MF sites. Data from MF 2 were not included in the regression analysis because of the probable high soil moisture content.

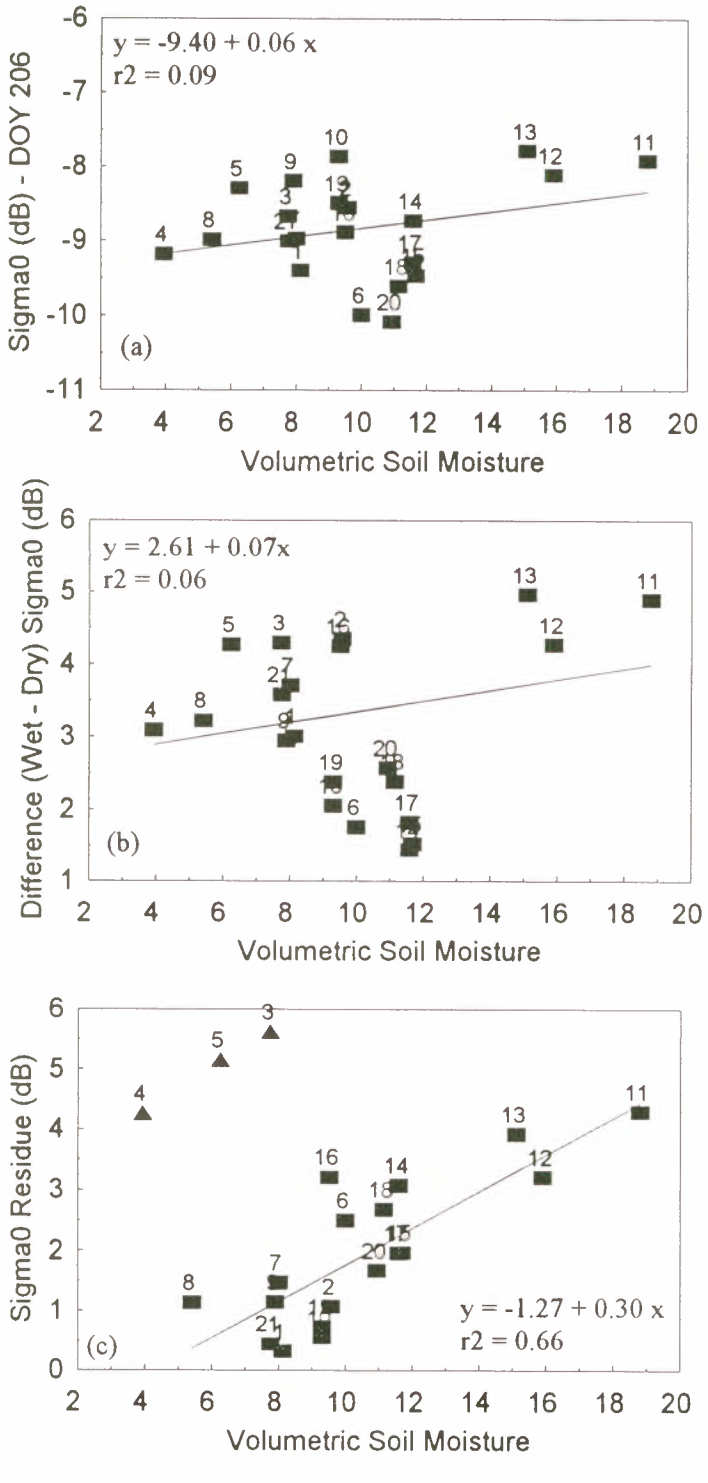


Fig. 4 – Scatterplot between radar backscattering coefficients and soil moisture content for validation sites (a) without any correction for soil roughness and vegetation effects; b) correcting for soil roughness effects; and (c) correcting for both soil roughness and vegetation effects. Sigma0 = radar backscattering coefficient. Sites 3, 4, and 5 were not included in the regression analysis due to a probable experimental or field measurement error).

# ERS SAR Landuse Images generated by the ESRIN Interferometric Quick-Look Processor for the Analysis and Monitoring of Land Surface Characteristics

**Betlem Rosich & Maurizio Fea**

*European Space Agency (ESA/ESRIN)*, via G. Galilei, C.P. 64, 00044 Frascati, Italy
ph: (+39.06) 94180.945/940, fax: (+39.06) 94180.280, e-mail: (brosich,mfea)@esrin.esa.it

**ABSTRACT**

An interferometry related application that has recently attracted a lot of interest from the scientific community is the exploitation of the coherence information derivable from ERS SAR image data to evaluate land surface characteristics and its changes in time. Interferometric techniques can provide very valuable and unique information for monitoring land surface changes, regardless the cloud cover (which makes difficult the use of optical data) or the strong wind conditions (which makes less reliable the use of SAR intensity images only). This paper briefly describes the information content in these coherence images and provides and example of the exploitation of this information over an area in Central America. The example here presented has been processed with an ERS SAR Interferometric Quick Look (IQL) processor developed at ESRIN. The main characteristics of this processor and its key outputs are also described in the paper.

*Keywords:* SAR Interferometry, Coherence, Land Use.

## 1. INTRODUCTION

The confidence on the enormous potential of SAR Interferometry is increasing every day. This regards not only the most known applications as the generation of Digital Elevation Models (DEM) or the detection of surface movements, but particularly those applications related to land use analysis and monitoring. However, there is still the need to investigate and better understand the real potential and limitation of these techniques, and this is the purpose of the work being still carried out.

The paper is focussed on the use of interferometric images for land use analysis and change monitoring. The ERS mission characteristics make possible to create interferometric pairs with different time interval between two acquisitions over the same area. This interval of time ranges from the minimum 1 day during the Tandem mission (which is the minimum time elapse between space-borne SAR images available today), to 3 days, 35 days and any multiple of them.

Clearly, the information contained in an interferometric pair depends strongly on the amount of time between the acquisitions. Limiting the discussion to land use applications, we can say that tandem pairs are the best suited for land use analysis while pairs with longer time interval are more suited for the analysis of surface changes.

## 2. METHODOLOGY

An interferometric pair of ERS SAR images (i.e. a pair of complex SAR images acquired over the same area at different times) can provide valuable information. On the one hand, by combining the phase information of both images (either using ERS.SAR.RAW or ERS.SAR.SLC products, where the phase information is still present), an interferogram can be generated. The interferogram represents the phase difference between the two images and therefore, it is the starting point for the further derivation of DEM or for the analysis of surface vertical movements.

On the other hand, the correlation between the two complex SAR images provides information related to the "similarities" between both data acquired and so between the characteristics of the surface at the two acquisition dates. This particular correlation is known as *interferometric coherence* ($\gamma$) and can be estimated as:

$$\gamma = \frac{E\{\mathrm{Im}_1 \cdot \mathrm{Im}_2^*\}}{\sqrt{E\{|\mathrm{Im}_1|^2\} \cdot E\{|\mathrm{Im}_2|^2\}}}$$

being $\mathrm{Im}_1$ one of the complex SAR images (ERS.SAR.SLC product) of the interferometric pair and $\mathrm{Im}_2$ the other complex SAR image over the same area.

The module of the interferometric coherence varies between 0 and 1 and clearly, the measured coherence will mainly depend on the time interval between acquisitions and on the surface characteristics (assuming a perfect co-registration between the two images).

Basically, as shorter is the time interval between acquisitions, less possible are the changes in the surface between acquisitions and therefore, higher may be the final coherence. However, the level of coherence for the same time interval between acquisitions will depend on the type of surface illuminated. On one hand, it will depend on how quickly the surface can change and on the other hand, on the scattering mechanism taking place on the surface.

Let's image two extreme cases: a very arid surface such as a desert and a very dynamic one, such the ocean. In the first case, interferometric coherence will be high event for long time intervals between acquisitions. However, in the second case, the changes in the surface are so rapid, that even for acquisitions very close in time, the correlation of the images will be very low. Clearly, between these two extreme cases, we can find any other situation.

From this brief discussion, the potential of the interferometric coherence for identifying different kinds of surfaces and for monitor their evolution in time is clear. In fact, it is particularly useful when it is combined with the traditional SAR intensity, since both informations (intensity and coherence) are proved to provide complementary information. .

In order to exploit the information provided by the coherence image, a new kind of ERS SAR product is being evaluated namely the Interferometric Land Use (ILU) image. It is generated from a pair of ERS SAR acquisitions by combining three derived dataset as follows: the mean SAR intensity of both acquisitions, usually visualised in the RGB *green* channel, the difference between both SAR intensities, usually in the *blue* channel, and the interferometric coherence, usually in the *red* channel. The result is a colour composite image joining the traditional information provided by two single SAR images with the additional information provided by the coherence between them.

This basic idea has been already applied over some areas in Europe (Wegmuller, 1996 and Borgeaud, 1996), and the interesting results obtained strongly stimulate to continue investigating the possibilities of this technique.

The ILU images presented in this paper are generated with an ERS SAR Interferometric Quick Look processor installed at ESRIN (in Frascati, Italy), which is briefly described section 4.

## 3. AN EXAMPLE OVER CENTRAL AMERICA

A Tandem pair over an area of about 100 km x 560 km over Mexico and Guatemala, has been processed with the IQL and corresponding ILU and IBP images are presented here (fig.2 and fig.3). The SAR tandem pair was acquired the 8th/9th of April 1996 (ERS-1 Orbit 24742, ERS-2 Orbit 5069). A map of the area is shown in fig.1. Several features can be observed in these images.

First of all, a global overview of the images gives an idea of the variety of land surfaces in the area. The *Laguna de los Terminos* appears in the top of the images (fig2 & fig.3). As it is expected, very low coherence is obtained over the water. Going south, we arrive at a quite flat area where some forest and cultivated areas can be distinguished. The level of the topography can be easily derived from the IBP image when we take into account that the altitude of ambiguity for this interferometric pair is approximately 90 m. This means that the change in altitude for each colour fringe in the IBP image is about 90 m. Therefore, the wide fringes appearing south of *Laguna de los Terminos*, indicates a maximum change in altitude of around 320 m from east to west (less than 4 fringes are obtained). The Salinas River (fig.4) is clearly present in blue in the ILU image (low coherence, low intensity and notable change in intensity), with the cities of Emilio Zapata and Tenosiqueda Pino Suarez appearing in yellow (high coherence, high SAR intensity, low intensity change) close to the river.

It is interesting to see the loss of coherence that takes place when we pass from the plain scarcely vegetated plain (red areas in the ILU image) to the *Meseta Agua Escondida* (mostly green in the ILU). This change in coherence (fig.4) shows the characteristic coherence behaviour of forest areas. Due to the fact that over forest, the dominant backscattering mechanism is the volumetric one, and due also to the effect of wind and small variations in the trees leaves, the two SAR complex signals present low correlation over forest.

It can also be observed that as the topography gets higher, the interferometric fringes are narrower, following the height variations in a similar to the iso-altitude curves in a topographic map. South to the *Sierra de los Cuchumanes*, the volcanic area is clearly visible in the image (fig.5). The Atitlan Lake is present on the left of the image and the volcanoes Toliman, Atitlan, Fuego and Agua appear from west to east. Inhabited areas around the volcanoes show up as bright yellow spots, among which the city of Guatemala is particularly visible in the eastern part of the image.

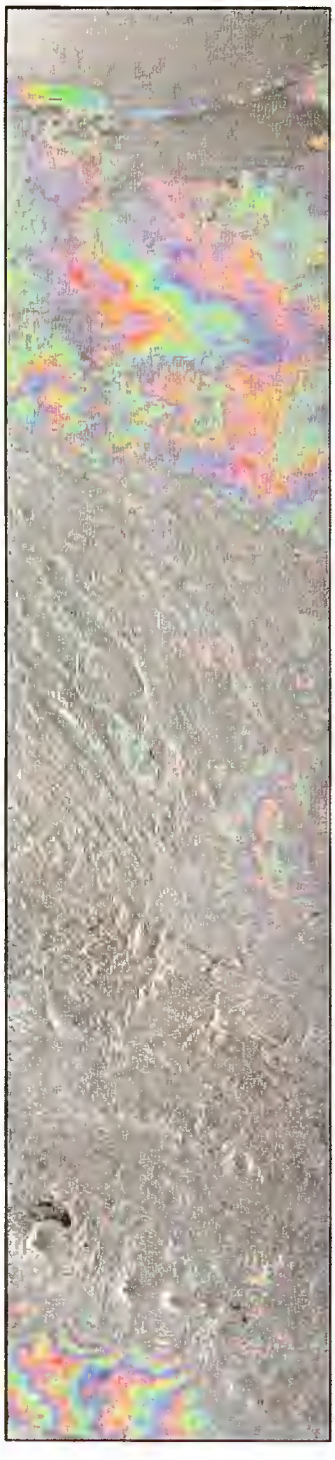

Fig. 2 IBP image

Fig. 3 ILU image


Fig.1 Map of the area with the location of the processed data.

Fig. 4. Zoom of the ILU image over Salinas River and Meseta Agua Escondida.

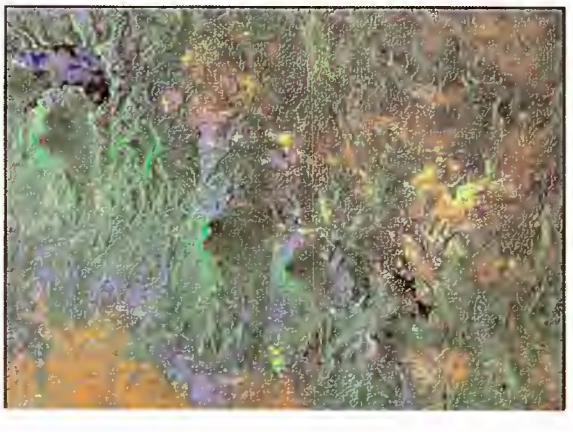

## 4. AN ERS SAR INTERFEROMETRIC QUICK LOOK (IQL) PROCESSOR

A prototype implementation of this IQL processor exists at ESRIN. This is a high-throughput SAR processor running on a Silicon Graphics Power Challenge platform equipped with an 8xR8000 CPU and 2 GBytes of memory. The IQL can process, in one operation, large (>1000 km) strips of ERS SAR acquisitions.

The output products of the IQL processor are:

- **Interferometric Browse Product (IBP)**
  A combination of three images:
  - Interferometric Phase (ranging from 0 to $2\pi$ projected on a colour wheel)
  - Interferometric Coherence (ranging from 0 to 1)
  - Averaged SAR Radiometric Intensity of both acquisitions.

  The coherence is used as a soft mask: over areas with a coherence $\approx$ <- 0.2, the SAR intensity is shown (grey-scale); over the areas with coherence $\approx$ -> 0.2 the Interferometric Phase is shown.
  The IBP product gives mainly an indication of the ERS SAR data quality for topographic mapping applications. Distinct interferometric fringes could be further unwrapped to produce a Digital Elevation Model (DEM) of the Earth's surface.

- **Interferometric Land Use (ILU)**
  A Red-Green-Blue (RGB) combination of three quantities:
  - Interferometric Coherence (Red channel)
  - Averaged SAR Radiometric Intensity of both acquisitions (Green channel)
  - SAR Radiometric Intensity Change between the two acquisitions (Blue channel).

  The ILU product gives an indication of the ERS SAR data quality for classification of Land Surface type. The relation between ILU image colours (assuming the above channel assignments) and land surface type under current investigation gives the following preliminary understanding:

  ***Red/Yellow*** areas correspond to high coherence, high intensity, small intensity changes - typically urban centres, bare rock, stable agricultural fields

  ***Green*** areas correspond to low coherence, high intensity, small intensity changes - typically heavily vegetated areas (e.g. forest) and/or layover regions (e.g. mountain peaks/ridges)

  ***Blue*** areas correspond to low coherence, low intensity, big intensity changes: typically water surfaces (sea & inland water) and possibly soil transport in desert areas.

The IBP and ILU products can be produced at Browse resolution (configurable, currently at 200 m pixels), ground-range projected.

In addition, the IQL processor can output separately, each of the following information:
- SAR Radiometric Intensity image for the first acquisition
- SAR Radiometric Intensity image for the second acquisition
- Interferometric Coherence image
- Interferometric Phase image.

In terms of performance, the Interferometric Quick Look processor can generate IBP + ILU products in under 10 minutes from raw data on disk for an area corresponding to a ERS full frame (i.e. 100 x 100 km$^2$). The processing of a 100 x 1000 km$^2$ strip takes typically under 2 hours, including input of raw data from either a Sony D-1 digital cassette or Digital Linear Tape (DLT).

Some ILU and IBP images wide world are being systematically processed at ESRIN with the IQL processor. They can be consulted on-line at the following web address: http://earth1.esrin.esa.it/INSI

## 4. CONCLUSIONS

The Interferometric Browse and Land Use products generated by an Interferometric Quick Look processor are useful tool for a preliminary analysis of large regions, specifically of areas where a Digital Elevation Model could be derived with good accuracy, and of the type of surface cover and use. In this sense, the ILU image can constitute a first glance analysis over a large region along the satellite orbit to quickly identify urban settlements, deforested or burned forest areas, water bodies, cultivated zones, and so on. Finally, it is suggested to explore the ESA Web site at:

***http://earthnet.esrin.esa.it***

where information about the current and future Earth Observation missions of ESA and related operations are described.

### References

U. Wegmuller, C.L. Werner, Land Applications using ERS-1/2 Tandem Interferometry. *Fringe 96 Workshop on ERS SAR Interferometry,* Zurich, Sep. 1996 (ESA SP-406)

M. Borgeaud, U. Wegmuller, On the use f ERS SAR Interferometry for the retrieval of Geo- and Bio-Physical Information. *Fringe 96 Workshop on ERS SAR Interferometry*, Zurich, Sep. 1996 (ESA SP-406).

# Participants

# PARTICIPANTS



Ana María Hernández
CONAE
Paseo Colón, 751
Capital Federal
1063 - Buenos Aires
**ARGENTINA**

Carlos Moyano
CONAE
Paseo Colón, 751
Capital Federal
1063 - Buenos Aires
**ARGENTINA**

Natália Marlenko
Universidad de Buenos Aires
Departamento de Geografia
Puán 408, C.P 1406
Buenos Aires
**ARGENTINA**

Haydee Karszenbaum
CAERCEM-CONICET
Satellite Radiometry Division
Julian Alvarez, 1218
Buenos Aires
**ARGENTINA**

Graciela Marin
Secr. de Mineria de la Nacion
Servicio Geologico-Minero Argentino
Av. Julio A. Roca 651 - 10ºPiso
Buenos Aires
**ARGENTINA**

Laura Adriana Frulla
Consejo Nac.de Invest. Científicas
y Técnicas
Julián Alvarez 1218
Buenos Aires
**ARGENTINA**

Alberto Giraldez
CONAE
R. Freire 4450
Buenos Aires
**ARGENTINA**

Oscar Humberto Bustos
Universidad Nacional Córdoba
Ciudad Universitaria
Córdoba
**ARGENTINA**

Mirta A. Raed
Universidad Nacional de Luján
Depto. Ciencias Básicas
C.C. 221 Rutas 5 Y 7
Luján - Buenos Aires
**ARGENTINA**

Guillermo Raúl Angeles
Universidad Nacional del Sur
Curso Internacional 1998
12 de Octubre y San Juan - 4to.piso Univ
Bahia Blanca
**ARGENTINA**

Sophie Moreau
ABTEMA
Casilla 14248
La Paz
**BOLIVIA**

José Carlos Ferreira
CESP
Rua Bicudo de Brito, 771
Vila Guarani - Jabaquara
São Paulo 04316-060 SP
**BRASIL**

Carbeny Capote
Universidade de São Paulo
Depto. Geologia Econômica/Geociências
Caixa Postal 11.348
São Paulo 05422-970 SP
**BRASIL**

Humberto N. Mesquita Jr.
Universidade de São Paulo
Rua do Matão, 321 - Travessa 14
Cidade Universitária
São Paulo
**BRASIL**

Ricardo José de Paula S. Guimarães
INPE
Rua Dr. Souza Alves, 123
Centro - Taubate
**SP - BRASIL**

Marco Antonio Chamon
INPE
Av. dos Astronautas, 1758 - Jd.Granja
São José dos Campos
**SP - BRASIL**

Corina da Costa Freitas
INPE
DPI/OBT
Av. dos Astronautas, 1758 - Jd. Granja
São José dos Campos
**SP -BRASIL**

Ana Carolina P. Rezende
INPE
Av. dos Astronautas, 1758
Jardim da Granja
São José dos Campos
**SP - BRASIL**

Camilo Daleles Rennó
INPE
Av. dos Astronautas, 1758 - Jd.da Granja
São José dos Campos
**SP - BRASIL**

Francisco Maldonado
INPE - SERE
Av. dos Astronautas, 1758 - Jd.Granja
São José dos Campos
**SP - BRASIL**

Ivan Bergier Tavares de Lima
INPE
Av. dos Astronautas, 1758
Caixa Postal 515
São José dos Campos
**SP - BRASIL**

Luciano Vieira Dutra
INPE
DPI
Av. dos Astronautas, 1758 - Jd. Granja
São José dos Campos
**SP - BRASIL**

Manoel Araújo Sousa Jr.
INPE
DPI
Av. dos Astronautas, 1758 - Jd. Granja
São José dos Campos
**SP - BRASIL**

Marcelo Cordeiro Thalês
INPE
Av. dos Astronautas, 1758
Jardim da Granja
São José dos Campos
**SP - BRASIL**

Marcelo Francisco Sestini
INPE
Av. dos Astronautas
Caixa Postal 515 - Jd. Granja
São José dos Campos
**SP - BRASIL**

Milton Cezar Ribeiro
INPE
DPI
Av. dos Astronautas, 1758 - Jd. Granja
São José dos Campos
**SP - BRASIL**

Nilo Sérgio de Oliveira Andrade
INPE
Pós-Graduação/Sere
Av. dos Astronautas, 1758 - Jd. Granja
São José dos Campos
**SP - BRASIL**

Sidnei João Siqueira Sant'Anna
INPE
DPI
Av. dos Astronautas, 1758 - Jd.Granja
São José dos Campos
**SP - BRASIL**

Tomoyuki Ohara
INPE
Depto. DSR
P.O.Box 515
São José dos Campos
**SP - BRASIL**

Vanessa Madrucci
INPE
Av. dos Astronautas, 1758
Jardim da Granja
São José dos Campos
**SP - BRASIL**

Wilson Cabral de Sousa Junior
INPE
Pós-Graduação/Sere
Av. dos Astronautas, 1758 - Jd. Granja
São José dos Campos
**SP - BRASIL**

Gerardo Kuntschik
INPE
IAI
Av. Astronautas, 1758 -Jd. Granja/CP 515
São José dos Campos
**SP - BRASIL**

Sérgio Monteiro Soares
INPE - DPI
Av. dos Astronautas , 1758 - Jd. Granja
São José dos Campos
**SP - BRASIL**

Roberto Pinto Souto
INPE
Rua Plutão, 70
Jardim da Granja
São José dos Campos
**SP - BRASIL**

Maurício dos Santos Simões
INPE - SERE
Av. Astronautas, 1758 - Jd.Granja
São José dos Campos
**SP - BRASIL**

Eduardo Viegas Dalle Lucca
INPE
DPI
H 09 A - Apto. 301 - CTA
São José dos Campos
**SP - BRASIL**

Darcton Policarpo Damião
Centro Técnico Aeroespacial
IEAv - Instituto de Estudos Avançados
C.P. 6044
São José dos Campos
**SP - BRASIL**

Fabio Roque da Silva Moreira
INPE
Rua Itororó, 571
Apto. 46 B - Vila Piratininga
São José dos Campos
**SP - BRASIL**

Enrico Campos Pedroso
Universidade Estadual de Campinas
Instituto Geociências/DMG
Cx. Postal 6152
Campinas
**SP - BRASIL**

Fátima N.S. Medeiros
Cybernetic Vision Group
University of São Paulo
Caixa Postal 369
São Paulo
**SP - BRASIL**

Hiromi Suzana Y. Sassagawa
INPE
Rua Itororó, 571 - 75A - V. Bandeirantes
São José dos Campos
**SP - BRASIL**

María Silvia Pardi Lacruz
INPE
Sere
Av. Astronautas, 1758 - Jd.Granja
São José dos Campos
**SP - BRASIL**

Antonio Henrique Correia
INPE
CTA
São José dos Campos
**SP - BRASIL**

Andréa de Fátima Carvalho Ferreira
Instituto Tecnológico de Aeronaútica
CTA - Hotel de Trânsito de Oficiais
Apto 313, Vila das Acácias
São José dos Campos
**SP - BRASIL**

Maddalena Turchini
INPE
Rua Afonso C. de Siqueira, 278
Ed. Itajai, App. 33 - Vila Adyana
São José dos Campos
**SP - BRASIL**

Luciana Spinelli Araujo
INPE
Rua Major João Prudente, 111
Vila Prudente
Caçapava
**SP - BRASIL**

João Firminiano da Conceição Filho
Universidade Estadual Paulista
Rua 10, 2417
Santana
Rio Claro
**SP - BRASIL**

Humberto Costa de Souza
Instituto de Ciências e de Computação
Rua Vitor Manoel de Souza Lima, 328
Apartamento 37 - Jardim Bethânia
São Carlos
**SP - BRASIL**

Nelson Delfino D'Avila Mascarenhas
Universidade Federal de São Carlos
Dept. de Computação
Rodovia Washington Luiz, Km 235 C.P 676
São Carlos
**SP – BRASIL**

Eduardo Piza Pereira Gomes
Escola Politécnica USP
Rua Curucá, 299
Centro
Tietê
**SP - BRASIL**

Edson Alves Carrilho
Instituto de Cartografia Aeronáutica
Praça Senador Salgado Filho, s/n
Aeroporto Santos Dumont - Prédio do ICA
Centro - Rio de Janeiro
**RJ - BRASIL**

Clayton de Souza Pontes
PETROBRÁS - Petroleo Brasileiro S/A
E&P, GEREX, GEINOF
Av. República do Chile, 65 - sala 1301E
Rio de Janeiro
**RJ - BRASIL**

Alexandre Veiga do Amaral
Secretaria Municipal de Meio Ambiente
Rua Afonso Cavalcante, 445 - Sala 1237
Cidade Nova
Rio de Janeiro
**RJ – BRASIL**

Cláudia Ribeiro França
Secretaria Municipal de Meio Ambiente
Rua Afonso Cavalcante, 445 - Sala 1237
Cidade Nova
Rio de Janeiro
**RJ - BRASIL**

Elena Quevedo Benegas
Secretaria Municipal de Meio Ambiente
Rua Afonso Cavalcante, 445 - Sala 1237
Cidade Nova
Rio de Janeiro
**RJ - BRASIL**

Gilberto Hernandes
PETROBRÁS - Petroleo Brasileiro S.A
Rua General Canabarro, 500
7 andar - Maracanã
Rio de Janeiro
**RJ - BRASIL**

Thomaz Corrêa e Castro da Costa
Universidade Federal de Viçosa
Depto. de Engenharia Florestal
Av. P.H. Rolfs, s/n
Viçosa
**MG - BRASIL**

Lázaro Nonato V. de Andrade
Universidade do Estado da Bahia
Estrada das Barreiras, s/n
Naranduba
Salvador
**BA - BRASIL**

Flávia Regina Álvares de Lima Ramalho
Análise de Imagem
Rua do Bom Jesus, 143 - 4 Pavimento
Bairro do Recife
Recife
**PE - BRASIL**

Ana Lúcia Bezerra Candeias
Univ. Federal de Pernambuco
DECart
Av. Prof. Morais Rego, 1235 Cid. Univer.
Recife
**PE - BRASIL**

Klaus Leite Pinto Vasconcellos
Universidade Federal Pernambuco
Departamento de Estatística
Caixa Postal 7851
Recife
**PE - BRASIL**

Luciano B. da Silva
Universidade Federal de Pernambuco
Departamento de Estatística
Cidade Universitária
Recife
**PE - BRASIL**

Antonio Jorge Heluy do Nascimento
INCRA
Av. Santos Dumont
Anil
São Luis
**MA - BRASIL**

José Reinaldo Moura Bezerra
INCRA
Av. Santos Dumont
Anil
São Luis
**MA - BRASIL**

Mario Ivan Cardoso de Lima
IBGE
DIGEO/N
Av. Serzedelo Correa, 331
Belém
**PA - BRASIL**

Jaime Mauricio Cardoso Ferreira
Ministério do Exército
Av. Marechal Bittencourt, 97
Compensa I
Manaus
**AM - BRASIL**

Edvaldo Sousa Alves
INCRA
Edifício Palácio do Desenvolvimento
15 andar
Setor Bancário Norte - Brasília
**DF - BRASIL**

Ricardo Araújo Pereira
INCRA
Edifício Palácio do Desenvolvimento
15 andar
Setor Bancário Norte - Brasília
**DF - BRASIL**

Luiz Rios
Faculdades Objetivos
SGA Sul 913, Bloco III - Direção
Asa Sul
Brasília
**DF - BRASIL**

Moacir da Silveira
Diretoria de Serviço Geográfico
Q.G.Ex - Bloco F - 2º Piso
Setor Militar Urbano
Brasília
**DF - BRASIL**

Candido Nunes da Silva Filho
Estado Maior do Exército
Q.G.Ex. - Bloco A
3º - Piso - SMU
Brasília
**DF - BRASIL**

Sylvio Lucas da Gama Imbuzeiro
Estado Maior do Exército
Q.G.Ex. - Bloco A
3º - Piso - SMU
Brasília
**DF - BRASIL**

Selma Aparecida Gomes
FASE-Fed. de Órgãos p/Assist.Social e Educ.
Travessa Quintino Bocaiúva, 1259
Nazaré
Belém
**PA - BRASIL**

Calvero Moreira Xavier
INCRA
Edifício Palácio do Desenvolvimento
15 andar
Setor Bancário Norte - Brasília
**DF - BRASIL**

Francisco Rodrigues Fernandes Neto
INCRA
Edifício Palácio do Desenvolvimento
15 andar
Setor Bancário Norte - Brasília
**DF - BRASIL**

Joselisa Maria Chaves
Universidade de Brasília
SQN 303 - Bloco A
Apartamento 203 - Asa Sul
Brasília
**DF - BRASIL**

Sérgio Almeida
CISIPAM
SPO - Área 5 - Quadra 3
Bloco J - Setor Policial
Brasília
**DF - BRASIL**

Romualdo Potengy Revoredo Filho
Diretoria de Serviço Geográfico
Q.G.Ex - Bloco F - 2º Piso
Setor Militar Urbano
Brasília
**DF - BRASIL**

Carlos Roberto Fernandes de Oliveira
Estado Maior do Exército
Q.G.Ex. - Bloco A
3º - Piso - SMU
Brasília
**DF - BRASIL**

Oswaldo Oliva Neto
Exército Brasileiro
Q.G.Ex - Bloco H
Setor Militar Urbano - COTER
Brasília
**DF - BRASIL**

Hiroyuki Nemoto
Inst.Bras.Meio Amb.e Rec.Nat.Renováveis
Sain L4 - Norte
Asa Norte - Ed. Sede IBAMA
Brasília
**DF - BRASIL**

Silvana Pataro Moreira
Inst. Bras. Meio Ambiente e Rec. Naturais
DIRCOF-BRA 95/028
Sain-Av L-4 Norte, Ed. Sede IBAMA
Brasília
**DF - BRASIL**

José Mauro Martini
Dep.Nac.de Produção Mineral
ACSE I - Conj. 03
Lote 21 - Centro
Palmas
**TO - BRASIL**

Nelson Almeida Jr.
Empresa Brasileira Pesquisa Agropecuaria
DEPT. CPAP
Rua 21 de Setembro, 188 - P.O.Box 109
CORUMBA
**MS - BRASIL**

Aquiles Krukoski
INCRA-PR
Rua Dr. Faivre 1210
Centro
Curitiba
**PR - BRASIL**

Stela Maris Alves Ascenço
INCRA-PR
Rua Dr. Faivre 1210
Centro
Curitiba
**PR -BRASIL**

Lúcia Pinto Camargo
Universidade Federal de Santa Catarina
Departamento de Ecologia e Zoologia
Campus Universitário - Trindade
Florianópolis
**SC - BRASIL**

Alvaro Alves F. Ferreira
1ª. Divisão de Levantamento
Rua Cleveland, 250
Santa Tereza
Porto Alegre
**RS - BRASIL**

Marcelo Alessandro Nunes
Inst. Bras. Meio Ambiente e Rec. Naturais
DIRCOF-BRA 95/028
Sain-Av L-4 Norte, Ed. Sede IBAMA
Brasília
**DF - BRASIL**

Edson Eyji Sano
Empresa Brasileira de Pesquisa Agropecuária
Centro de Pesquisa do Cerrado
BR. 020 Km 18 - CP 08223
Planaltina
**DF - BRASIL**

Edileusa Melo
Empresa Brasileira Pesquisa Agropecuaria
Dept. CPAP
Rua 21 de Setembro, 188 - P.O.Box 109
CORUMBA
**MS - BRASIL**

Nelson Carlos Rosot
Universidade Federal do Paraná
Departamento de Silvicultura e Manejo
Rua Bom Jesus, 650 - Juvevê
Curitiba
**PR - BRASIL**

Rossini Barbosa Lima
INCRA-PR
Rua Dr. Faivre 1210
Centro
Curitiba
**PR - BRASIL**

Yeda Oliveira
Embrapa
Rua do Marfim 8
Barreirinha
Curitiba
**PR - BRASIL**

José Roberto Provesi
Universidade do Vale do Itajaí
R.Uruguai,458 - Centro
Itajaí
**SC - BRASIL**

Paulo Roberto Pelufo Foster
Universidade Federal de Pelotas
CPMet / FMet Centro de Pesq. Meteor.
Rua Com. Joaquim Dias, 166
Colina do Sul - Pelotas
**RS - BRASIL**

Chuck Livingstone
Canada Centre For Remote Sensing
Applications Division
588 Booth Street - 3nd Floor
Ottawa - Ontario - K1A 0Y7
**CANADA**

Paul Budkewitsch
Canada Centre For Remote Sensing
Applications Division
588 Booth Street - 3nd Floor
Ottawa - Ontario - K1A 0Y7
**CANADA**

Jorge Galbiati
Universidad Catolica de Valparaiso
Casilla 4059
Valparaiso
**CHILE**

Martin C. Farias S.
Universidad Catolica do Chile
Centro de Percepción Remota y SIG
Av. Vic. Mackenna - 4860
Macul Santiago
**CHILE**

Héctor Allende O.
Universidad Técnica Federico Santa María
Casilla 110-V
Valparaíso
**CHILE**

Carlos G. Pattillo B.
Pontificia Universidad Catolica
Centro de Percepción Remota & SIG
Av. Vic. Mackenna – 4860, Cas. 306
Santiago 22 - Correo Interno 906
**CHILE**

Chris J. Oliver
Defense Research Agency
St.Andrews Road
Malvern - Worcestershire - WR14 3 PS
**UK**

Shaun Quegan
Sheffield Centre for Earth Obs. Science
University of Sheffiel/HICKS Bldg.
Hunsfield Road - Sheffield S3 7RH
**UK**

Thuy Le Toan
CESBIO
18 Edouard Belin - Bpi 2801
F-31055 Toulouse
**FRANCE**

Olimpia Arellano Neri
Faculty of Engineering
DEPFI-UNAM
Cd. Universitaria-Apdo. Postal 70-256
Mexico
**DF - MEXICO**

Jorge Lira
Instituto de Geofísica
Circuito Institutos
A.P. 22-560 - Delegación Tlalpan
**MEXICO**

Tan-Duc Guyenne
ESA/ESTEC
Keplerlaan 1
2200-AG Noordwijk
**THE NETHERLANDS**

Dar Roberts
University of California
Dept. of Geography, EH3611
Santa Barbara CA 93106
**USA**

Maurizio Fea
ESA/ESRIN, Earth Obs. Dept.
via Galileo Galilei
Frascati
**ITALY**

Paul Rosen
JPL, California Inst. of Technology
4800 Oak Grove Drive
Pasadena, CA 91109-8099
**USA**

**European Space Agency**
**Agence spatiale européenne**

*Contact: ESA Publications Division*
c/o ESTEC, PO Box 299, 2200 AG Noordwijk, The Netherlands
Tel (31) 71 565 3400 - Fax (31) 71 565 5433